

**CHARACTERISATION OF FRICTION STIR
WELDED AISI-SS316L AND P91 PIPES**

Thesis submitted by

SURESH GAIN

**Doctor of Philosophy
(Engineering)**

**DEPARTMENT OF MECHANICAL ENGINEERING
FACULTY COUNCIL OF ENGINEERING & TECHNOLOGY
JADAVPUR UNIVERSITY
KOLKATA, INDIA**

2023

**JADAVPUR UNIVERSITY
KOLKATA-700032, INDIA**

INDEX NO. 97/19/E

1. Title of Thesis:

CHARACTERISATION OF FRICTION STIR WELDED AISI-SS316L AND P91 PIPES

2. Name, Designation & Institution of the Supervisor:

Dr. Suman Kalyan Das

Associate Professor,

Mechanical Engineering Department,

Jadavpur University, Kolkata-700032

3. List of Publications (Referred Journals):

i) **Suresh Gain**, Suman Kalyan Das, Sanjib Kumar Acharyya, Dipankar Sanyal, “Exploring Friction Stir Welding for joining 316L Steel Pipes for Industrial Applications: Mechanical and Metallurgical Characterization of the joint and Analysis of Failure,” Engineering Failure Analysis, 150, 107331 (2023). <https://doi.org/10.1016/j.engfailanal.2023.107331> [SCIE]

ii) **Suresh Gain**, Suman Kalyan Das, Sanjib Kumar Acharyya, Dipankar Sanyal, “Friction Stir Welding of Industrial grade AISI 316L and P91 Steel Pipes: A Comparative Investigation based on Mechanical and Metallurgical properties”, International Journal of Pressure Vessel and Piping, 201,104865(2023). <https://doi.org/10.1016/j.ijpvp.2022.104865>. [SCIE]

iii) **Suresh Gain**, Dipankar Sanyal, Sanjib Acharyya, Suman Kalyan Das “Friction Stir Welding of AISI-316L steel pipes: Mechanical and Metallurgical characterization of the joint”, Proceedings of the Institution of Mechanical Engineers Part E: Journal of Process Mechanical Engineering 236(6) 2382-2393 (2022), <https://doi.org/10.1177/09544089221096104>. [SCI]

iv) **Suresh Gain**, Suman Kalyan Das, Dipankar Sanyal, Sanjib Acharyya “Mechanical and metallurgical properties of friction stir welded joint of austenitic steel pipes at position control mode”, Materials Today: Proceedings, 65(8), 3912-3919 (2022), <https://doi.org/10.1016/j.matpr.2022.07.197>. [SCOPUS]

v) **Suresh Gain**, Suman Kalyan Das, Dipankar Sanyal, Sanjib Kumar Acharyya “Influence of Process Parameters on Microstructure and Mechanical Properties of Friction Stir Welded P91 Industry Grade Steel Pipes”, Welding in the world, WITW-D-22-00556. (**SCIE, Communicated**)

4. List of Patents: Nil

5. List of Presentations in National/ International Conferences:

i) **Suresh Gain**, Suman Kalyan Das, Dipankar Sanyal, Sanjib Acharyya, “Effect of Spindle Speed on Austenitic Stainless Steel Pipe Weldment Produced by Friction Stir Welding.” 1st International Conference on Mechanical Design and Manufacturing, IEST Shibpur, 27th - 28th April 2023, Paper ID: ICMDM 2023-222.

ii) **Suresh Gain**, Suman Kalyan Das, Dipankar Sanyal, Sanjib Acharyya “Mechanical and metallurgical properties of friction stir welded joint of austenitic steel pipes at position control mode.” International Conference on Materials Science and Sustainable Manufacturing Technology, Coimbatore, 20th-21st May 2022, Paper ID ICMSSMT2022141.

iii) **Suresh Gain**, Suman Kalyan Das, Dipankar Sanyal, Sanjib Acharyya “Friction stir welding of austenitic stainless-steel pipes” National Conference on Sustainable Development and Circular Economy in Civil Engineering, Heritage Institute of Technology Kolkata, 16th-17th December 2021, Paper ID: A-084.

iv) **Suresh Gain**, Suman Kalyan Das, Dipankar Sanyal, Sanjib Acharyya. “Effect of process parameters on Force trends during friction stir welding of AISI-316L pipes”, International Conference on Thermal Engineering and Management Advances, hosted by Jalpaiguri Government Engineering College, 19th-20th December 2020, Paper ID: MM1570.

6. List of Book Chapters:

i) Suman Kalyan Das, **Suresh Gain**, Prasanta Sahoo, “Friction Stir Welding”. Springer Nature Switzerland AG, J. Paulo Davim (Ed.), pp 1-39, 13th February 2021.

ii) **Suresh Gain**, Dipankar Sanyal, Sanjib Kumar Acharyya, Suman Kalyan Das, “Effect of process parameters on Force trends during friction stir welding of AISI-316L pipes, Advances in Thermal Engineering, Manufacturing, and Production Management, Springer Nature Singapore, S. Kumar Ghosh et al.(Ed.), pp 279-287, 02nd July 2021.

This page is left blank intentionally

STATEMENT OF ORIGINALITY

I Suresh Gain registered on 03.06.2019 do hereby declare that this thesis entitled “CHARACTERISATION OF FRICTION STIR WELDED AISI-SS316L AND P91 PIPES” contains literature survey and original research work done by the undersigned candidate as part of Doctoral studies.

All information in this thesis have been obtained and presented in accordance with existing academic rules and ethical conduct. I declare that, as required by these rules and conduct, I have fully cited and referred all materials and results that are not original to this work.

I also declare that I have checked this thesis as per the “Policy on Anti Plagiarism, Jadavpur University, 2019”, and the level of similarity as checked by iThenticate software is 3%

Signature of Candidate: *Suresh Gain*

Date: *28/02/2023*

Certified by Supervisor(s):

(Signature with date, seal)

1. *Sumankalyan Das*
28/02/2023

Associate Professor
Dept. of Mechanical Engineering
Jadavpur University, Kolkata-32

This page is left blank intentionally

CERTIFICATE FROM THE SUPERVISOR

This is to certify that the thesis entitled "*CHARACTERISATION OF FRICTION STIR WELDED AISI-SS316L AND P91 PIPES*" submitted by *Shri Suresh Gain*, who got his name registered on *03.06.2019* for the award of *Ph.D. (Engineering)* degree of *Jadavpur University* is absolutely based upon his own work under my supervision and neither his thesis nor any part of the thesis has been submitted for any degree/ diploma or any other academic award anywhere before.

Suman Kalyan Das
28/02/2023

(Dr. Suman Kalyan Das)

Signature of the Supervisor

and date with Official Seal

Associate Professor
Dept. of Mechanical Engineering
Jadavpur University, Kolkata-32

Acknowledgement

I had the chance to work with significant number of individuals who extend their hands with caring assistance to accomplish this thesis. Hence, it is my sincere duty to acknowledge the support and contributions of all and express gratitude to all who were directly or indirectly associated with this research work.

First of all, I express my deepest gratitude to my supervisor, Dr. Suman Kalyan Das for his encouragement, inspiration, invaluable guidance and support throughout my PhD work. His consistent direction, consolation, dynamic help and sagacious contributions helped this dissertation to be successful. I truly feel honoured to have received the chance to work under his direction. I have learned a lot from him starting from his cool, calm, composed personality, controlling adverse situation as well as to guide and counsel, without which completion of thesis work would have been extremely difficult. His personal character combined with professional ethics will remain a source of inspiration for the rest of my life.

I am thankful to Prof. Dipankar Sanyal and Prof. Sanjib Kumar Acharyya for their active support, insightful comments, and valuable suggestions. I could learn and enrich myself a lot during every moment of the interaction that I had with them. I have been fortunate to work under them and learn from their gigantic knowledge and experience which has given my career a legitimate shape. I would also like to express my gratitude to Prof. Akshay Kumar Pramanick and Prof. Pravash Chandra Chakraborty, for providing me access the FSW laboratory facilities at Department of Metallurgical and Material Engineering.

I would also like to acknowledge Ministry of Steel, DST, Government of India for providing financial assistance and sophisticated equipment for the research work. A special thanks to Dave Hofferbert and his team at Bond technologies, USA for installing the pipe welding turntable and educating me to operate the FSW machine. The experimental work was carried out in Friction Stir Welding lab of the Department of Metallurgical and Material

Engineering of Jadavpur University, Kolkata. Hence, thanks are also due to all technical staffs related to welding technology centre of Jadavpur University, Kolkata.

I would also like to express my gratitude to Dr. Mrinmoy Jana, Dr. Sukalpa Chaudhury, for their continuous and useful support and advice. Mrinmoy you educated me in operating the INSTRON-5581 where tensile tests could be successfully carried out. Thanks are due to the lab mates of FFDA, who constantly helped me for mechanical testing. I would like to convey my thanks to the Head of the Department, the Laboratory-in-Charge, Machine Element Laboratory and all the academic and technical staffs of Mechanical Engineering Department, Jadavpur University, Kolkata. Apart from that, I would also like to thank to my friends, juniors, seniors past and present members of machine elements laboratory whose support, suggestions and contributions favoured me for carrying out this work.

I do heartily acknowledge the support received during characterisation studies viz. Scanning Electron Microscope, Energy Dispersive X-ray Analysis, X-ray diffraction facility of welded samples at Central Glass and Ceramic Research Institute (CGCRI), Kolkata and National Institute of Technology, Durgapur (NIT Durgapur). Moreover, I would like to thank all the researchers in this field whose published literatures have greatly helped me in getting an insight towards the experimental work. I could really acquire a lot of knowledge from these publications.

Finally, I thank my beloved parents whose unimaginable perseverance, unlimited love, and unapproachable commitment have been stupendous. I thank to my wife and my daughter for their patience and constant support without which this work couldn't have been finished. I would like to thank all my family members specially my elder brother (Shri Sukesh Chandra Gain), who plays a huge role in my life. Without his support it would have never been possible to complete the journey of doctoral research.

Suresh Gain

About the Author

Shri Suresh Gain completed his B.Tech in Mechanical Engineering in 2010 from Kalyani Government Engineering College (under West Bengal University of Technology now MAKAUT). In 2013, he completed M.Tech in Mechanical Engineering under Production specialization from Indian Institute of Technology, Delhi. Thereafter he was employed as Assistant Professor of Mechanical Engineering Department in Camellia School of Engineering and Technology, Kolkata for five years. Due to his inclination towards higher studies, he joined as a Research Fellow for a project sponsored by Ministry of Steel (DST), Govt. of India at Jadavpur University. Shri Gain is interested in doing research in welding techniques and material characterization. He has six years of research experience on friction stir welding and friction stir processing. So far he has published five papers in peer- review journals and two book chapters.

This page is left blank intentionally

I would like to dedicate this work to

My parents & my nation

This page is left blank intentionally

Abbreviations

A_{cm}: Curve in Fe-C equilibrium diagram separating stable austenite zone above and austenite-cementite zone below

A_{C1}: Curve in Fe-C equilibrium diagram separating stable austenite-ferrite and austenite-cementite zone above and ferrite and ferrite-cementite zone below

A_{C3}: Curve in Fe-C equilibrium diagram separating stable austenite zone above and austenite-ferrite zone below

A_{C3}/A_{C1}: Zone between A_{c1} and A_{c3} curves

AS: Advancing side

ASS: Austenitic stainless steel

BCC: Body-centered cubic

BCT: Body-centered tetragonal

BM: Base metal

CGHAZ: Coarse-grain heat affected zone

CS: Carbon steel

CDRX: Continuous dynamic recrystallization

CRT: cathode ray tube

CSEF/M: Creep strength enhanced ferritic/martensitic

DDRX: Discontinuous dynamic recrystallization

DRX: Dynamic recrystallization

EBS: Electron backscatter diffraction

EDM: Electro discharge machining

EDX: Energy-dispersive X-ray

FC: Force control

FCC: Face-centered cubic

FESEM: Field emission scanning electron microscope

FGHAZ: Fine-grain heat affected zone

FSS: Ferritic stainless steel

FSW: Friction-stir welding

GTAW: Gas tungsten arc welding

HAGB: High angle grain boundary

HAZ: Heat affected zone

HIC: Hydrogen-induced cracking

HSLA: High-strength low alloy

ICHAZ: Inter-critical heat affected zone

LAGB: Low angle grain boundary

MX: Spheroidal precipitates of FCC carbides or nitrides of V or Nb.

M_s: Martensite start temperature

M_f: Martensite finish temperature

M₂₃C₆: Stable FCC structured carbides of Fe, Cr, Mo and Mn

ODS: Oxide dispersion strengthened

OM: Optical microscope

PAG: Prior austenite grain

PAGB: Prior austenite grain boundary

PC: Position control

PCBN: Polycrystalline cubic boron nitride

RS: Retreating side

SAW: Submerged-arc welding

SCC: Stress-corrosion cracking

SDSS: Super duplex stainless steel

SEM: Scanning electron microscope

SMAW: Shielded-metal arc welding

SS: Stainless steel

SZ: Stir zone

TEM: Transmission electron microscope

TMAZ: Thermo-mechanically affected zone

Cr(V,Nb)N: Z phase

(Fe,Cr)₂(Mo,W): Laves phase

UTS: Ultimate tensile strength

W-Re: Tungsten rhenium

XRD: X-ray diffraction

YS: Yield strength

This page is left blank intentionally

Table of Contents

List of Publications and Presentations from the Thesis	i
Statement of Originality	iii
Certificate from the supervisor	v
Acknowledgement	vii
About the Author	ix
Dedication	xi
Glossary	xiii
Table of Contents	xvii
List of Figures	xxvii
List of Tables	xxxix
Abstract	xli
<i>Chapter 1: Introduction</i>	<i>1-21</i>
1.1 Introduction	1
1.2 Fundamental of friction stir welding	3
1.3 Advantages and limitations of friction stir welding	7
1.4 Joining configurations	9
1.5 Friction stir welding setup	10
1.5.1 Linear welding setup	10
1.5.1.1 Dedicated setups for FSW	10

1.5.1.2 Adapting a milling machine – low cost setup	11
1.5.2 Pipe or circular welding setup	13
1.5.2.1 Attaching a rotary mandrel unit	13
1.5.2.2 Portable setups – larger scale welding	14
1.5.2.3 Customized setup	14
1.5.3 Machine Control modes in FSW setups	15
1.5.3.1 Position control mode	15
1.5.3.2 Force control mode	15
1.5.4 Issue of the presence of ejection hole	15
1.5.4.1 Designing a wedge to transfer the hole	16
1.6 Applications of friction stir welding	17
1.6.1 Marine and shipbuilding industries	17
1.6.2 Aerospace and aviation industries	17
1.6.3 Railway industry	18
1.6.4 Automobile industry	18
1.6.5 Power Plants	19
1.7 Present work	19
1.8 Outline of the thesis	20
1.9 Contribution of the thesis	20
1.10 Closure	21

Chapter 2: Literature review	23-50
2.1 Introduction	23
2.2 Friction stir welding tools	24
2.2.1 Tool materials for friction stir welding	25
2.2.1.1 Tool material for low-temperature alloys	26
2.2.1.2 Tool materials for high-temperature alloys	27
2.2.1.2.1 Polycrystalline cubic boron nitride (PCBN) tool	27
2.2.1.2.2 Tungsten (W) based tool	27
2.2.1.2.3 Other tool materials	28
2.2.2 Geometry of friction stir welding tool	28
2.2.2.1 Shoulder diameter and surface features	29
2.2.2.2 Pin geometry and features	31
2.3 Parameters in friction stir welding	34
2.3.1 Spindle speed	34
2.3.2 Welding speed	34
2.3.3 Tilt angle of tool	35
2.3.4 Other parameters	35
2.3.4.1 Forces	35
2.3.4.2 Plunge depth	36
2.4 Work-piece material	36
2.4.1 Friction stir welding of aluminum alloys	37
2.4.2 Friction stir welding of magnesium alloys	37
2.4.3 Friction stir welding of copper alloys	38

control mode	58
3.5.3 Friction stir welding of P91 pipes in force	
control mode	59
3.6 Sample preparation for weld characterization	60
3.6.1 Sample preparation for study of mechanical	
properties	60
3.6.2 Sample preparation for microstructure study	61
3.7 Study of mechanical properties	62
3.7.1 Hardness study	62
3.7.2 Tensile properties study	64
3.8 Study of metallurgical properties	65
3.8.1 Optical microscope	65
3.8.2 Field emission scanning electron microscope	66
3.8.3 Energy dispersive X-ray analysis	67
3.8.4 X-ray diffraction	68
3.9 Sequence of experiments	69
3.10 Closure	71
<i>Chapter 4: AISI-316L steel pipe welding at position control mode</i>	73-94
4.1 Introduction	73
4.2 Pre-characterization at position control mode	74

4.3 Physical examination of AISI-316L weldments	82
4.3.1 Surface of welded samples	83
4.3.2 Cross section of welded samples	84
4.4 Study of mechanical properties	85
4.4.1 Hardness behaviour	85
4.4.2 Study of tensile properties	87
4.5 Metallurgical study	88
4.5.1 Optical microscopy of welded samples	88
4.5.2 Scanning electron microscopy of welded samples	91
4.5.3 Energy dispersive X-ray analysis of welded samples	93
4.6 Closure	94
<i>Chapter 5: AISI-316L pipe welding at force control mode</i>	<i>95-118</i>
5.1 Introduction	95
5.2 Physical examination of weldments	95
5.2.1 Surface of welded samples	97
5.2.2 Cross section of welded samples	97
5.3 Study of mechanical properties	100
5.3.1 Hardness behaviour	100
5.3.2 Study of tensile properties	102
5.4 Metallurgical study	106

5.4.1 Optical microscopy of welded samples	106
5.4.2 Scanning electron microscopy of welded samples	109
5.4.3 Energy dispersive X-ray analysis of welded samples	114
5.4.4 X-ray diffraction analysis of welded samples	117
5.5 Closure	117
<i>Chapter 6. P91 steel pipe welding at force control mode</i>	<i>119-139</i>
6.1 Introduction	119
6.2 Physical examination of P91 weldments	119
6.2.1 Surface of welded samples	121
6.2.2 Cross section of welded samples	122
6.3 Study of mechanical properties	123
6.3.1 Hardness behaviour	123
6.3.2 Study of tensile properties	125
6.4 Metallurgical study	127
6.4.1 Optical microscopy of welded samples	127
6.4.2 Scanning electron microscopy of welded samples	129
6.4.3 Energy dispersive X-ray analysis of welded samples	133
6.4.4 X-ray diffraction analysis of welded samples	138
6.5 Closure	138
<i>Chapter 7. Comparative study between AISI-316L and P91 pipe</i>	

<i>welding</i>	141-165
7.1 Introduction	141
7.2 Comparison of the weldments based on physical examination	141
7.2.1 Surface of welded samples	143
7.2.2 Cross section of welded samples	143
7.3 Comparison of mechanical properties of weldments	144
7.3.1 Hardness behaviour	144
7.3.2 Study of tensile properties	148
7.4 Comparison of metallurgical characteristics of the weldments	152
7.4.1 Optical microscopy of welded samples	152
7.4.2 Scanning electron microscopy of welded samples	158
7.4.3 Energy dispersive X-ray analysis of welded samples	161
7.4.4 X-ray diffraction analysis of welded samples	164
7.5 Closure	165
Chapter 8. Conclusions and future scope	167-173
8.1 Introduction	167
8.2 Conclusions from the physical examination of weldments	168
8.3 Conclusions from hardness behaviour of weldments	168

8.4 Conclusions from the study of tensile properties	169
8.5 Conclusions from the microstructure study	170
8.6 Conclusions from energy dispersive X-ray analysis of welded samples	171
8.7 Conclusions from X-ray diffraction analysis of the welded samples	171
8.8 Future scope of work	172
<i>References</i>	<i>175-191</i>

This page is left blank intentionally

List of Figures

Figure No.		Page no.
Figure 1.1	Schematic diagram of FSW: (a) Butt joint layout; (b) Tool entering into work piece and (c) Welding nomenclature	2
Figure 1.2	(a) Various heat affected zones and (b) Tilt of FSW tool (exaggerated representation)	5
Figure 1.3	Various regions in a friction stirred weld	6
Figure 1.4	Joint configuration of FSW welding	10
Figure 1.5	Photograph of a linear FSW setup	11
Figure 1.6	Vertical milling machine converted to FSW setup for linear welding	12
Figure 1.7	Circular welding (a) rotary mandrel fitted to existing linear FSW setup and (b) pipes fitted on the mandrel	14
Figure 1.8	(a) Schematic for transfer of exit hole and (b) zoomed view of the wedge where the exit hole will be transferred	16
Figure 2.1	Wear rate of tool vs. rotation of tool in rpm	25
Figure 2.2	Various types of shoulder and pin geometry	28
Figure 2.3	Features and geometry of PCBN coated tool	31
Figure 2.4	Schematic of FSW with respective forces	38
Figure 3.1	FSW tool employed for pipe welding with major dimensions	

	in mm	53
Figure 3.2	Complete friction stir welding setup for pipe welding	54
Figure 3.3	Pipe with backing plate	54
Figure 3.4	Cooling arrangements in the FSW setup	55
Figure 3.5	Description of FSW zones with reference to hot metal working	56
Figure 3.6	Friction stir welding process for pipes	57
Figure 3.7	(a) Outer surface and (b) inner surface of welded pipe	59
Figure 3.8	Tensile test samples cut from P91 pipes	61
Figure 3.9	Polishing machine	62
Figure 3.10	Vickers micro hardness tester	63
Figure 3.11	Hardness measurement scheme for welded samples (a) horizontal scheme (b) vertical scheme	64
Figure 3.12	Universal testing machine with loaded specimen	65
Figure 3.13	Optical microscope setup	66
Figure 3.14	SEM along with the EDX setup	67
Figure 3.15	Flow chart of sequence of experiments	70
Figure 4.1	Variations of (a) Forces, (b) Spindle torque and achieved Z- depth with time for FSW of AISI-316L pipes at 250rpm, 100mm/min and 6mm Z-depth setting	77

Figure 4.2	Variations of (a) Forces, (b) Spindle torque and achieved Z-depth with time for FSW of AISI-316L pipes at 300rpm, 100mm/min and 6mm Z-depth setting	78
Figure 4.3	Variations of (a) Forces, (b) Spindle torque and achieved Z-depth with time for FSW of AISI-316L pipes at 325rpm, 100mm/min and 6mm Z-depth settings	78
Figure 4.4.	Variations of (a) Forces, (b) Spindle torque and achieved Z-depth with time for FSW of AISI-316L pipes at 350rpm, 100mm/min and 6mm Z-depth settings	79
Figure 4.5	Variations of (a) Forces, (b) Spindle torque and achieved Z-depth with time for FSW of AISI-316L pipes at 400rpm, 100mm/min and 6mm Z-depth settings	79
Figure 4.6	Variations of (a) Forces, (b) Spindle torque and achieved Z-depth with time for FSW of AISI-316L pipes at 450rpm, 100mm/min and 6mm Z-depth settings	80
Figure 4.7	Bar-chart comparing the forces at position control mode (a) X-force, (b) Y-force, (c) Z-force, (d) spindle torque	82
Figure 4.8	Groove defects observed during FSW of 316L pipe at position control mode	83
Figure 4.9	Cross sections of FSW sample at position control mode (a) 250rpm and 100mm/min (b) 300rpm and 100mm/min (c) 325rpm and 100mm/min (d) 350rpm and 100mm/min (e) 400rpm and 100mm/min (f) 450rpm and 100mm/min	84

Figure 4.10	Hardness values across the cross section of welded samples	86
Figure 4.11	Maximum hardness of welded samples compared to BM	86
Figure 4.12	Stress vs strain plot of samples welded at PC mode	87
Figure 4.13	Optical micrograph of FSW sample at 250-100-6 (a) SZ - TMAZ (RS), (b) SZ- TMAZ (AS); at 300-100-6 (c) SZ - TMAZ(RS) (d) SZ- TMAZ (AS); at 325-100-6 (e) SZ - TMAZ(RS) (f) SZ- TMAZ (AS)	89
Figure 4.14	Optical micrograph of FSW sample at 350-100-6 (a, b) SZ – TMAZ (RS) and SZ- TMAZ (AS); at 400-100-6 (c, d) SZ – TMAZ (RS) and SZ- TMAZ (AS); at 450-100-6 (e, f) SZ – TMAZ (RS) and SZ- TMAZ (AS)	90
Figure 4.15	SEM images of welded samples (a) 250-100-6, (b) 300-100-6, (c) 325-100-6, (d) 350-100-6, (e) 400-100-6, (f) 450-100-6	91
Figure 4.16	Line EDX analysis of sample welded at 400-100-6 (a) horizontal line plot and (b) corresponding SEM image; (c) vertical line plot and (d) corresponding SEM image	92
Figure 4.17	Line EDX analysis of sample welded at 450-100-6 (a) horizontal line plot and (b) corresponding SEM image; (c) vertical line plot and (d) corresponding SEM image	93
Figure 4.18	The color code used for different element during line EDX analysis for welded samples at position control mode (a) C, (b) Si, (c) S, (d) Cr, (e) Mn, (f) Fe, (g) Ni, (h) Mo	94

Figure 5.1	Identifying parameters for appropriate welding	96
Figure 5.2	Photograph of the top surface of welded joint of AISI-316L pipes for different parameter combinations	98
Figure 5.3	Cross section of FSW AISI-316L steel pipes, samples (a) ASS1 (b) ASS2 (c) ASS3 (d) ASS4	99
Figure 5.4	Cross section of FSW AISI-316L steel pipes, samples (a) ASS5 (b) ASS6 (c) ASS7 (d) ASS8	100
Figure 5.5	Variation in hardness values across the cross section of as received BM and welded samples	101
Figure 5.6	Stress vs strain plot of AISI-316L welded samples	103
Figure 5.7	Yield, ultimate tensile strength and percentage of elongation for AISI-316L BM and welded samples	104
Figure 5.8	Comparison of joint efficiency of AISI-316L samples	105
Figure 5.9	Location of failure for the tensile tested samples	105
Figure 5.10	Optical micrograph of welded AISI-316L steel pipe sample (at 50mm/min) (a) SZ-TMAZ(AS) (ASS1), (b) SZ (ASS1), (c) SZ-TMAZ(RS) (ASS1) (d) SZ-TMAZ(AS) (ASS2), (e) SZ (ASS2), (f) SZ-TMAZ(RS) (ASS2), (g) SZ-TMAZ(AS) (ASS3), (h) SZ (ASS3), (i) SZ-TMAZ(RS) (ASS3), (j) SZ-TMAZ(AS) (ASS4), (k) SZ (ASS4), (l) SZ-TMAZ(RS) (ASS4)	107
Figure 5.11	Optical micrograph of welded AISI-316L steel pipe sample (at 100mm/min) (a) SZ-TMAZ(AS) (ASS5), (b) SZ (ASS5), (c)	

	SZ-TMAZ(RS) (ASS5) (d) SZ-TMAZ(AS) (ASS6), (e) SZ (ASS6), (f) SZ-TMAZ(RS) (ASS6), (g) SZ-TMAZ(AS) (ASS7), (h) SZ (ASS7), (i) SZ-TMAZ(RS) (ASS7), (j) SZ-TMAZ(AS) (ASS8), (k) SZ (ASS8), (l) SZ-TMAZ(RS) (ASS8)	108
Figure 5.12	SEM micrograph of (a) TMAZ-SZ (ASS1), (b) zoomed view of SZ (ASS1), (c) TMAZ-SZ (ASS2), (d) zoomed view of SZ (ASS2), (e) TMAZ-SZ (ASS3), (f) zoomed view of SZ (ASS3), (g) TMAZ-SZ (ASS4), (h) zoomed view of SZ (ASS4)	110
Figure 5.13	SEM micrograph of (a) TMAZ-SZ (ASS5), (b) zoomed view of SZ (ASS5), (c) TMAZ-SZ (ASS6), (d) zoomed view of SZ (ASS6), (e) TMAZ-SZ-BM (ASS7), (f) zoomed view of SZ (ASS7), (g) TMAZ-SZ-BM (ASS8), (h) zoomed view of SZ (ASS8)	111
Figure 5.14	Average grain size for different weld zones (a) Sample ASS3 and (b) Sample ASS4	112
Figure 5.15	Line EDX analysis of sample ASS2: (a), (b) secondary electron images, (c) line EDX color code for A-B line, (d) average composition for A-B and (e) average composition for C-D	113
Figure 5.16	Elemental EDX map of welded sample ASS8 (a) secondary images of map EDX (b) average composition for EDX map (c) color code for map EDX	114
Figure 5.17	Photograph of used and new FSW tools	116
Figure 5.18	XRD patterns of (a) BM, (b) sample ASS2, (c) sample ASS4	116

Figure 6.1	Identifying parameters for appropriate welding of P91 steel pipes	120
Figure 6.2	Photograph of the top surface of the P91 steel pipes welded at different parameter combinations	121
Figure 6.3	Cross section of FSW P91 steel pipes, sample number (a) FSS3 (b) FSS4 (c) FSS6 (d) FSS7	121
Figure 6.4	Hardness values across the cross section of welded samples	124
Figure 6.5	Maximum hardness of the welded samples compared to BM	124
Figure 6.6	Stress vs strain plot of P91 welded specimens	126
Figure 6.7	Tensile tested sample (a) top view (b) side view	126
Figure 6.8	Yield and ultimate tensile strength of P91 base metal and welded samples	127
Figure 6.9	Optical micrograph of FSW P91 steel pipe samples FSS1 (a) TMAZ-RS and BM (b) SZ (c) SZ and TMAZ-AS; FSS2 (d) TMAZ-RS and BM (e) SZ (f) SZ and TMAZ-AS; FSS3 (g) TMAZ-RS and BM (h) SZ (i) SZ and TMAZ-AS; FSS4 (j) TMAZ-RS and BM (k) SZ (l) SZ TMAZ-AS and BM	128
Figure 6.10	Optical micrograph of FSW P91 steel pipe samples for FSS5 (a) TMAZ-RS and BM (b) SZ (c) TMAZ-AS; FSS6 (d) SZ, TMAZ-RS and BM (e) SZ (f) SZ, TMAZ-AS and BM; FSS7 (g) SZ and TMAZ-RS (h) SZ (i) SZ and TMAZ-AS; FSS8 (j) SZ and TMAZ-RS (k) SZ (l) TMAZ-AS and BM	129

Figure 6.11	SEM images of as received P91 steel pipes	130
Figure 6.12	SEM micrograph of P91 weldments, sample FSS1 (a) SZ-TMAZ (b) SZ; FSS2 (c) SZ-TMAZ (d) SZ; FSS3 (e) TMAZ (f) SZ; FSS4 (g) TMAZ (h) SZ	132
Figure 6.13	SEM micrograph of P91 weldments, sample FSS5 (a) SZ-TMAZ (b) SZ; FSS6 (c) TMAZ (d) SZ; FSS7 (e) SZ-TMAZ (f) SZ; FSS8 (g) TMAZ (h) SZ	133
Figure 6.14	Line EDX analysis of sample FSS5 (a), (b) secondary electron images for line EDX analysis and (c), (d) corresponding line plots	134
Figure 6.15	The colour code used for different elements during line EDX (a) C (b) O (c) Si (d) S (e) Cr (f) Mn (g) Fe (h) Mo	135
Figure 6.16	Line EDX analysis of sample FSS6 (a), (b) secondary electron images for line EDX analysis and (c), (d) corresponding line plots	135
Figure 6.17	Line EDX analysis of sample FSS7 (a), (b) secondary electron images for line EDX analysis and (c), (d) corresponding line plots	136
Figure 6.18	Map EDX analysis of welded sample (a) Map for EDX analysis (b) corresponding map plots (c) C (d) O (e) Si (f) S (g) Cr (h) Mn (i) Fe (j) Mo	137
Figure 6.19	X-ray diffraction of welded samples	138

Figure 7.1	Photograph of the top surface of welded joints of AISI-316L and P91 pipes	143
Figure 7.2	Surface appearances along the cross section of the weldments (a) AISI-316L pipe weldment (b) P91 pipe weldment	144
Figure 7.3	Variation of hardness values across the weld cross section (a) AISI-316L welded samples (b) P91 welded samples	145
Figure 7.4	Comparison of maximum hardness values for AISI-316L and P91 welded samples in horizontal direction	146
Figure 7.5	Variation of hardness values as a function of distance from top surface (a) AISI-316L welded samples (b) P91 welded samples	147
Figure 7.6	Comparison of maximum hardness values for AISI-316L and P91 welded samples in vertical direction	147
Figure 7.7	Yield and ultimate tensile strength of AISI-316L pipe weldments	149
Figure 7.8	Yield and ultimate tensile strength of P91 pipe weldments	150
Figure 7.9	Failure location of tensile tested samples (a, b) AISI-316L welded samples and (c, d) P91 welded sample	150
Figure 7.10	Influence of spindle speed on UTS of (a, b) AISI-316L welded samples (c, d) P91 welded samples	151
Figure 7.11	Optical micrograph of welded AISI-316L steel pipe samples (at 50mm/min) (a) SZ-TMAZ (ASS1), (b) SZ (ASS1), (c) SZ-	

	TMAZ (ASS2), (d) SZ (ASS2) (e) SZ-TMAZ (ASS3), (f) SZ (ASS3), (g) SZ-TMAZ (ASS4), (h) SZ (ASS4)	153
Figure 7.12	Optical micrograph of welded AISI-316L steel pipe samples (at 100mm/min) (a) SZ-TMAZ (ASS5), (b) SZ (ASS5), (c) SZ-TMAZ (ASS6), (d) SZ (ASS6), (e) SZ-TMAZ (ASS7), (f) SZ (ASS7), (g) SZ-TMAZ (ASS8), (h) SZ (ASS8)	154
Figure 7.13	Optical micrograph of welded P91 steel pipe samples (at 50mm/min) (a) SZ-TMAZ (FSS1), (b) SZ (FSS1), (c) SZ-TMAZ (FSS2), (d) SZ (FSS2), (e) SZ-TMAZ (FSS3), (f) SZ (FSS3), (g) SZ-TMAZ (FSS4), (h) SZ(FSS4)	156
Figure 7.14	Optical micrograph of welded P91 steel pipe sample (at 100mm/min) (a) SZ-TMAZ (FSS5), (b) SZ (FSS5), (c) SZ-TMAZ-BM (FSS6), (d) SZ (FSS6), (e) SZ-TMAZ (FSS7), (f) SZ (FSS7), (g) TMAZ-BM (FSS8), (h) SZ (FSS8)	157
Figure 7.15	SEM micrograph of welded AISI-316L steel pipe sample (a) TMAZ-SZ(AS), (b) TMAZ-SZ(RS), (c) TMAZ, (d) SZ	159
Figure 7.16	SEM micrograph of welded P91 steel pipes sample (a) TMAZ(AS), (b) TMAZ(RS), (c) SZ(AS), (d) SZ(RS)	160
Figure 7.17	Line EDX analysis of welded AISI-316L steel pipes samples (a, b) secondary electron images and the corresponding plot of horizontal line (c, d) secondary electron images and the corresponding plot of vertical line	162

Figure 7.18	The colour code used to indicate different element during line EDX for AISI-316L welded sample (a) C (b) O (c) Si (d) Cr (e) Mn (f) Fe (g) Ni (h) Mo (i) S	162
Figure 7.19	EDX analysis of welded P91 steel pipes samples (a, b) secondary electron images and the corresponding plot of horizontal line (c, d) secondary electron images and the corresponding plot of vertical line	163
Figure 7.20	The colour code used to indicate different element during line EDX for P91 welded the sample (a) C (b) O (c) Si (d) S (e) Cr (f) Mn (g) Fe (h) Mo	163
Figure 7.21	X-ray diffraction of AISI-316L and P91 welded sample	164

This page is left blank intentionally

List of Tables

Table No.		Page no.
Table 2.1	Features of tool and their advantages	32
Table 2.2	FSW of different types of steel with various plate thickness, tool material, spindle speed and welding speed	40
Table 3.1	Chemical composition of as received AISI-316L pipes	52
Table 3.2	Chemical composition of P91 austenitic stainless steel	52
Table 3.3	FSW parameters for PC mode welding of AISI-316L pipes	57
Table 3.4	FSW parameters for FC mode welding of AISI-316L pipes	58
Table 3.5	FSW parameters for FC mode welding of P91 pipes	60
Table 4.1	Process parameters values under PC mode experiments	74
Table 5.1	FSW parameters selected for welding AISI-316L steel pipes	96
Table 5.2	Weight percentage and atomic percentage of elements present in welded sample ASS8	115
Table 6.1	FSW parameters for joining P91 steel pipes	120
Table 6.2	Peak temperature values recorded during FSW of P91 steel pipes at different parameter combinations	121
Table 6.3	Weight and atomic percentage of existing elements found after map EDX analysis of welded sample	137
Table 7.1	FSW welding parameters for AISI-316L and P91 pipes	142

Abstract

Friction stir welding (FSW) is a relatively newer technique in the domain of solid state joining but has found multiple utility in various industries across the world. By employing FSW, several issues that conventional fusion welding poses viz. distortion, low efficiency, etc. can be avoided. FSW has been highly suitable for welding metals viz. aluminum and magnesium which were highly challenging to be welded by conventional welding techniques. For this reason, FSW has been embraced by aerospace and marine industries which require welding of large aluminum panels. Joining of dissimilar metals is one of the interesting aspects that FSW is found to handle quite easily as joining occurs much below the actual melting temperature of the metals. Research is also underway for welding metals having high melting points (steel and titanium based alloys) using FSW in an efficient manner.

Efficient welding of pipelines is a vital need for industries like power plants, marine, food and chemical industries. Pipe welding is frequently required in various applications involving transfer of fluids. In fact, the weldment becomes a point of higher concern when the temperature of the flowing fluid is high especially in power plant based applications. Due to the inherent challenges associated with circular pipe welding viz. weld configuration, curved geometry at the weld zone, ovality issues, etc. the optimal combination of weld parameters for linear welding may not be one to one mapped in case of pipe welding even though keeping the material to be welded the same as that of pipes.

In the present work, FSW is conducted individually on industrial grade pipes made of AISI-316L and P91 steel. Both these pipes are employed in various power plant based applications and efficient joining of them is a vital concern to the industry. Initially, welding is carried out in position control mode of AISI-316L steel pipes by varying parameters viz.

spindle speed (RPM), transverse speed/feed rate (mm/min) and tool depth (mm) to get an idea about the welding process and to assess the effect of these parameters on the mechanical properties of the weldment. Based on the weld quality and the data recorded during the welding process, the optimum vertical force is determined. This sets the stage for carrying out the welding in force control (FC) mode of the machine which seems to be the logical option considering some degree of variation noticed in the pipe geometry. Under FC mode, the effect of two parameters i.e. spindle speed (rpm) and welding speed (mm/min) on the weld characteristics of the two steel pipes have been investigated. Microhardness and tensile tests have been conducted to assess the mechanical strength of the joints. Microstructure evaluation by optical microscopy (OM) and field emission scanning electron microscopy (FE-SEM) is done in order to comprehend the mechanical performance of the weldments. Both the steel pipes displayed beyond 100% joint efficiency at optimal combination of parameters. AISI-316L steel exhibited better joint strength at low welding speed whereas P91 steel showed the same at higher welding speed. Stir zone of both the welded samples revealed higher hardness values than respective base metals (BM). However, this increase is significant in case of P91 steel. The optimal parameter combination produced defect free weld. Thermo-mechanically affected zone (TMAZ) in case of P91 is wider compared to AISI-316L as revealed by optical microscopy (OM) and field emission scanning electron microscopy (FE-SEM). The results indicate that FSW is able to produce high quality joints in both AISI-316L and P91 steel pipes which may be useful for industrial based applications.

Chapter 1

Introduction

Outline of the chapter: *1.1 Introduction, 1.2 Fundamental of friction stir welding, 1.3 Advantages and limitations of friction stir welding, 1.4 Joining configurations, 1.5 Friction stir welding setup, 1.5.1 Linear welding setup, 1.5.1.1 Dedicated setups for FSW, 1.5.1.2 Adapting a milling machine – low cost setup, 1.5.2 Pipe/circular welding setup, 1.5.2.1 Attaching a rotary mandrel unit, 1.5.2.2 Portable setups – larger scale welding, 1.5.2.3 Customized setup, 1.5.3 Machine Control modes in FSW setups, 1.5.3.1 Position control mode, 1.5.3.2 Force control mode, 1.5.4 Issue of the presence of ejection hole, 1.5.4.1 Designing a wedge to transfer the hole, 1.6 Applications of friction stir welding, 1.6.1 Marine and shipbuilding industries, 1.6.2 Aerospace and aviation industries, 1.6.3 Railway industry, 1.6.4 Automobile industry, 1.6.5 Power Plants, 1.7 Present work, 1.8 Outline of the thesis, 1.9 Contribution of the thesis, 1.10 Closure*

1.1 Introduction

Solid state welding based on friction heating has been around for quite some time now. Friction stir welding (FSW) is an advancement of this technique which is effective in joining materials below their melting point while at the same time producing an efficient joint. The Welding Institute (TWI), UK is credited with having invented this particular welding technology, which is considered to be one of the latest developments in the last few decades in the field of metal joining (Besharati-Givi and Asadi 2014). FSW created a revolution, especially in the case of difficult to weld (by traditional methods) metals viz. aluminum (2xxx and 7xxx series), which could now be joined rather easily and effectively. Besides,

FSW gave rise to the possibility of effectively joining dissimilar metals. Because of its huge potential, FSW technology has been readily accepted by the fabricating industry and is now used worldwide.

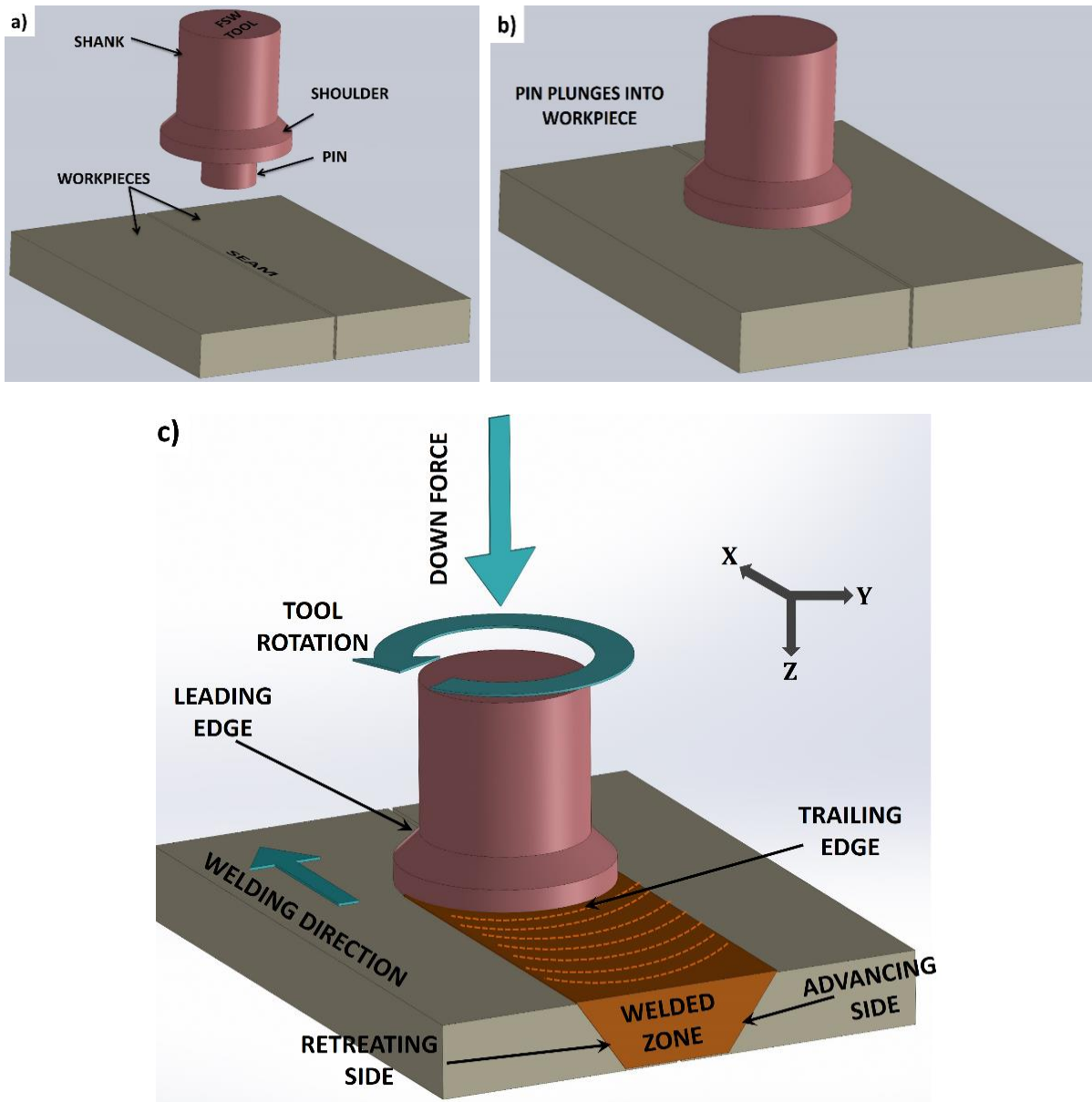


Figure 1.1 Schematic diagram of FSW (a) Butt joint layout, (b) tool entering the work piece and (c) welding nomenclature

FSW employs a rotating tool that has a shoulder and a pin extending below it. The pin is plunged into the intended weld line (joint area) between the two plates to be joined till the shoulder contacts the surface of the work pieces. Obviously, the work pieces should be

rigidly clamped to prevent their separation due to the generated forces from the rotating tool. Frictional heat generated between the tool shoulder and the work piece surface softens the material. By stirring action, the pin that enters the work piece creates a material flow. This way, the material from the two work pieces are intermixed and gets solidified as the tool progresses forward forming the joint. As bulk of the material melting is avoided, common issues in fusion welding viz. solidification and liquitation cracks, distortion, porosity, etc. can be prevented.

FSW is a solid-state joining process that is capable of creating high quality and high strength joints with minimal distortion. This process can create the commonly encountered butt and lap joints and can also deal with wide range of material thicknesses and lengths. As modern applications demand for stronger, more cost effective and efficient joints that use less energy, FSW seems to be a well suited answer. In addition, FSW offers an environmentally benign solution to these challenges and at the same time is a very quick process. This has led to its advancement from initiation to industrial acceptance within a very short period of time.

1.2 Fundamentals of friction stir welding

In FSW, a non-consumable rotating tool is employed to join two objects. The tool comprises of three parts viz. shank, shoulder and pin (refer to Figure 1.1a). The shank connects the tool to the FSW machine whereas the shoulder rubs against the work pieces providing necessary frictional heating. The pin plunges into the seam line between the work pieces (refer to Figures 1.1a and 1.1b). This plunging is caused by a combination of downward force and pin rotation. The plunging is one of the vital phases of the FSW process, as the thermo-mechanical conditions are initiated in this phase, setting the stage for the start of the weld. Once the pin fully penetrates into the work piece, the shoulder provides the necessary friction heating, making the material soft (below its melting point temperature). Penetration of the

tool results in plastic deformation in the work piece and friction that leads to further heat production (Bisadi et al. 2014). The plasticized material, pressed by the tool's shoulder, flows around the pin due to the stirring action of the tool. As per Figure 1.1c, the right portion of the tool where the tool rotation direction (anticlockwise for the present case) and the direction of tool traverse make the same vectorial sense is denoted as the advancing side. In this portion of the work piece due to tool advancement, material tries to flow back but is resisted due to the rotation of the tool pin (Mishra et al. 2014 a). Left portion of the tool (direction of tool traverse and tool rotation have opposite vectorial sense) is denoted as the retreating side and material flow here, aided by the rotation of the pin, is relatively easier. As the tool advances, it is greeted by fresh cold work piece material on the leading edge (front side) and the material is swept to the retreating side, which may influence the overall material flow and the appearance of nuggets. The back side (trailing edge) of the tool, on the other hand, continues to supply heat (due to friction) to the vacated weld region influencing the microstructure of the zone. During welding, the portion of the work piece in contact with the tool can be roughly categorized into various zones, as seen in Figure 1.2a. As per the illustration, the material in front of the tool is first pre-heated and is then subjected to the initial deformation as the tool nears. Below the shoulder and near the pin, the material suffers severe plastic deformation and is subjected to extrusion by the pin. The shoulder forges down the work piece material due to the provided tilt at the back side of the pin. And finally, the material cools as it comes out of the influence of the tool. The work piece material experiences these zones in a cyclic manner as the tool progresses along the intended weld line in the work pieces.

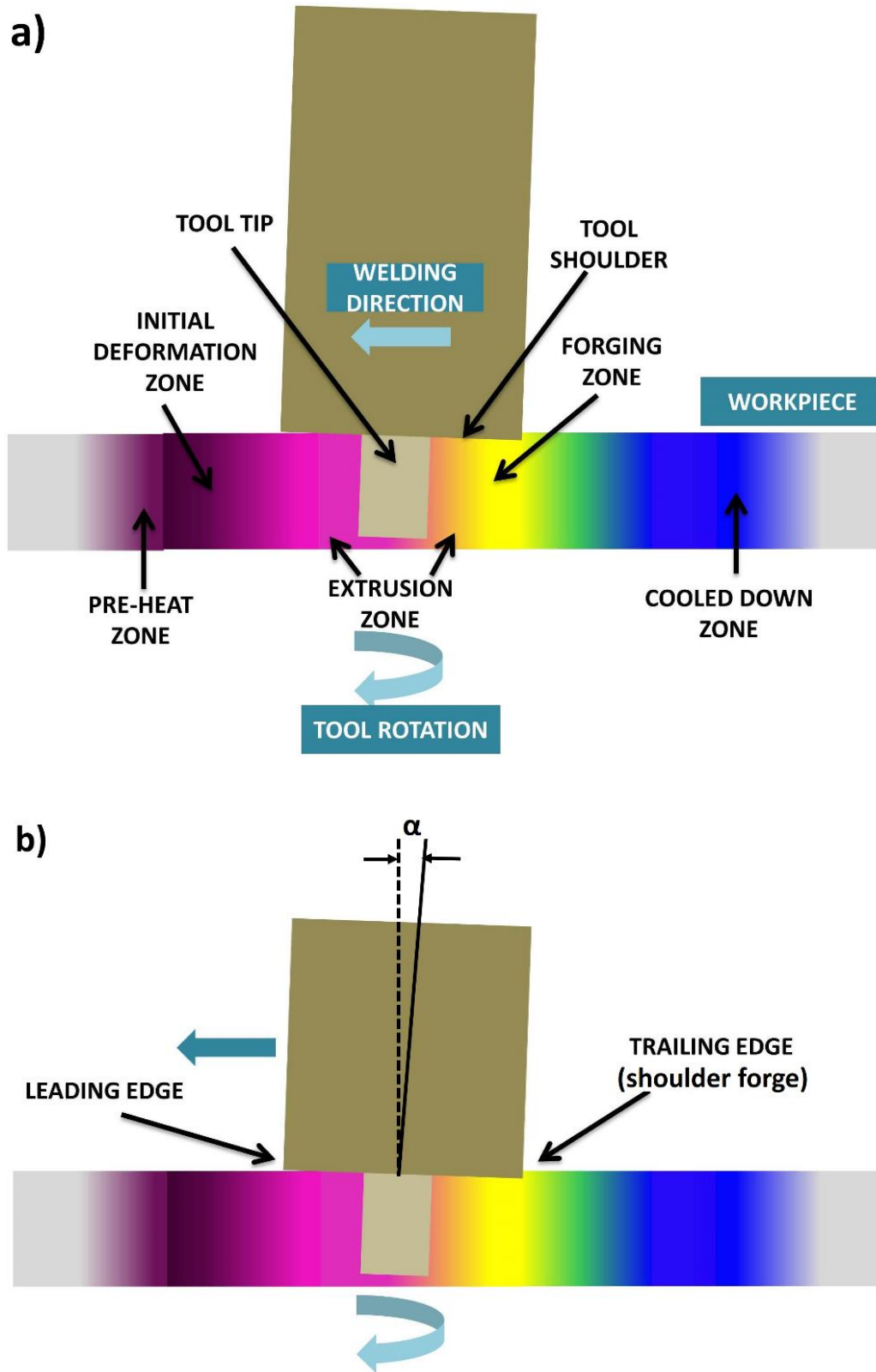


Figure 1.2 (a) Various heat affected zones and (b) Tilt of FSW tool (exaggerated representation)

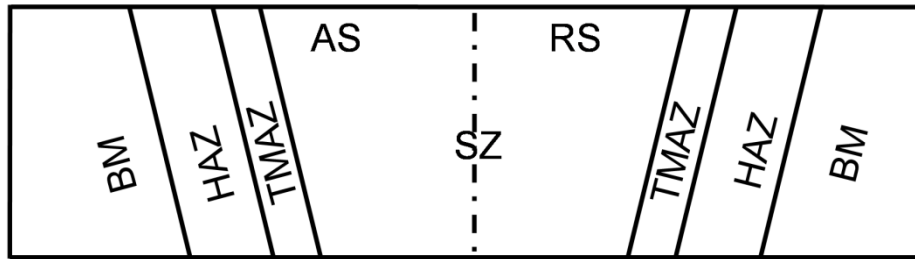


Figure 1.3 Various regions in a friction stirred weld

A typical FSW weld cross-section consists of different regions, which are as follows: unaffected base metal (BM), heat affected zone (HAZ), thermo-mechanically affected zone (TMAZ) and stir zone (SZ) (refer to Figure 1.3).

- Unaffected base metal (BM): -This region is never deformed and remains completely unaffected by the welding, even though it may have been exposed to thermal cycle on a lower level. These zones are typically located far from the welding area.
- Heat affected zone (HAZ): -This region is much nearer to the central weld portion, and its microstructure gets affected due to the heat from the welding. Hence, its mechanical properties also undergo a change. However, material is believed not to undergo plastic deformation.
- Thermo-mechanically affected zone (TMAZ): - The material in this region lies in and around the weld centre and is severely affected by heat and plastic deformation. When welding aluminum, there is a possibility that significant plastic strain occurs in TMAZ without the occurrence of recrystallization. When this situation occurs, a thin boundary separating recrystallized and deformed regions within the TMAZ can be observed through a microscope. This recrystallized zone is known as a weld nugget.
- Stir zone (SZ): - There is generally a distinct boundary between the recrystallized zone (weld nugget) and the deformed zones of the TMAZ and the weld nugget is the fully recrystallized area. This zone is called the stir zone.

1.3 Advantages and limitations of friction stir welding

The FSW process has a host of advantages, which has led to its quick acceptance by the industry. It has an edge over the other welding techniques when considering both the weld microstructure and the joint performance. Besides, FSW doesn't suffer from common defects in welding viz. porosity, solidification cracking, etc. Some of the advantages of the FSW process are as follows:

❑ *Good mechanical and metallurgical properties*

FSW operates in the solid state of the material, thereby aiding in the dynamic recrystallization of the weld zone. Due to stir action of the pin, grain refinement occurs which leads to the development of fine grained structure. As a result, the mechanical properties of the work piece (hardness, tensile strength, fracture strength) improve along the joint portion.

❑ *Less distortion (low heat input)*

During FSW, the peak temperature remains lower than the melting point temperature of the work piece material. Compared to arc welding or any other conventional welding techniques, the heat input for FSW is low. Less heat input leads to less residual stress, which leads to reduced distortion. Due to shoulder pressure and low residual stress in FSW, the joint remains quite smooth, eliminating the need for a post weld machining operation.

❑ *Improved energy efficiency*

As no melting is involved during FSW, the process consumes less energy. Besides, there are no harmful emissions, as no filler material is used.

❑ *Improved joint efficiency*

The ratio of strength of the welded joint to that of the base metal defines the efficiency of a welded joint. The joint efficiency of FSW is primarily determined by the weld process parameters. It is important to select suitable process parameters for achieving 100% joint

efficiency. For some metals, joint efficiency can exceed 100% by using the FSW technique, which is impossible to achieve by other welding techniques.

❑ *Welding in all positions*

Due to the absence of a weld pool, this welding technology can be employed for joining along all directions, i.e. vertical, horizontal, etc.

❑ *Increased fatigue life*

For the welding of structural components and in the transportation industries, fatigue life evaluation is most essential. In the aerospace sector too fatigue strength of the weldment is a major concern. Because of the lower residual stress and peak temperature, the welded joint has a longer fatigue life than BM. The fatigue strength of FSW joint is in general higher compared to arc welding.

❑ *Improved safety and environmentally friendly*

FSW is a fully automatic process. No toxic gas or spatter is produced, which makes this technique safe for the welder and reduce the chances of causing hazard.

❑ *Welding of dissimilar materials*

The joining of different metals with different melting temperatures by arc welding is difficult. This is because lower melting temperature metal will start to melt before reaching the melting temperature of high temperature work piece. For welding dissimilar materials or joining composite materials with higher strength, this solid state welding technique is suitable.

❑ *Non-consumable tool*

The FSW technique employs a non-consumable tool made of tool steel, poly cubic boron nitride (PCBN), or other materials depending on the workpiece material. Hence, the continuous requirement for filler material is eliminated, reducing the associated costs. Furthermore, the possibility of harmful gas production is reduced.

The limitations of friction stir welding are as follows: -

❑ *Presence of an ejection hole / exit hole*

In the FSW technique, an ejection hole remains on the work piece when the tool is withdrawn from it. In many applications, the presence of this ejection hole is not acceptable, viz. marine industries and aerospace industries. A run off tab can be used to eliminate this hole, or a suitable work piece may be attached at the end of the process so that the ejection hole can be placed on that extra work piece material. This necessitates additional arrangements, which raises the cost.

❑ *High initial investment*

During FSW, high forces are produced by the machine. To handle this level of force, the fixture design and equipment costs increase. The tool used for this technique is also very costly. All these make the cost of the machine quite high, pushing it beyond the reach of smaller companies. Besides, for manufacturing a single product or a small number of products, this technique may not be economical.

❑ *Less flexible*

This joining technique is less flexible compared to the manual arc welding process, and it is difficult to join plates of different thicknesses.

1.4 Joining configurations

Most of the traditional joint configurations in welding are possible to achieve through the friction stir welding process. These include the lap joint, butt joints and fillet joint (refer to Figure 1.4). By combining these configurations, most of the joints encountered in practice can be realized. Moreover, FSW can be applied for both linear as well as circular welding.

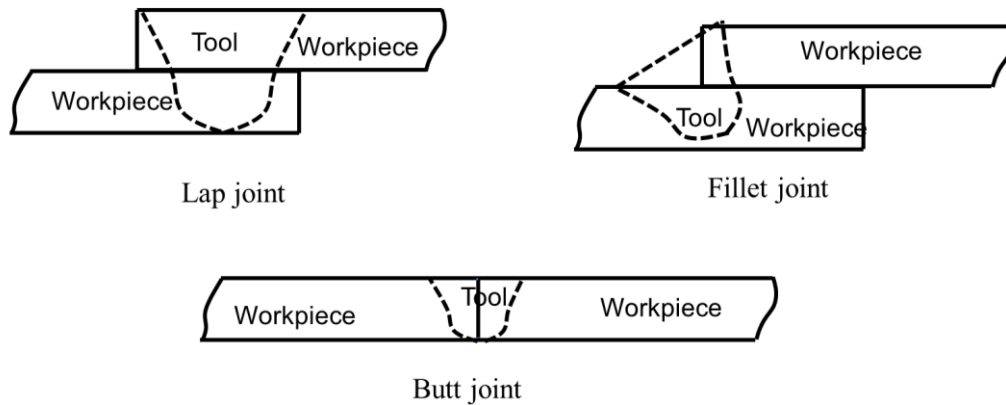


Figure 1.4 Joint configurations in FSW welding

1.5 Friction stir welding setup

1.5.1 Linear welding setup

1.5.1.1 Dedicated setups for FSW

Specialized machines for carrying out FSW are available in the market. These setups are equipped with a proper bed, a suitable jig and fixtures for fixing the work pieces as well as the welding tool. The tool can normally be given motion in three directions (X, Y and Z). There are sensors to measure forces encountered by the tool in various directions. As well as sensors to monitor temperature (at the weld zone) and a host of other parameters viz. spindle speed, displacement of the tool, etc. There is also provision to provide inclination to the tool. Cooling systems are provided for safeguarding the machine components which have direct metallic contact with the tool and may be is subjected to a very high temperature during welding. The entire machine is generally controlled numerically by a computer system. The advantages of using such machines normally reflect in higher quality welds.

Now, the five important process parameters in case of FSW are as follows: -

- a) Position of the tool
- b) Orientation of the tool
- c) Load applied

d) Rotational speed of the tool

e) Travel speed of the tool

The selection of the range of these parameters is based on the materials that are planned to be welded. Figure 1.5 displays a photograph of a linear FSW setup.

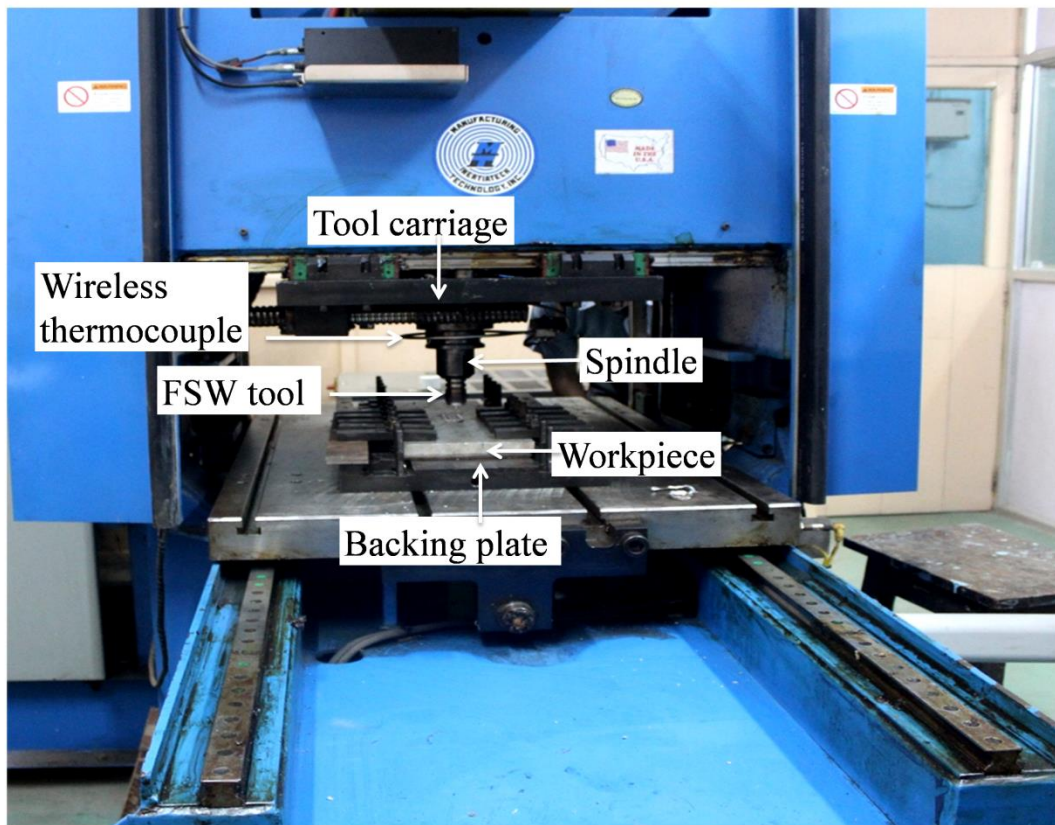


Figure 1.5 Photograph of a linear FSW setup

1.5.1.2 Adapting a milling machine – low cost setup

The issue with the dedicated setups is their higher cost and hence these are limited to those industries that have sufficient funds to invest in them. Thus, technologists have aimed to create a cost-effective solution so that the benefits of the FSW process can be reaped by industries worldwide. The configuration of the milling machine seemed suitable for its adaptability towards the FSW process. Milling machines are a very common machine that can be found almost anywhere, so it seemed like a viable solution to the huge investment cost

required to set up dedicated FSW machines. However, the spindles in milling machines are not designed to endure the radial and thrust loads expected during the FSW process. Moreover, traditional milling machines do not offer precise load control or load monitoring. Thus, high quality weld is difficult to produce though the milling machine setup. Many researchers however use this type of setup to gain knowledge about the FSW process.

Some companies have also developed FSW units which can be retrofitted to any conventional milling machine to convert it into a FSW setup. Although these type of setups cannot be a 100% replacement for dedicated FSW setups. Nevertheless, these converted machines can produce a decent weld quality and are simple to operate. Figure 1.6 shows a milling machine converted to a FSW setup.

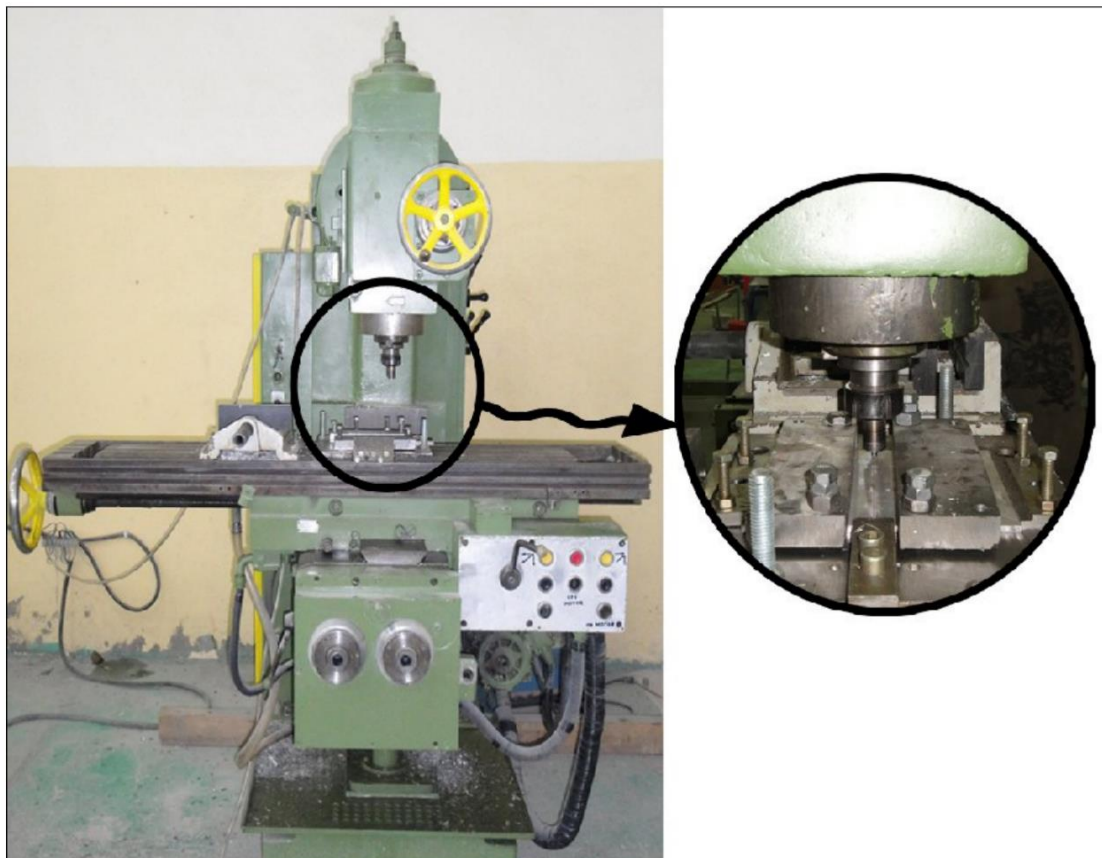


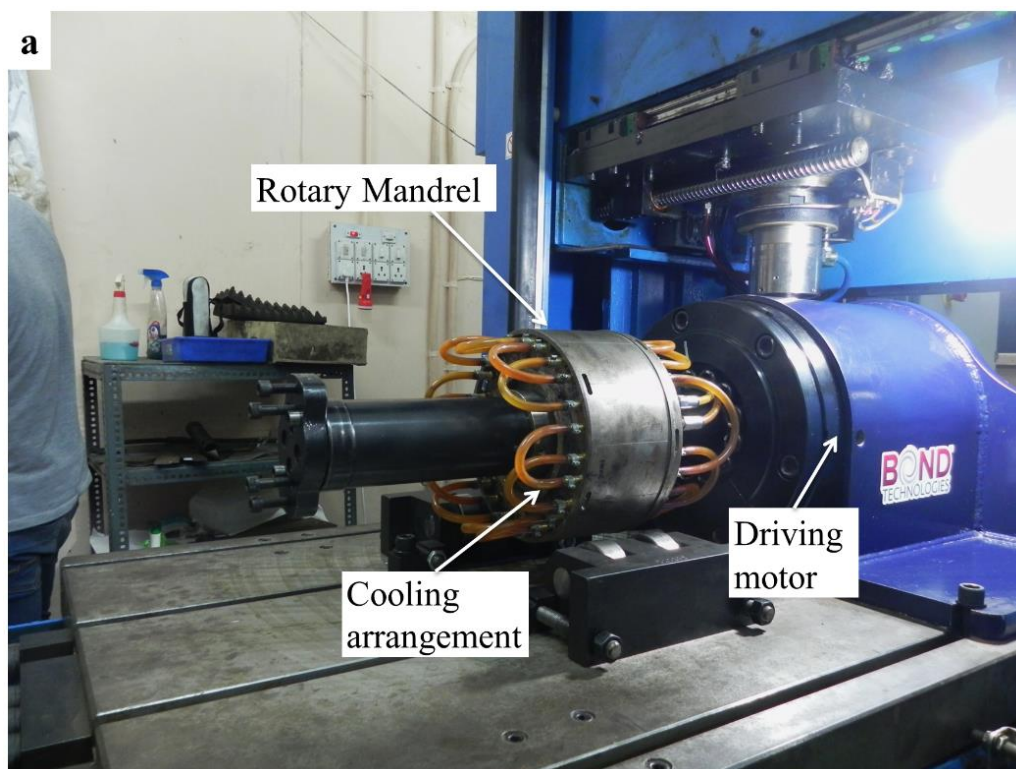
Figure 1.6 Vertical milling machine converted to FSW setup for linear welding (Tolehah et al. 2011) – reprinted under Creative Commons license

1.5.2 Pipe or circular welding

Circular welding is mainly used for welding pipes. Although several configurations have been devised, the basic fundamental of welding pipe is to make use of a precision mandrel that can be inserted into the pipe pair, thus producing a seam over it. As of now, there are primarily two setups for circular welding which are elaborated as follows:

1.5.2.1 Attaching a rotary mandrel unit

An attachment consisting of a rotary turntable and mandrel can convert an existing setup for linear welding to a circular welder. Sometimes, the attachment consists of an expanding mandrel, which can hold pipes with diameters varying within a certain range. Generally, in these types of setups, the FSW tool remains fixed and the rotating mandrel rotates the pipes, thus producing the weld. It is obvious that the rotation of the mandrel is precisely controlled. Figure 1.7 shows a typical linear FSW machine fitted with a rotary mandrel for pipe welding.



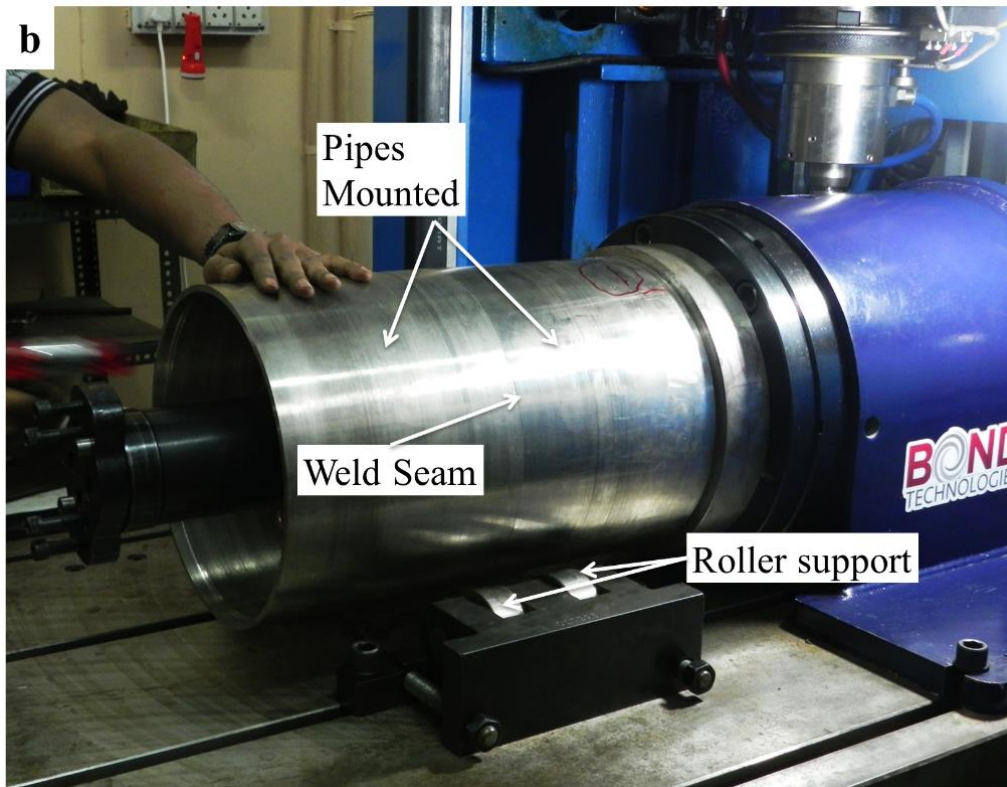


Figure 1.7 Circular welding (a) a rotary mandrel fitted to an existing linear FSW setup, and
(b) pipes fitted on the mandrel

1.5.2.2 Portable setups – larger scale welding

For carrying out the welding of larger and longer pipes, portable welding machines are also available. This setup has the advantage of being installed in the field. In this setup, normally the arrangement is such that the tool moves along the weld seam, producing the weld, as it is difficult to rotate the huge and heavy mandrel supporting the pipes.

1.5.2.3 Customized setup

Again, as in the case of linear welding, customized setups for pipe welding can be availed from the major players in the field. These setups provide a fast and precise solution for pipe welding, which can be beneficial to relevant fabricators.

1.5.3 Machine control modes in FSW setups

1.5.3.1 Position control mode

In position control (PC) mode, a closed loop servo is used for controlling the tool position, with a position encoder as feedback. Position control mode is a control mode, which is used in the machine controller to adjust the position of the FSW tool. The distance between the actual position of the tool and the target position at each instant is known as the position error. This is commensurate with the plunging rate demand for each phase of welding. A proportional controller estimates the spindle torque by multiplying the instantaneous error with a machine-set constant referred to as the proportional gain. Position control mode is used to maintain a constant depth of weld.

1.5.3.2 Force control mode

In force control (FC) mode, a constant force value must be applied to the motion stage where the position will vary. In this control mode, the axis changes from position control to force control and the force becomes independent of position control. In pipe welding, pipes frequently deal with issues viz. dimensional inaccuracy and ovality, which need to be managed by operating the FSW setup in force control (FC) mode. Hence, FC mode is preferred so that the downward force is maintained at the desired level and good quality weldments are produced.

1.5.4 Issue of the presence of ejection hole

As already discussed, that FSW tool leaves an ejection hole on the work piece at the end of the weld. This may not be a problem in the case of jobs requiring linear welding, as some allowance for this can be incorporated into the job and can be later cut off. However, in the case of circular welding, which warrants a sort of continuity, the presence of an ejection hole

will make the joint vulnerable and hence unacceptable. Thus, some special arrangements have been devised to eliminate this problem.

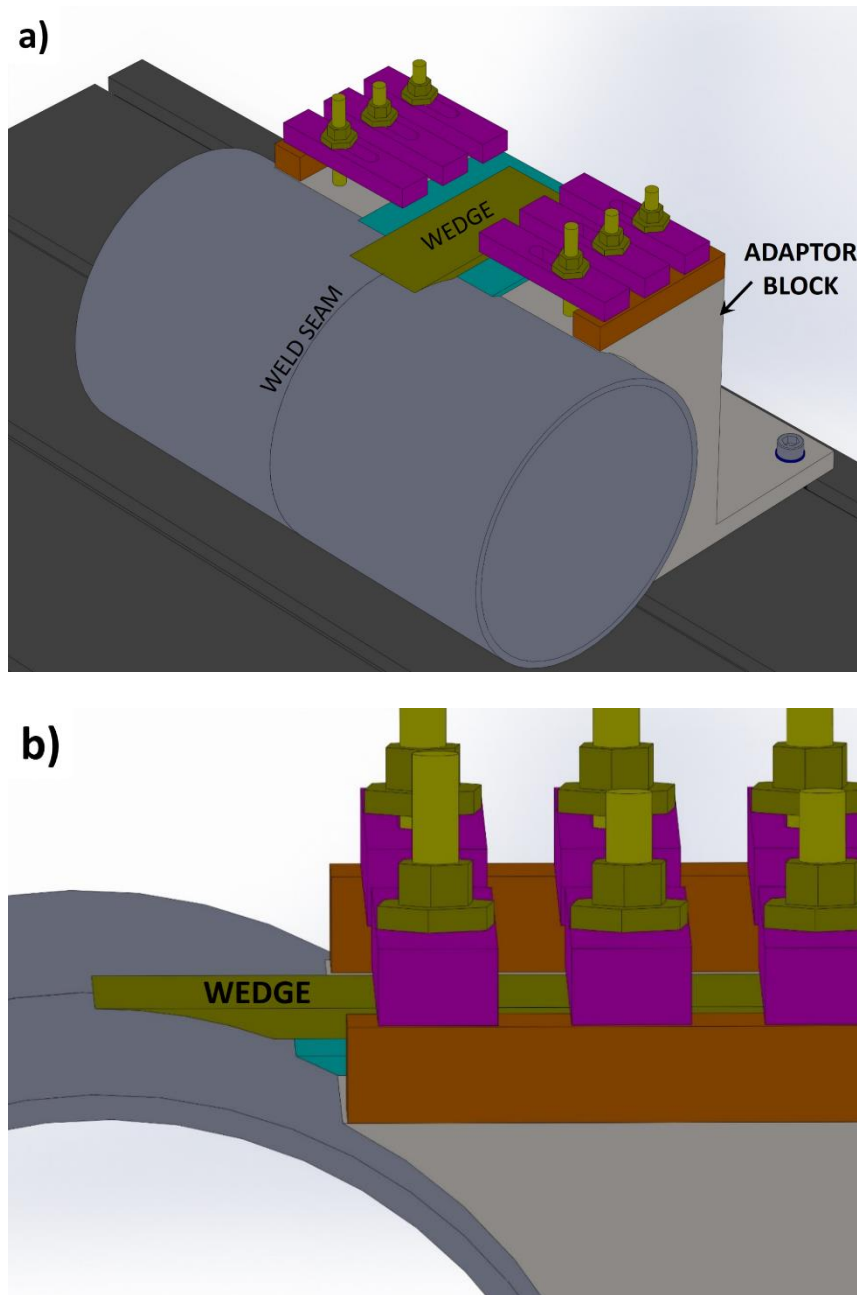


Figure 1.8 (a) Schematic transfer of the exit hole and (b) zoomed view of the wedge to which the exit hole will be transferred.

1.5.4.1 Designing a wedge to transfer the hole

This has been one of the preferred ways of getting rid of an ejection hole in the case of pipe welding. In this case, an extra wedge block is attached by temporary means to the pipe,

preferably at the starting point of the weld track (refer to Figure 1.8a). Now, once the welding is complete and the tool again gets to the starting point, a tangential motion is given to the tool, which makes it gradually shift to the attached block, thus leaving the ejection hole on the wedge rather than on the pipe. The attachment is then removed by hammering or minor machining. A zoomed view of the wedge connected to the pipe is illustrated in Figure 1.8b.

1.6 Applications of friction stir welding

Friction stir welding (FSW) is a new welding technique that is used in many applications, including shipbuilding and the marine industry. In the aerospace industry, large tanks for satellite launch vehicles have been produced by friction stir welding. FSW is also used in the railway industry, automobile industry, and transportation.

1.6.1 Marine and shipbuilding industries

The marine and shipbuilding industries were among the first to put the FSW process to use after its development. In fact, the first commercial use of FSW was recorded at Sapa (Sweden) in 1996, when this process was utilized to weld hollow aluminum panels for freezer tanks for fish. Apart from this, FSW has been found suitable for fabricating sections of boats and ships as well as marine structures. In fact, pre-fabricated aluminum panels made with FSW is commercially available for water vessels viz. ferry boats, cruise ships, as well as offshore platforms employed for oil mining. Thus, constructing these structures are now much quicker and easier. FSW has been used to build the Japanese Super Liner Ogasawara, which can carry 740 persons and has a maximum speed of 42.8 knots (Kalle 2010).

1.6.2 Aerospace and aviation industries

FSW has been widely accepted by the aerospace and aviation industries. The welding of various components in aircraft, including skin to various stiffeners viz. spars, ribs, etc. are done with FSW. FSW is found to reduce manufacturing costs and weights compared to

riveting. In some cases, they also eliminate the need for machining (from solids). TWI has created the first commercial aircraft, the Eclipse 500 by replacing the traditional riveting and bonding processes by FSW.

FSW has been tremendously used by NASA for manufacturing large tanks for their satellite launch vehicles. Many of the fuel tanks for satellites are now fabricated much more quickly and efficiently with the help of FSW. The FSW technique is normally considered for the fabrication of the following systems and their parts:

- Wings, fuselages
- Cryogenic fuel tanks for space vehicles
- Aviation fuel tanks
- Military and scientific rockets

1.6.3 Railway industry

FSW in the railway industry is primarily used for the production of aluminum panels for rolling stock. These panels are used for the side walls, under carriages as well as the roof panels of trains. By using FSW, many of the limitations of traditional fusion welding viz. low life, distortion and warping in the panels could be avoided. By realizing these benefits, many of the railway manufacturing industries have employed FSW for producing modern passenger rail cars from longitudinal aluminum extrusions with integrated stiffeners.

1.6.4 Automobile industry

The automotive industry has also embraced FSW for the production of door panels. Many big shots in the automotive companies viz. Ford, General Motors, Volvo, etc. have experimentally undertaken the use of FSW for the manufacturing of drive shafts and space frames (Kallee 2010). A new variant of FSW known as friction stir spot welding (FSSW) is increasingly used for the production of aluminum components for automotive applications.

1.6.5 Power plants

One of the applications of FSW includes the welding of pipes intended for use in supercritical and ultra-supercritical thermal power plants. In these power plants, fluids at high pressure and temperature need to be carried through pipes, which need to be joined with near about 100% efficiency. Thus, FSW offers a potential solution in this case. Moreover, FSW can effectively weld creep resistant steel used for making these pipes. Now, these materials utilized in the power plants should exhibit high strength up to approximately 600°C temperature. By employing the FSW technique, the welded zone contributes to higher thermal fatigue life. This allows them to increase the operating temperature to a higher level and thus increase the overall efficiency of the power plant.

1.7 Present work

The present work assesses the employability of FSW towards obtaining efficient joints in pipes made of AISI-316L and P91 steels. Initially, welding is carried out in position control mode on AISI-316L pipes by varying weld parameters viz. spindle speed (RPM), welding speed/feed rate (mm/min) and tool depth (mm), to get an idea of the welding process and evaluate the effect of these parameters on the properties of the weldment. Based on the weld quality and the data recorded during the welding process, the optimum downward force is determined. With this downward force, further welding is carried out in FC mode. The influence of process parameters viz. spindle speed (RPM) and welding speed (mm/min), on the microstructure and mechanical properties (viz. hardness and tensile strength) of the pipe weldments are studied in detail. In fact, some definite correlation is observed between the mechanical properties of the weldments and the microstructure evolved. Microstructural evaluation of the pipe welds is carried out through an optical microscope (OM), field emission scanning electron microscope (FE-SEM), energy dispersive X-ray analysis (EDX) and X-ray diffraction (XRD). The optimal combination of weld parameters that yield

efficient weldments in AISI-316L and P91 steel pipes is identified using the overall information.

1.8 Outline of the thesis

The present thesis is divided into eight chapters. The first chapter introduces the friction stir welding process, joining configuration and friction stir welding setup. The second chapter represents a review of the current literature based on tool materials, geometry of the tool, work-piece material, process parameters used for friction stir welding. The experimental details and instruments used for mechanical and metallurgical characterization of the current weldments are presented in the third chapter. The fourth chapter presents the pre-characterization analysis and physical examination of AISI-316L pipe welding in position control mode, while the fifth chapter deals with the mechanical and metallurgical characterization of AISI-316L pipe welding in force control mode. The sixth chapter contains a mechanical and metallurgical study of P91 pipe welding in force control mode. The performance of FSW for joining AISI-316L and P91 pipes is compared in Chapter Seven. The final chapter eight concludes the current work and presents the future scope in this area.

1.9 Contribution of the thesis

The present thesis attempts to develop a procedure for effectively joining large (greater than 250mm) AISI-316L steel pipes and P91 steel pipes using FSW. The effect of two parameters i.e. spindle speed (rpm) and welding speed (mm/min), on the weld characteristics of the two steel pipes has also been investigated. The optimal combination of parameters is obtained by carrying out mechanical and metallurgical characterization on both the pipe weldments. The results obtained from the current work displayed more than 100% joint efficiency at the optimal combination of parameters. The welded samples revealed higher hardness values than the respective base metals. The results indicate that FSW is able to produce high quality

joints in both AISI-316L and P91 steel pipes, which will be useful for the power plant industry. Moreover, the thesis opens a door for conducting FSW for joining such large diameters of other grades of steel pipes in order to fulfil the upcoming needs of many other industries like food processing, petroleum, etc.

1.10 Closure

The present chapter introduces the fundamentals of FSW along with the advantages and limitations of FSW. Various joining configurations, different types of FSW setup and the applications of FSW are described in detail. This chapter also includes descriptions of the current work as well as an outline of the thesis. Finally, contributions from the present work are described.

This page is left blank intentionally

Chapter 2

Literature review

Outline of the Chapter: 2.1 Introduction, 2.2 Friction stir welding tools, 2.2.1 Tool materials for friction stir welding, 2.2.1.1 Tool material for low-temperature alloys, 2.2.1.2 Tool materials for high-temperature alloys, 2.2.1.2.1 Poly-cubic boron nitride (PCBN) based tool, 2.2.1.2.2 Tungsten (W) based tool, 2.2.1.2.3 Other tool materials, 2.2.2 Geometry of friction stir welding tool, 2.2.2.1 Shoulder diameter and surface features, 2.2.2.2 Pin geometry and features, 2.3 Parameters in friction stir welding, 2.3.1 Spindle speed, 2.3.2 Welding speed, 2.3.3 Tilt angle of tool, 2.3.4 Other parameters, 2.3.4.1 Forces, 2.3.4.2 Plunge depth, 2.4 Work-piece material, 2.4.1 Friction stir welding of aluminum alloys, 2.4.2 Friction stir welding of magnesium alloys, 2.4.3 Friction stir welding of copper alloys, 2.4.4 Friction stir welding of titanium alloys, 2.4.5 Friction stir welding of steel, 2.4.5.1 Findings from FSW of steel, 2.4.5.2 Friction stir welding of AISI-316L steel plates and pipes, 2.4.5.3 Friction stir welding of P91 steel plates and pipes, 2.5 Summary of the literature review, 2.6 Motivation for the present work, 2.7 Closure

2.1 Introduction

FSW process parameters, such as welding speed, spindle speed, tool plunge depth, tool tilt angle, spindle torque, and the downward force acting on the tool during welding, have a significant effect on the heat generation during the process, which affects the temperature distribution and the material flow. Heat generation and material flow during the welding process are essential factors for producing good quality weldments. The process parameters play a vital role in the evolution of the mechanical and metallurgical properties of the joint

produced. The following text presents the state of the art in the field of FSW with emphasis on the workpiece and tool materials as well as the effect of the weld process parameters on the mechanical and metallurgical behaviour of the joint.

2.2 Friction stir welding tools

The tool plays an important role in the successful welding through FSW process. The tool consists of three main parts viz. the shank, shoulder and the pin. Broadly, the tool has a couple of functions: (a) heating a localized area and making the material soft and (b) initiating the flow of the softened material (Nandan et al. 2008). The friction generated (at the shoulder and pin) due to the rotation of the tool provides localised heating that leads to material plasticization (softening) around the tool pin. The rotation of the tool together with its translation (tool traverse) helps in the flow of the soft/plasticized material from the leading side to the trailing side. This transfer of material helps in filling the hole that is generated by the pin, thus forming the joint. The shoulder supplies the majority of the frictional heat and also prevents the escaping of softened material out of the weld zone (Mishra and Ma 2005). Thus, the quality of the weld depends a lot on the design of the shoulder and that of the pin. However, the microstructure and mechanical properties of the stir zone and HAZ zone of FSW also depend on the tool material and its properties (Cevik et al. 2016). For welding aluminum alloys and soft metals, these techniques achieved practical success. However, the design and selection of the tool became very important while welding hard alloys viz. steel, nickel alloys and titanium alloys, as the life of the tool was shortened considerably and the cost increased. Thus, there has been a concerted effort to develop cost-effective tools that at the same time have a longer life.

2.2.1 Tool materials for friction stir welding

Tool materials for FSW of high-temperature alloys should have excellent mechanical properties so that they can perform successfully at higher operating temperatures (above 900°C). The properties include ductility, hardness, thermal conductivity and coefficient of thermal expansion. The selection of the tool material depends on the recrystallization temperatures of the work piece. Tool materials are required to have necessary strength to survive the process temperature as well as fatigue strength and fracture toughness at the same temperature conditions (Mishra et al. 2014b). Besides, the tool also needs to have suitable wear characteristics as well as thermal and chemical stability (inert towards the work piece material). However, the final deciding factor remains the quality of the weld produced by the tool. Steel is the popular choice as tool material for welding of aluminum and magnesium alloys. PCBN (Polycrystalline Cubic Boron Nitride) and W-based tools, on the other hand, have been used for welding hard material such as steel, titanium, etc.

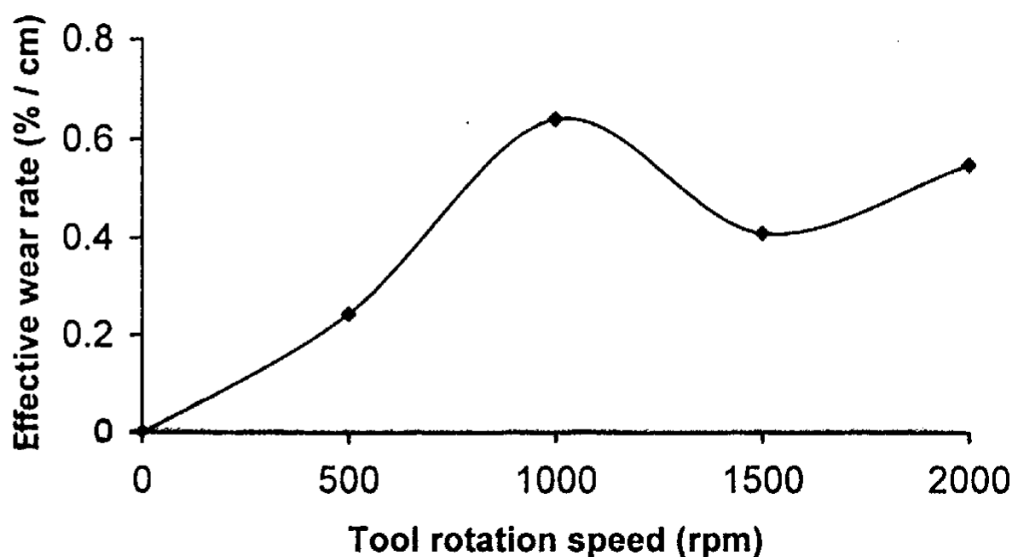


Figure 2.1 Wear rate of tool vs. rotation of tool in rpm (Prado et al. 2001) - reprinted with permission from Elsevier

2.2.1.1 Tool material for low-temperature alloys

It is easy to find suitable tool material for processing aluminum alloys, as aluminum is softer and has a lower melting point than many of the other metals. For FSW of aluminum alloys, the tool material is required to sustain the process conditions. Besides, it should also possess certain properties viz. fracture toughness, long fatigue life, wear resistance, chemical stability and thermal stability. Tool steel (H13 tool steel) and cobalt based super-alloy (MP159) are among the common tool materials used for FSW of aluminum and its alloys (Mishra et al. 2014b; Rai et al. 2011). Prado et al. (2001) employed tool steel for FSW of aluminum MMC (aluminum alloys 6061+20% Al₂O₃). They found that the tool was quite effective and suffered minimal wear in case of welding Al 6061 compared to when Al₂O₃ particles were added. They further found that the tool suffered maximum wear when operated at 1000 rpm post which the wear decreased but in an irregular manner (see Figure 2.1). An increase in the fluidity of the material and the turbulence in the particle flow beyond 1000 rpm may be the reason for this decrement.

FSW for joining dissimilar metals has also been carried out successfully by various researchers. Chen and Lin (2010) used AISI 4140 tool steel to perform an experiment to optimise the FSW process parameters when welding AISI 400 low carbon steel and AA6061 aluminium alloy. Lee et al. (2009) successfully achieved a lap joint between Al-Mg alloy and low carbon steel using a tool made of tool steel. They carried out the welding without excessive tool wear by putting the Al-Mg alloy plate above the steel plate. This way, the tool made direct contact with the Al-Mg alloys instead of the steel plate. Meran and Kovan (2008) employed X155CrMoV12-1 tool steel (cold worked) for welding copper and brass.

2.2.1.2 Tool materials for high-temperature alloys

2.2.1.2.1 Polycrystalline cubic boron nitride (PCBN) tool

Harder materials (alloys of steel, nickel and titanium) are always difficult to weld and selecting the proper FSW tool for welding these materials is challenging. PCBN, which is only second to diamond in hardness, is the preferred tool material for welding these materials (Rai et al. 2011). A PCBN tool is known to maintain its strength and hardness at elevated temperatures. The wear rate of PCBN is low because of its thermal and chemical stability, which is superior to diamond (Rai et al. 2011). It is particularly inert to iron. Moreover, PCBN has a low coefficient of friction (COF), which results in a smooth surface on the weld. However, PCBN tools are very costly due to the requirement of high pressure and temperature during their manufacturing.

2.2.1.2.2 Tungsten (W) based tool

Tungsten based composites is one of the popular choices as the tool material for FSW of steel. Pure tungsten has very poor toughness at room temperature and its wear rate is also high when welding materials viz. steel and titanium based alloys. Thus, researchers have employed a variety of tools based on tungsten viz. W-La₂O₃, WC-Co, WC, W-Mo and W-Re for FSW of steel and other hard materials (Rai et al. 2011). These tool materials possess most of the properties needed for welding of hard materials. The hardness of WC is ~1650HV and it has excellent toughness (Rai et al. 2011). WC and W-La₂O₃ have been utilized as tool materials in most of the investigations related to joining sheets of carbon steel and stainless steel by FSW. The most common W-based tool material is W-Re (W-25 wt% Re) (Rai et al. 2011). The addition of rhenium enhances the hot strength of the material, which reduces the deformation of the pin during its insertion into the work piece. Re also improves the wear resistance of the material (Rai et al. 2011). This material has a lesser tendency to fracture because of its lower ductile to brittle transition temperature, which is approximately 50°C.

2.2.1.2.3 Other tool materials

Super alloys based on cobalt (Co) or nickel (Ni) have sometimes been employed as tool materials for FSW of steel. Si_3N_4 is also used as the tool material for welding because it has desirable properties viz. higher hardness, a low coefficient of thermal expansion and higher thermal conductivity. However, the work piece material may be contaminated with Si and N upon using this tool. Thus, the Si_3N_4 tool is provided with a coating of TiC or TiN to prevent this contamination. Lee et al. (2005) successfully carried out FSW of titanium with a sintered TiC tool. Also, a cooling arrangement is provided so that the excess heat can be extracted from the tool to prevent its damage. Molybdenum based alloy tools are employed to weld titanium and steel work pieces. Tool wear is found to be greater in the case of welding metal matrix composites than soft alloys, as the former consists of hard abrasive particles. The tool's spindle speed as well as its traverse speed can affect the tool's life. Tool life is found to be optimum when a lower rotational speed is used with a relatively higher traverse speed (Lee et al. 2005).

2.2.2 Geometry of friction stir welding tool

Heat generation rate, transverse force, torque and the thermo-mechanical aspect of the experiments depend on the tool geometry. The geometry of the tool also affects the material (plasticized) flow of the work piece. The various features of the tool viz. shoulder diameter, shoulder surface, shape, size, the nature of the tool surface and the pin geometry influence the weld quality. The following factors complicate the selection of an appropriate shoulder with pin geometry (Mishra et al. 2014c):

- Dimension of work piece, which determines its capacity to act as a heat sink.
- Required efficiency of the joint.
- The forces expected on the tool so that the tool can survive mechanical failures.

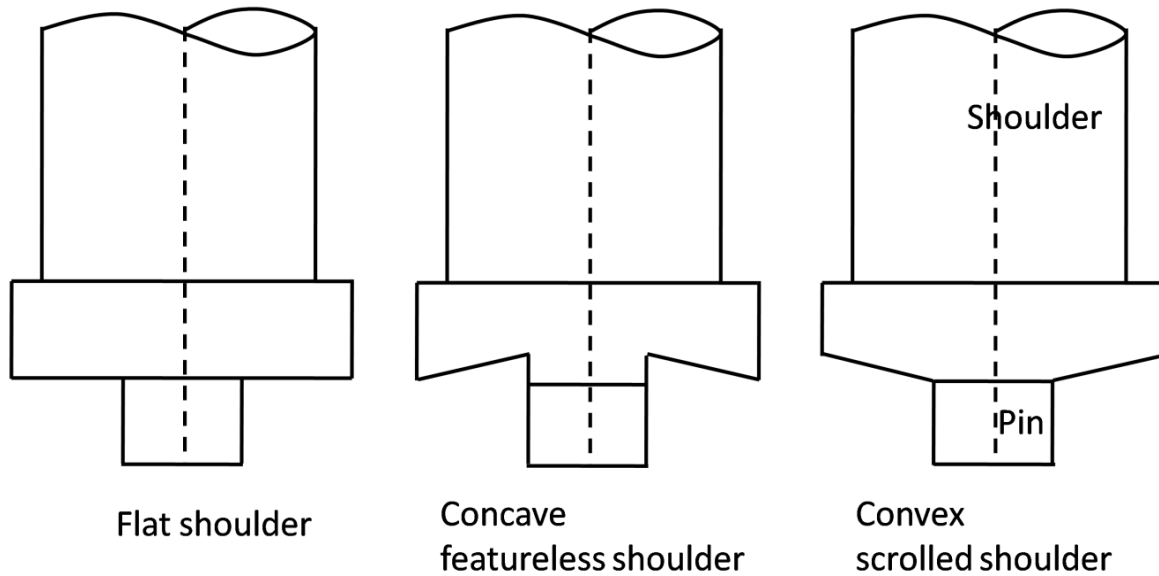


Figure 2.2 Various types of shoulder and pin geometry

2.2.2.1 Shoulder diameter and surface features

The diameter of the FSW tool shoulder is a particularly important parameter as it determines the amount of friction heat produced due to the rubbing of the shoulder surface against the work piece surface. The thickness of the work piece determines the shoulder diameter of the tool. This is because for good welding, the material should be softened adequately. Now, as the thickness of the work piece increases, it requires more heat for softening. This can only be generated by a larger shoulder diameter. Furthermore, as the size of the work piece increases, it acts as a larger heat sink, necessitating a greater supply of heat to plasticize the material. However, it is worth noting here that higher heat generation is also possible by increasing the rotational speed of the tool as well as decreasing the feed rate. A suitable shoulder diameter results in splendid joint properties.

Features of the shoulder surface also affect the characteristics of the weld. Traditionally, the shoulder surface can be flat, concave or convex (refer to Figure 2.2). Among these, the flat face shoulder is the easy to manufacture. But the flat shoulder fails to contain the plasticized material within the weld zone, leading to excessive material flash. As

a result, tools with a flat shoulder surface are typically used at a tilt angle. To solve this issue, the concave shoulder was conceptualized, which is found to be quite effective and is the most commonly used tool nowadays. The third variety can be a tool with a convex shoulder, which causes material displacement away from the pin. The benefit of using a tool with a convex shoulder is that it can handle plates of thickness varying within a certain range as well as plates with issues of flatness. To reduce the material displacement issue, convex shoulders are generally provided with features viz. scrolls, knurling, ridges, grooves, spirals and circular steps. These features help increase the material's friction as well as shear and deformation. This leads to better mixing of the softened materials, which yields good weld characteristics (Zhang et al. 2012). Moreover, when a convex shoulder with scrolls are used, in vertical force control mode (machine maintains the specified force), for any increase in penetration depth, the area of contact between the shoulder and the work piece increases. This reduces the vertical force and to maintain it, the depth of penetration decreases, returning the tool to its previous position. Similarly, when there is a decrease in the penetration depth, the contact area between the shoulder and work piece decreases. As a result of the increased vertical force, the penetration returns to its original value. So friction stir welding with a convex scroll shoulder maintains a constant plunge depth.

Sorensen et al. (2009) studied the role of the geometry of the tool on the weld characteristics. They selected a tool with a convex shoulder and a steep spiral. According to their study, the shoulder's radius of curvature as well as the pitch of the spiral have a significant influence on the welding. Changing the shoulder from convex to concave may change the mode of failure of the weld as well as its microstructure. Similar phenomena may occur when a flat tool is changed to a concave one. Hirasawa et al. (2010) studied friction stir welding with cylindrical, triangular, tapered, and triangular taper pin geometries on flat, concave, and convex tool shoulders. Their studies show that a concave triangular pin results

in spot welds of enhanced strength. Li et al. (2010) explained that the angle of the shoulder surface influences the vertical force; based on the radius of the tool pin. They reported that a convex shoulder with a scroll results in higher stability of the FSW process.

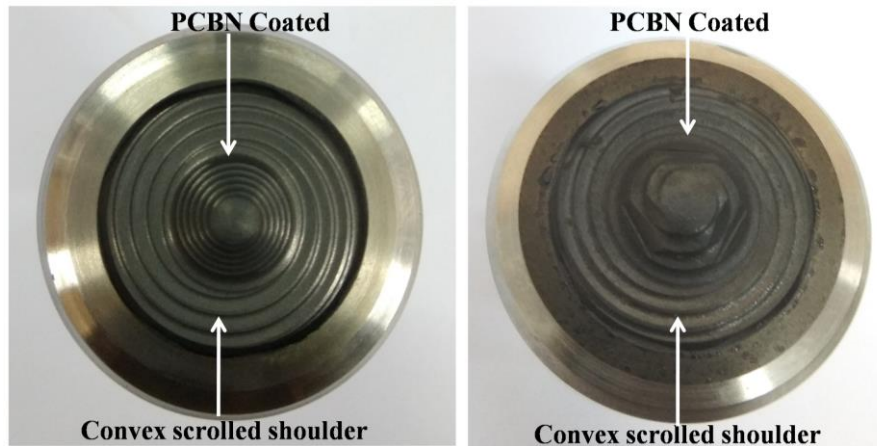


Figure 2.3 Features and geometry of PCBN coated tool

2.2.2.2 Pin geometry and features

In FSW, the pin penetrates the work piece and mixes the softened material and hence playing an important role in the process. Thus, the shape and size of the pin would influence the quality of the weld. The pin length is selected based on the thickness of the work piece to be welded. As material softening occurs to some extent beyond the tip of the pin, the pin length is normally taken to be a bit shorter than the actual work piece thickness. As a convention, the pin length is taken as 0.85-0.95 of the thickness of the work piece (Mishra et al. 2014c). In the case of the diameter of the pin, a smaller diameter is normally preferred because it helps reduce the HAZ in size. But again, a tool with a smaller diameter is weak and vulnerable to failure, especially when the tool is plunging down and the vertical force acting on it is at its peak. The pin can also fracture if it faces a higher shear load due to insufficient softening of the material during welding. As a thumb rule, the diameter of the pin is taken as 1/3 of the diameter of the shoulder. A pin diameter of approximately 1/3 of the shoulder diameter is generally used.

Table 2.1 Features of tool and their advantages (Mishra et al. 2014b) -reprinted with permission from Springer Nature

Tool feature	Design variation		Advantage
Shoulder	Convex with scroll	Curved geometry	Able to join work pieces of different thickness. The scrolls help in containing material in the weld zone.
	Concave (standard design)	Tapered geometry	Able to join work pieces of different thickness. The scrolls help in containing material in the weld zone.
		Smooth surface	Due to concavity, material contains in weld zone. Tilt of the tool is needed.
		Scrolled surface	The normal force on the tool is reduced. The thickness of weld zone reduces. Tool tilt is not required.
Pin	Cylindrical	Flat bottom	Very common. Machining is easy.
		Round bottom	Wear of the tool reduces during penetration. Joint strength at the root of the weld improves.
		With flats	Plastic strain as well as temperature increases in nugget zone.

	Conical	Threaded cone	Lateral force generation is lower than cylindrical pins.
		Stepped spiral	Employed for high melting point metals. Good strength.
		With flats	Plastic strain as well as temperature increases in the nugget zone.
	Whorl		Lower transverse force on tool.
	MX Triflute		Refined version of whorl pin
Threadless		Reduces tool wear in extreme situations.	
Retractable		Exit hole can be eliminated.	

The shape of the pin and the features present on it were found to affect the material flow. Cylindrical and truncated conical shapes are the well-known pin shapes (Mishra et al. 2014b). There is no downward push for a cylindrical pin when the materials flow from the front to the back of the tool. When the pin is truncated conically, some downward force component is generated, leading to material flow in a downward direction. This is important while welding high temperature materials. The addition of features to the pin aids the vertical flow of material along with the breaking of the flow. The various features and geometry of the PCBN tool system are illustrated in Figure 2.3. The variety of tool designs and their features, along with their advantages, are summarized in Table 2.1.

2.3 Parameters for friction stir welding

2.3.1 Spindle speed

It is seen that a variety of parameters affect the FSW joint parameters. Thus, their interrelationship makes the situation quite complex and difficult to understand. According to the inventor of FSW, Wayne Thomas, the three most important welding parameters are spindle speed or tool rotational speed (along with the direction i.e. CW or CCW), welding speed or transverse speed of the tool and tilt angle of tool (Thomas and Dolby 2003). The rotation of the tool has several implications. Firstly, frictional heating from the rubbing of the shoulder surface to the work piece is affected. Secondly, the tool rotation also affects the mixing of the softened material. Higher tool rotation results in greater heat generation and more material softening. The spread of the HAZ is also quite an extent affected by the tool rotation. The spindle speed depends on the material type as well as the thickness of the work piece being joined.

2.3.2 Welding speed

Welding speed or tool traverse speed also impacts the weld characteristics. Material is transferred from the leading edge to the trailing edge due to the translation of the tool. Welding speed along with tool rotational speed determines whether enough heat is being supplied to the processed material, which is favourable for the development of desired metallurgical and mechanical properties. Lowering the welding speed causes excessive heat generation and slows the welding process. At high speed, heat generation is low, which may not be desirable as it puts higher loads on the front side of the advancing tool (material is not softened enough). Thus, an optimum spindle speed needs to be selected based on a particular case of FSW, depending on the type of material and thickness of the work piece being used. A smooth material flow around the tool pin is always desired. In fact, the choice of feed rate along with spindle speed decide the heat generation and material flow, which also leads to

reduced forces acting on the tool. Stevenson et al. (2015) identified the high cost and short lifespan of FSW tools, as well as the slow welding speed, as major barriers to the commercialization of steel FSW.

2.3.3 Tilt angle of tool

Tool tilt angle is another important FSW process parameter that influences the weld characteristics. In the case of linear welding, the tilt of the tool is the angle of inclination of the spindle with respect to the work piece surface. The tool is normally given a backwards tilt, which gives more open space in front of the tool while forging of the work piece material is done by the back of the shoulder behind the pin. This is particularly true for featureless shoulders, which, due to the tilt, can effectively contain the stirred material. Transfer of material from the leading to the trailing edge is also aided by the tilt of the tool. In general, a tilt angle between 0 and 3° is selected for optimum weld quality (Mishra et al. 2014d). Takahara et al. (2008) reported that the tensile strength of the welded joint is sufficiently maintained by limiting the backward tilt up to 3 degrees.

2.3.4 Other parameters

2.3.4.1 Forces

Considering the forces in three directions w.r.t. the tool in a FSW system (refer to Figure 2.4), the downward force acting on the tool (Z-force) is the most important one that affects the welding. It is to be noted here that normally FSW machines can be operated in two modes viz. position control and force control. In the former case, the machine tries to maintain the position command given to the tool (plunge depth) while recording the forces as a response. In the force control mode, the machine tries to maintain the force given as an input. As already mentioned, the Z-force value is normally specified, while the plunge depth can vary. Higher Z-force results in increased plunge depth as well as greater heat generation, thus

playing its part in material softening and the corresponding phenomena. The other two forces viz. longitudinal force or transverse force (X-directional force) and lateral force (Y- force), are normally recorded as responses. However, these forces give an indication regarding the quality of the weld produced. In some cases, defects in the weld can be predicted by observing the trends in the force values recorded during the FSW process.

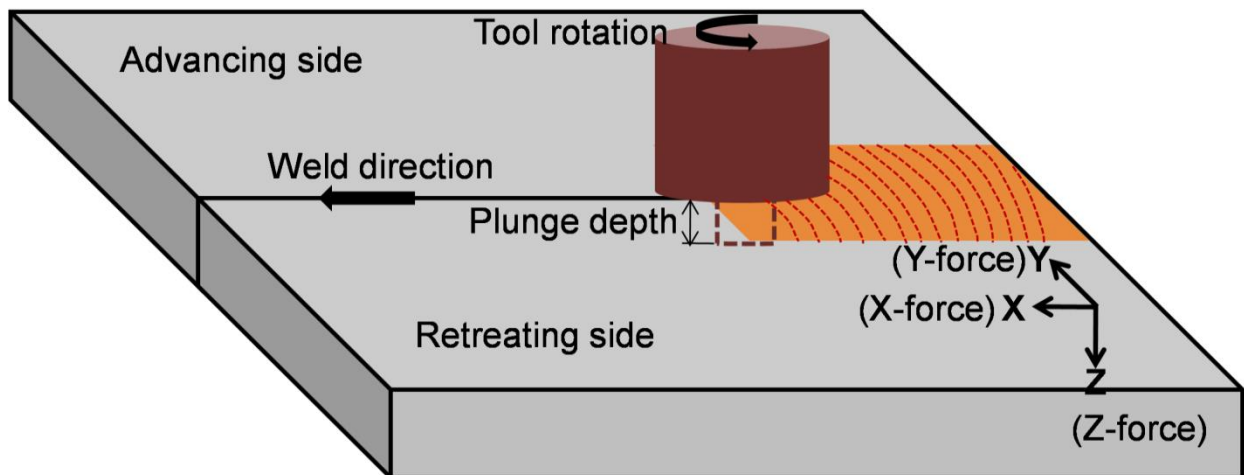


Figure 2.4 Schematic of FSW with respective forces

2.3.4.2 Plunge depth

The plunge depth is also an essential parameter for FSW. Whether the tool has fully penetrated the work piece is ensured by the plunge depth. Moreover, it ensures the necessary vertical force needed for heat generation. Excessive plunge depth may cause the pin to reach up to the reverse side of the work piece resulting in its welding with the backing plate.

2.4 Work-piece material

Welding aluminum and its alloys is the primary reason behind the development of the FSW technique (Thomas et al. 2003, Threadgill et al. 2009). This welding technique can also be applied for joining other non-ferrous materials such as copper, magnesium, etc. (Lee and Jung 2004, Nakata et al. 2001). Later, FSW is further developed to carry out welding of high temperature materials like titanium and steel and their alloys. Recently, great focus has been

paid to the welding of dissimilar metals and alloys (Larsson et al. 2000) using FSW due to their commercial importance and inability to be joined by conventional welding techniques.

2.4.1 Friction stir welding of aluminum alloys

Aluminum is one of the most useful alloys in different industries such as aviation, aerospace, marine, automotive, and rail (Fahimpour et al. 2012). This metal cannot be welded by gas welding because of its poor weldability. Aluminum resistance welding and arc welding are both expensive and require specialised techniques. The FSW technique has been found to be highly suitable for welding aluminum alloys due to their mechanical properties and low density. Different series of aluminum alloys, viz. 2XXX, 3XXX, 4XXX, 5XXX, 6XXX, 7XXX, can be welded by this technique (Genevois et al. 2005, Gan et al. 2008, Peel et al. 2003, Fahimpour et al. 2012, Rodrigues et al. 2009). Zn, Mg, Cu, Mn, Si are the alloying elements present in pure Al alloys. Work hardening and heat treatment are the two processes through which aluminum alloys get further strengthened.

In the case of aluminum, FSW is generally processed by tool steel, which has high-temperature strength and toughness. The temperature achieved during welding aluminum alloys remains approximately between 400-500°C. Another parameter is the maximum downward force reached during the insertion of the tool. The peak force during tool plunging is a combination of vertical force and transverse force. The choice of process parameters is highly important for producing a defect free weld and high joint efficiency. Another major factor for the FSW of Al alloys is the welding time, which is very important for the shipbuilding and aviation industries.

2.4.2 Friction stir welding of magnesium alloys

Sheets of magnesium alloys are usually manufactured by casting or die casting process and these alloys have high formability. Welding of cast magnesium alloy sheets is challenging

due to the relatively high coefficient of thermal expansion, which causes deformation and distortion in welds Czerwinski (2011). The formation of pores in arc welding or gas welding makes the welding defective. So, solid-state welding process is the preferred choice for joining cast magnesium alloy sheets. Researchers have conducted FSW on AZ31 AZ31B, AZ31B, AZ1, AZ61A, AM60, AMX60 (Daras et al. 2012, Esparza et al. 2003, Chen et al. 2012, Razal et al. 2012, Liao et al. 2009, Xunhong and Kuaishe 2006, Yang et al. 2013) sheets. Nakata et al. (2001) have studied FSW on AZ91 sheet of 6.4 mm sheet thickness. They have successfully carried out FSW in the case of the butt joint and optimized the process parameters. At optimum condition, combination of 50 mm/min traverse speed and 1240-1750rpm of spindle speed is found to yield good quality weldments. They suggested that welding speeds higher than the optimum level as well as tool rotation speeds lower than the optimum level may result in a lack of bonding and the formation of voids.

2.4.3 Friction stir welding of copper alloys

Conventional fusion welding techniques find it difficult to weld copper alloys. This is because of the high thermal diffusivity of copper, which is about 10-100 times higher than that of steel and nickel alloys (Mishra et al. 2014c). Higher thermal diffusivity requires higher heat generation, leading to low welding speeds (traverse speed). Several researchers have attempted to join pure copper and its alloys through friction stir welding. FSW of 1.5-50 mm thick copper plates at variable process parameters has been successfully performed by Lee and Jung (2004), Park et al. (2004), Nakata (2005), and Mishra and Jeganathan (2017).

2.4.4 Friction stir welding of titanium alloys

It is possible to weld a variety of titanium based alloys using a conventional fusion based technique viz. gas tungsten arc welding (GTAW). However, post welding, the joint requires heat treatment, which lengthens the process step and increases production costs (Murthy et al.

1998, Sarma et al. 2020). FSW can eliminate this requirement of post-weld heat treatment in titanium alloys. Little information is available on the FSW of titanium alloys. Researchers have suggested that during FSW of Ti alloys, peak temperature in the nugget zone exceeds 1000°C (Li et al. 2020) which is above the β transus temperature of 995°C. In general, it has been mentioned that the peak temperature in the heat-affected zone remains below the β transus temperature (Zhang et al. 2008a).

2.4.5 Friction stir welding of steel

Now-a-days, the FSW technique is focused on joining various types of steel. Steel being the most important engineering material, it constitutes the major components in various structures, buildings, machines, etc. FSW studies have been conducted on low carbon steel (Habibi et al. 2018), austenitic stainless steel (AISI-316L, 304L) (Kumar et al. 2018, Rooyen et al. 2022)), super austenitic stainless steel (Li et al. 2017), high strength low alloy (HSLA-65) steel (Wei and Nelson 2012), super duplex stainless steel (SAF 2507) (Sato et al. 2005), duplex stainless steel (DH-36) (Tingey et al. 2015), and creep resistance steel (P91) (Li et al. 2019). The selection of weld process parameters and the tool material depends on a particular variety of steel as well as the plate thickness. For FSW of steel, shielding by an argon gas environment is provided to protect both the weld zone and the tool from oxidation. As already mentioned, FSW produces much lower heat compared to fusion welding. As a result, the former has a lower chance of metallurgical changes in the HAZ of the material. Furthermore, the chances of distortion and residual stresses in steel are reduced in the case of FSW, making it suitable for welding thicker plates as required in the shipbuilding and heavy manufacturing industries. The issue of hydrogen cracking in steels is also non-existent in the case of FSW, as it's a solid state joining process. Table 2.2 summarizes the FSW of steel at various plate and pipe thicknesses, tool material, spindle speed, and welding speed.

Table 2.2 FSW of different types of steel with various plate thicknesses, tool material, spindle speed and welding speed

Work piece material	Plate thickness (mm)	Tool material	Spindle speed (rpm)	Welding speed (mm/min)	References
0.45% carbon steel	2	WC	250-1000	100	(Imam et al. 2016)
Medium carbon low alloy S45C	2	WC	400	100, 200, 300, 400, 500	(Imam et al. 2015)
st37 steel	2	Tungsten alloy	450-560	50-160	(Karami et al. 2016)
High Ni steel (24 wt%)	1.6	WC	200, 300, 400	400	(Miura et al. 2015)
AISI 304L SS	3.2	W alloy	300, 500	102	(Reynolds et al. 2003)
AISI304L steel	10	WC-Co	630	20, 32, 50, 80	(Sabooni et al. 2015)
304L steel	2.5	WC	1000	40-100	(Meran et al. 2007)
304L steel	12.5	PCBN	250	100	(Liu and Nelson 2016)
304L steel	12.7	-	63-69 95-135	25.4	(Rooyen et al. 2022)
AISI-316L steel	3	W doped	400-800	45	(Kumar et al. 2016)

		with 1% La ₂ O ₃ .			
AISI-316L steel	3	W-Re	500	45 - 85	(Ramesh et al. 2019)
AISI-316LN steel	3	-	600	50	(Rajasekaran et al. 2021)
AISI 409M ferritic stainless steel	4	W-alloy	1000	90	(Lakshminarayanan and Balasubramanian 2012a)
Super-austenitic stainless steel S32654sheets	2.4	W-Re	300, 400	100	(Li et al. 2017)
Duplex stainless steel SAF 2205	2	WC-based material	400	50	(Emami et al. 2018)
Super duplex stainless steel SAF 2507	4	PCBN	450	60	(Sato et al. 2005)
UNS S32750 super duplex stainless steel	2	WC-based	700-1000	40-80	(Sarmadi et al. 2021)
2205 duplex stainless steel	4	W-Re alloy	600	30, 50	(Zhao et al. 2021)
SAF 2507 super duplex stainless	4	W-Re alloy	350, 700	60	(Cao et al. 2022)

steel					
API-5LX80 steel plates	12	PCBN	300, 350, 500	100	(Santos et al. 2010)
API-X100 pipeline steel	6.5	W-Re	600	50	(Cui et al. 2016)
HSLA-65 steel	6.45	PCBN	300- 600	50-200	(Wei and Nelson 2012)
Naval grade HSLA steel	5	W-La ₂ O ₃	600	30	(Nathan et al. 2016)
High nitrogen stainless steel	2	Si ₃ N ₄	400	50, 100, 200, 300	(Miyano et al. 2011)
DH36 steel	6	PCBN coated W-Re	450	250	(Tingey et al. 2015)
Oxide dispersion strengthened (ODS) MA956 steel plates	4	PCBN tool	25,50,100	500,400	(Brewer et al. 2015)
18%Ni maraging steel	5.2	PCBN tool inserter in WC shank	250	25	(Meshram et al. 2017)
Dissimilar steels of grade 304 and st37	3	WC-Co	400, 800	50	(Jafarzadegan et al. 2012)
P91 steel plate	3	PCBN coated	1000	100	(Kalvala et al. 2016)

2.4.5.1 Findings from the studies on FSW of steel

In the case of FSW of steel, the major challenges remain achieving good joint properties and a long tool material life while sustaining the intense heat and pressure required for welding high melting-point materials like steel (Husain et al. 2015). Meshram et al. (2014) achieved acceptable strength in a 4mm thick joint by employing a plunging depth of only 3.72 mm, surpassing the pin length by only 100mm. This clearly establishes the suitability of the tool for joining steel sheets of equal thickness that could vary between 4 and 6mm.

A PCBN tool with a convex scrolled shoulder of diameter 36.8mm, pin diameter of 5.7mm and pin length 1.2mm was used for ferritic stainless steel joining (Cho et al. 2013). They indicated that the strong material flow mainly progresses on the retreating side of the tool. Mironov et al. (2011) investigated the PCBN tool, which consists of a convex scrolled shoulder for joining S31254 super austenitic stainless steel plates of 6 mm, and focused on the grain development mechanism for these grades of super-austenitic stainless steel. PCBN–WRe tools with Re–W alloy reinforced with 60% volume PCBN with a threaded conical pin and a convex threaded shoulder were successfully employed to carry out welding on API-5L X80 steel (Avila et al. 2015). The performed fracture toughness and the fracture surfaces showed predominantly ductile behaviour. Wei and Nelson (2012) also joined 6.45mm thick plates of HSLA-65 steel using a PCBN convex scrolled shoulder tool. They found that mechanical properties decrease linearly as the heat generation exceeds 1308 J/mm.

Brewer et al. (2015) welded oxide dispersion strengthened (ODS) steel by FSW with welding speeds of 25mm/min, 50mm/min, 100mm/min and spindle speeds of 500 rpm, 400 rpm, and 400 rpm, respectively. During their experiment, a steady downward force value of 17.8 kN was involved. They found residual stress in the joint is inversely proportional to heat generation in the SZ and the HAZ. Miyano et al. (2011) joined 2mm thin high nitrogen-stainless steel plates with a spindle speed of 400rpm at different welding speeds of 50, 100,

200 and 300mm/min. They observed improved tensile strength and ductility of the welded joint compared to the base metal. They also reported that welding speeds of 100 mm/min produced the best mechanical properties.

The influence of FSW process parameters on the tensile properties and microstructures of the joint was investigated by Karami et al. (2016). They observed that at lower rpm and higher transverse speeds, defects appeared on the surface due to a lack of sufficient heat generation. Imam et al. (2015) joined medium carbon low alloy steel (S45C) and obtained improved mechanical properties at a fixed rotational speed of 400rpm and at different welding speeds ranging from 100-500 mm/min. Khodir et al. (2012) have done their experimentation on high carbon steel at varying spindle speeds from 100 to 400rpm and a constant welding speed of 100 mm/min. They reported higher values of hardness, yield and ultimate tensile strengths at higher spindle speeds. Spindle speeds of 100-800rpm and welding speeds of 25-400mm/min yielded higher joint strength compared to the base metal (Cui et al. 2007). High nitrogen nickel-free austenitic stainless steel plate welding was done at a travelling speed of 100mm/min and a spindle speed of 400rpm (Li et al. 2015). The welding was successfully performed under force control mode with 20kN vertical load and without any tilt angle. Lakshminarayanan and Balasubramanian (2012a, 2012b) applied spindle speeds and welding speeds of 1000rpm and 90mm/min respectively, for joining 409M ferritic stainless steel. The joint showed higher fatigue life and fatigue crack growth resistance compared to the base metal. Ronevich et al. (2017) employed a PCBN tool to join X52 steel pipe with an outer diameter of 340mm and a nominal thickness of 6.35mm meant for hydrogen transport. A vertical load of 67kN and welding speed of 102mm/min are found to yield good quality pipe welds.

2.4.5.2 Friction stir welding of AISI-316L steel plates and pipes

AISI-316L is one of the popular varieties of austenitic stainless steels. These designations with an "L" at the end indicate low carbon content that makes the steel less prone to precipitation of Cr-rich particles in grain boundaries. Such precipitation causes Cr depletion within the grains, thereby degrading the corrosion resistance of the material (Kumar et al. 2018, Chen et al. 2012). Though the higher Mo content in the AISI-316L grade imparts its higher pitting resistance, higher unwanted precipitation of hard sigma phase intermetallics of $(\text{Fe,Ni})_x(\text{Cr,Mo})_y$ could arise at high welding temperatures (Sabooni et al. 2015, Meran et al. 2007). Existing friction-stir welding and processing studies of these low-carbon steels revealed insignificant precipitations and macro defects with proper selection of tool speed, spindle rotation and axial force for sheets or plates of certain thicknesses (Kumar et al. 2016, Meshram et al. 2014, Ramesh et al. 2019).

For welding AISI-316L steel sheets, Kumar et al. (2016, 2018) employed W tool doped with 1% La_2O_3 and Meshram et al. (2014) used PCBN coated W-Re tool. At 600rpm spindle speed, Kumar et al. (2018) found the hardness at the weld zone to be higher than those at 400 and 800rpm speeds under weld speed of 45mm/min and 12kN vertical downward force adopted in all the three cases. The highest gradient of hardness was noticed on the retreating side of the thermo-mechanically affected zone in case of the sample welded at 600rpm spindle speed. A consistent pattern of the smallest average equiaxed grain size of $5\pm 3\mu\text{m}$ was observed within the weld zone in comparison to 10 ± 2 and $15\pm 3\mu\text{m}$ grain sizes at 400 and 800rpm respectively. A reduction of the post-weld tensile strength to 97% of the base metal observed by Kumar et al. (2018) points out to the necessity of containing the increased hardness below a limit. Meshram et al. (2014) indeed reported an enhancement of the tensile strength of 104% of the base metal with 37% elongation at 8mm/min tool speed and 1100 rpm spindle speed by working under position-control mode with a constant plunge

depth of 3.72mm. Meshram et al. (2014) achieved acceptable strength in a 4mm thick joint by employing a plunging depth of only 3.72mm surpassing the pin length by only 100mm. This clearly establishes the suitability of the tool for joining sheets of equal thickness that could vary between 4 and 6mm.

Ramesh et al. (2019) joined 3mm thick AISI-316L steel sheets under constant 9kN downward force and 500rpm spindle speed. Over the range of constant tool speeds between 45 and 85mm/min, they found the highest joint strength at 65mm/min speed setting. In a friction stir processing study on 15mm thick AISI-316L steel plates, Chen et al. (2012) detected lower sigma phase precipitation at higher tool speed and lower spindle speed ensuring a lower maximum processing temperature. Their experiments involved tool speeds of 16, 20 and 24mm/min spindle speeds of about 38, 47.5 and 57rpm and axial loads of 25, 30 and 35kN. Like the study of Kumar et al. (2018), a correlation between the grain size and hardness distribution on the retreating side was reported. Clearly, most of these studies (Kumar et al. 2018, Ramesh et al. 2019, Chen et al. 2012, Sabooni et al. 2015) were accomplished under the force-control mode, in contrast to a study under the position-control mode (Meshram et al. 2014). No comparison of the findings under these two different control modes of working exists.

2.4.5.3 Friction stir welding of P91 steel plates and pipes

In thermal and nuclear power plants, 9%Cr ferritic / martensitic stainless steel (FSS) is widely used due to their stable mechanical and metallurgical properties at elevated operating temperatures (Pandey et al. 2017, Sunilkumar et al. 2021). P91 is one such ferrite alloy that meets the stringent requirements and is commonly used in power plant industries. This grade of steel is also known as 9Cr -1Mo steel and comes in a variety of compositions. P91 is able to maintain strength at elevated temperature conditions up to about 600°C. It is used to make different parts of a power plant i.e. super-heaters coils, steam piping. Application of P91

effectively allows for enhancing the operating temperature, thereby increasing the efficiency of power plant. Now, the main issue for joining P91 steel by fusion welding is hydrogen-induced cracking (HIC), which is induced by the hydrogen in the electrodes. Hence, researchers have used FSW to join such steels. Li et al. (2019) used a modified 9Cr-1Mo steel plate to conduct FSW experiments and were successful in obtaining defect-free welding joints. Kalvala et al. (2016) joined a 3mm thick P91 steel plate by FSW to investigate the resulting microstructural changes and creep behaviour. A few researchers have also employed FSW to effectively join steel pipes. This is because of the requirement for slow rotation of the pipes, which provides the desired welding speed. Kang et al. (2016) used FSW to join 9Cr-1Mo oxide dispersive-strengthened steel tubes.

Perceiving the dearth of knowledge in the literature on FSW of large steel pipes (which find significant application in supercritical and ultra-supercritical power plants), the current work attempts to effectively join AISI-316L pipes and P91 pipes with FSW. A systematic study is conducted by varying the tool rotation speed (or spindle speed) and the welding speed (or feed rate) suitably and observing their impact on the tensile strength and hardness of the pipe joints. Microstructural characterization of the joints is also undertaken in order to correlate or explain the joint performance. Carrying out circular FSW (as in pipes) effectively requires a different set of know-hows compared to linear welding. Hence, the present study is expected to come up with some new knowledge in the field of pipe welding, which may be interesting for the research community as well as the next generation of power plants and defense industries.

2.5 Summary of the literature review

According to a review of the existing literature, many works have been carried out to joint aluminium (Gan et al. 2008, Sutton et al. 2004), magnesium (Yang et al. 2013, Pareek et al.

2007), titanium (Zhang et al. 2008b, Pasta and Reynolds 2008, Edwards and Ramulu 2010, Reynolds et al. 2005), and steel sheet or plates (Sabooni et al. 2015, Li et al. 2017, Sarmadi et al. 2021) by the FSW using different tools. Proper selection of tool material is important in obtaining a good quality weld. The tool material should be chemically stable and have high toughness and hot hardness at the operating temperature (Li et al. 2015, 2017). Sustaining the intense heat and pressure is necessary for the tool in order to weld high melting-point materials like steel (Husain et al. 2015, Kumar et al. 2016). FSW process parameters, such as welding speed, spindle speed, tool plunge depth, tool tilt angle, spindle torque and the downward force acting on the tool during welding, have a significant effect on producing good quality weldments. The choices of welding speed and spindle speed are important in order to maintain a good flow of material around the tool while minimizing forces on the tool. Welding speed along with the spindle speed determines whether the amount of heat generation during the process is favourable to improve the metallurgical and mechanical properties (Ramesh et al. 2019). For good weldments, many researchers used force control mode. Li et al. (2015) successfully performed FSW to join high nitrogen nickel-free austenitic stainless steel plate welding in force control mode with 20kN vertical load. Ronevich et al. (2017) employed FSW to join X52 steel pipe for hydrogen transport. They applied a vertical load of 67kN and found it to yield good quality pipe weldments.

From the present review, it can be seen that the majority of works revolve around linear welding. There is a dearth in the literature for works related to pipe welding, which is very important and relevant to many industries. Due to the variation in pipe thickness, welding in position control mode resulted in inconsistent weldments around the pipe. This is primarily due to variations in the available downward force, which is one of the most important factors in achieving good quality weldments in pipe welding. An adequate amount

of downward force is responsible for the generation of sufficient frictional heat, which in turn is responsible for material softening during the welding process.

2.6 Motivation for the present work

FSW is a solid-state joining process that is capable of creating high quality and high strength joints with minimal distortion. As modern applications demand stronger, more cost-effective, and more efficient joints that use less energy, FSW seems to be a well suited answer. In addition, FSW offers an environmentally benign solution to these challenges. This has led to its quick advancement from initiation to industrial acceptance. The potential of FSW, as evident from the existing studies, motivates exploring FSW for joining Cr-rich low-carbon steel pipes that have wide-scale industrial applications across power, marine, food and chemical industries. Most of the investigations were conducted to join flat plates or sheets. The joining of pipes by FSW is lacking in the literature. However, the same is a challenging work that may be of interest to welding technology researchers.

Hence, developing and studying methods for joining pipes by FSW (for AISI-316L austenitic steel pipes and P91 ferritic steel pipes) would indeed be of great interest to the scientific community. In the present study, the selected AISI-316L pipe size (around dia. 275 mm) is suitable for various purposes viz. transportation of oil and various fluids, whereas P91 steel is used in critical applications related to power generation and defense. Pipe joints capable of enduring service conditions and at the same time being economical is a win-win situation for the industry. Hence, achieving a higher efficient joint on these pipes is crucial for the relevant industries. The present work attempts to provide a better knowledge of the welding process for joining AISI-316L and P91 steel pipes by FSW in an efficient manner. Considering the challenges of pipe welding, emphasis is placed on the pre-characterization of

the welding process, which would provide a better understanding of the welding method. Moreover, process parameters are suitably varied in order to obtain high quality joints.

2.7 Closure

The current chapter presents an extensive literature review on FSW of various types of low temperature as well as high temperature materials with respect to different grades of tool materials. Various process parameters viz. spindle speed, welding speed and their influence on friction stir welding of different materials are also addressed. The FSW of steels and other ferrous alloys has also been extensively discussed. Finally, the motivation for the present work is described.

Experimental details

Outline of the Chapter: *3.1 Introduction, 3.2 Pipe procurement and machining, 3.3 Tool for steel pipe welding, 3.4 Experimental setup, 3.4.1 Machine setup, 3.5 Welding experiment, 3.5.1 Friction stir welding of AISI-316L pipes in position control mode, 3.5.2 Friction stir welding of AISI-316L pipes at force control mode, 3.5.3 Friction stir welding of P91 pipes at force control mode, 3.6 Sample preparation for weld characterization, 3.6.1 Sample preparation for study of mechanical properties, 3.6.2 Sample preparation for microstructure study, 3.7 Study of mechanical properties, 3.7.1 Hardness Study, 3.7.2 Tensile properties study, 3.8 Study of metallurgical properties, 3.8.1 Optical microscope, 3.8.2 Field emission scanning electron microscope, 3.8.3 Energy dispersive X-ray analysis, 3.8.4 X-ray diffraction, 3.9 Sequence of experiments, 3.10 Closure*

3.1 Introduction

In FSW, heat generation is an important aspect based on which the quality of weldments is determined. As heat generation is dependent on the applied downward force, spindle speed and feed rate, the present investigation begins with pre-characterization, test based on mechanical and metallurgical assessment of weldments under position control (PC) mode on AISI-316L pipes in order to determine the suitable downward force. With this downward force value, a systematic study is carried out in force control (FC) mode to obtain more efficient welded joints for both AISI-316L and P91 pipes. Mechanical and metallurgical examinations of the welded samples are also performed to consolidate the findings. Welding in FC mode is preferable in order to take care of the minor variations in thickness and

circularity observed in the available pipes. Such a procedure would indeed be valuable to narrow down the range of parameter settings prior to identifying the optimum setting for unexplored combinations of tool and workpiece materials.

3.2 Pipe procurement and machining

The pipes were procured from a vendor dealing in steel plates and pipes. The procured pipes had an internal diameter of 259mm and the external diameter of 272mm. The pipes were then machined to join by FSW technique. The chemical composition of the as-received AISI-316L austenitic stainless-steel pipe is given in Table 3.1. The presence of 17.4% chromium provides corrosion resistance, which makes the steel is sometimes referred to as marine-grade stainless-steel. The chemical composition of the as received P91 material is given in Table 3.2.

Table 3.1 Chemical composition of as received AISI-316L pipes

Element	C	Mn	Si	S	P	Cr	Ni	Mo
Wt %	0.023	1.85	0.48	0.018	0.024	17.4	10.42	2.14

Table 3.2 Chemical composition of P91 austenitic stainless steel

Element	C	Mn	Si	S	P	Cr	Ni	Mo
Wt %	0.0746	0.552	0.395	0.0081	0.0257	9.35	0.188	0.887

3.3 Tool for steel pipe welding

For the welding of the pipes, a PCBN coated tool with a W-Re shank by Megastir, USA, is employed. Figure 3.1 shows the details of the tool. The convex coating on the inner part of the tool face of 36.8mm diameter has two parts. At the inner part, there is a conical pin of

3.62mm axial length and 9.2mm diameter. This pin projects out from a scrolled shoulder of slowly increasing diameter over short axial steps. Such convex shaping over a total axial length of 6mm coating makes the tool usable for producing joints of varying thicknesses over a broader range.

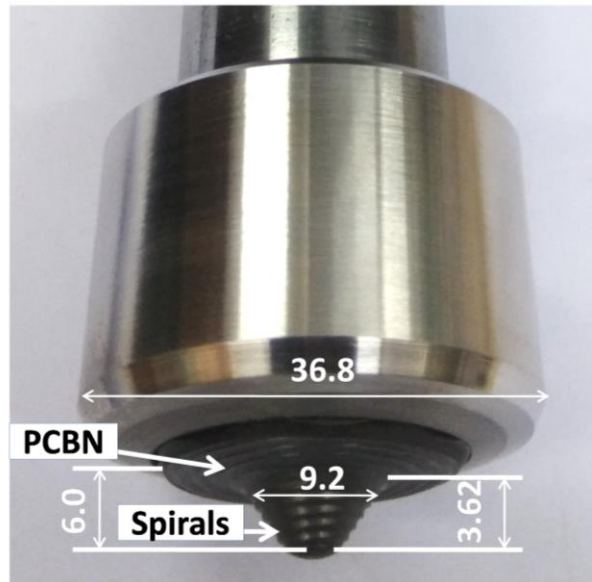


Figure 3.1 FSW tool employed for pipe welding with major dimensions in mm

3.4 Experimental setup

3.4.1 Machine setup

A dedicated FSW setup (Research Machine 1A-0.7) by Megastir, USA, has been used for carrying out the welding experiments. A programmable rotary turntable is attached to this machine, where the pipe segments are mounted. The welding machine is capable of applying a maximum torque of 186N-m about the spindle axis, a maximum downward force (Z-force) of 67kN and maximum lateral force (X or Y force) of 22.25kN. On the mandrel of the rotary turntable, pipes to be welded are mounted with suitable backing plates for protecting the mandrel against damage during the welding process. An arrangement of circulating coolants prevents overheating of the tool and the mandrel during operation. The FSW setup and

backing plate arrangement employed for the pipe welding is illustrated in Figures 3.2 and 3.3, respectively. The cooling arrangement provided in the FSW setup is shown in Figure 3.4.

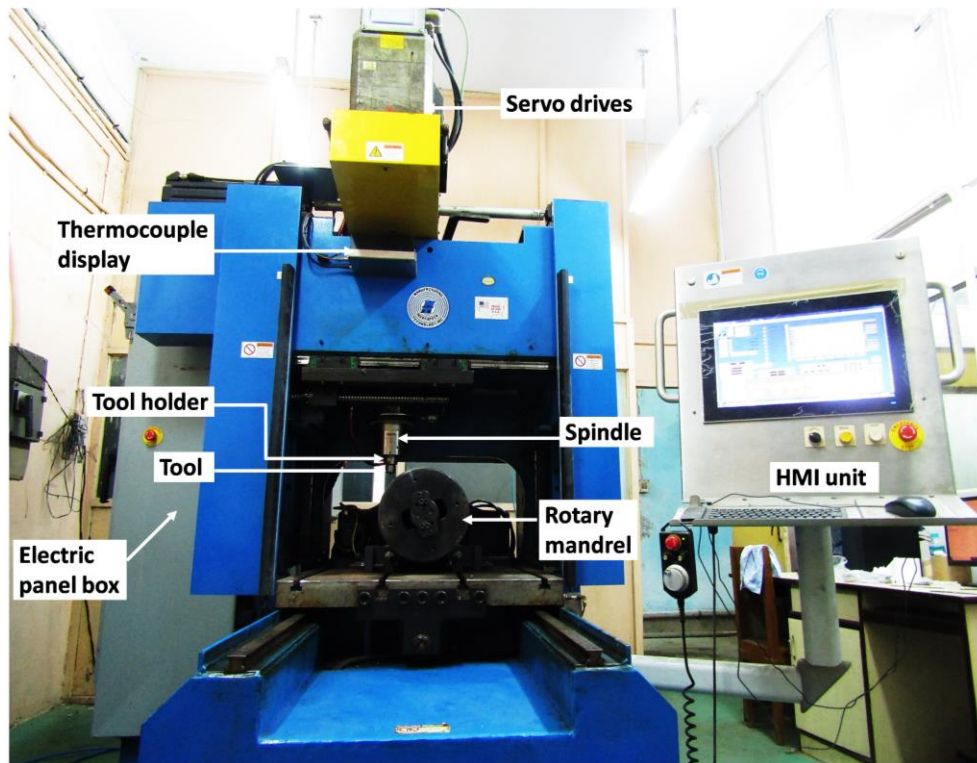


Figure 3.2 Complete friction stir welding setup for pipe welding

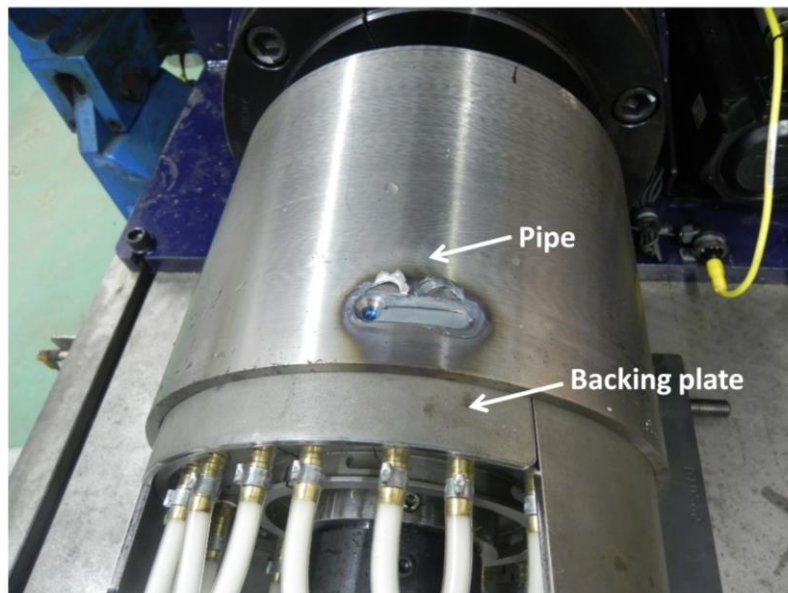


Figure 3.3 Pipe with backing plate

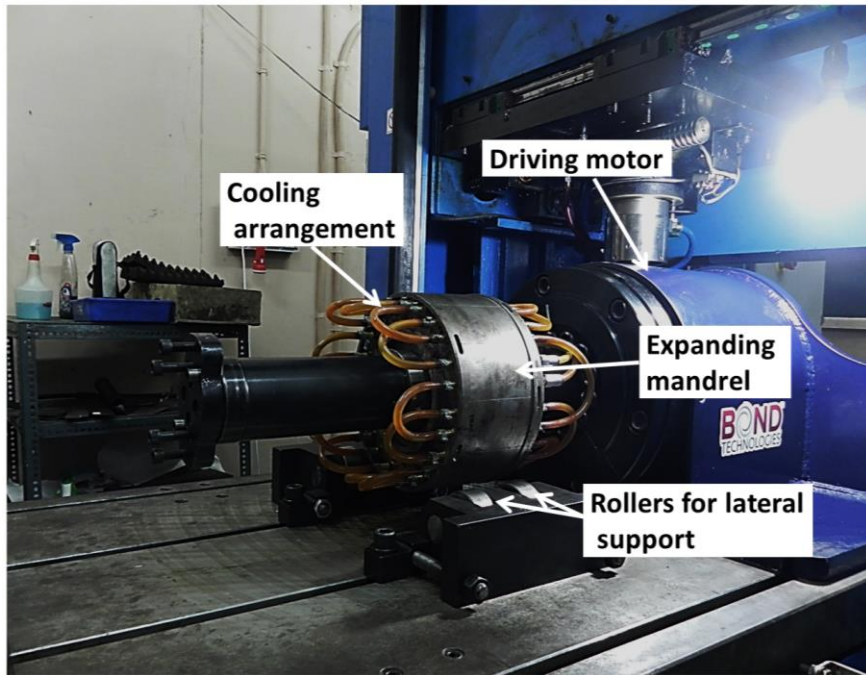


Figure 3.4 Cooling arrangements in the FSW setup

3.5 Welding Experiment

3.5.1 Friction stir welding of AISI-316L pipes in position control mode

The welding of pipes is accomplished at a constant rotational speed of the spindle, holding the tool, throughout the process, which has three major steps. These steps are-

- Downward engagement or plunging of the tool into the wall of the stationary pipe.
- Welding the pipes by rotation of the mandrel at the desired angular speed (ω).
- Upward extraction of the tool from the stationary pipe after welding is over.

The speed along the Y direction given by $V=\omega R$ for a pipe of outer diameter $2R$ is referred to as the linear welding speed. For pre-characterization experiments on pipes of 273mm outer diameter and 6.75mm thickness, welding is carried out under position control (PC) mode with 6mm plunging depth. Figure 3.5 shows the description of different zones of FSW with reference to hot metal working.

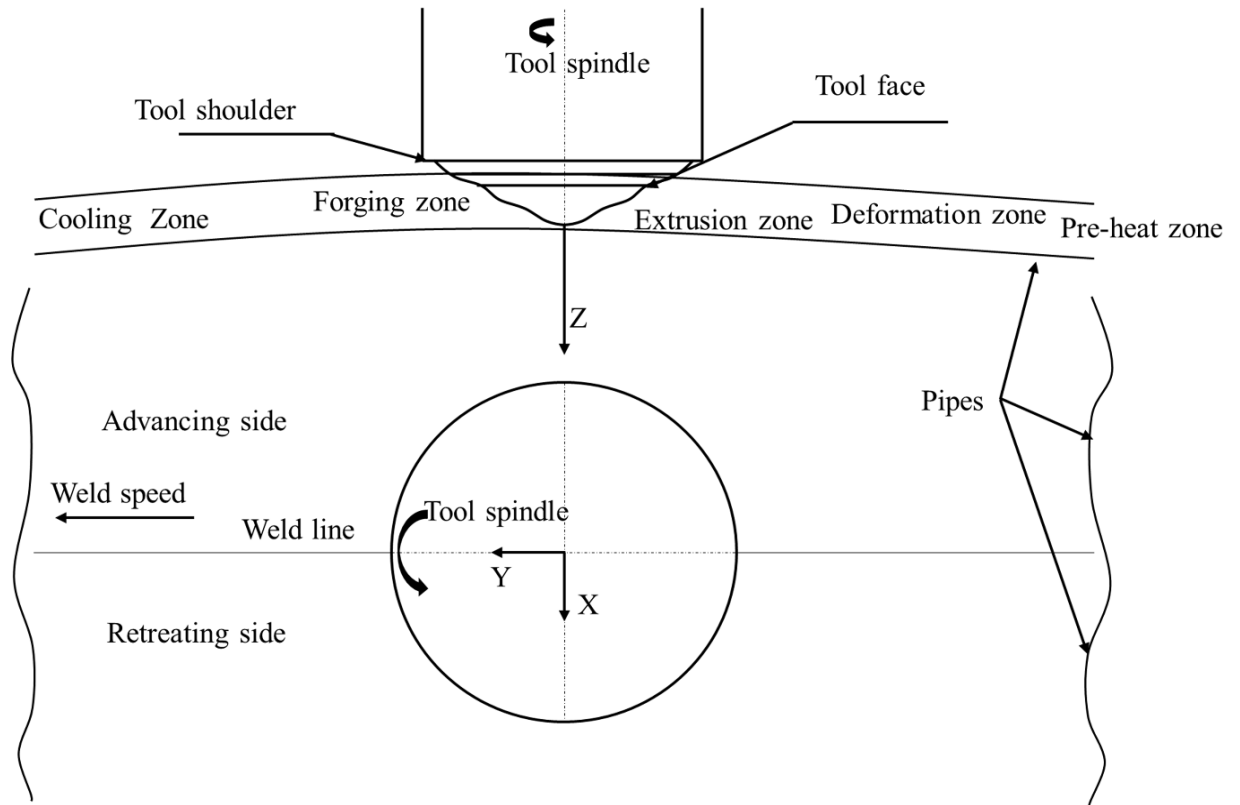


Figure 3.5 Description of FSW zones with reference to hot metal working

In FSW, heat generation is an important aspect based on which the quality of weldments is decided. Now, heat generation is dependent on the applied downward force, spindle speed and feed rate. In position control mode, the feed rate is fixed at 100mm/min whereas the spindle speed is varied. Now, considering the aspect of heat generation, an experimental scheme comprising of a combination of the two said parameters in regular intervals is not found to be suitable for achieving decent welding. In fact, similar reporting is available in the literature (Kumar et al. 2019). The present work is done with a set of parameter values that are selected after a significant number of trials. Table 3.3 lists the key parameters for preparing the joints.

In each experiment, a null adjustment has been made to set the tool at a chosen distance of 3mm above the pipe surface with the tool axis aligned to the intended weld seam separating the two pipe segments. Then the tool spindle has been allowed to acquire the

specified speed followed by imparting the plunging motion in two phases. First, the feed is set at a faster rate of 20mm/min through air over the null distance. In the second phase, the tool is made to enter the pipe material at a rate of 10mm/min. Figure 3.6 depicts a closer look at pipe welding in progress, along with the associated details.

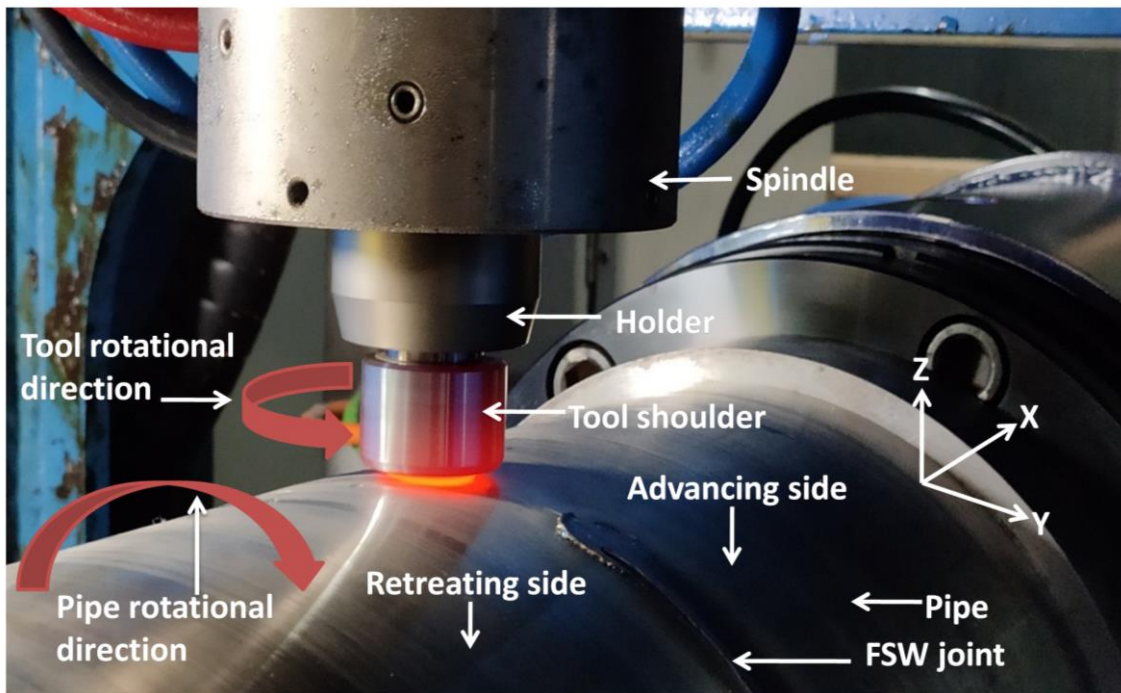


Figure 3.6 Friction stir welding process for pipes

Table 3.3 FSW parameters for PC mode welding of AISI-316L pipes

Expt. No	Control mode (PC/FC)	Z-Force (kN)	Spindle speed (rpm)	Feed rate (mm/min)	Plunge depth (mm)
1	PC	Free	250	100	6
2	PC	Free	300	100	6
3	PC	Free	325	100	6
4	PC	Free	350	100	6
5	PC	Free	400	100	6
6	PC	Free	450	100	6

Table 3.4 FSW parameters for FC mode welding of AISI-316L pipes

Expt. No.	Control mode (PC/FC)	Z-Force (kN)	Spindle speed (rpm)	Feed rate (mm/min)
1	FC	35	250	50
2	FC	35	300	50
3	FC	35	350	50
4	FC	35	400	50
5	FC	35	450	50
6	FC	35	500	50
7	FC	35	550	50
8	FC	35	600	50
9	FC	35	650	50
10	FC	35	700	50
11	FC	35	250	100
12	FC	35	300	100
13	FC	35	350	100
14	FC	35	400	100
15	FC	35	450	100
16	FC	35	500	100
17	FC	35	550	100
18	FC	35	600	100
19	FC	35	650	100
20	FC	35	700	100

3.5.2 Friction stir welding of AISI-316L pipes in force control mode

Welding in FC mode is preferable in order to take care of the minor variations in thickness and circularity observed in the available pipes. Such a procedure would indeed be valuable to

narrow down the range of parameter settings prior to identifying the optimum welding conditions for unexplored combinations of tool and workpiece materials. AISI-316L grade austenitic stainless steel pipes have been welded in force control mode. For the current experiment, the downward force has been taken as 35kN for all welding experiments. A counter clockwise rotation (CCW) movement has been given to the tool as recommended by the manufacturer. FSW of AISI-316L pipes by force control mode has been carried out at combinations of various spindle speeds and welding speeds as given in Table 3.4. Figure 3.7 shows the outer surface and inner surface of a welded AISI-316L pipe under FC mode. A penetration limit of 6mm is given in FC mode welding to prevent welding of pipes with the backing plates. An infrared thermometer capable of measuring -50°C to 1980°C of model no-HTC, IRX-68 has been used to measure the temperature at the weld zone during the welding.

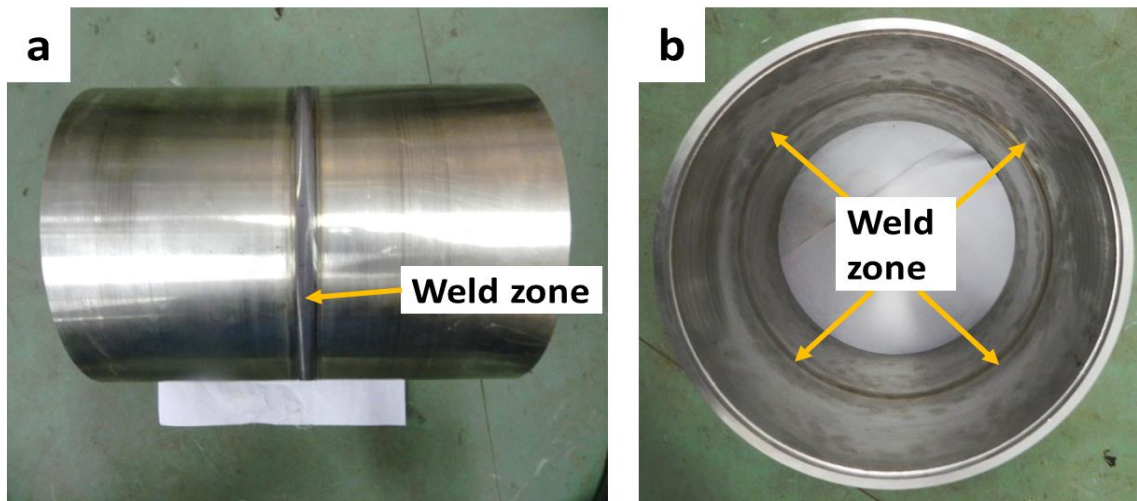


Figure 3.7 (a) Outer surface and (b) inner surface of welded pipe

3.5.3 Friction stir welding of P91 pipes in force control mode

Taking cue from the AISI-316L pipe welding, FC mode welding is carried out for P91 steel pipes. The parameters for the welding experiments are presented in Table 3.5. The same infrared thermometer has been used to measure the temperature at the weld zone during the welding.

Table 3.5 FSW parameters for FC mode welding of P91 pipes

Expt. No.	Control mode (PC/FC)	Z-Force (kN)	Spindle speed (rpm)	Feed rate (mm/min)
1	FC	35	250	50
2	FC	35	300	50
3	FC	35	350	50
4	FC	35	400	50
5	FC	35	450	50
6	FC	35	500	50
7	FC	35	550	50
8	FC	35	600	50
9	FC	35	650	50
10	FC	35	700	50
11	FC	35	250	100
12	FC	35	300	100
13	FC	35	350	100
14	FC	35	400	100
15	FC	35	450	100
16	FC	35	500	100
17	FC	35	550	100
18	FC	35	600	100
19	FC	35	650	100
20	FC	35	700	100

3.6 Sample preparation for weld characterization

3.6.1 Sample preparation for study of mechanical properties

For tensile test, samples have been prepared as per ASTM-E8 standard having a gauge length of 50mm, width 12mm and thickness 4mm. The samples have been extracted along the

transverse direction to the weldments by wire cut electro discharge machining (EDM). A schematic illustration of the tensile test sample with dimensions has been shown in Figure 3.8. For hardness evaluation, samples have been cut along the cross section having 30mm length from the joint. Subsequent to cutting, each hardness sample has been polished in a double-disc polishing machine made by Metlab Equipments & Engineering System, India (refer to Figure 3.9) by using emery paper of grades 120, 400, 800, 1000, 1200, 1600, 2000 and 2500.

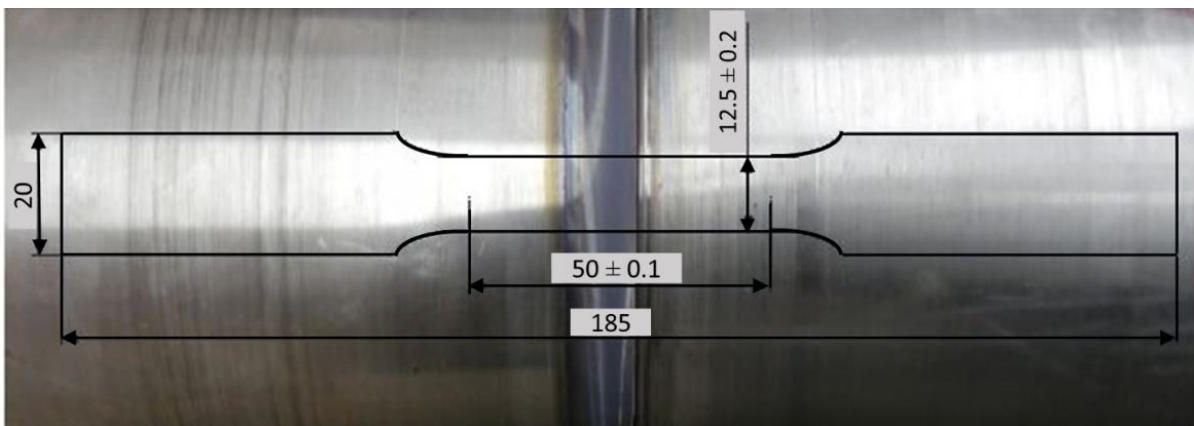


Figure 3.8 Tensile test samples cut from P91 pipes

3.6.2 Sample preparation for microstructure study

The samples for the metallographic study have been cut along the weld cross section by wire cut EDM in order to avoid excessive heat generation and also to get precise cutting. After extraction, the samples have been polished using different grades of emery papers ranging from 120 to 2500 grit. A final polish has been done using 6 μ m, 2 μ m and 1 μ m diamond slurry. After polishing, the samples have been etched for 80second with a reagent consisting of nitric acid, hydrochloric acid and water.



Figure 3.9 Polishing machine

3.7 Study of mechanical properties

3.7.1 Hardness study

The hardness of a material represents its ability to resist surface penetration or being permanently deformed when a load is applied. Microhardness is measured by getting hardness values in a small area using a small indentation. Vicker microhardness is one of the hardness measurement techniques that uses a diamond indenter of pyramid shape with a square base and an apex angle of 135° . The Vickers hardness test is a commonly used test due to its wide load range capability. The hardness value is measured based on applied load divided by square of the diagonal of the impression made by the indenter. Vickers hardness (HV) is calculated by the following equation: -

$$HV = 1.8534F / d^2$$

Equation 3.1

where, F is the load in kilogrammes of force and d is the average of two diagonals created by the pyramidal indenter in millimeters. The surface of the test samples is to be finished. In the present work, cross sections of welded samples were polished with SiC emery paper for hardness study.

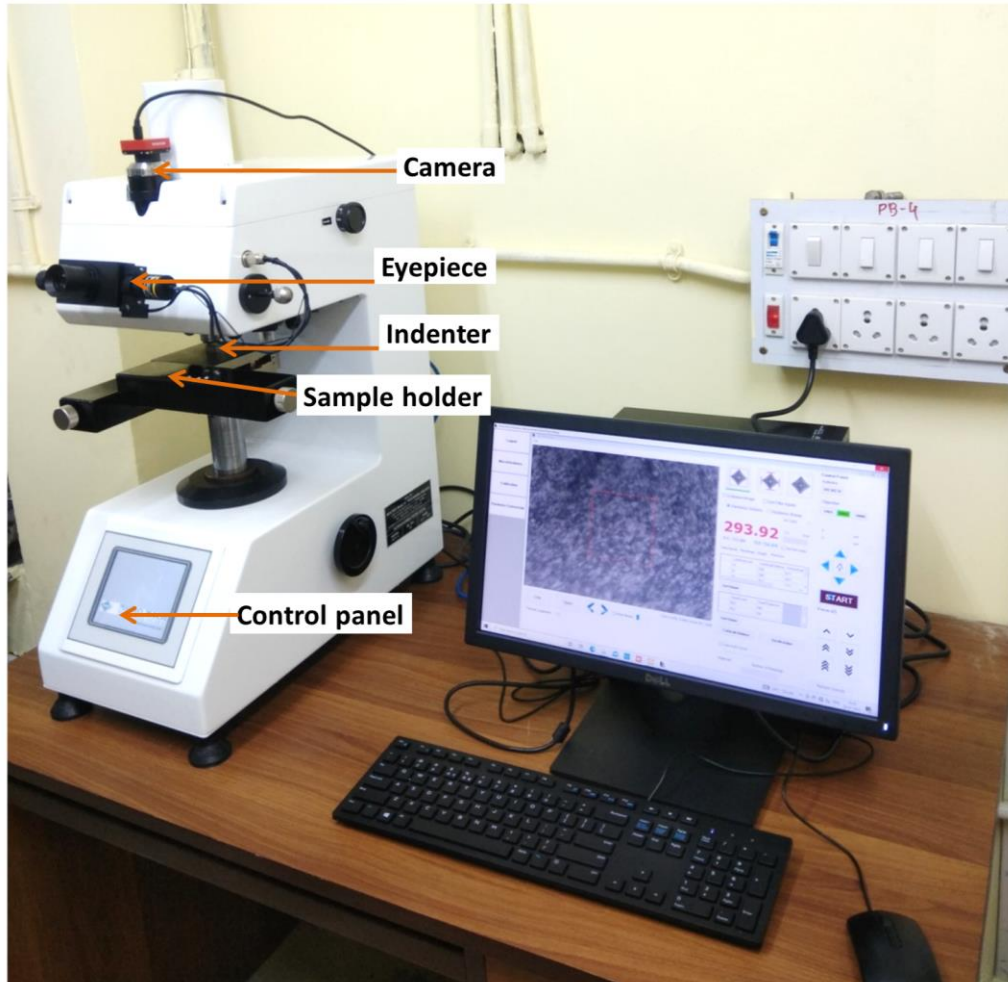


Figure 3.10 Vickers micro hardness tester

Vickers microhardness values have been measured along the cross section of the welding samples using a microhardness tester of model number MMV-A manufactured by Micro-Mech Technologies, India (shown in Figure 3.10). The hardness values were measured along the cross section of the welded joint and the indentations were taken at every 2mm interval by setting the load at 500gm and the dwell time of 10s (refer to Figure 3.11). The

microhardness values have been measured in all the zones of the welded samples as well as BM.

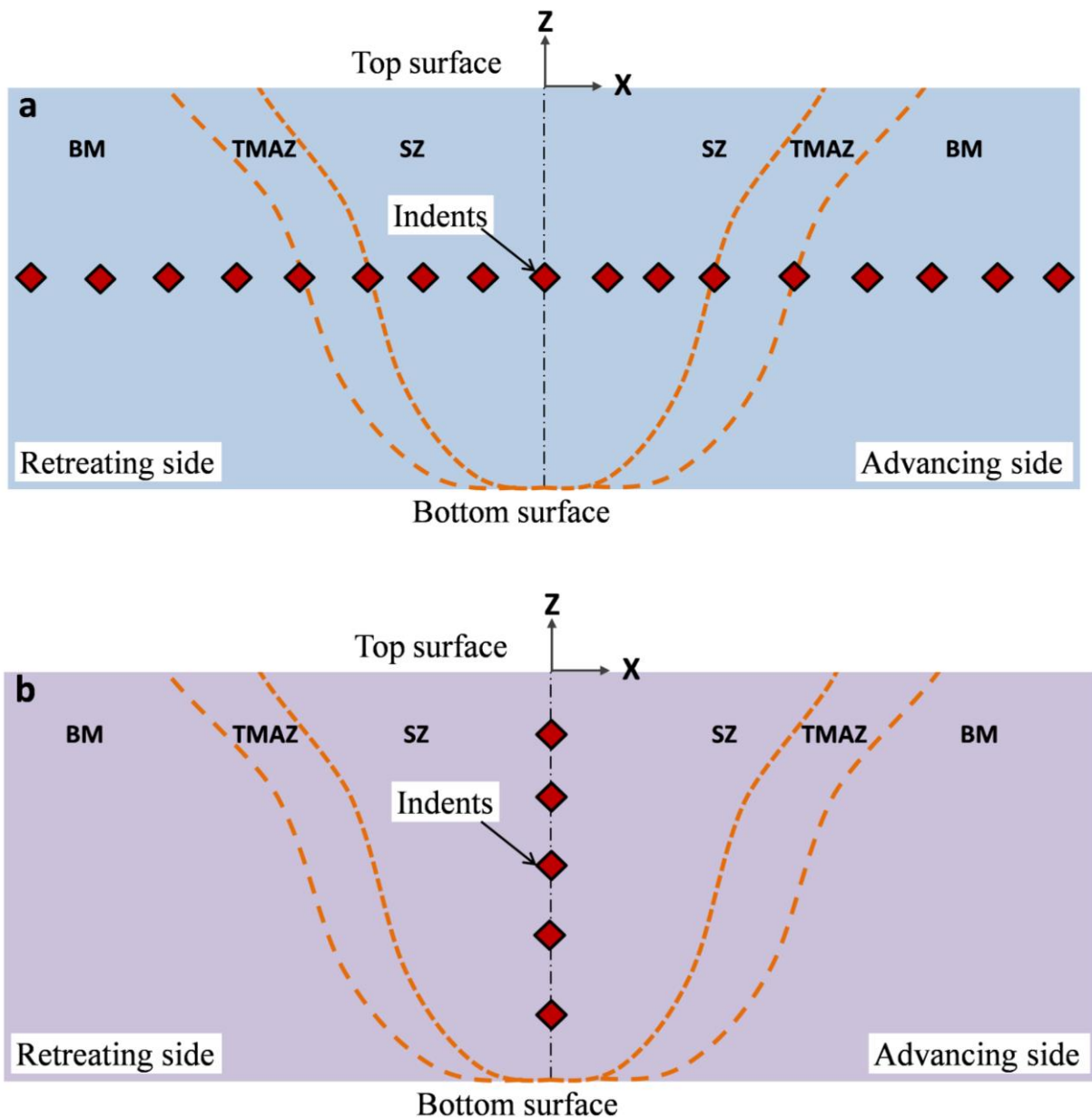


Figure 3.11 Hardness measurement scheme for welded samples (a) horizontal scheme (b) vertical scheme

3.7.2 Tensile properties study

Uniaxial tensile test is done in order to achieve material properties such as yield strength, ultimate tensile strength and percentage of elongation. A computerized universal testing machine of 100kN load capacity by Instron, India has been used to conduct the tensile tests.

BISS hydraulic wedge grip (model no. AC-05-11T3, India) has been employed to carry out the tensile tests with a maximum load setting of 40kN under normal ambient condition (32°C) as shown in Figure 3.12. The samples have been prepared as per the ASTM-E8 standard having a gauge length of 50mm, width of 12mm and thickness of 4mm. The samples have been extracted along the transverse direction of the weldments. The tensile tests were conducted at a 10^{-3} strain rate.

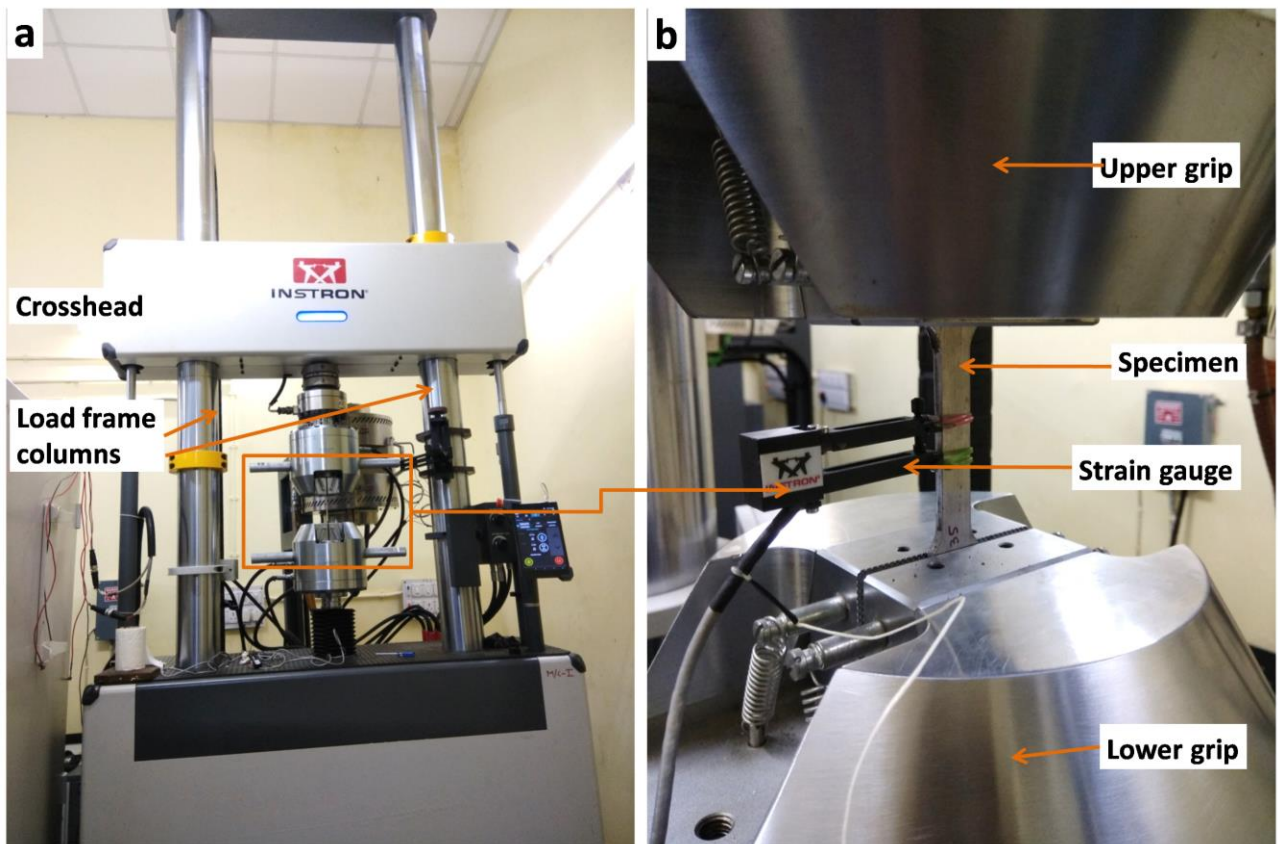


Figure 3.12 Universal testing machine with loaded specimen

3.8 Study of metallurgical properties

3.8.1 Optical microscopy

The characterization of the material helps to better understand its properties, physical behaviour, and performance from a certain perspective and explain the same. Microscopic techniques are required to study and characterize materials. The optical illumination system is

the main component of the optical microscope. The samples surface is required to be ground to a mirror finish. This is done by using successively finer emery paper and polishing powder. The final microstructure is developed by etching. For the current study, FSW samples were polished with different grades of SiC emery papers. Metallographic polishing is done with diamond paste on polishing cloths. For the current study, samples are observed by an optical microscope (Leica DM 2700M, Germany) to analyze the weld cross section (refer to Figure 3.13).

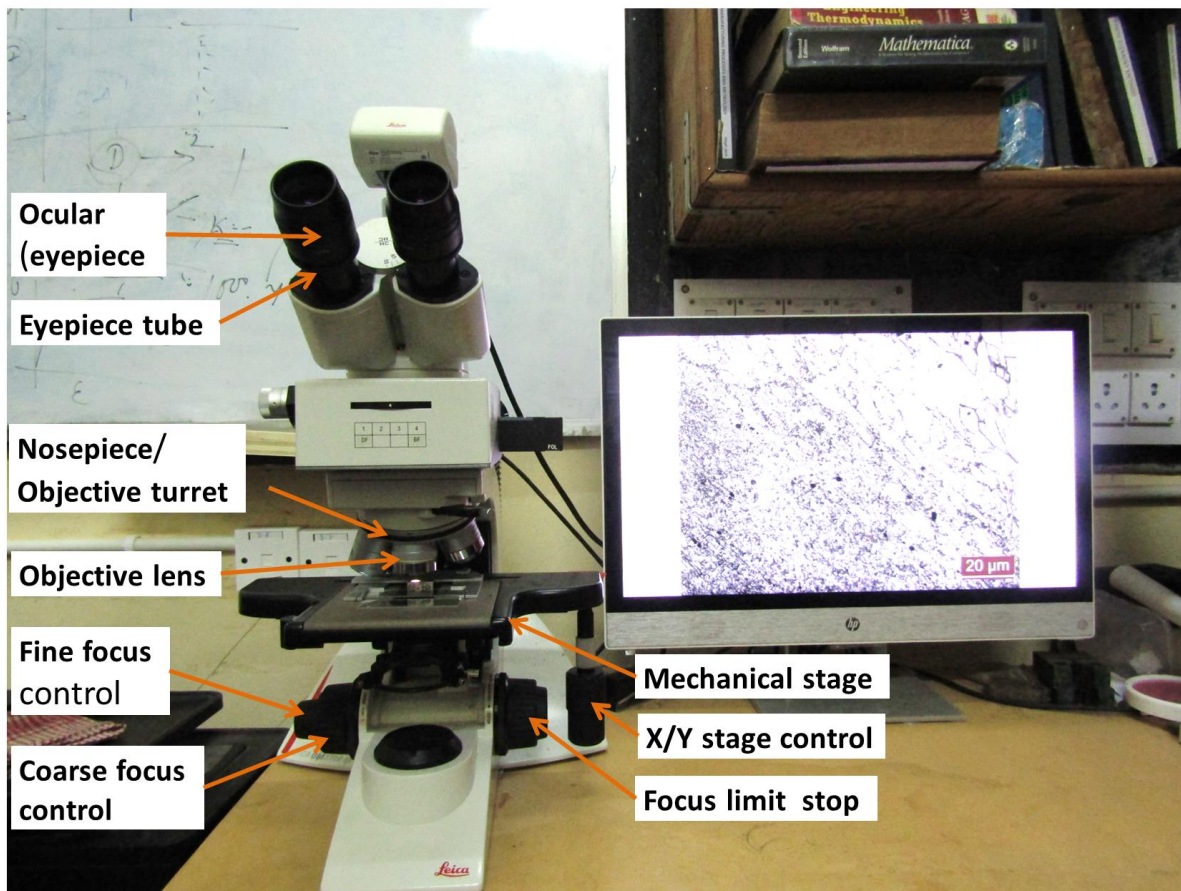


Figure 3.13 Optical microscope setup

3.8.2 Field emission scanning electron microscope

Scanning electron microscopy is a very useful technique to observe in detail the microstructure of different zones (unaffected BM, HAZ, TMAZ, and SZ) of the FSW samples. In the scanning electron microscopy technique, the surface of a sample is scanned

with an electron beam. The reflected electron beam is collected (Callister and Rethwisch 2018) and then displayed at the equal scanning rate on a cathode ray tube (CRT) monitor. The magnification in SEM ranges from about 10 to 50000 times and with a significant depth of field. In the current study, AISI-316L and P91 welded samples were observed by SEM to identify the grain structure and microstructure of the weld zone. A field emission scanning electron microscope (FESEM SUPRA 35VP, Carl Zeiss, Germany) has been used to get a detailed look into the weld zone (refer to Figure 3.14).

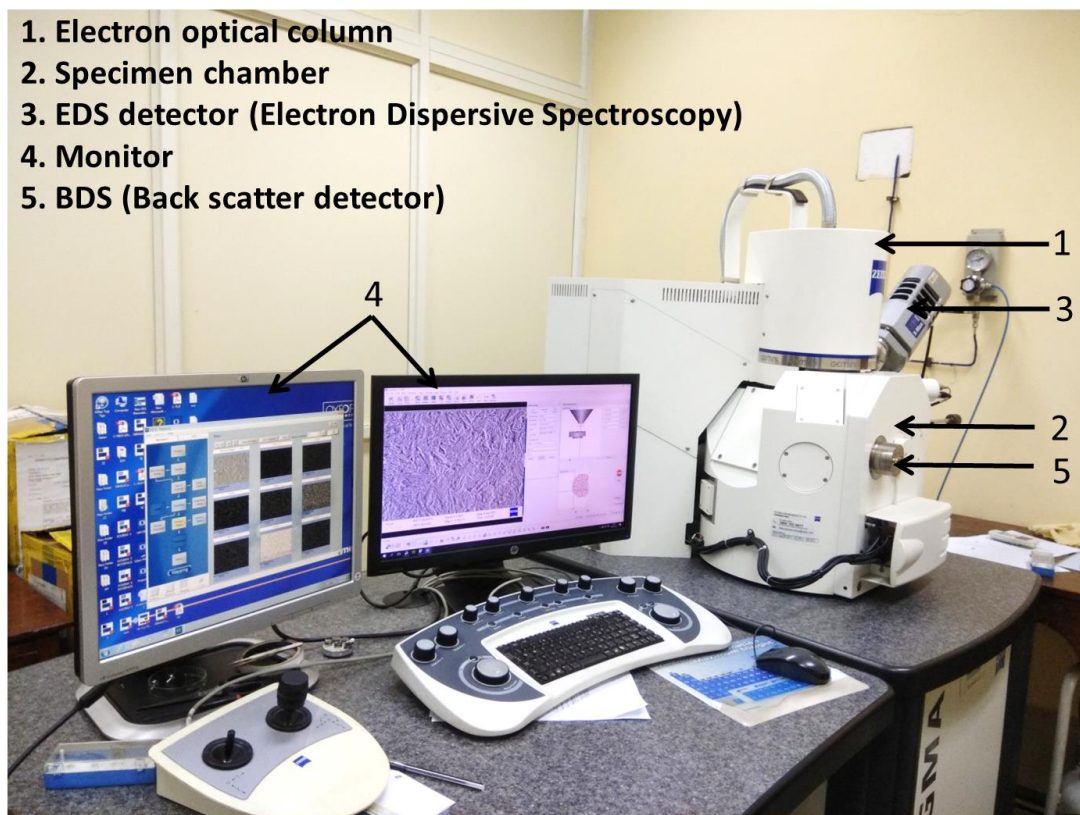


Figure 3.14 SEM along with the EDX setup

3.8.3 Energy dispersive X-ray analysis

Energy dispersive X-ray analysis is used to determine the elemental composition of the sample. In the EDX technique, a particle beam is directed at the surface of the material under investigation, which in turn induces the emission of secondary or backscattered particles (photons, electrons). These secondary particles can be characterized to get the composition of

the cross section of the joint surface. EDX and SEM are both used with the same electron source. EDX can either be used to analyze composition at a point or over a wide area. Specific elements can also be mapped over a test surface by scanning for X-ray emission at a specified energy. In the current study, EDX is done for the compositional analysis of the FSW AISI-316L and P91 welded pipe samples. This indicates the presence of alloying elements (Cr, Mn, Mo, V, Nb, Fe, C) by their weight percentages and atomic percentages, which helps in determining whether any tool material constituents are being deposited or not. In EDX, the penetration of electrons into a sample is in the range of 0.1 to 1 μm and hence, elemental composition can be accurately detected within this range of thickness of the friction stir welded samples.

An EDX attachment available with the FESEM instrument has been used to get the elemental compositional analysis of the welded samples (refer to Figure 3.14). The potential while conducting EDX is maintained at 20 kV.

3.8.4 X-ray diffraction

X-ray diffraction (XRD) is a non-destructive testing method that determines the crystal structure of the material. The XRD technique is based on diffraction, which is the elastic scattering (change of direction) of the motion of the electromagnetic waves without any energy loss. The use of diffraction methods is of great importance in the analysis of crystalline solids. XRD has a wide range of applications in materials characterization for the determination of crystal structure, orientation, phase identification, and the detection of any trace compounds in materials. An X-ray diffractometer has an X-ray source, a rotating sample holder, a series of counters to monitor the diffracted X-ray's intensity. In XRD, monochromatic light X-rays are used. These bands denote destructive and constructive interference of the scattered X-rays. The rotation of the sample helps to detect the diffracted pattern, which is a series of dark and light bands. The angular spacing between dark and light

bands indicates the size of the inter-planar spacing, which is used to determine the compounds present in the samples. Identification of compounds can be obtained by comparing the X-ray diffraction graph of an unknown sample with the standard spectra obtained from the JCPDS (Joint Committee on Powder Diffraction Standards) database. XRD is useful for the analysis of bulk samples. Hence, XRD is found to be helpful for evaluating the FSW specimens in the current work.

An X-ray diffraction (ULTIMA IV XRD system, Rigaku, Japan) has been used to detect the phases in the weld zone. The machine was operated at 45kV and 40mA using $\text{CuK}\alpha$ radiation with the Bragg Brentano geometry, with a step size of 0.02 (2 theta value), step time of 3s from 10 to 95° for AISI-316L samples and from 40 to 120° 2 θ range for P91 samples.

3.9 Sequence of experiments

All the experiments in the present study are done in sequence so that proper and logical inferences can be drawn from the experimental results. A flow chart of the sequence of experiments is shown in Figure 3.15. The investigation begins with pre-characterization tests, mechanical and metallurgical examinations under PC mode for AISI-316L steel pipes for finding the joint strength. As the results was not according to expectation hence machine control mode has been shifted. This sets the stage for carrying out further welding in the FC mode by using force settings within the acceptable range established by the analysis of the pre-characterization results. Welding in FC mode is preferable in order to take care of the minor variations in thickness and circularity observed in the available pipes. Such a procedure would indeed be valuable to narrow down the range of parameter settings prior to identifying the optimum setting for unexplored combinations of tool and work piece

materials. In FSW, heat generation is an important aspect based on which the quality of weldments is decided.

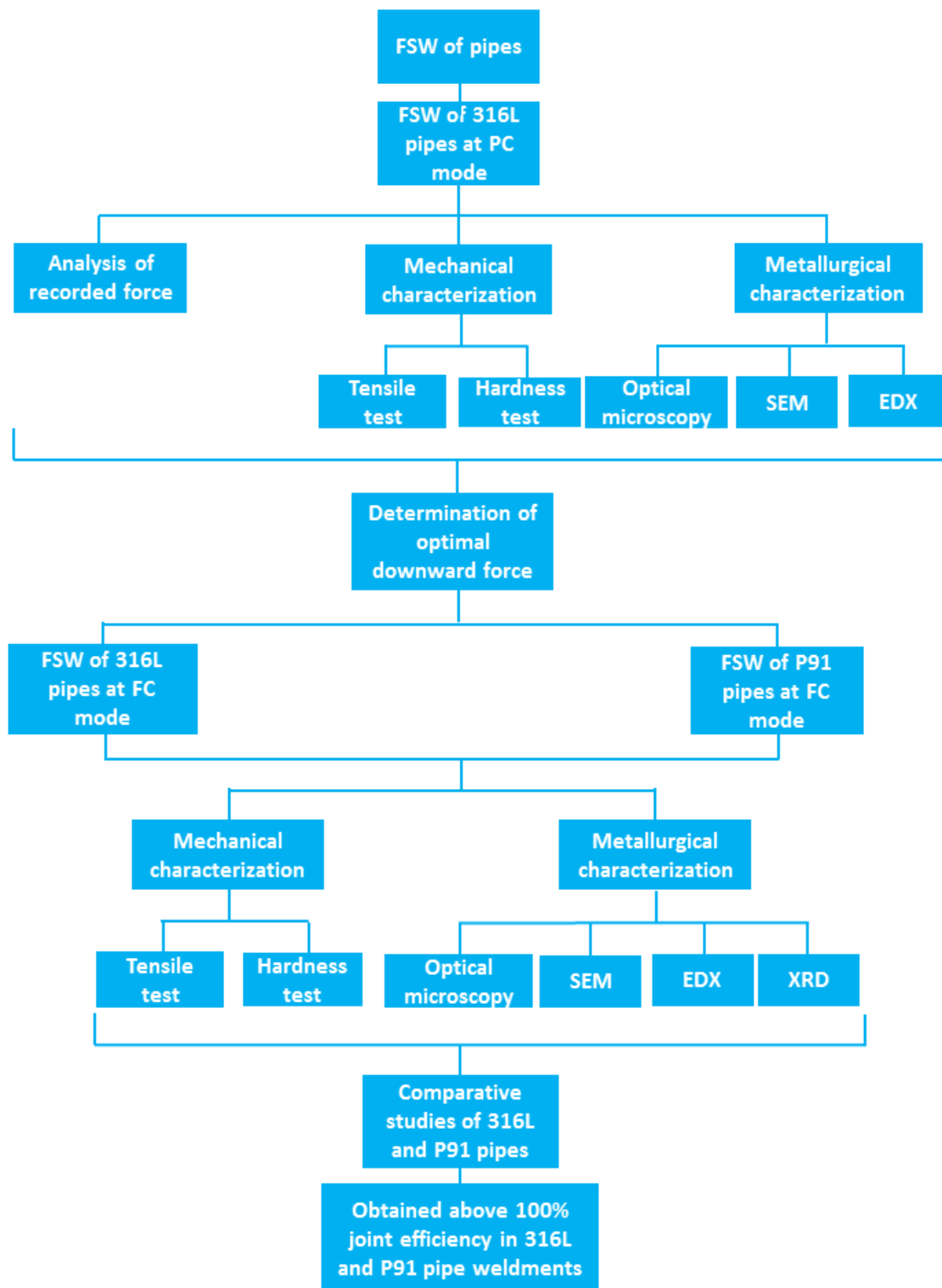


Figure 3.15 Flow chart of the sequence of experiments

Now, heat generation is dependent on the applied downward force, spindle speed and feed rate. In the present study, the downward force is fixed at 35kN whereas the other two parameters are varied. Now, considering the aspect of heat generation, an experimental scheme comprising a combination of the two said parameters at regular intervals is found to be suitable for optimized the parameter for higher joint strength. P91 stainless steel pipes were joined using the same downward force setting, and mechanical and metallurgical characterization was performed to achieve optimum joint strength.

3.10 Closure

This chapter presents the details of the experimentation in position control and force control used for FSW of AISI-316L and P91 steel. Initially, the tool for steel pipes and the experimental setup are discussed in detail. Then the mechanical testing methods, viz. hardness, tensile tests, are discussed, with details on the machines used for the tests. After that, the microstructure studies viz. microscopy, compositional analysis and phase transformation and their equipment details, are presented. Finally, the sequence of experimentation is discussed.

This page is left blank intentionally

AISI-316L steel pipe welding at position control mode

Outline of the Chapter: *4.1 Introduction, 4.2 Pre-characterization at position control mode, 4.3 Physical examination of AISI-316L weldments, 4.3.1 Surface of welded sample, 4.3.2 Cross section of welded sample, 4.4 Study of mechanical properties, 4.4.1 Hardness behavior, 4.4.2 Study of tensile properties, 4.5 Metallurgical study, 4.5.1 Optical microscopy of welded samples, 4.5.2 Scanning electron microscopy of welded samples, 4.5.3 Energy dispersive X-ray analysis of welded samples, 4.6 Closure*

4.1 Introduction

In the current work, welding have been conducted in position control mode to determine the suitable downward force and the range of parameters (spindle speed, welding speed) to join austenitic stainless steel AISI-316L pipes. Due to the inherent challenges associated with circular pipe welding viz. weld configuration, curved geometry at the weld zone, ovality issues, etc. the optimal combination of weld parameters for linear welding cannot be one to one mapped in case of pipe welding even though keeping the material to be welded the same as that of pipes. Hence, actual pipe welding needs to be carried out in order to understand the FSW process dynamics and to understand the exact effect of the process parameters on the weld quality and performance. In position control mode, the parameters viz. spindle speed (RPM), welding speed/feed rate (mm/min) and tool depth (mm) are varied in order to get an idea about the welding process and to assess the effect of these parameters on the weldment. Based on the weld quality and the data recorded during the welding process, mechanical and

metallurgical examinations of the welded samples are also performed to consolidate the findings.

4.2 Pre-characterization at position control mode

An important control variable, which is used in the machine controller to adjust the spindle torque, is called the position error. This is defined as the distance of the actual position of the tool from its target position at each instant commensurate with the plunging rate demand for each phase. A proportional controller estimates the spindle torque by multiplying the instantaneous error with a machine-set constant referred to as proportional gain. Position control mode was used to maintain constant depth of penetration for the tool. Pre-characterization tests are conducted in PC mode to determine the suitable downward force. Welding is performed under the position control mode against the call of 6mm of engagement depth into the pipe material. The average values of vertical force (Z-force) and spindle torque at the welding phase during experiments are recorded. Experiments 1-6 have been executed under position-control mode during which both the engagement as well as welding phases are shown in Table 4.1.

Table 4.1 Process parameter values under PC mode experiments

Expt. No.	Control mode	Z-Force (kN)	Spindle speed (rpm)	Feed rate (mm/min)	Plunge depth (mm)	Remarks
1	PC	Free	250	100	6	For determining suitable downward force by varying spindle speed at welding speed
2	PC	Free	300	100	6	
3	PC	Free	325	100	6	
4	PC	Free	350	100	6	
5	PC	Free	400	100	6	
6	PC	Free	450	100	6	

At the beginning, the static friction in the Z guide gives rise to steep rise of error resulting in a proportional rise to a high spindle torque apparent in Figures 4.1 to 4.6. As the tool starts moving downward by overcoming the friction, the error starts falling almost as steeply as evident from the corresponding sharp drop of the spindle torque. The termination of a brief initial phase of imperceptible downward tool motion is observed to be associated with a momentary rise in the spindle torque to about 130N-m and a subsequent fall to a much lower value around 22kN. While the rise can be attributed to a jerk at the beginning of significant motion, the fall is certainly due to the much lower dynamic friction.

The significant tool motion corresponds to a downward speed close to the specified rate of 20mm/min in air that is sustained by a nearly constant low spindle torque working against the friction in the spindle bearing and the guide. Since the tool faces no material resistance during its 3mm travel at a speed close to the specified rate of 20mm/min in air before the tip touches the pipe, the torque remains low. Corresponding to the downward tool traverse specified at a rate of 20mm/min over 3mm, the duration of the first phase is estimated as 9s long. The initial lag in the commencement of perceptible tool motion pushes the instant of termination of the air travel beyond 9s. This is evident from the onset point a while after 9s for the sudden reduction in the slope of variation of the Z-depth, at which the tool speed drops close to 10mm/min rate specified for the plunging through the pipe material. The estimated duration of the material plunging specified as 6mm at a lower rate of 10mm/min is 36s. Next, a dwell period of 1s has been specified prior to start of the pipe rotation. Thus, the starting instant of the pipe rotation for the welding phase is obtained as 46s that is shown by the vertical dashed line separating the phase of engagement from welding labelled respectively as E and W in Figures 4.1 to 4.6.

As the tool plunges into the material, sharp increases are observed for both the spindle torque and the Z-force with time in Figures 4.1 to 4.6. The rise of spindle torque is due to a

rise in the rate of the error that is expected on account of higher resistance to penetration faced by the convex tool face. The slope discontinuities apparent in the variations of both torque and Z-force could be attributed to discrete but progressive flattening of the tool curvature from the tip to the shoulder. There are right-handed spirals on the tool face coming in contact with the pipe segments. In view of the sharper curvature up to increase of tool radius to 9.2mm from the pointed tip, the rate of rise of the spindle torque initially remains relatively lower. Up to 9.2mm radius and 3.62mm axial length of the conical portion, the tool face contains a spiral with 0.64 threads per mm. The tool face has two spirals with 0.332mm threads per mm between the radii of 9.2mm and 36.8mm.

On the blunter face of the tool, the two spirals are much wider and act like shoulders on the pipe tilted at a small angle with respect to the normal to the tool axis. As this part of the tool plunges into the pipes during the further downward movement, the area under the tool coming in contact with the pipe segments undergoes substantial increments with the progressive flattening of the tool curvature. The accompanying increases in both the friction and the force sustaining the tool plunging give rise to successive sharper rise in the spindle torque. It is evident from each of Figures 4.1 to 4.6 that over a long duration, the rise in the spindle torque during the tool plunging remains sufficient for sustaining the specified rate close to 10mm/min. The error starts falling when the specified 6mm Z-plunging into the pipe wall is approached by the tool. This leads to fall in both the spindle torque and the Z-force. Consequently, the rate of plunging starts dropping sharply from the specified rate of 10mm/min leading to a continuation of the plunging for a while with the concomitant welding caused by the mandrel rotation.

Figure 4.3 corresponds to welding executed under the position control mode against the demand of 6mm of engagement depth into the pipe material. However, the finally acquired steady Z-depth of 5.6092mm is clearly lower than the demand of 6mm. The

difference between the demand and the steady output in each experiment is called the steady error. A positive steady error is a characteristic feature of the proportional control of the spindle torque, since no error would imply no power on the tool to penetrate into the pipe material to sustain the welding or overcome the friction to keep the spindle rotating. The lag of the onset of significant Y component of tool force that ploughs into fresh pipe material from the start of the pipe rotation could be attributed to the time taken by the pipe to acquire the specified speed. A corresponding X component of tool force emerges, since the linear welding speed corresponding to the pipe rotation favors and opposes the material flow on account of that arising from the linear velocity due to the tool rotation at the advancing and retreating sides respectively.

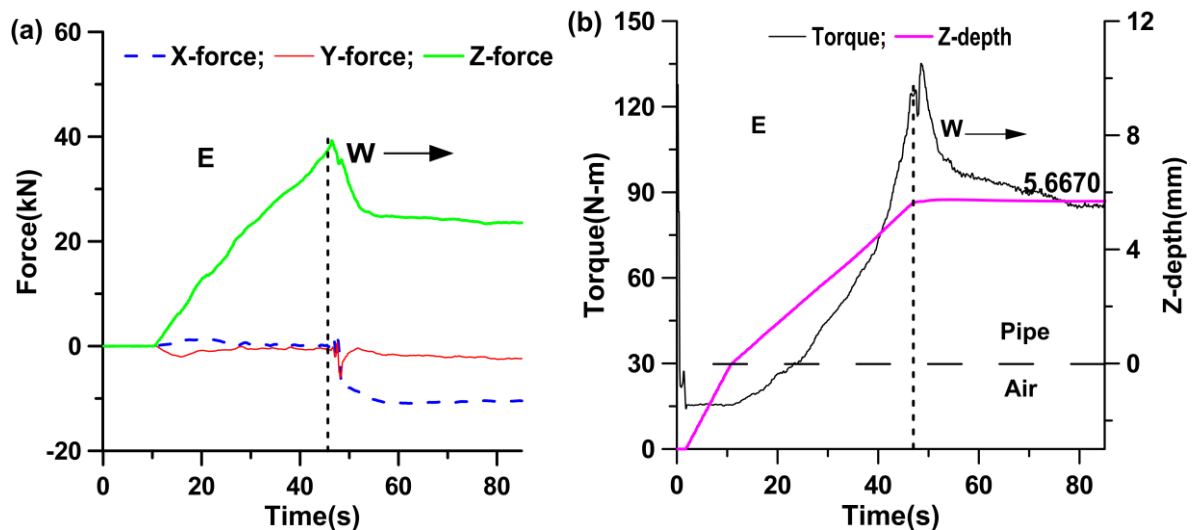


Figure 4.1 Variations of (a) Forces, (b) Spindle torque and achieved Z-depth with time for FSW of AISI-316L pipes at 250rpm, 100mm/min and 6mm Z-depth settings

Figure 4.1 to 4.6 show the average engagement length achieved in all the cases is seen to be very near to 5.65mm. Of course, the welding depth is expected to be greater than the engagement depth. The vertical force (Z-force) and the spindle torque can be seen to approach their peak values, as the tool engagement increases, reflected in the figures through increase in Z-depth. Thereafter, the force and the torque become nearly steady as the process moves over

to the welding zone. Clearly, the horizontal forces (X-force and Y-force) start developing as soon as the welding begins. These appear to be much lower than the Z-force. The lateral force along X direction could be ascribed due to the advancing and retreating nature of the pipe motion across the welding line with respect to the tool rotation.

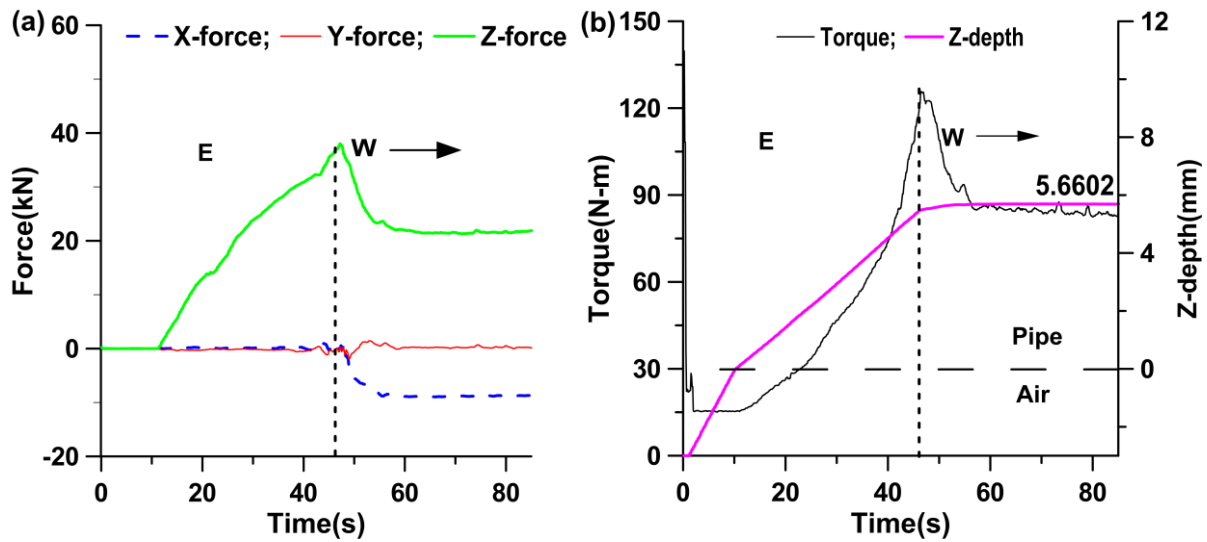


Figure 4.2 Variations of (a) Forces, (b) Spindle torque and achieved Z-depth with time for FSW of AISI-316L pipes at 300rpm, 100mm/min and 6mm Z-depth settings.

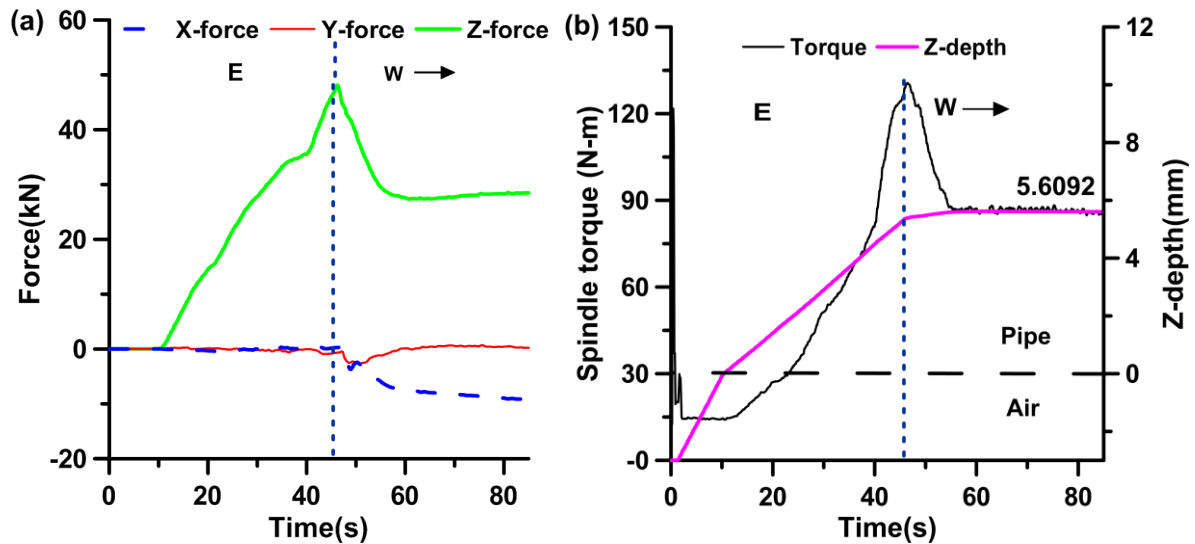


Figure 4.3 Variations of (a) Forces, (b) Spindle torque and achieved Z-depth with time for FSW of AISI-316L pipes at 325rpm, 100mm/min and 6mm Z-depth settings

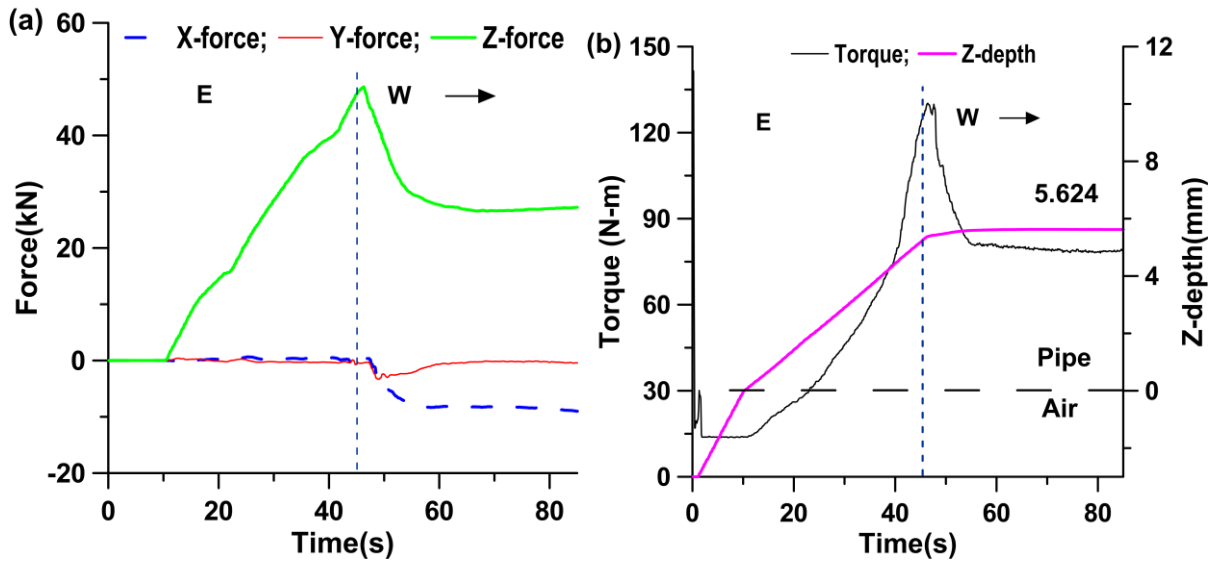


Figure 4.4. Variations of (a) Forces, (b) Spindle torque and achieved Z-depth with time for FSW of AISI-316L pipes at 350rpm, 100mm/min and 6mm Z-depth settings

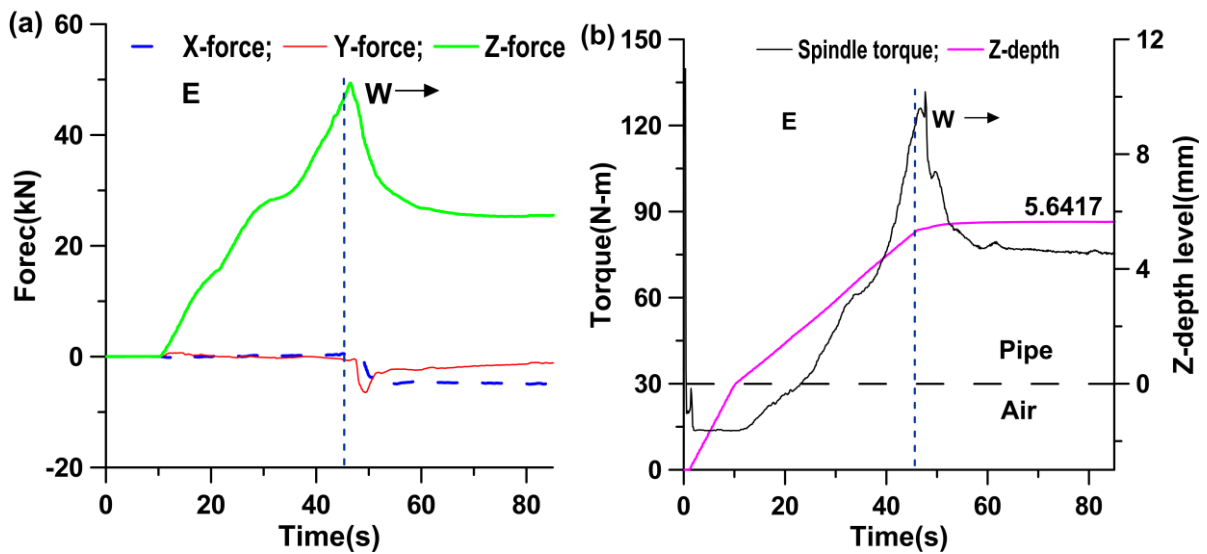


Figure 4.5 Variations of (a) Forces, (b) Spindle torque and achieved Z-depth with time for FSW of AISI-316L pipes at 400rpm, 100mm/min and 6mm Z-depth settings

For 250rpm and 100mm/min combination the vertical force lies between 23.39kN to 38.19kN in the welding zone (Figure 4.1a). The spindle torque varies from 131.18 N-m to 82.20 N-m (Figure 4.1b). At the start and end of the welding zone, the X-forces are respectively -0.20kN and -10.93kN, and the Y-forces are respectively -1.31kN and -2.5kN (refer to Figure 4.1a).

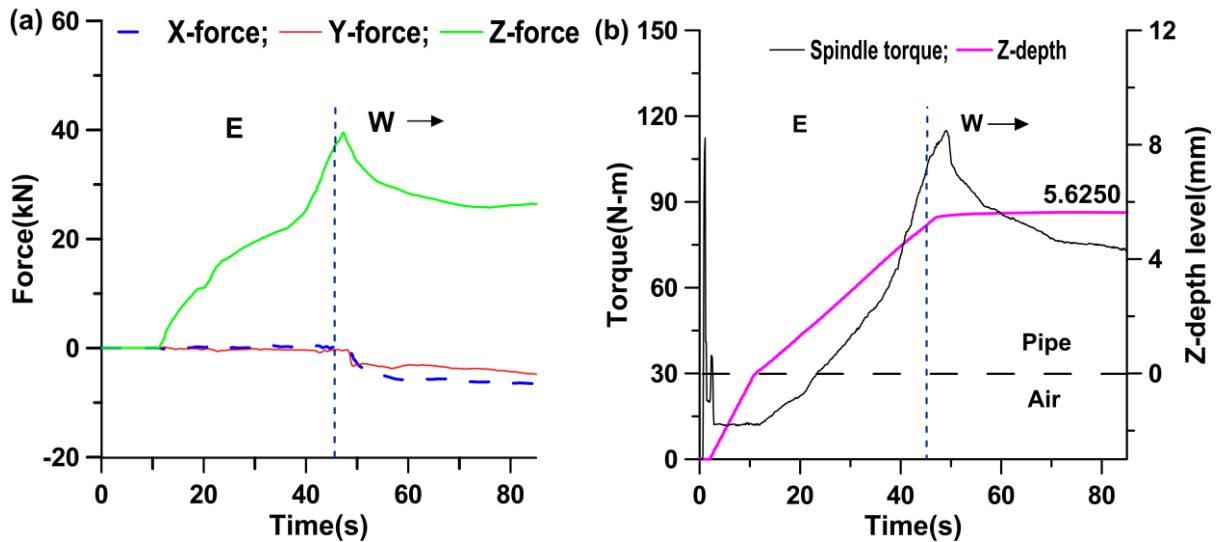


Figure 4.6 Variations of (a) Forces, (b) Spindle torque and achieved Z-depth with time for FSW of AISI-316L pipes at 450rpm, 100mm/min and 6mm Z-depth settings

For the combination of 300rpm spindle speed and 100mm/min welding speed, the Z-force achieved is 37.03kN at the start of welding zone and 21.62kN observed at the end of welding (refer to Figure 4.2a). Spindle torque of 125.28N-m and 83.16N-m are noticed at the start and end of the welding zone respectively (refer to Figure 4.2b). The X-force values perceive -0.37kN, -8.63kN respectively at start and end of welding zone. The Y-force varies from -0.21kN to 0.23kN within welding zone (refer to Figure 4.2a). A good surface quality welding achieved visually at these parameter combinations. Here, observed two peaks of the vertical force in Figure 4.2(a) could be due to well separated events of attaining the maximum Z-depth and the onset of the mandrel rotation overcoming the static friction. The first one may be due to force acting on the tool pin on reaching depth of penetration and the second peak may be for shoulder contact with the workpiece.

For 325rpm and 100mm/min combination the vertical force lies between 28.33kN to 46.84kN in the welding zone (refer to Figure 4.3a). The spindle torque varies from 125.71 N-m to 83.66 N-m (refer to Figure 4.3b), which is higher than the previous set of parameters (Expt. 2 in Table 4.1). At the start and end of the welding zone, the X-forces are respectively

-0.20kN and -10.10kN, and the Y-forces are respectively -0.44kN and 0.38kN (refer to Figure 4.3a).

The vertical force is approximately similar (43.5kN at welding start) for the combination of parameters 350rpm, 100mm/min and 400rpm, 100mm/min. It has been noticed that X-force, Y-force Z-force, and spindle torque plots are almost identical for these two set of parameters (refer to Figure 4.4 and Figure 4.5).

For welding of 450rpm,100mm/min the vertical force recorded is 36.9kN at the start of welding zone (refer to Figure 4.6). This is greater than second set of parameters (Expt. 2) (refer to Figure 4.2), but lower than the remaining four sets of parameters (Expt. 1, Expt. 3, Expt. 4 and Expt. 5) (refer to Figure 4.1, Figure 4.3, Figure 4.4 and Figure 4.5).

The average value of forces and the torque recorded during the welding process are compared with the help of bar charts as shown in Figure 4.7. Nearly steady values of forces and torque of are reported in the charts. The lateral force X is found to increase with increase in spindle speed upto 350rpm and then falls (refer to Figure 4.7a), though the maximum values of X-force is found at 250 rpm spindle speed. The force Y during the welding process does not show any prominent trend (refer to Figure 4.7b). However, the vertical Z-force (refer to Figure 4.7c) and spindle torque (refer to Figure 4.7d) is found to possess a definite correlation with spindle speed. Both force and the torque increase with increase in spindle speed from 300 rpm to 325 rpm beyond which it falls marginally with increase in the spindle speed. This correlated decrement could be attributed to the softening of the material due to high heat generation from increased friction (due to increased Z-force).

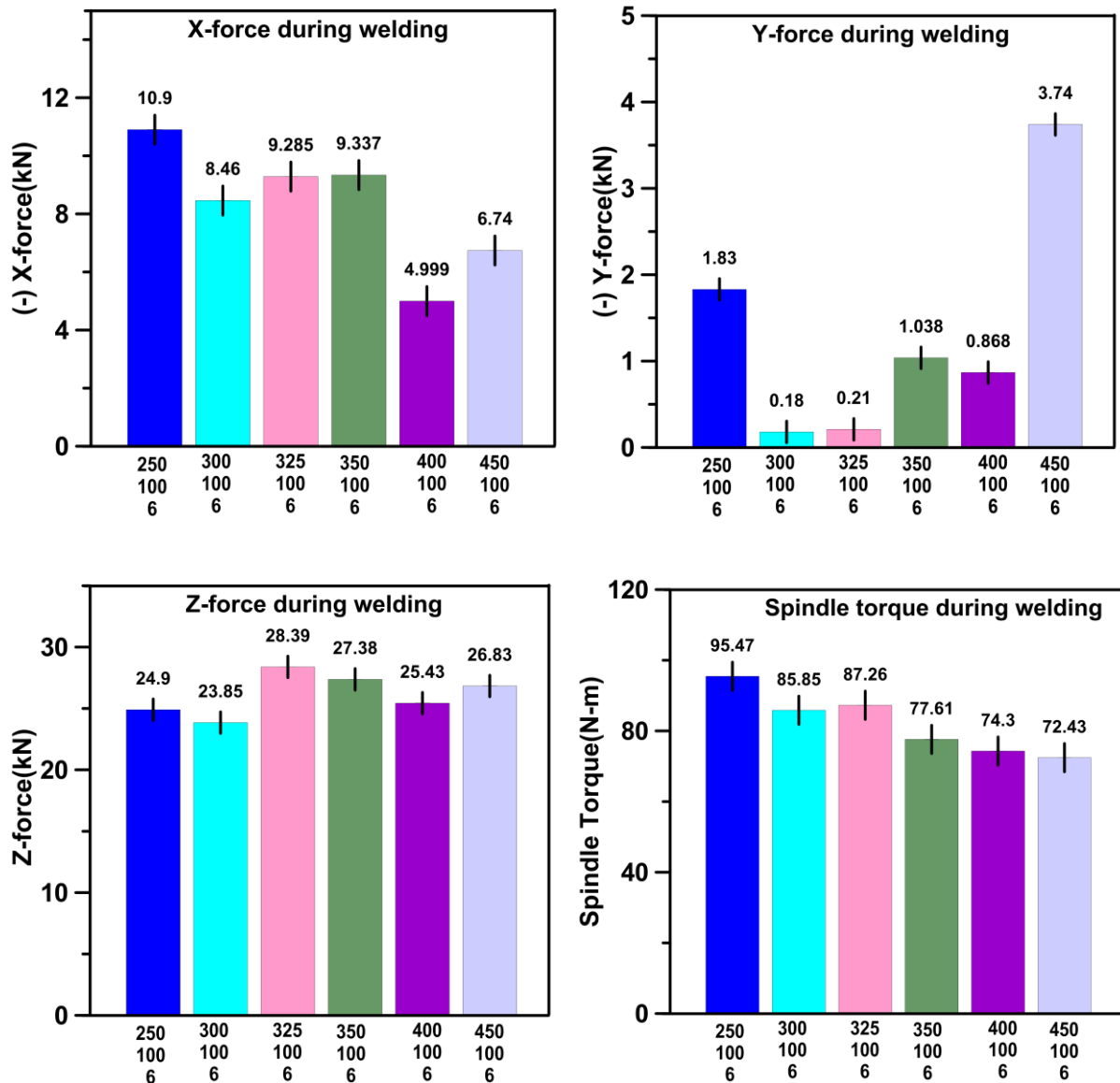


Figure 4.7 Bar-chart comparing the forces at position control mode (a) X-force, (b) Y-force, (c) Z-force, (d) spindle torque

4.3 Physical examination of AISI-316L weldments

Sectorial welds of about 150 mm arc length were carried out for studying the effect of parameter variation on the properties of the weldments. This length was selected based on the requirement of various test samples that need to be cut from a particular welded zone.

4.3.1 Surface of welded samples

In Figure 4.8, a groove defect is noted along advancing side of the welding zone to emerge under the position-control mode experiments. This defect could be attributed to inadequate frictional heating due to the lack of maintaining the requisite vertical force under the position control mode. Now, the lack of circularity in case of pipes is expected to cause deviation in the axial force under the position control mode welding in case of pipes. Moreover, at higher spindle speed, surface defects as observed in Figure 4.8(f) seem to arise from excess heat generation.

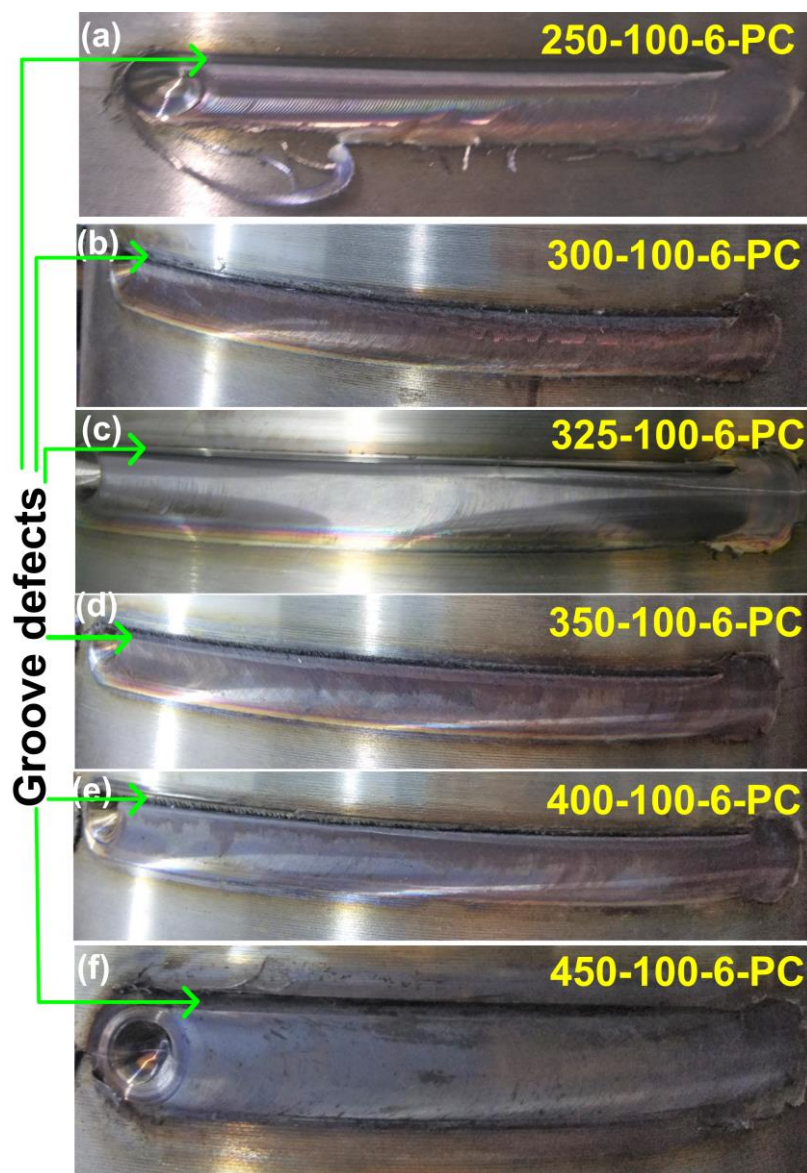


Figure 4.8 Groove defects observed during FSW of AISI-316L pipe at position control mode

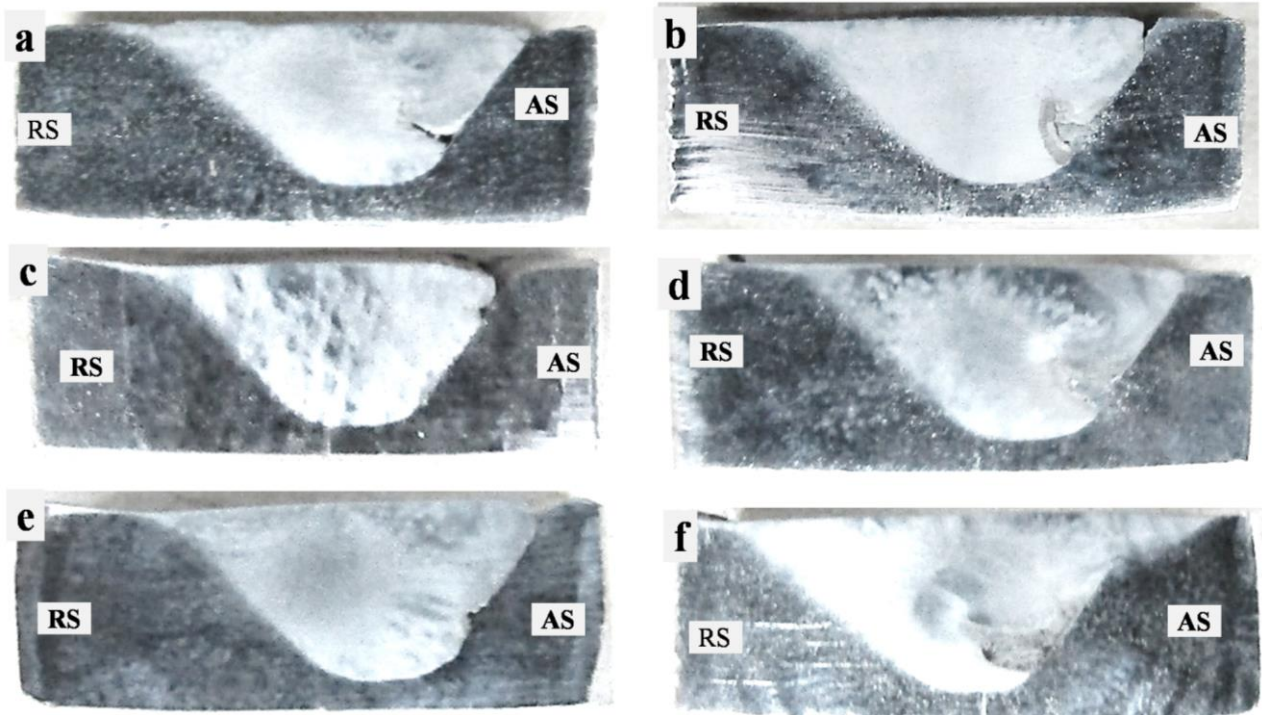


Figure 4.9 Cross sections of FSW sample at position control mode (a) 250rpm and 100mm/min (b) 300rpm and 100mm/min (c) 325rpm and 100mm/min (d) 350rpm and 100mm/min (e) 400rpm and 100mm/min (f) 450rpm and 100mm/min

4.3.2 Cross section of welded samples

The photographs of the weld cross sections are shown in Figure 4.9. A tunnel defect is observed between the stir zone and heat affected zone interface at the advancing side in welded samples shown in Figure 4.9. These are expected to be more prominent at lower spindle speed, due to insufficient heat generation leading to lack of material flow (Aydin 2014). The phenomenon of material flow is driven by the shoulder and the pin. The pin is responsible for producing better and uniform material coalescence in the SZ. For pipe welding, where tilt angle is not applicable, the plasticized material pushes uphill to the shoulder by the pin where the same plasticized material is pushed back into the weld zone by the tool shoulder to achieved material coalescence (Kumar et al. 2020).

4.4 Study of mechanical properties

4.4.1 Hardness behaviour

Vickers microhardness values were taken across the cross section of FSW welded joint at 2mm intervals as seen in Figure 4.10. As per the scheme, all the zones viz. SZ, TMAZ and BM are subjected to hardness evaluation for better understanding of the physical properties of the weldment. The hardness results for all the samples are shown in Figure 4.10. Overall, it is found that in the weld zone there is a marked improvement in the hardness of the base metal (BM) jumping from about 175HV to more than 231HV. In some cases, the hardness reaches as high as 250HV which is about 40% improvement in hardness of the base metal. The hardness values in the SZ are relatively higher than the HAZ. This is due to the grain refinement occurring in the former (Ramesh et al. 2019, Hajian et al. 2015) which play a significant part in the exhibiting higher strength and hardness in materials. According to Hall-Petch relation (Equation 4.1) strength is improved by reduction of grain size. Decreasing the grain size increases grain boundary which resists the dislocation motion leading to enhanced strength (Cao et al. 2022).

$$\sigma = \sigma_0 + k/\sqrt{d} \quad \text{Equation 4.1}$$

where σ is yield strength, d is average grain diameter, σ_0 and k are Hall-Petch constant. Hall-Petch equation shows an inverse relation between hardness and grain size (Heidarian and Mostafapoor 2022).

Smaller grain size yields more grain boundaries which act as the main obstacle for slip dislocation thus contributing to hardness of materials. Compared to aluminum-based alloys, steel and related alloys don't display a distinctive TMAZ in the weld microstructure. In the current study, based on the observations by optical microscopy a narrow zone

displaying elongated grain structure, which is also non-equiaxed is roughly marked as the TMAZ. However, as indentation can't be assured in this narrow zone, the hardness of TMAZ

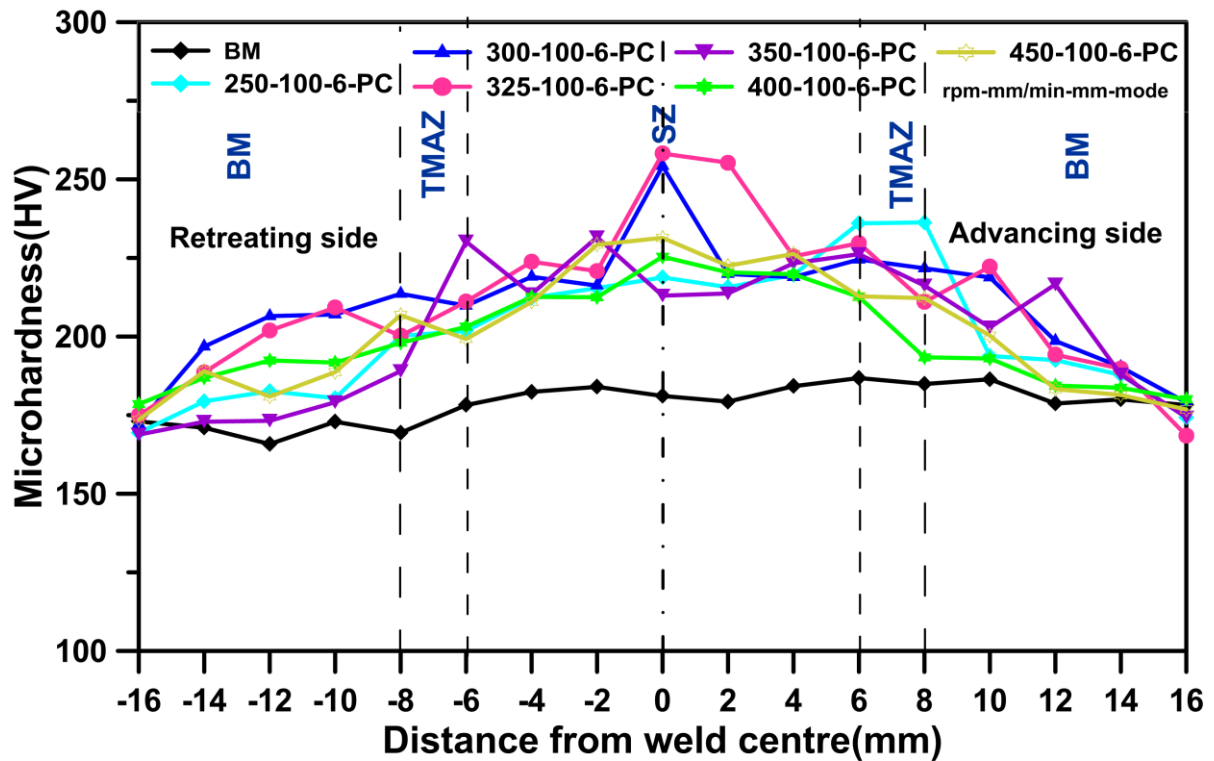


Figure 4.10 Hardness values across the cross section of welded samples

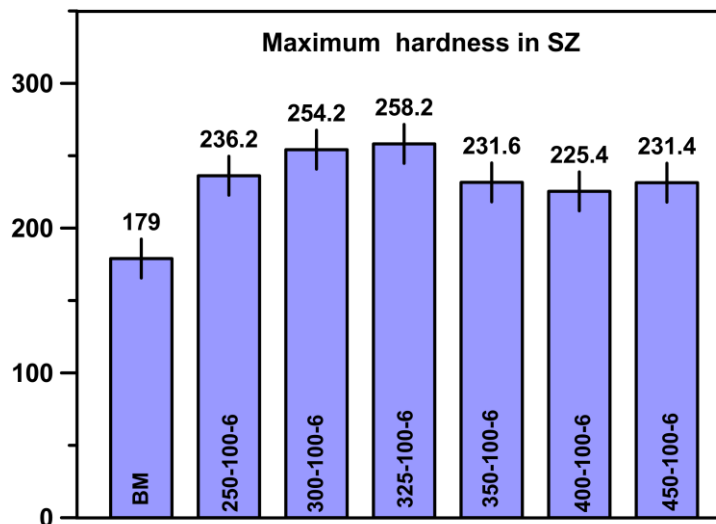


Figure 4.11 Maximum hardness of welded samples compared to BM.

can't be specifically determined and hence has not been mentioned in the hardness study. However, the interfacial zone at the boundary of SZ and HAZ show relatively higher

hardness (compared to SZ) which may be attributed to cumulative effects of factors viz. presence of high dislocation density and sub grain boundary (Sabooni et al. 2015). In TMAZ grain dislocation is influenced by severity of material strain and heat generation of the material (Kumar et al. 2018). Hardness values at the SZ and HAZ exhibit similar trends in all the samples getting lowered thereafter as one moves towards the BM region. The SZ of samples welded at 325rpm -100mm/min-6mm parameter combination exhibits the highest hardness of about 258.2HV (refer to Figure 4.11). In fact, the average hardness of the SZ of Sample (welded at 325rpm -100mm/min-6mm) is higher compared to others samples.

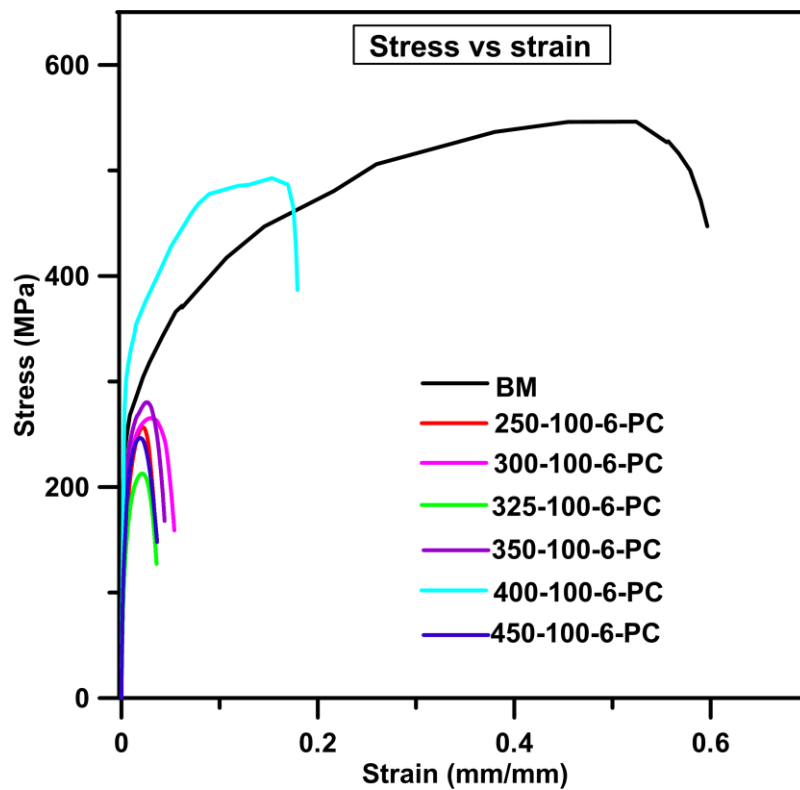


Figure 4.12 Stress vs strain plot of samples welded at PC mode

4.4.2 Study of tensile properties

The results of the tensile test of the welded joint along with that of the base metal are illustrated in Figure 4.12. Ultimate tensile strength and yield strength of base metal are revealed as 551MPa and 246.7MPa respectively. The ultimate tensile strength for sample welded at 400-100-6 is approximately 482.2MPa and the yield strength is 280.6MPa

respectively. The maximum joint efficiency is achieved as 87.51% when welded at welding speed 100mm/min with 400rpm spindle speed at position control mode. Discontinuous dynamic recrystallization is the responsible mechanism for grain refinement in SZ which improves the joint strength. The yield strength of the welding joint is increases due to grain refinement and work hardening.

4.5 Metallurgical study

4.5.1 Optical microscopy of welded samples

Optical micrograph of welded samples of AISI-316L pipes are shown in Figure 4.13 and Figure 4.14. Optical micrographs are captured for both sides of the SZ viz. retreating side and advancing side. The microscopy images are captured such that SZ-TMAZ-BM are visible. The changes in grain size is observed at different zones i.e. ultra-fine grains in SZ, reoriented and deformed fine grain in TMAZ and original grain in unaffected BM. Micro-crack and void defects are observed in advancing side of the welded sample. Similar schemes are followed for the samples welded with parameter combinations of 350-100-6, 400-100-6, 450-100-6 at position control mode (refer to Figure 4.14.).

Equiaxed grain exhibit more grain boundary area which limit the slip dislocation. Due to restriction of dislocation motion, the material with equiaxed grains shows higher hardness. Two types of dynamic recrystallizations are the mostly responsible for grain refinement in FSW of austenitic stainless steel viz. discontinuous dynamic recrystallization (DDRX) and continuous dynamic recrystallization (CDRX). Formation of equiaxed grain in SZ occurs due to discontinuous dynamic recrystallization and the formation of sub grain boundary in SZ is caused due to continuous dynamic recrystallization (CDRX). This confirms the reason for higher hardness of the stir zone as observed previously. On careful observation, TMAZ emerges as a zone with deformed (elongated) grains in a particular direction. The elongated

and reoriented grains are produced due to the shearing action of the shoulder of the rotating tool. As this zone consists of highly deformed grains with significant elongation, they may weaken the joint in some cases where dislocation may be higher (Song et al. 2009).

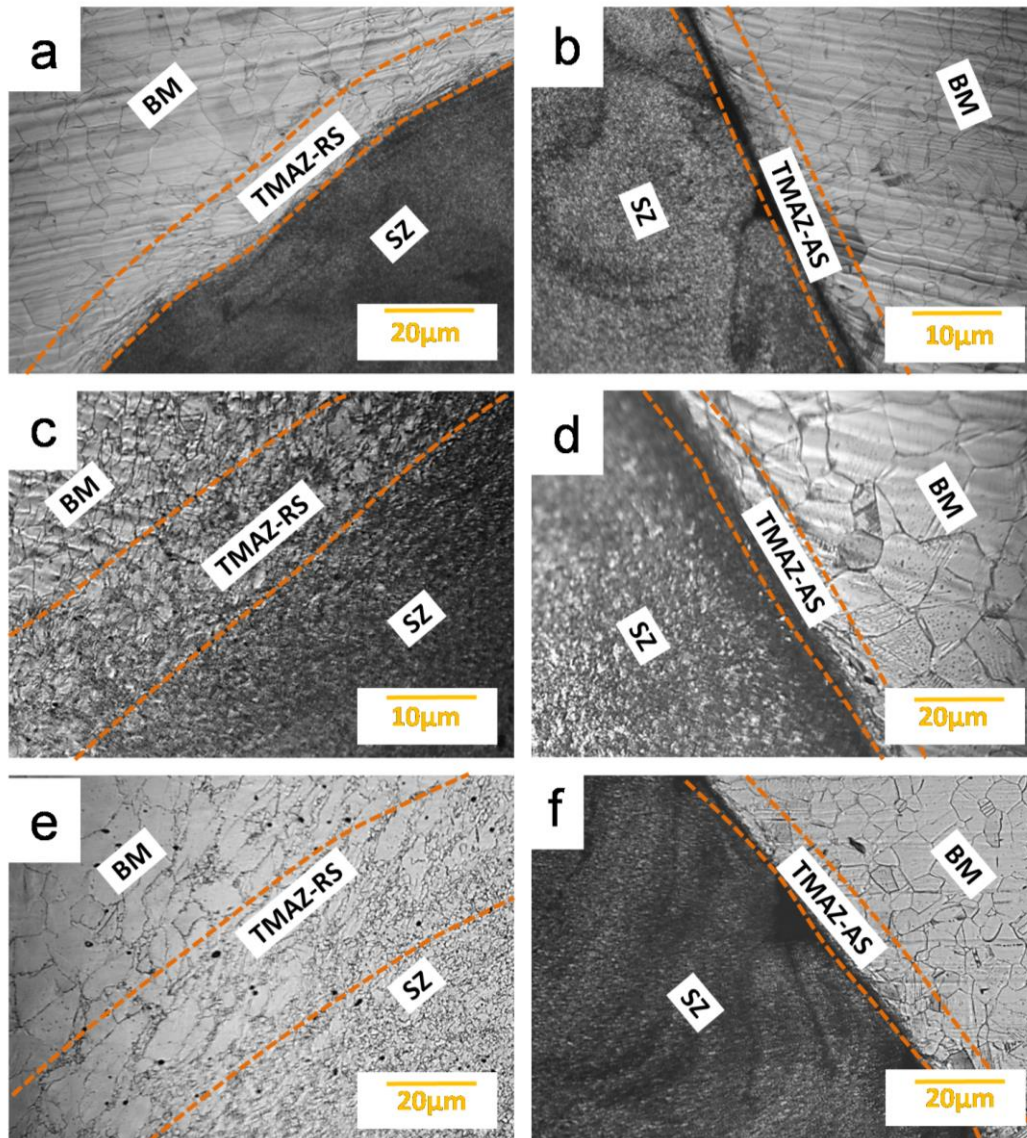


Figure 4.13 Optical micrograph of FSW sample at 250-100-6 (a) SZ - TMAZ (RS), (b) SZ- TMAZ (AS); at 300-100-6 (c) SZ – TMAZ (RS) (d) SZ- TMAZ (AS); at 325-100-6 (e) SZ - TMAZ(RS) (f) SZ- TMAZ (AS)

In a typical FSW, the shear effect of the tool shoulder and pin is more on the AS than RS as the material flows around the tool from AS to RS (Park et al. 2003). As a result of this, sharper TMAZ is noticed in the AS micrograph compared to the RS micrograph (refer Figure

4.13(b) and 4.14(d). The thermal conductivity is lower for stainless steel which delays the friction heat propagation along lateral direction. Hence, HAZ zone is absent for this types of steel. The occurrence of the twin crystals is not visible in the SZ which could be attributed to the breakup of initial twin boundaries because of the stir action associated with intense plastic deformation. Due to crystallographic rotation, the original twins get destroyed in the SZ.

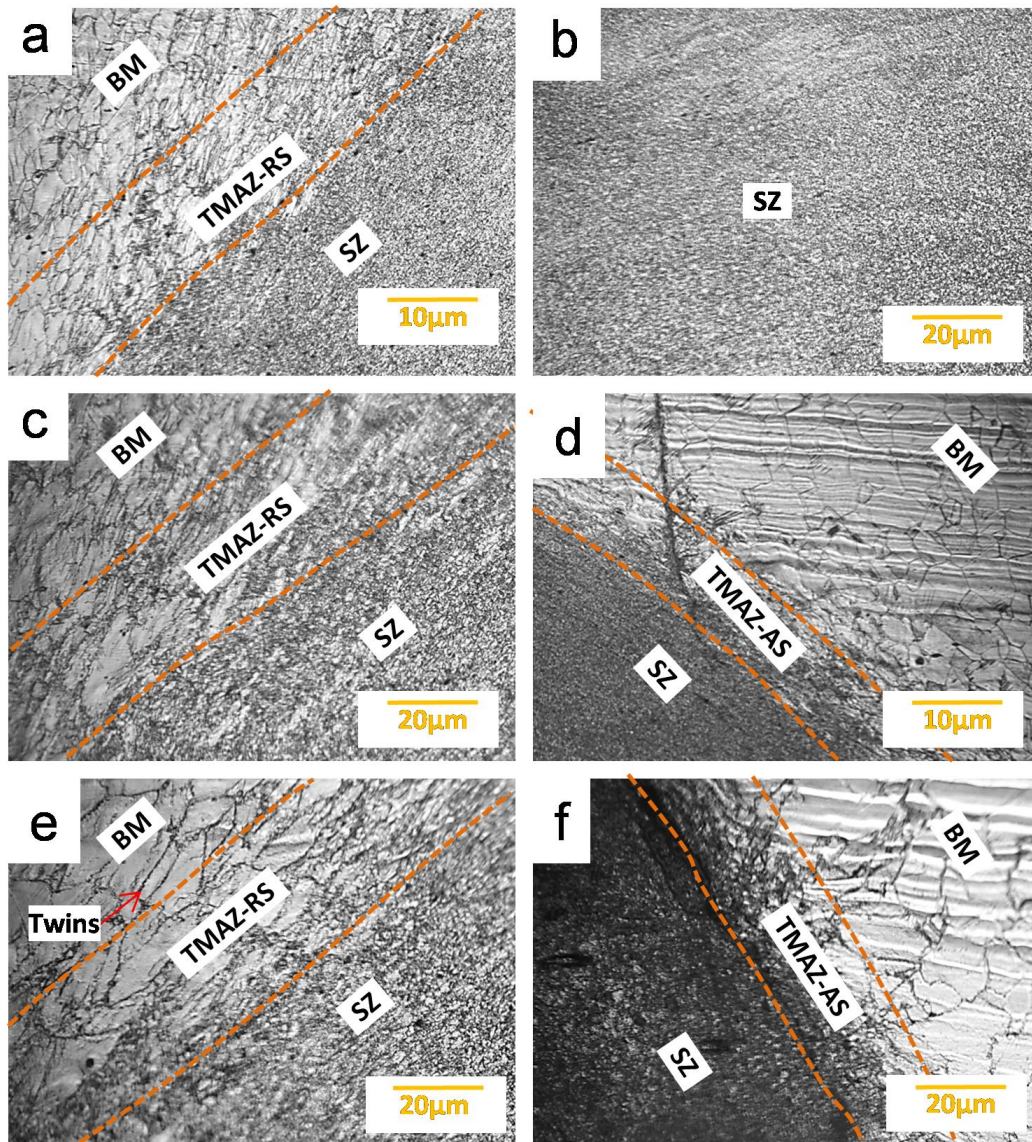


Figure 4.14 Optical micrograph of FSW sample at 350-100-6 (a, b) SZ – TMAZ (RS) and SZ- TMAZ (AS); at 400-100-6 (c, d) SZ – TMAZ (RS) and SZ- TMAZ (AS); at 450-100-6 (e, f) SZ – TMAZ (RS) and SZ- TMAZ (AS)

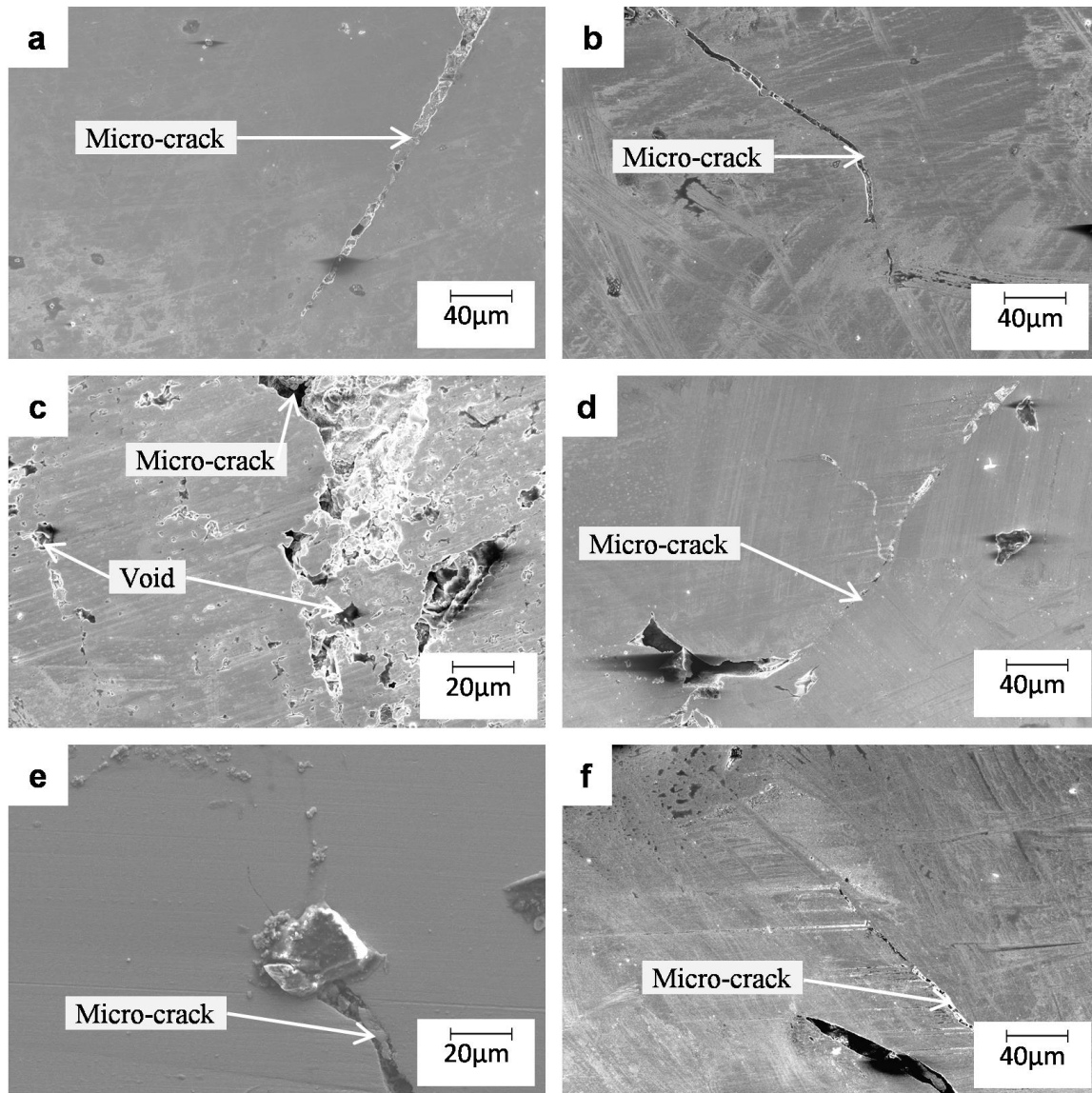


Figure 4.15 SEM images of welded samples (a) 250-100-6, (b) 300-100-6, (c) 325-100-6, (d) 350-100-6, (e) 400-100-6, (f) 450-100-6

4.5.2 Scanning electron microscopy of welded samples

Detailed microstructural study of the weldments is done through field emission scanning electron microscope as seen in Figure 4.15. Two types of defects are noticed in the welded zone viz. micro-cracks and void defects. Micro-crack defect is observed close to AS at the interface of SZ and the TMAZ. The occurrence of the crack may be attributed either to the interstitial elemental precipitation (Mironov et al. 2011) or insufficient friction heat contributed by low spindle speed and less vertical force. Lack of softening and material flow

may be responsible for appearance of the micro-cracks. The micro-crack defect may be partly responsible for the lower mechanical properties in the joint area as compared to the base metal. The void defects may have appeared due to lack of material flow in case of high transverse speed and low spindle speed combinations. The void formation occurred due to fast cooling of the material within the SZ before being filled with the stirred material (Sato et al. 2005). Humphreys and Hatherly (2012) observed that in crystalline materials, the grain size along with the dislocation and interface defects within grains and on grain boundaries depend on the deformation work.

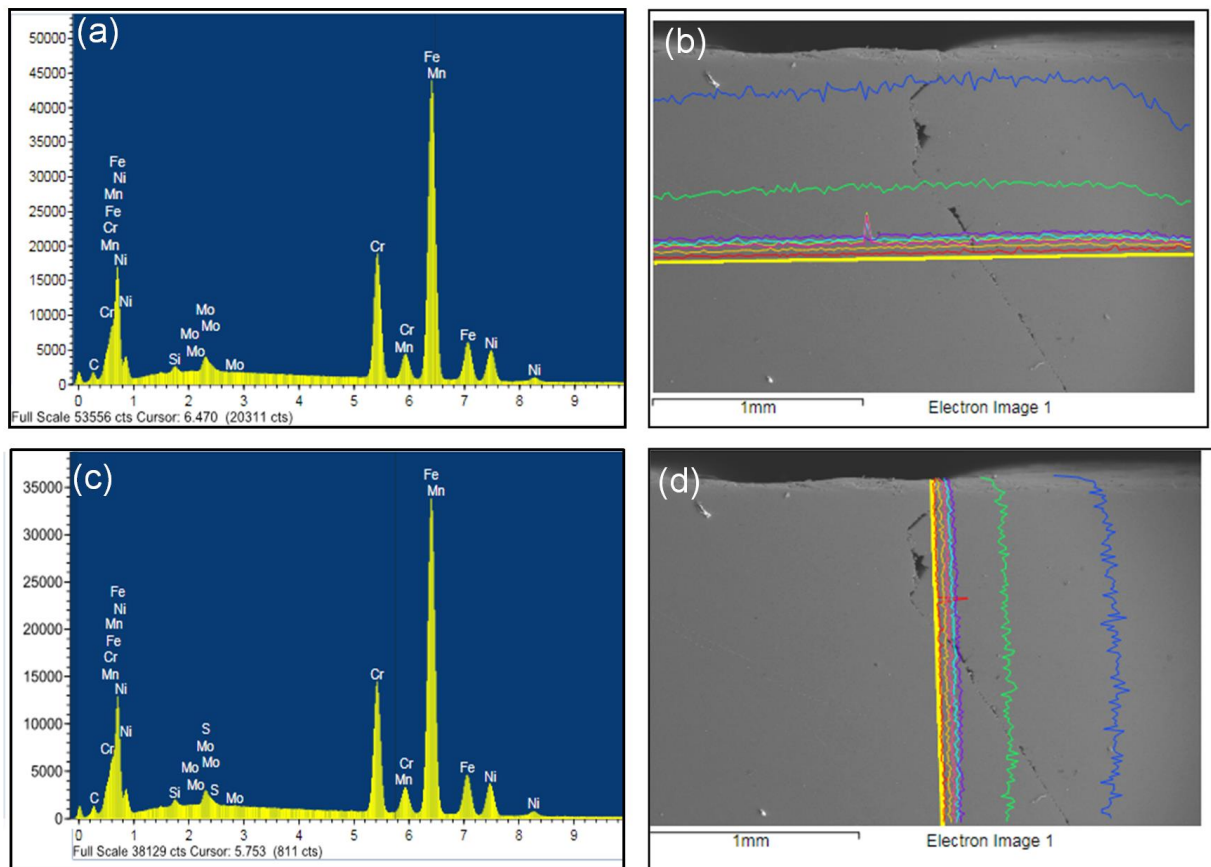


Figure 4.16 Line EDX analysis of sample welded at 400-100-6 (a) horizontal line plot and (b) corresponding SEM image; (c) vertical line plot and (d) corresponding SEM image

4.5.3 Energy dispersive X-ray analysis of welded samples

The line EDAX (horizontal and vertical line) technique was used to determine the elemental composition at from various zones of the welded samples. Plots and corresponding SEM images of line (horizontal line) EDAX analysis of the samples, welded at 400-100-6 is shown in Figure 4.16(a) and 4.16(b). The vertical line EDAX analysis of welded samples (welding done at 400-100-6) is shown in Figure 4.16(c) and 4.16(d). Figure 4.17 shows the line EDX analysis of samples welded at 450-100-6 parameters combination. The color code used for different elements during line EDX is shown in Figure 4.18. Usual composition of AISI-316L is detected in the specimens. No extra boron (B) and nitrogen (N) particles were found in the welded zone. This indicates that no tool wear happened during FSW at the specified welding process parameters.

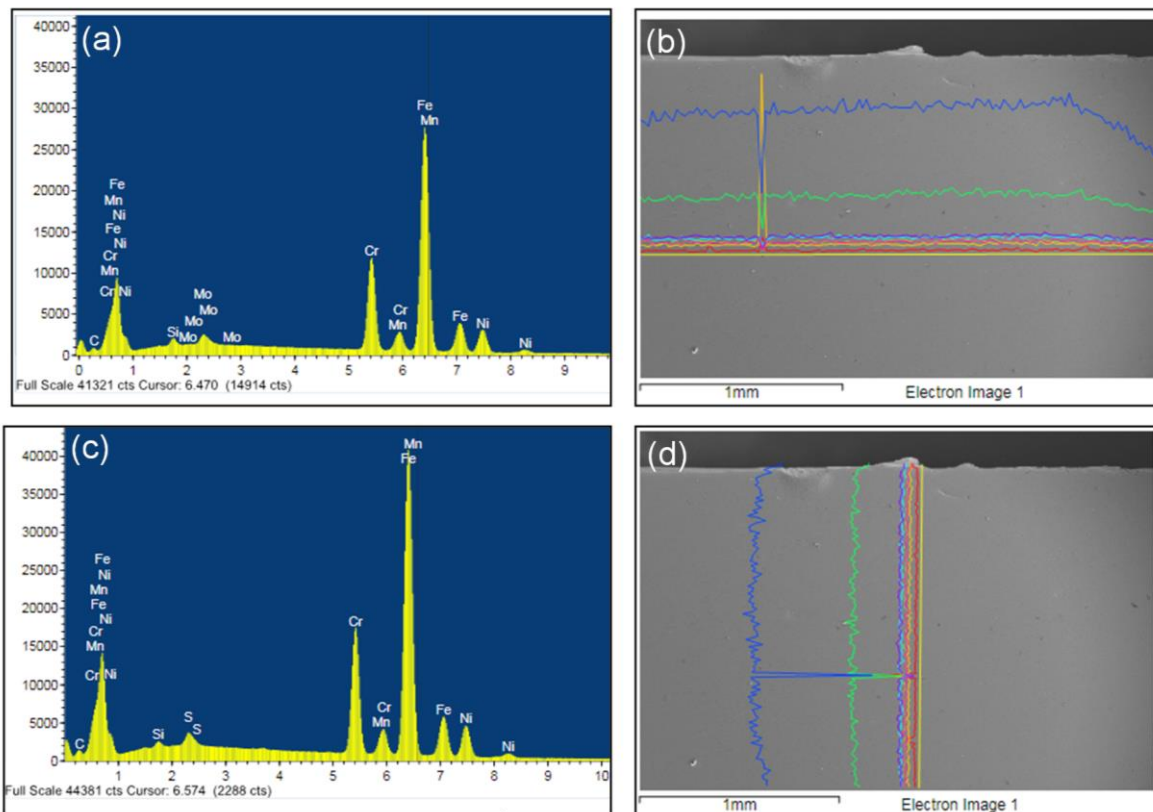


Figure 4.17 Line EDX analysis of sample welded at 450-100-6 (a) horizontal line plot and (b) corresponding SEM image; (c) vertical line plot and (d) corresponding SEM image

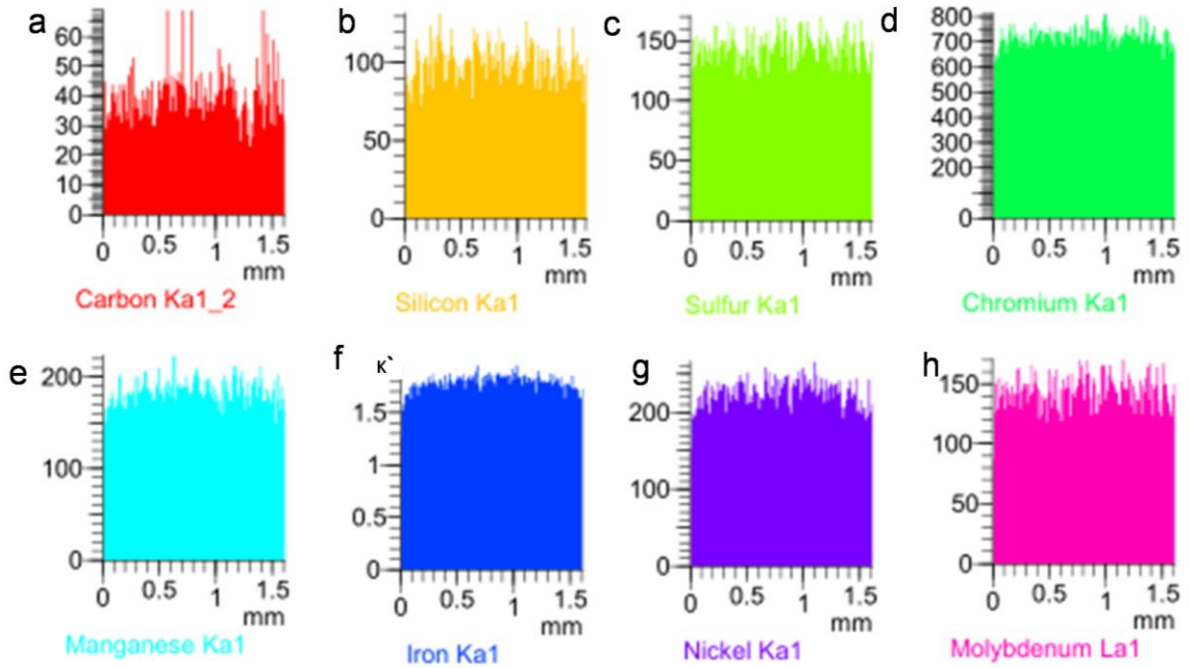


Figure 4.18 The color code used for different element during line EDX analysis for welded samples at position control mode (a) C, (b) Si, (c) S, (d) Cr, (e) Mn, (f) Fe, (g) Ni, (h) Mo

4.6 Closure

This chapter presents the details of the experimental results of AISI-316L pipes welded at position control mode. The micro-cracks and voids are detected in FE-SEM images which is due to inadequate heat generation and lack of material flow. The hardness values of the welded samples were significantly improved in SZ and TMAZ. The tensile test results of welded samples display lower strength and higher hardness compared to the base metal at position control mode. However, micro-cracks and voids are also noticed in FE-SEM images which are believed to be due to insufficient heat generation and lack of material flow. This shows the need to have an optimal heat generation during FSW process and further optimization of the process parameters under force control mode.

AISI-316L pipe welding at force control mode

Outline of the Chapter: *5.1 Introduction, 5.2 Physical examination of weldments, 5.2.1 Surface of welded samples, 5.2.2 Cross section of welded sample, 5.3 Study of mechanical properties, 5.3.1 Hardness behavior, 5.3.2 Study of tensile properties, 5.4 Metallurgical study, 5.4.1 Optical microscopy of welded samples, 5.4.2 Scanning electron microscopy of welded samples, 5.4.3 Energy dispersive X-ray analysis of welded samples, 5.4.4 X-ray diffraction analysis of welded samples, 5.5 Closure*

5.1 Introduction

In the current chapter FSW on AISI-316L steel pipes is studied. FSW of steel are mostly limited to linear welding. The current work attempts to effectively join of AISI-316L pipes by FSW. FSW is a potential answer to this concern considering its high efficiency. The investigation is carried out in a systematic manner by varying the spindle speed and the welding speed suitably under force control mode. The effect of process parameters on the weld properties is observed through microstructural characterization of the joints. Their impact on the tensile strength and hardness of the pipe joints is also undertaken in order to correlate the joint performance with its microstructural evolution.

5.2 Physical examination of weldments

In the present work, AISI-316L grade of austenitic stainless-steel pipes have been joined with force control mode. The downward force (F) value has been taken as 35 kN for all the

experiments whereas the maximum limit of tool penetration (d) was set at 6 mm. This force value is

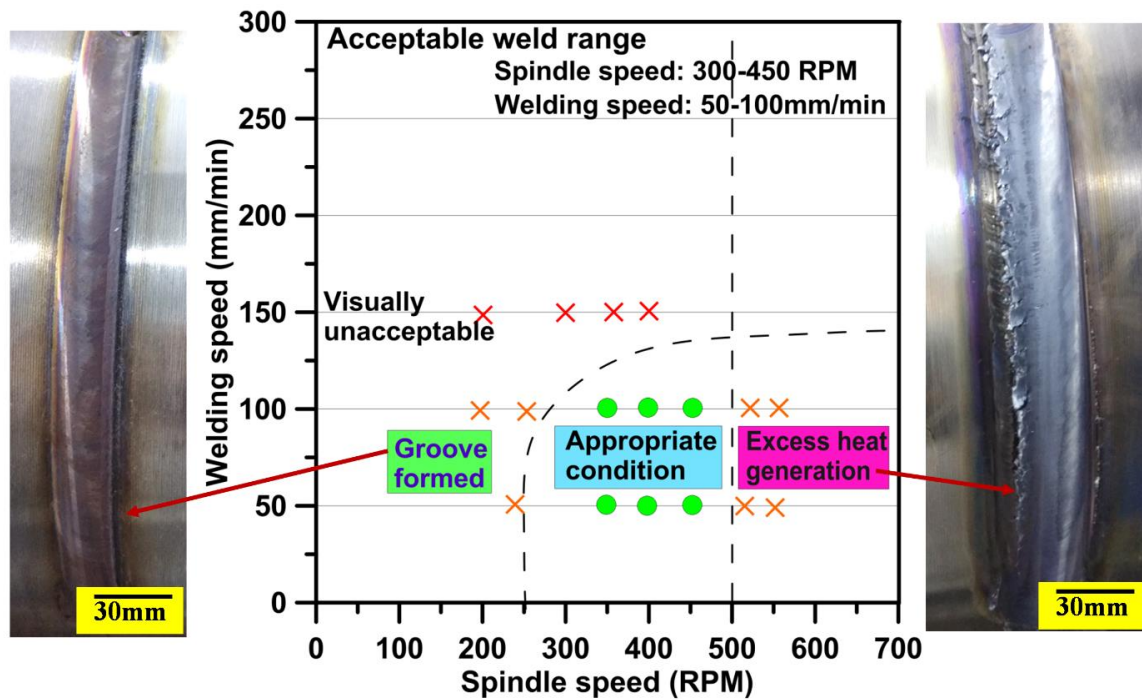


Figure 5.1 Identifying parameters for appropriate welding

Table 5.1 FSW parameters selected for welding AISI-316L steel pipes

Sl. no.	Sample no.	Spindle speed(N) rpm	Welding speed(v) mm/min	Control mode
1	ASS1	300	50	FC
2	ASS2	350	50	FC
3	ASS3	400	50	FC
4	ASS4	450	50	FC
5	ASS5	300	100	FC
6	ASS6	350	100	FC
7	ASS7	400	100	FC
8	ASS8	450	100	FC

selected based on pre-characterization welding experiments (as presented in Chapter 4) and found to yield good quality welds (Giorjão et al. 2019). After significant number of trials, the range of parameters resulting in acceptable weld quality (based on visual inspection) is identified as: spindle speed of 300–450rpm and welding speed of 50–100mm/min (refer to Figure 5.1). All the experiments and the corresponding nomenclature of weldments are presented in Table 5.1. Figure 5.2 shows the photograph of the welded pipes at different experimental conditions. No such defects or failure are apparent in the samples prepared under the force-control mode within the specified range of parameters. For carrying out further post-welding characterization, samples have been cut from the weld zone as well as the base metal.

5.2.1 Surface of welded samples

Photographs of the welded pipes at different experimental conditions are shown in Figure 5.2. No defect is observed within the range of parameters which indicates adequate heat generation and material flow throughout the process.

5.2.2 Cross section of welded samples

Visual examination has been made on the etched cross section of welded samples (Figure 5.3 and Figure 5.4). By visual examination, only root defect has been observed in the bottom of sample or inner side of one of the samples (refer to Figure 5.4(b)). It has also been observed that microstructure of the cross section of the welded samples are not homogeneous. Each welded sample shows three different regions i.e. SZ, TMAZ and BM. From cross section of the sample it has been clearly noticeable that the width of the SZ is higher at the top surface and gradually decreases at bottom of the samples that is comparable with basin shape (refer to Figure 5.3(c)).

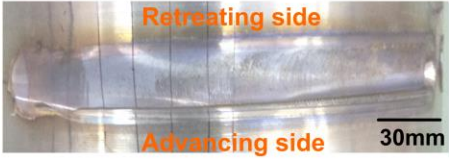
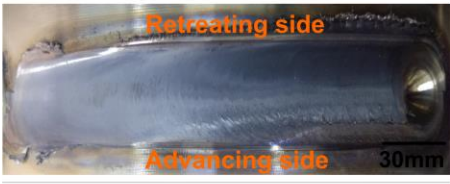
Sample no.	Process parameters	Photograph
ASS1	N-300rpm v-50mm/min d-6mm F -35kN	
ASS2	N-350rpm v-50mm/min d-6mm F -35kN	
ASS3	N-400rpm v-50mm/min d-6mm F -35kN	
ASS4	N-450rpm v-50mm/min d-6mm F -35kN	
ASS5	N-300rpm v-100mm/min d-6mm F -35kN	
ASS6	N-350rpm v-100mm/min d-6mm F -35kN	
ASS7	N-400rpm v-100mm/min d-6mm F -35kN	
ASS8	N-450rpm v-100mm/min d-6mm F -35kN	

Figure 5.2 Photograph of the top surface of welded joint of AISI-316L pipes for different parameter combinations (N-spindle speed, v- welding speed, d-tool penetration depth, F-downward force)

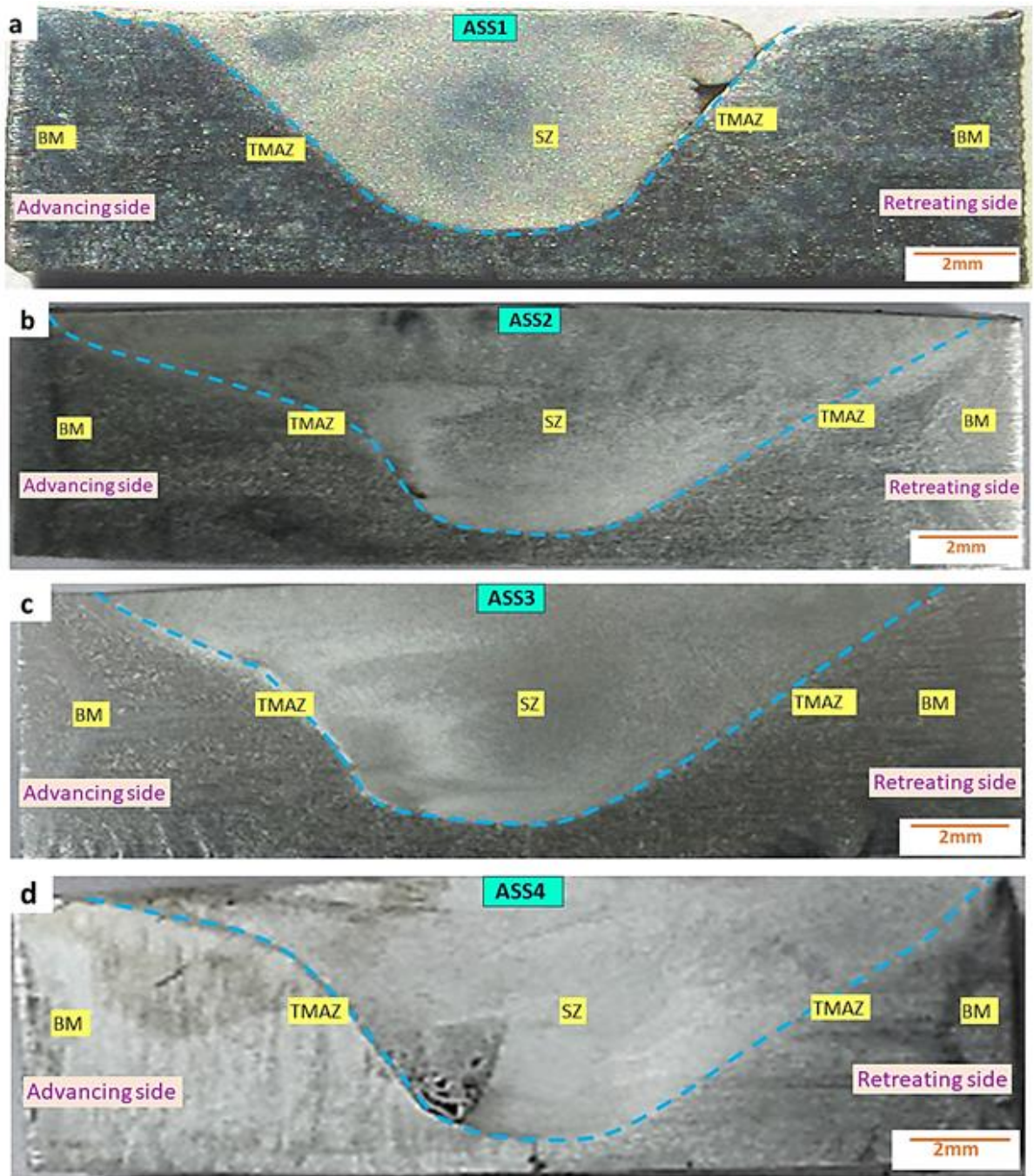


Figure 5.3 Cross section of FSW AISI-316L steel pipes, samples (a) ASS1 (b) ASS2 (c) ASS3 (d) ASS4 (BM-base metal, TMAZ- thermo-mechanically affected zone, SZ- stir zone)

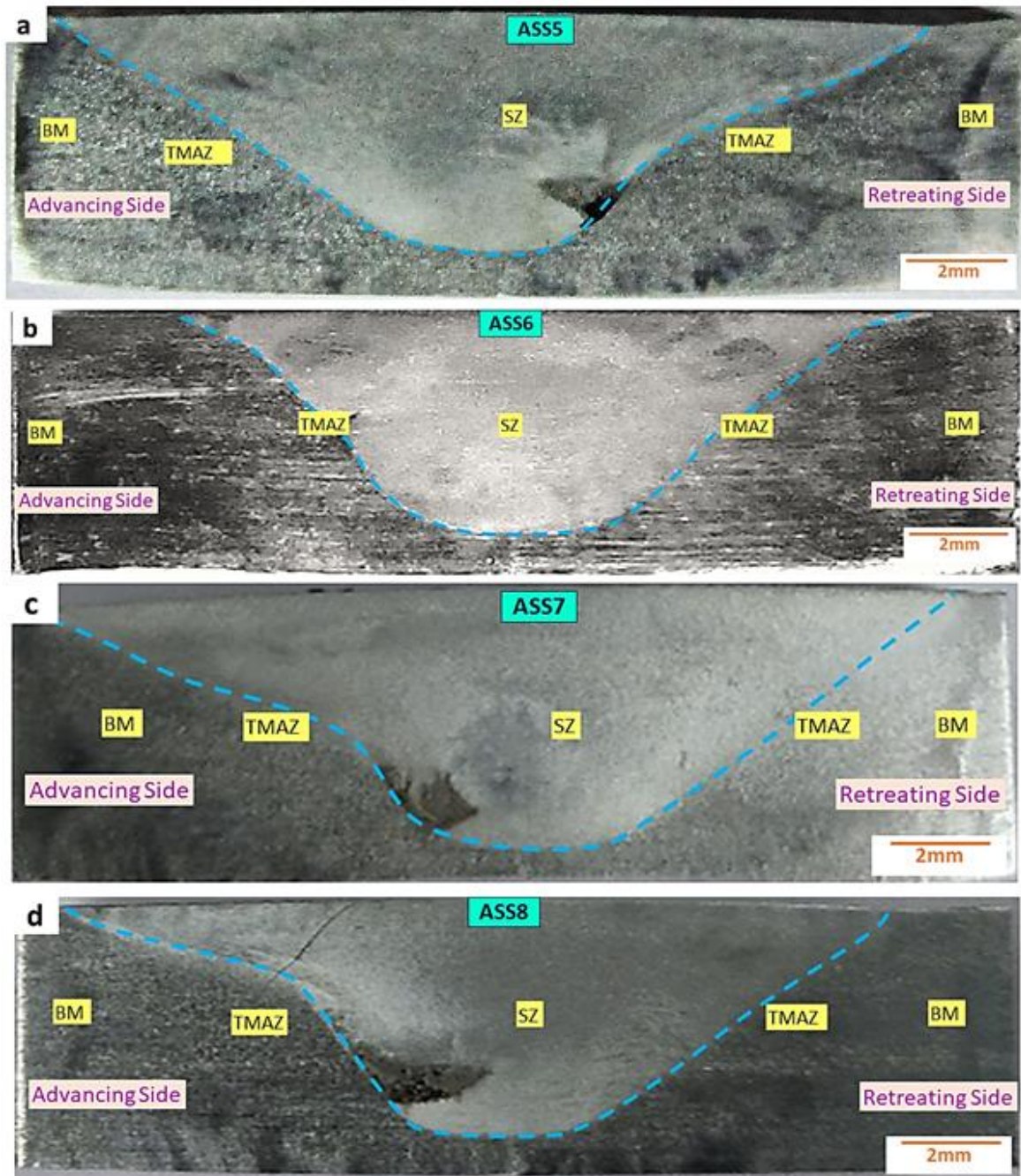


Figure 5.4 Cross section of FSW AISI-316L steel pipes, samples (a) ASS5 (b) ASS6 (c) ASS7 (d) ASS8 (BM-base metal, TMAZ- thermo-mechanically affected zone, SZ- stir zone)

5.3 Study of mechanical properties

5.3.1 Hardness behaviour

Hardness values have been measured at different zones viz. SZ, TMAZ, BM of the welded samples. The hardness values of BM are also reported for comparison. The average hardness

value of the BM is measured as 185HV. It has been noticed that in SZ, welded samples exhibit higher hardness compared to BM (refer to Figure 5.5). Among the different zones, SZ revealed higher hardness than that of TMAZ and BM. This was found to be true on both RS and AS of the weld. Maximum hardness value in SZ is measured as 255HV for sample welded at 400rpm spindle speed and 50mm/min welding speed. The foremost cause of higher hardness in SZ is fine equiaxed grain.

Maximum hardness, at AS of TMAZ is measured as 218 HV, whereas at RS the value is 206HV (for sample ASS3). Grain rearrangements during the recovery process are responsible for relatively lower hardness in TMAZ compared to SZ for welded sample. Moreover, presence of high dislocation density and sub-grain boundary are responsible for improved hardness in TMAZ compared to BM (Sabooni et al. 2015). Some variation in the hardness of the BM can be observed in Figure 5.5. This may be due to the influence of heat transfer from the weld zone during the welding process on the microstructure. However, the influence is not significant to refer the zone as HAZ.

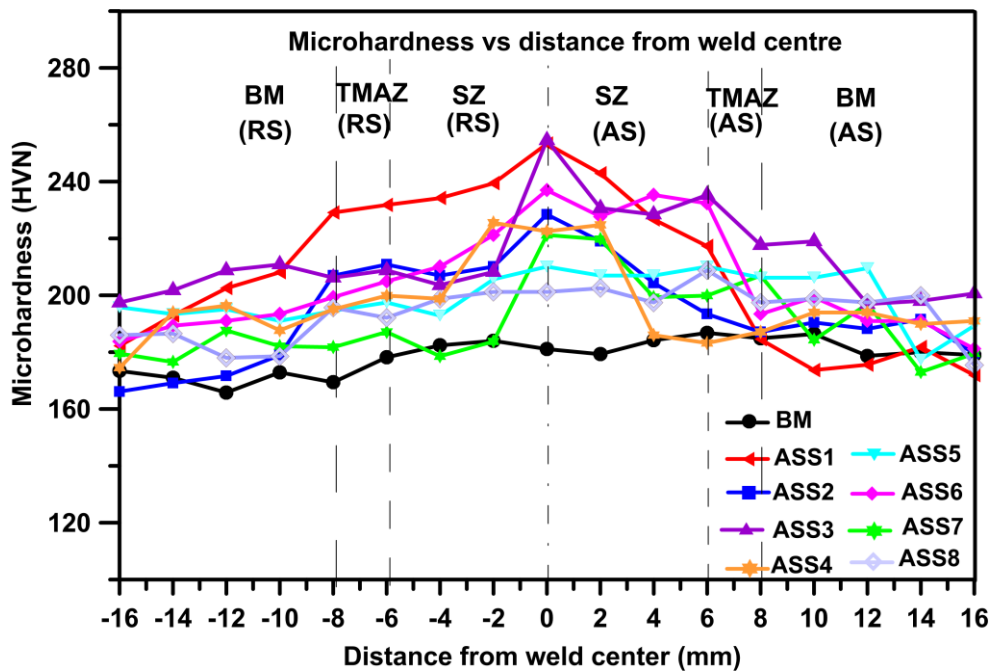


Figure 5.5 Variation in hardness values across the cross section of as received BM and welded samples

5.3.2 Study of tensile properties

Figure 5.6 shows the tensile properties of BM and welded samples joined at different combination of parameters. The ultimate tensile strength and the yield strength of as received BM have been found as 551MPa and 245.67MPa respectively. The strength of the welded specimen is visibly higher than that of BM which is primarily attributed to the grain refinement after welding (Sabooni et al. 2015). Figure 5.7 shows the yield strength, ultimate tensile strength, and percentage elongation of the BM and the welded samples. In general, the samples joined at lower welding speed (50mm/min) display higher UTS than the ones joined at higher welding speed (100mm/min). Specifically, the sample welded with 400rpm spindle speed and 50mm/min welding speed (samples ASS3) exhibits the maximum UTS i.e. 576.79MPa. The reduction in the grain size implies the increase in the grain boundary that restrict the dislocation motion, resulting in the enhancement of the strength of the weldments compared to the BM. High dislocation density along the grain boundaries in SZ is another reason for this display of higher strength. According to Li et al. (2017) properly welded sample can display above 100% efficiency. Now, during tensile test of a defect-free welded sample, tensile deformation shifted from SZ to BM as the former becomes strengthened. Due to shifting of strain location towards the BM, the stress also changes from uni-axial to multi-axial state which leads to increase in the resistance to further deformation by the welded sample. Hence, the overall joint efficiency of welded sample is improved (Li et al. 2017). In the current study, the maximum joint efficiency has been achieved as 104.68% (sample welded at 400rpm spindle speed and 50mm/min welding speed) compared to BM. Joint efficiencies of the samples welded at different combination of parameters are shown in Figure 5.8 through bar diagram. Figure 5.9 shows the fracture locations for the tensile tested samples. In case of BM, the fracture location has been observed outside of the gauge length (refer to Figure 5.9a). Whereas, the welded sample, the fracture location has been observed in

different zones. Samples ASS2 and ASS3 show higher weld strength compared to BM. In these samples, fracture locations are observed outside of the weld zone, as shown in Figure 5.9 (c, d). In case of welded samples viz. ASS1, ASS4, ASS5, ASS6, ASS7 and ASS8 (refer to Figure 5.9 (b, e, f, g, h, i)), the fracture is observed in the weld zone that indicates lesser strength compared to BM.

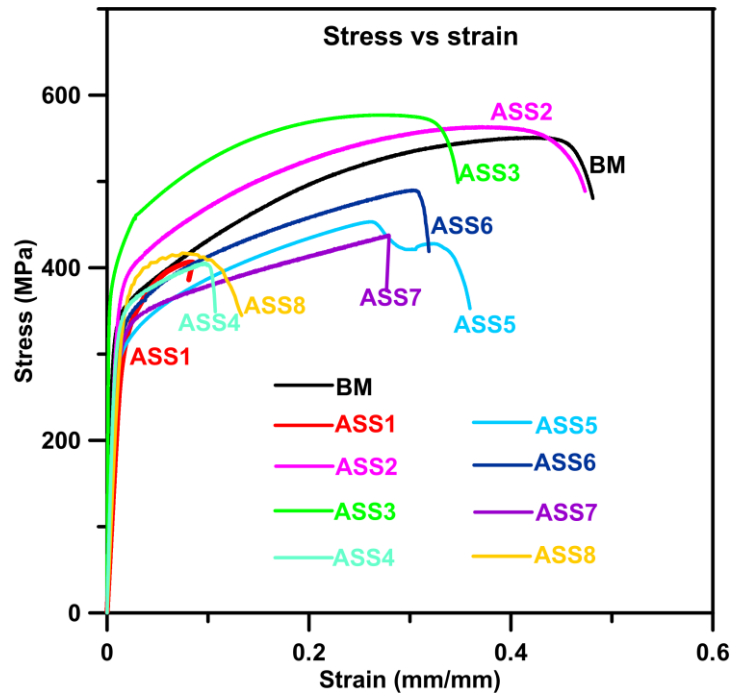


Figure 5.6 Stress vs strain plot of AISI 316L welded samples

The morphology of the fractured surface indicates ductile failure of the welded samples (Li et al. 2017). This is further validated by the higher percentage of elongation values for the samples (ASS2, ASS3, ASS5, ASS6 and ASS7). In case of sample ASS1, ASS4 and ASS8, the percentage elongation is comparatively less. This may be due to higher heat generation than optimal heat (due to higher spindle speed) as required for a good weldment. Heat generation during the FSW depends on the welding parameters, i.e., spindle speed and welding speed. With an increase in spindle speed or a reduction in welding speed, the amount of heat generation is high, which induces the material transformation. The lower ductility in SZ was associated with grain refinement and strain hardening characteristics. The

higher the strain hardening exponent, the lower the mean free path of the dislocation motion. This in turn restricts the acceleration of the dislocation motion against the grain boundary. (Kruml et al. 1997). As a result, after welding, the ductility of the joint decreases as compared to BM and similar results has been reported by other researchers (Kumar et al. 2019). Over a range of parameter combinations, heat generation is more than the process requirement, which is not favorable for achieving good weld strength and also causes the weld to become brittle in nature. For FSW of AISI-316L steel, higher welding speeds (100 mm/min) revealed comparatively lesser tensile strength than lower welding speeds (50 mm/min). At higher welding speeds, heat generation is not sufficient to attain proper joining up to the inner surface of the pipes (Ramesh et al. 2019). This may be the reason for the early tensile failure of the samples. The lower ductility displayed by the samples may also be due to a higher strain hardening rate and a reduction in grain size in SZ, which may restrict the accessible path for dislocation motion (Kumar et al. 2016).

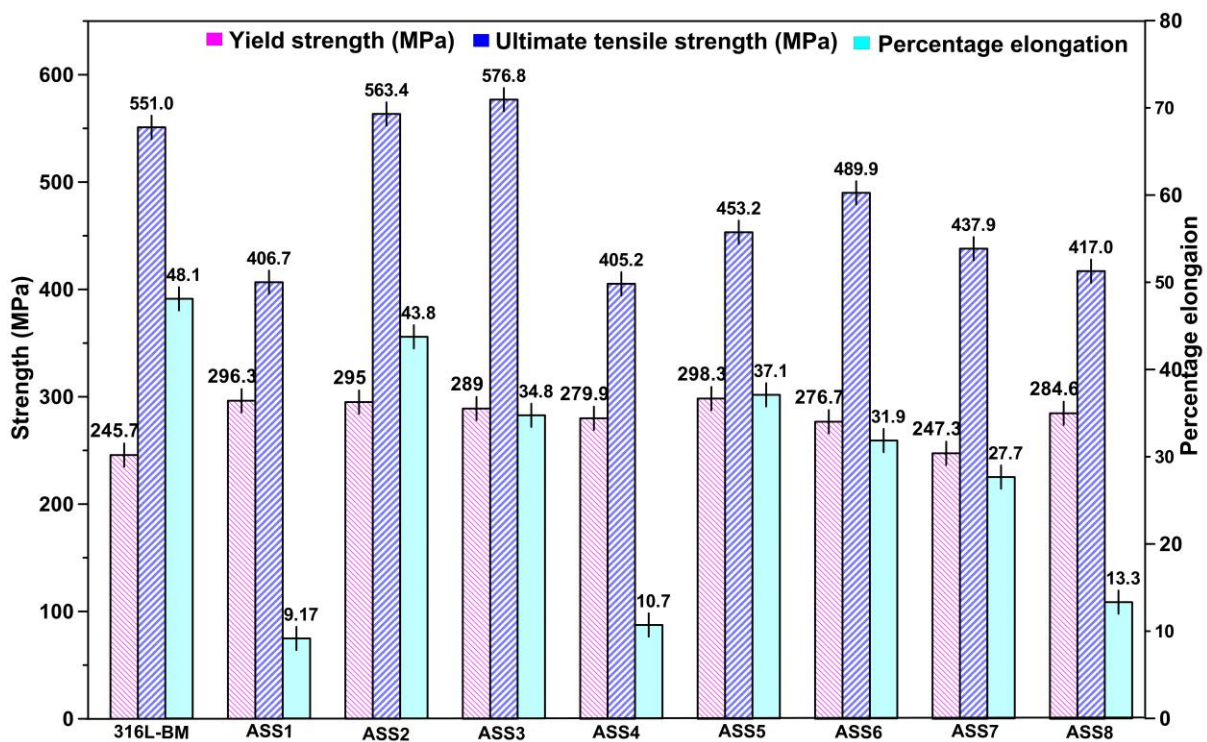


Figure 5.7 Yield, ultimate tensile strength and percentage of elongation for AISI-316L BM and welded samples.

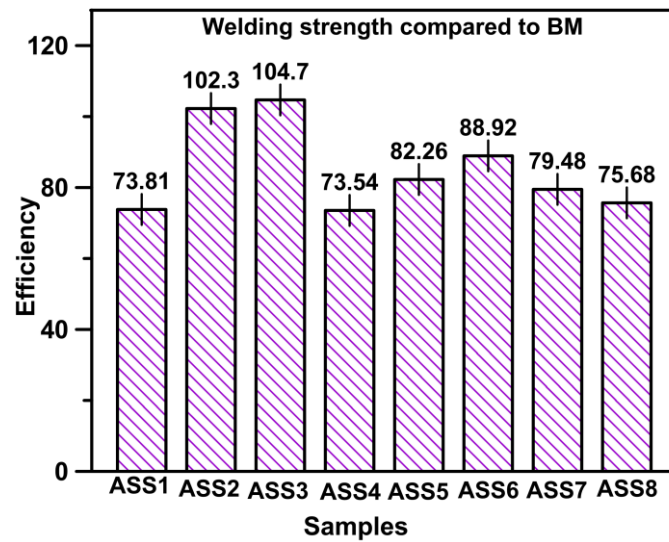


Figure 5.8 Comparison of joint efficiencies of AISI-316L samples

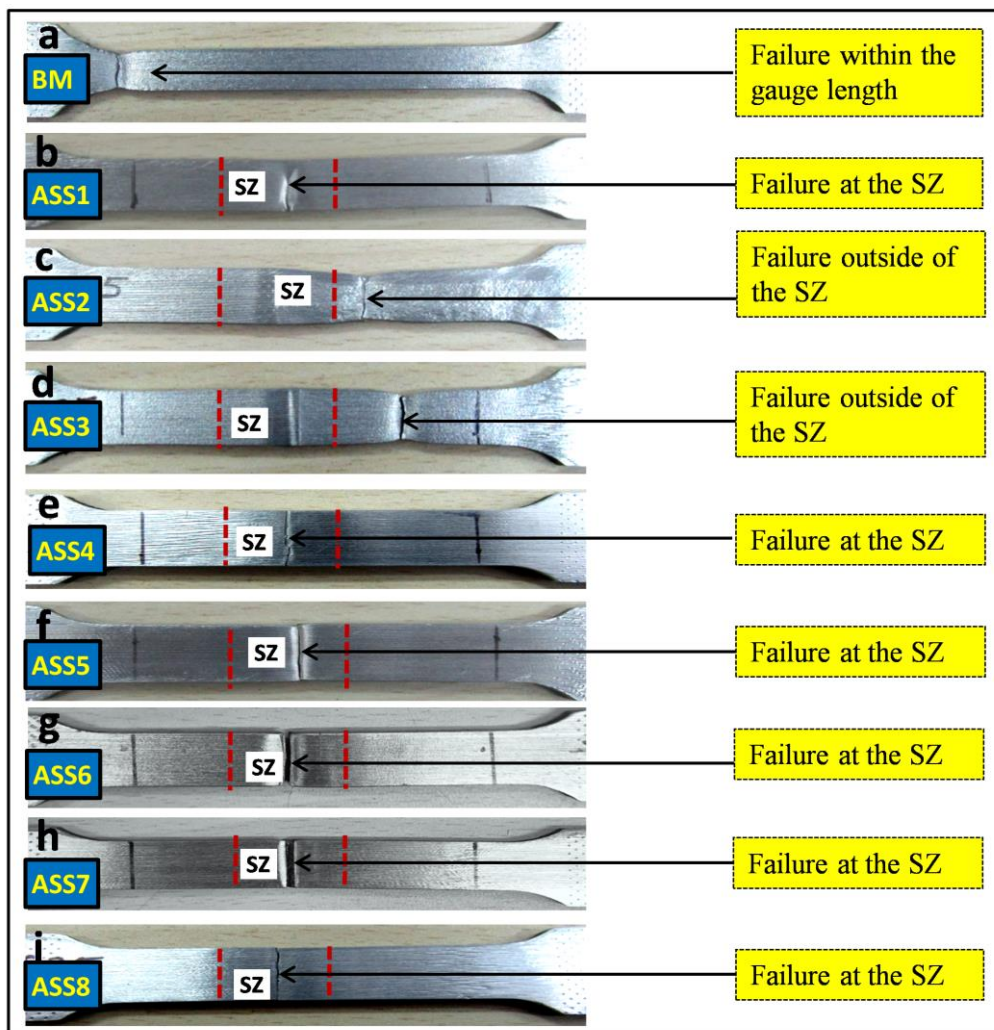


Figure 5.9 Location of failure on the tensile tested samples (red dashed line indicates the weld

zone)

5.4 Metallurgical study

5.4.1 Optical microscopy of welded samples

Optical micrographs distinctly shows the various zones (SZ, TMAZ and BM) of the weldments (refer to Figure 5.10 and 5.11). In general, ultrafine equiaxed grains are observed in SZ, enlarged reoriented grains are observed in TMAZ and original undeformed grains are visible in unaffected BM region (Ahl Sarmadi et al., 2021).

Heat generation during FSW is the primary factor affecting the grain refinement of the weldments. The pseudo heat index i.e. ω^2/v (where ω is spindle speed and v is welding speed) indicates that the contribution of spindle speed is much greater than welding speed in terms of heat generation (Hajian et al. 2015). Kumar et al. (2018) found that for higher heat generation, grain size become larger. During FSW of AISI-316L steel at a fixed welding speed, Hajian et al. (2015) also reported that higher spindle speed lead to greater heat generation causing larger grain size. Reynolds et al. (2003) also observed similar relation between spindle speed and average size of the formed grains. However, heat generation is not the only parameter affecting the grain size. The strain rate is also an influential parameter for grain size. Higher strain rate generated during welding produced lower grain size (Chabok and Dehghani, 2013). At higher strain rate, there is less time for dislocation movement and grain boundary relocation, leading to dynamic recrystallization (DRX) and resulting in fine grained microstructures. Now, heat generation and the stain rate are increased with spindle speed but they both have opposite effect on the grain size. According to Li et al. (2017), stain rate is more dominating factor than heat generation when grain refinement is concerned. Less number of twin boundaries are visible in SZ compared to BM (refer to Figure 5.11(e)). Due to the stirring action of the tool, the original twin boundaries are breakup.

The microstructure of TMAZ on AS and RS appear asymmetric. In advancing side of the welded samples, a sharp boundary is observed at the SZ and TMAZ interface (refer to

Figure 5.11(d)). In TMAZ, low peak temperature and low strain rate influence the dynamic recovery of the grain. Allotropic changes like formation of sub-grain boundary and grain dislocation have been found to be dominant in this region.

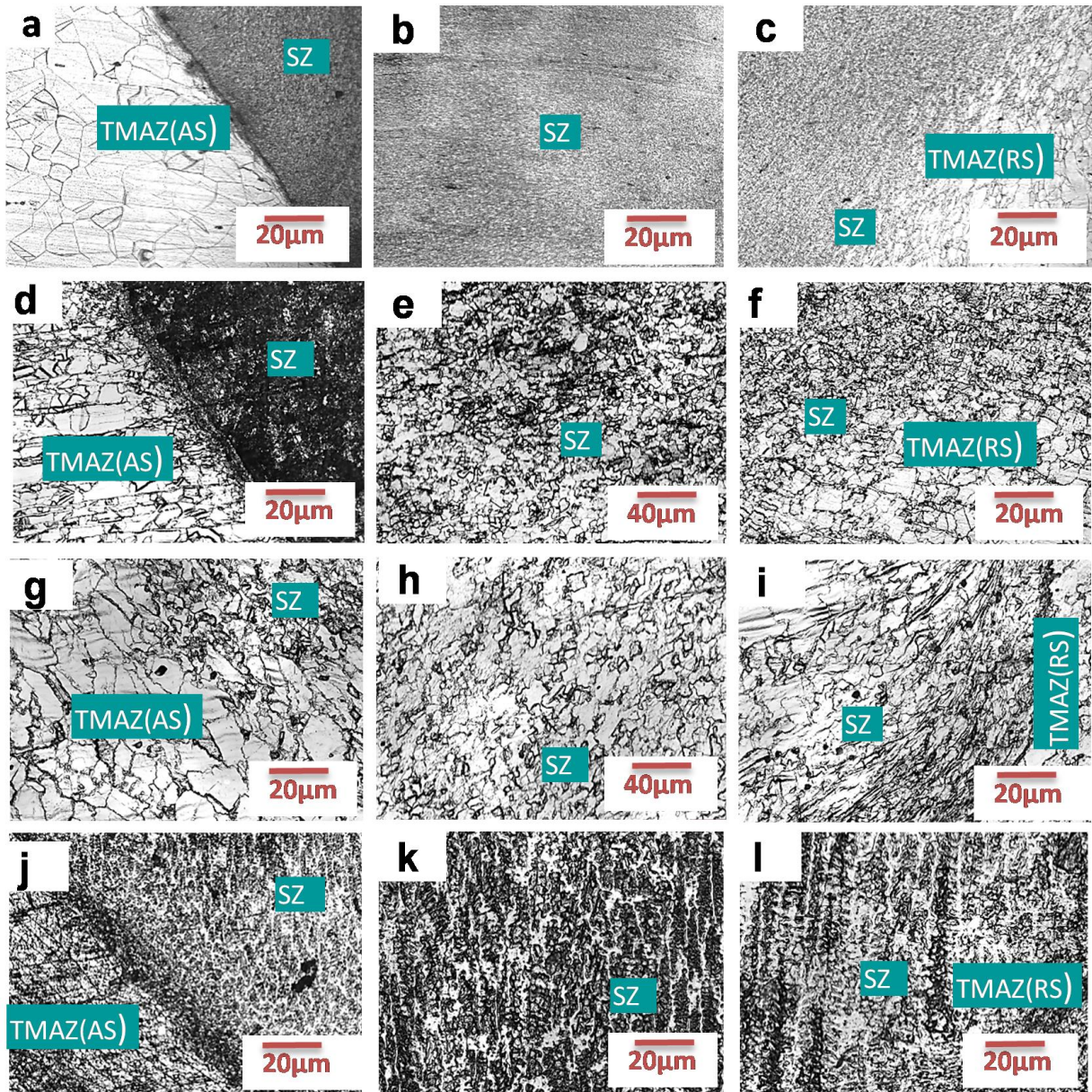


Figure 5.10 Optical micrograph of welded AISI-316L steel pipe sample (at 50mm/min) (a) SZ-TMAZ(AS) (ASS1), (b) SZ (ASS1), (c) SZ-TMAZ(RS) (ASS1) (d) SZ-TMAZ(AS) (ASS2), (e) SZ (ASS2), (f) SZ-TMAZ(RS) (ASS2), (g) SZ-TMAZ(AS) (ASS3), (h) SZ (ASS3), (i) SZ-TMAZ(RS) (ASS3), (j) SZ-TMAZ(AS) (ASS4), (k) SZ (ASS4), (l) SZ-TMAZ(RS) (ASS4)

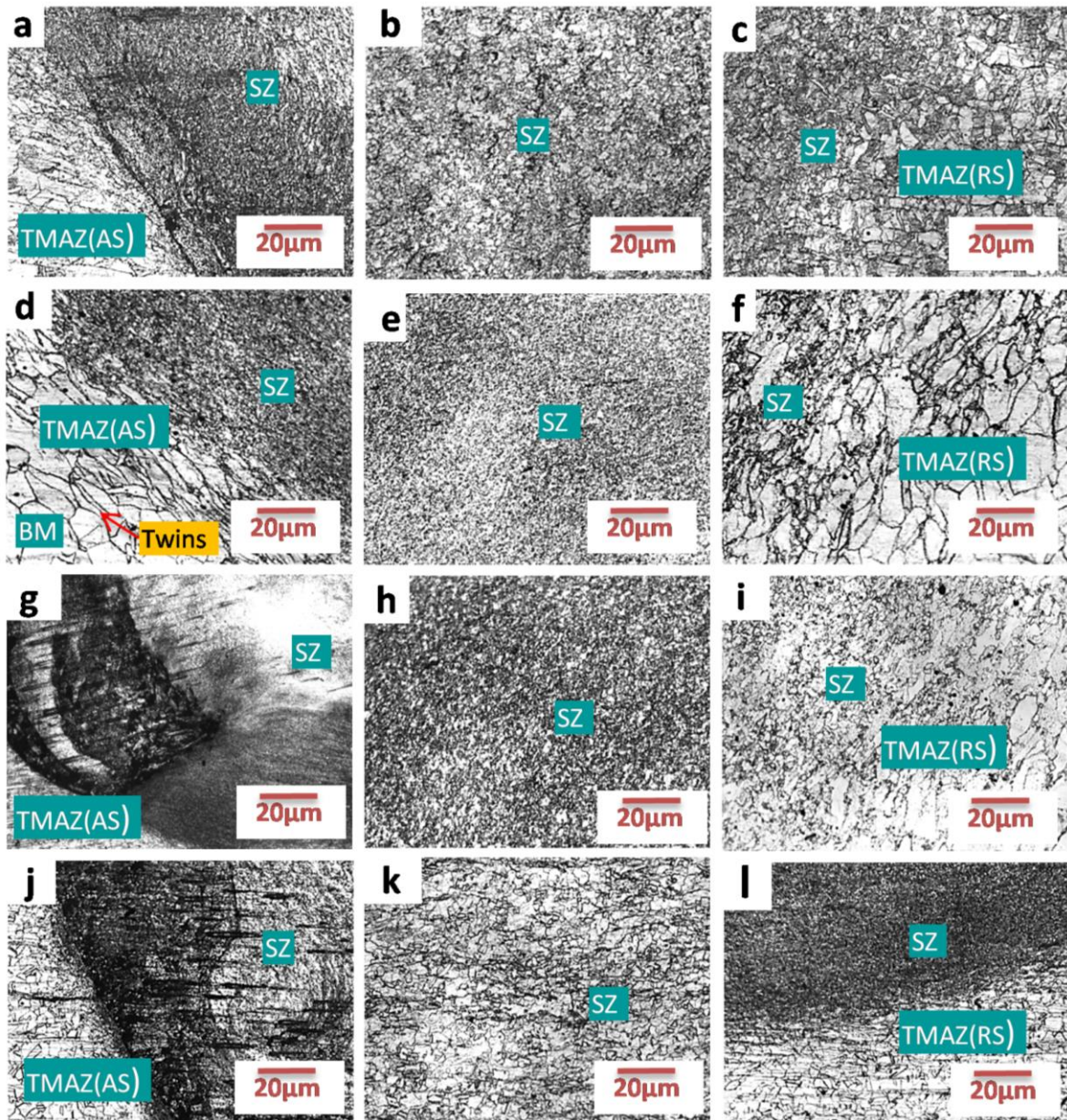


Figure 5.11 Optical micrograph of welded AISI-316L steel pipe sample (at 100mm/min) (a) SZ-TMAZ(AS) (ASS5), (b) SZ (ASS5), (c) SZ-TMAZ(RS) (ASS5) (d) SZ-TMAZ(AS) (ASS6), (e) SZ (ASS6), (f) SZ-TMAZ(RS) (ASS6), (g) SZ-TMAZ(AS) (ASS7), (h) SZ (ASS7), (i) SZ-TMAZ(RS) (ASS7), (j) SZ-TMAZ(AS) (ASS8), (k) SZ (ASS8), (l) SZ-TMAZ(RS) (ASS8)

Overall, from the OM results, it can be said that DRX (induced by frictional heating) is mainly responsible for the grain refinement in the SZ (Sato et al 2005). Apart from DRX, severe plastic deformation also promotes grain refinement in the SZ (Bhattacharyya et al.

2021). DRX is in general followed by static recrystallization. A symmetric SZ indicates uniform microstructural characterization throughout the welded zone as also observed by other researchers (Mishra and Ma, 2005).

5.4.2 Scanning electron microscopy of welded samples

Figure 5.12 and Figure 5.13 shows the scanning electronic micrographs of AISI-316L pipe samples welded at different combination of parameters. The interface of SZ and TMAZ are shown in Figure 5.12(a, c, e, g) and Figure 5.13(a, c, e, g), while the zoomed view of the SZ for the corresponding samples are shown in Figure 12(b, d, f, h,) and Figure 5.13(b, d, f, h,). In Figure 5.13(e, g) all the three zones viz. SZ, TMAZ, BM are distinctly revealed by the SEM images.

Interestingly, heat affected zone (HAZ) is not evident for any of the welded samples which may be due to relatively lower heat generation (Kumar et al. 2018) and low thermal conductivity of steel (Ramesh et al 2019). As the thermal conductivity of steel (~17 W/mK) is much lower compared to aluminum (~180 W/mK), HAZ is not visible for steel samples joined by FSW (Ramesh et al 2019). The SEM micrograph also provides evidence for the presence of transition zone between SZ and BM i.e TMAZ which is characterized by elongated and reoriented grains (refer to Figure 5.13(e, g)). This is produced due to plastic deformation and shearing action of the tool. Ultra-fine grains are observed in the SZ for reasons discussed before. As per the recommendation of Researcher's, (Lin et al. 2015, Duan et al. 2021) during FSW, the size of dynamic recrystallized grain depends on Zener-Hollomon parameter, i.e.

$$Z = \epsilon \exp (Q/RT) \quad \text{Equation 5.1}$$

Where, ϵ =rate of strain energy, R= universal gas constant, T=absolute temperature, Q=activation energy for deformation. Uniform grain refinement is achieved during DDRX under moderate to high Z values (Puli and Ram 2012).

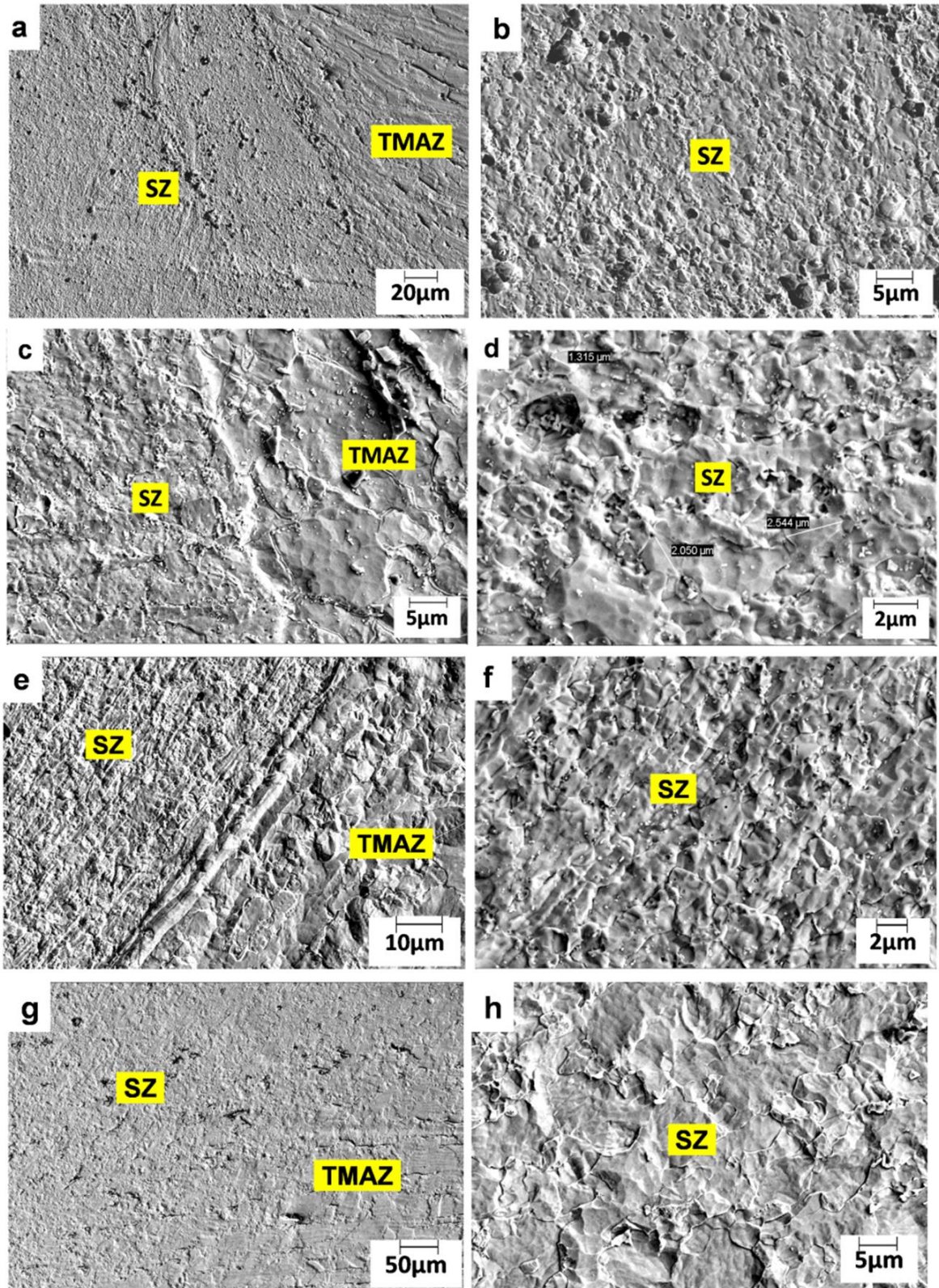


Figure 5.12 SEM micrograph of (a) TMAZ-SZ (ASS1), (b) zoomed view of SZ (ASS1), (c) TMAZ-SZ (ASS2), (d) zoomed view of SZ (ASS2), (e) TMAZ-SZ (ASS3), (f) zoomed view of SZ (ASS3), (g) TMAZ-SZ (ASS4), (h) zoomed view of SZ (ASS4)

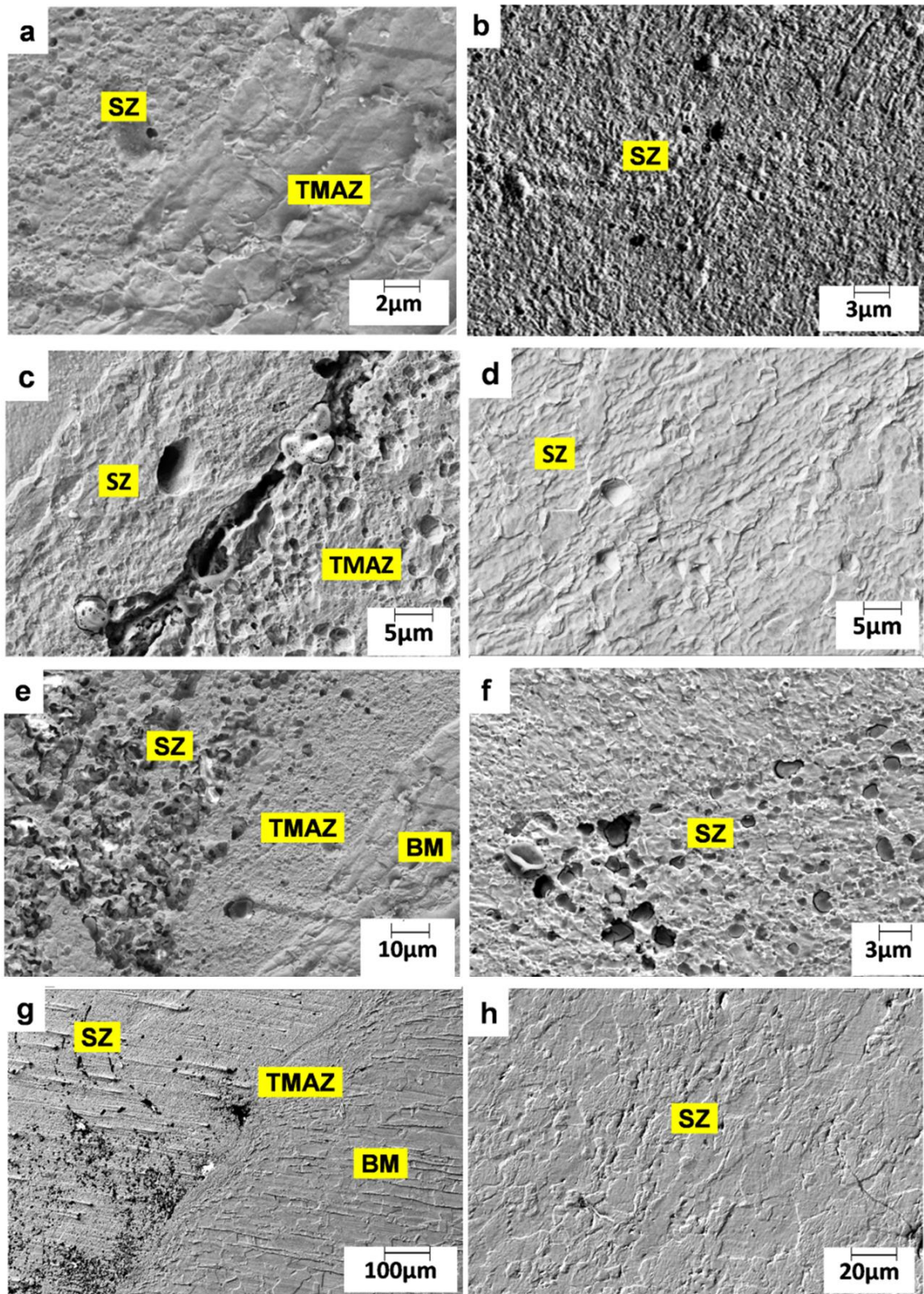


Figure 5.13 SEM micrograph of (a) TMAZ-SZ (ASS5), (b) zoomed view of SZ (ASS5), (c) TMAZ-SZ (ASS6), (d) zoomed view of SZ (ASS6), (e) TMAZ-SZ-BM (ASS7), (f) zoomed view of SZ (ASS7), (g) TMAZ-SZ-BM (ASS8), (h) zoomed view of SZ (ASS8)

Puli and Ram (2012) proposed that uniform grain refinement is achieved during DDRX under moderate Z values. They also state that for homogeneous grain size distribution, high Z values are expected. In this study, SZ shows homogeneous fine grain distribution in welded samples (refer to Figure 5.12 (f) and 5.13(b)), which confirmed that for the present sets of parameter combinations, Z values vary from moderate to high.

Large austenitic gains are observed in the unaffected base metal. TMAZ experiences lower temperature and lower strain compared to SZ, which may result in dynamic recovery rather than dynamic recrystallization in this zone (Tang et al. 2019). The average grain size of SZ, TMAZ (AS), and TMAZ (RS) are measured as $2.63\mu\text{m}$, $9.11\mu\text{m}$ and $9.82\mu\text{m}$ respectively for the sample welded at 350-50-6-FC35 parameter combinations (refer to Figure 5.14(a)). Now, the average grain size of BM is found to be $11.41\mu\text{m}$. Grain size is found to change with different spindle speeds. The average grain size in SZ at 450 rpm has been measured as $2.54\mu\text{m}$ (refer to Figure 5.14(b)). Higher spindle speed yielded ultrafine grain structure. From the SEM micrographs, no void or tunnel defect was found but porosity is observed in the samples ASS6, ASS7 and ASS8 (refer to Figure 5.13(c, e, g,)).

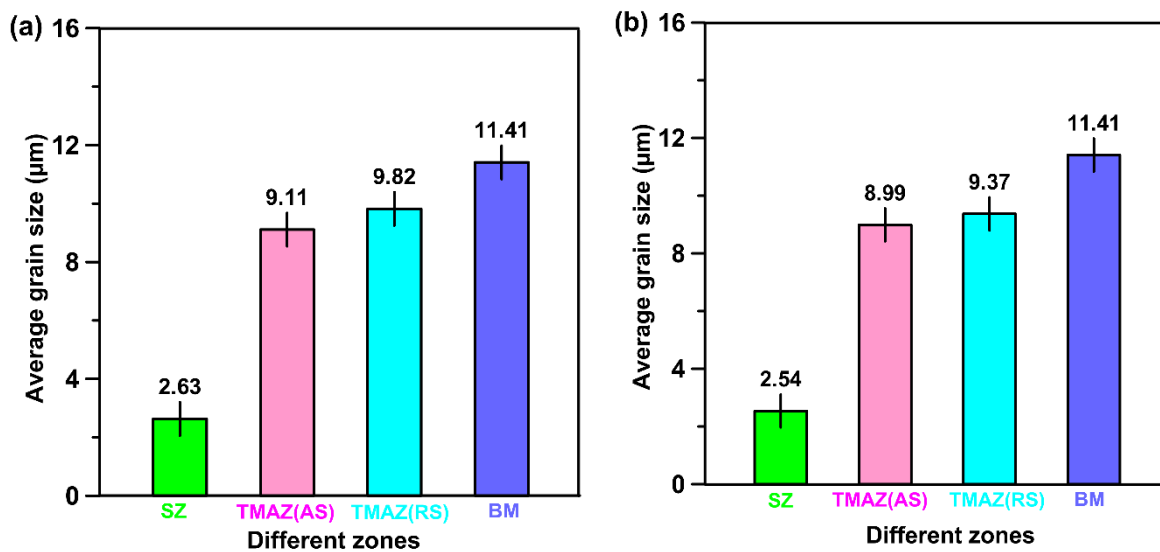


Figure 5.14 Average grain size for different weld zones (a) Sample ASS3 and (b) Sample

ASS4

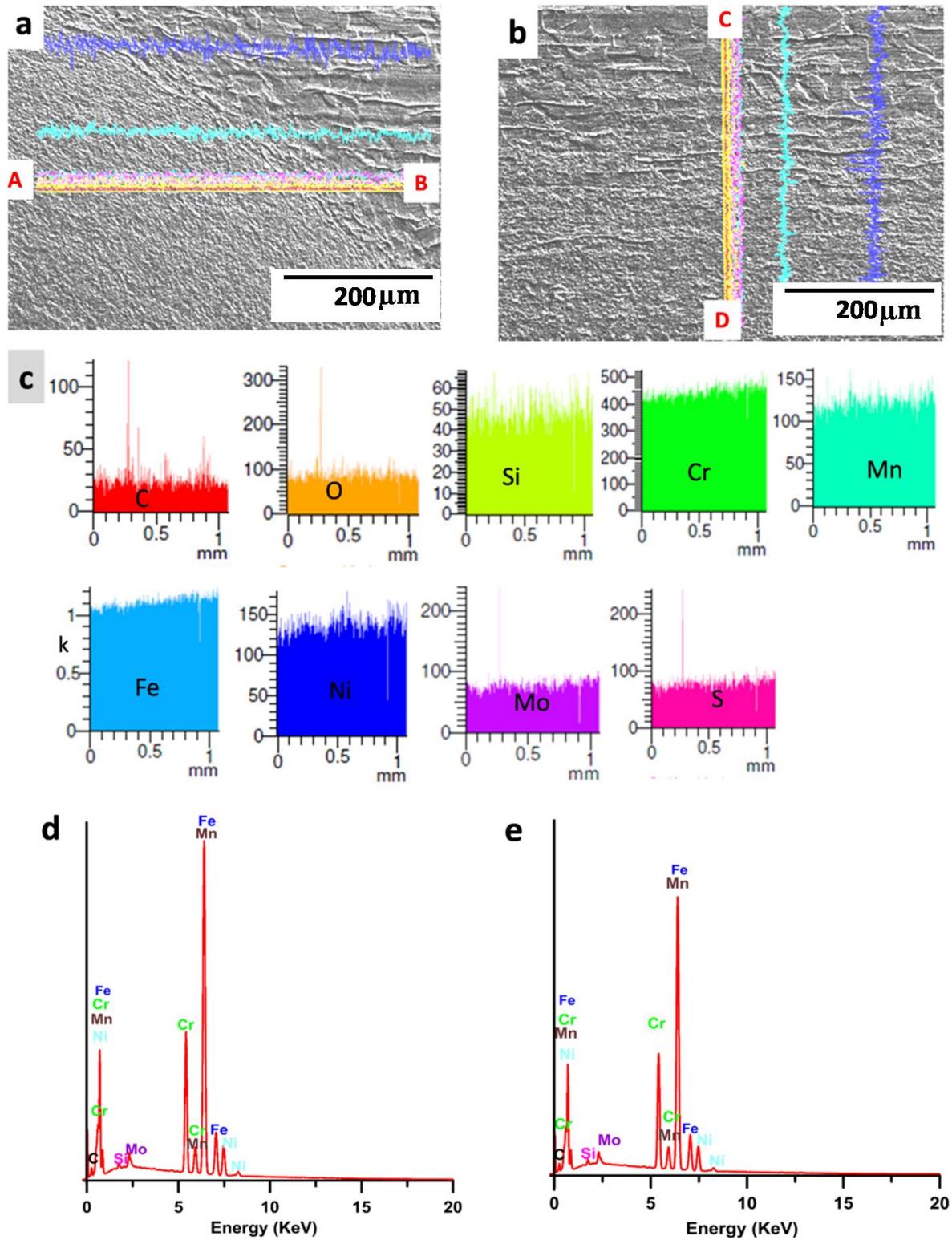


Figure 5.15 Line EDX analysis of sample ASS2: (a), (b) secondary electron images, (c) line EDX color code for A-B line, (d) average composition for A-B and (e) average composition for C-D

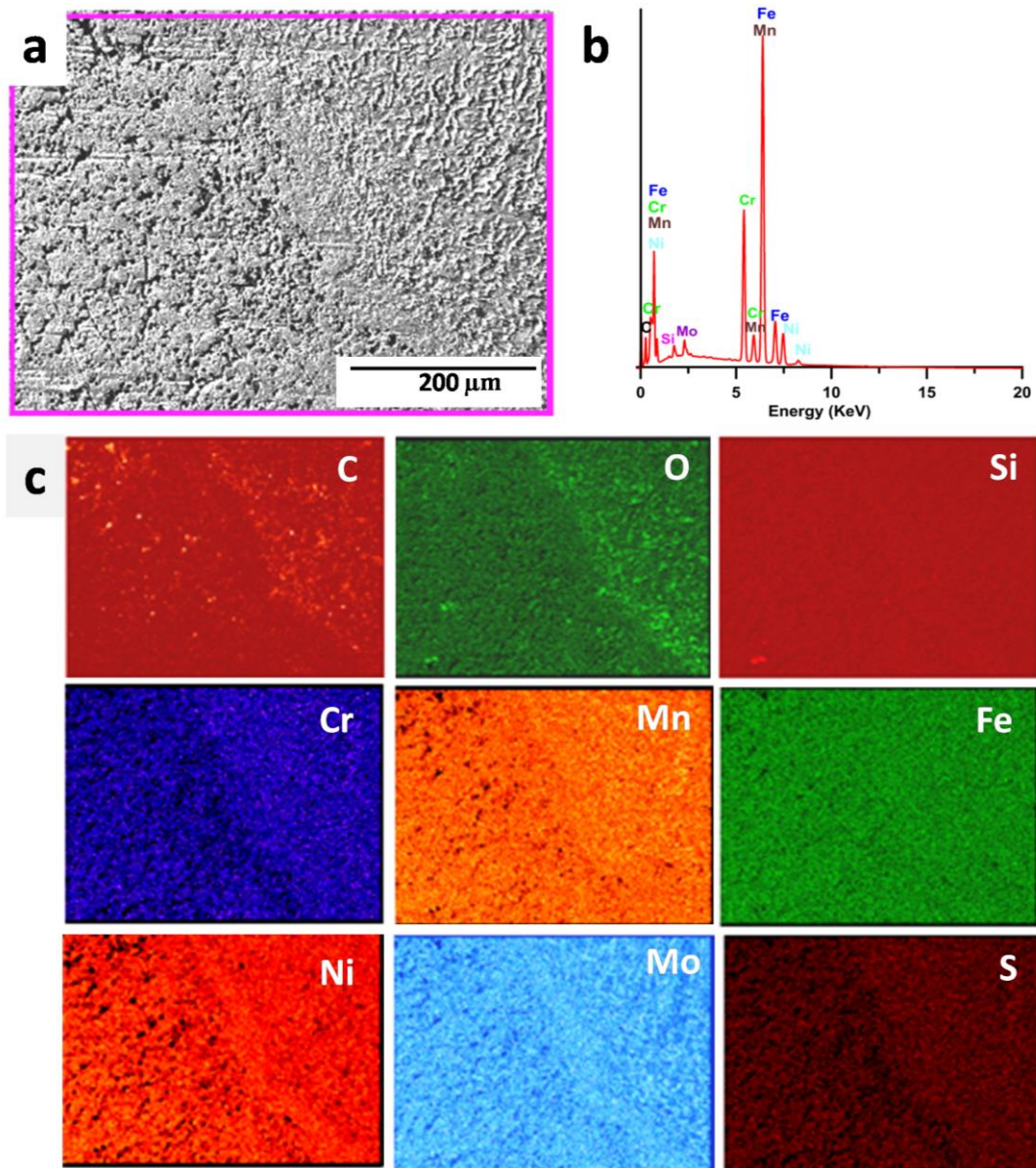


Figure 5.16 Elemental EDX map of welded sample ASS8 (a) secondary images of map EDX
 (b) average composition for EDX map (c) color code for map EDX

5.4.3 Energy dispersive X-ray analysis of welded samples

Line EDX has been performed to determine the different elements present on the welded samples, along the horizontal line A-B and vertical line C-D as indicated on the secondary electron images of the samples (refer to Figure 5.15). The A-B line has been drawn through all the three zones (SZ, TMAZ, and BM) for capturing the elements present on every zone of the welded samples. Whereas, line EDX along C-D is done to determine the elemental

variation vertically on the weld cross-section. None of the constituent elements of the FSW tool are detected in the samples indicating negligible wear from the tool. In fact, elemental mapping for the sample ASS8 (refer to Figure 5.16) is carried to confirm the presence of any tool element in the sample. ASS8 sample is chosen as welding is done with the highest spindle speed (450rpm) and welding speed (100mm/min) combination. For line EDX, the different line colors used for indicating different elements are shown in Figure 5.15 (c). EDX spectrum reveals the presence of mainly C, Cr and Ni inside the welded zone. No other extra elements like C, B, N, W, Re was found in the elemental maps, which further confirms that no tool wear occurred during the welding process. The elements present (weight percentage and atomic percentage) in welded sample found through map EDX are presented in Table 5.2. Further, the FSW tool used for welding shows no deformation or wear visually as compared to a new tool (refer to Figure 5.17). Hence, it can be mentioned that the PCBN coated W-Re tool is employed successfully for joining AISI-316L steel pipes by FSW.

Table 5.2 Weight percentage and atomic percentage of elements present in welded sample ASS8

Element	Weight (%)	Atomic (%)
Fe	63.76	42.94
C	3.93	12.30
Cr	16.52	11.94
Ni	8.56	5.48
Mn	1.54	1.05
Mo	1.92	0.75
Si	0.46	0.62
O	3.26	7.66
S	0.05	0.06



Figure 5.17 Photograph of used and new FSW tools

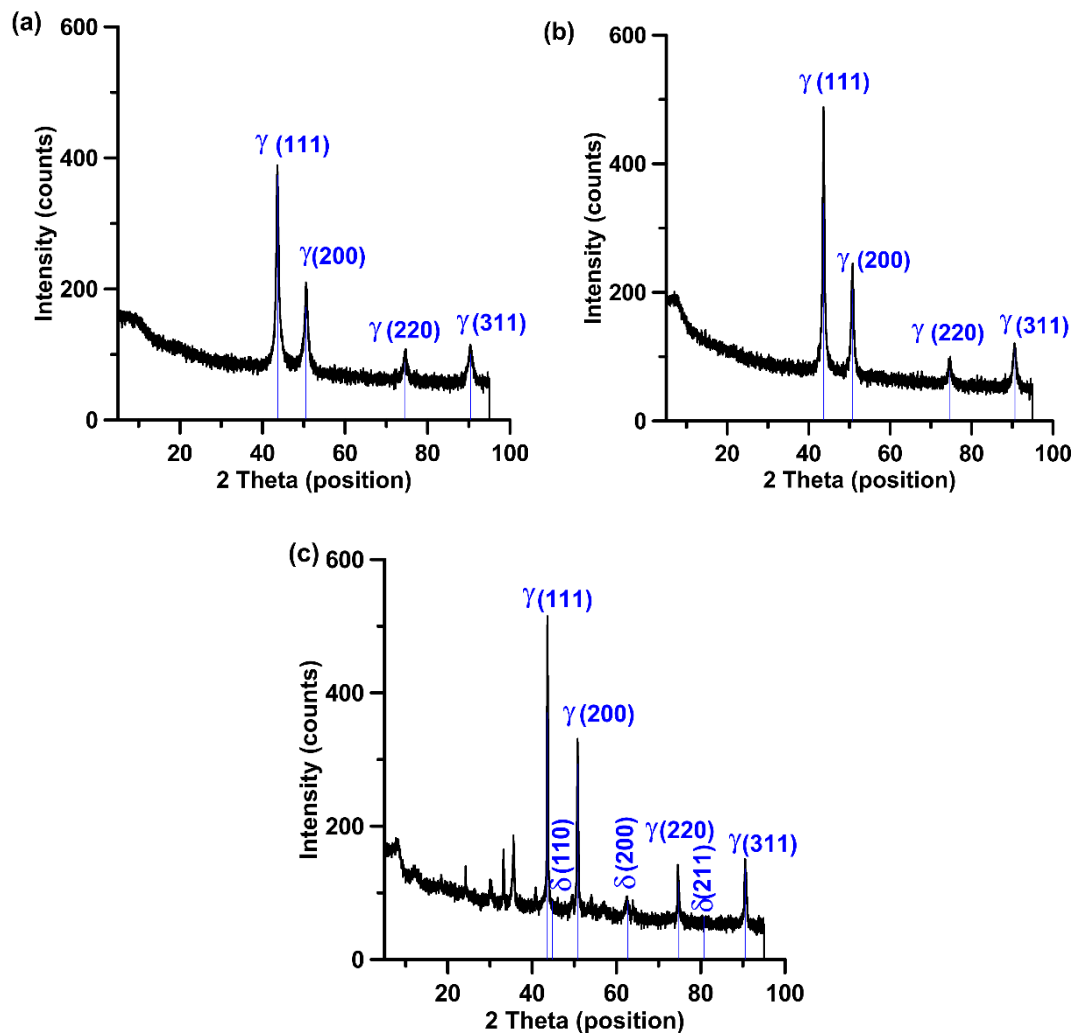


Figure 5.18 XRD patterns of (a) BM, (b) sample ASS2, (c) sample ASS4

5.4.4 X-ray diffraction analysis of welded samples

Figure 5.18 shows the XRD patterns of the as received AISI-316L steel samples and welded samples. Compared to BM, higher intensity peak of austenitic phase is seen in welded samples. According to Cullity (1978), the grain size is inversely proportional to the intensity of peak in the diffraction profile. The increased peak intensity of welded samples indicates that grain refinement has occurred during FSW. The higher intensity peak is observed within the range of 40-50°. Both BM and welded sample reveal the presence of austenitic phase. Existence of delta ferrite is observed in the sample ASS4 (welded at 450rpm spindle speed and 50mm/min welding speed) (refer to Figure 5.18(c)). No peaks of delta ferrite and sigma phase are seen under any other welding conditions.

At higher spindle speed, the joint strength as well as hardness are improved due to the formation of equiaxed grains. However, with increase of welding speed, joint strength deteriorates for the AISI-316L steel. Though, ductility of welded samples is found to be lower compared to BM. This lower ductility is mainly contributed by SZ which is associated with strain hardening and grain size reduction.

5.5 Closure

AISI-316L austenitic stainless-steel pipes have been successfully joined by FSW at different combinations of welding speed and spindle speed under force control mode. No defect is detected which indicate adequate heat generation and material flow throughout the process. It is found that both the welding process parameters have significant influence on the metallurgical and mechanical properties of the welded joints. The welded zone shows grain refinement with the smallest grains distributed over the SZ. This higher grain refinement in the SZ is as a result of DRX which is induced by severe heating and plastic deformation. In fact, increase in the spindle speed results in ultrafine grains. A narrow TMAZ is observed

between the SZ and the BM, where dynamic recovery takes place, and which constitutes elongated and re-oriented grains. The grain refinement in the SZ, presence of grain dislocation in TMAZ is responsible for the improved display of strength and hardness. However, ductility of the weldment is found to be lower than the BM but within acceptable limits.

P91 steel pipe welding at force control mode

Outline of the Chapter: *6.1 Introduction, 6.2 Physical examination of P91 weldments, 6.2.1 Surface of welded samples, 6.2.2 Cross section of welded sample, 6.3 Study of mechanical properties, 6.3.1 Hardness behavior, 6.3.2 Study of tensile properties, 6.4 Metallurgical study, 6.4.1 Optical microscopy of welded samples, 6.4.2 Scanning electron microscopy of welded samples, 6.4.3 Energy dispersive X-ray analysis of welded samples, 6.4.4 X-ray diffraction analysis of welded samples, 6.5 Closure*

6.1 Introduction

Friction stir welding (FSW) is conducted on P91 ferritic /martensitic steel pipes. These grades of steel pipes are popular in industries related to power generation including nuclear power plants and defense related applications. A systematic study is conducted by varying the spindle speed and the welding speed suitably and observing their impact on the tensile strength and hardness of the pipe joints. Microstructural characterization of the joints is also undertaken in order to correlate/explain the joint performance.

6.2 Physical examination of P91 weldments

The current work attempts to effectively join P91 pipes with FSW. A systematic study is conducted by varying the spindle speed and the welding speed suitably and observing their impact on the tensile strength and hardness of the pipe joints. Hence, for carrying out further post-welding characterization. After significant number of trials, the range of parameters resulting in acceptable weld quality (based on visual inspection) is identified as: spindle

speed between 400-600rpm and welding speed between 50-100mm/min (refer to Figure 6.1). No defects or failure are apparent in the samples prepared under force control mode within these range of parameters. Table 6.1 shows the various weld conditions and their nomenclature used in the study.

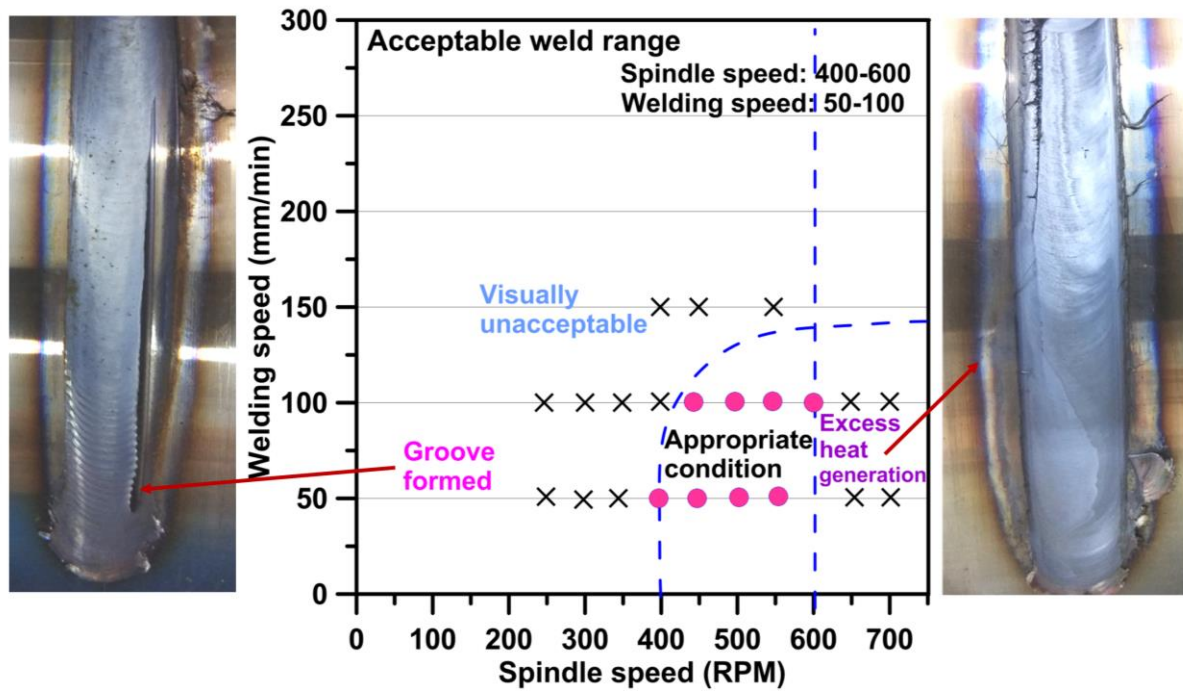


Figure 6.1 Identifying parameters for appropriate welding of P91 steel pipes

Table 6.1 FSW parameters for joining P91 steel pipes

Sl. no.	Sample no.	Spindle speed (rpm)	Welding speed (mm/min)	Control mode	Z-force values (kN)
1	FSS1	400	50	FC	35
2	FSS2	450	50	FC	35
3	FSS3	500	50	FC	35
4	FSS4	550	50	FC	35
5	FSS5	450	100	FC	35
6	FSS6	500	100	FC	35
7	FSS7	550	100	FC	35
8	FSS8	600	100	FC	35

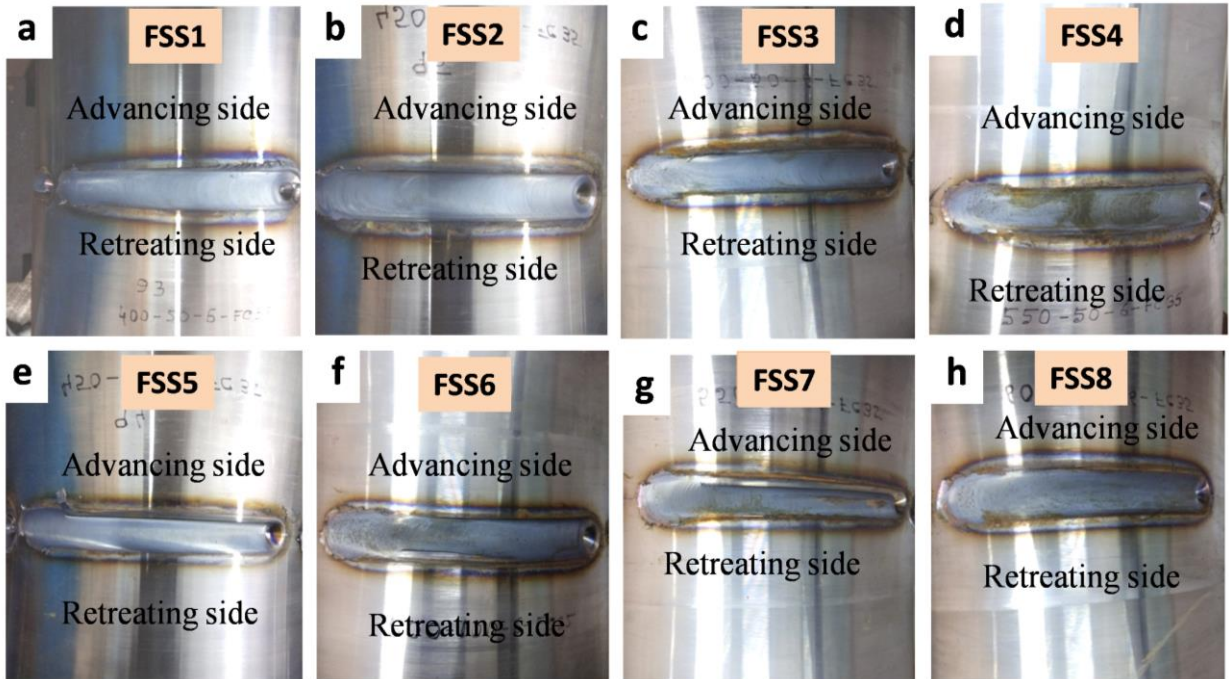


Figure 6.2 Photograph of the top surface of the P91 steel pipes welded at different parameter combinations

Table 6.2 Peak temperature values recorded during FSW of P91 steel pipes at different parameter combinations

Sample no.	FSS1	FSS2	FSS 3	FSS4	FSS5	FSS6	FSS7	FSS8
Temperature (°C) at weld zone	767	794	819	892	771	798	827	886

6.2.1 Surface of welded samples

Figure 6.2 shows the images of top surface of pipe welded using different parameter combinations. Most of the parameter combinations have yielded defect free weld. A few of them show defect which may have been caused due to either high or insufficient heat generation. During welding, peak temperature values have been recorded and are given in Table 6.2. The values of the temperature are quite commensurate with the spindle speed and welding speed combinations i.e. higher spindle speed and lower welding speed yield higher

peak temperature and vice versa.

6.2.2 Cross section of welded sample

By analyzing the weld cross section, three different zones are clearly visible viz. stir zone (SZ), thermo-mechanical affected zone (TMAZ) and base metal (BM). Figure 6.3 clearly exhibit the typical basin shaped cross sectional view which indicates the material flow during friction stir welding as governed by the tool (Ramesh et al. 2017).

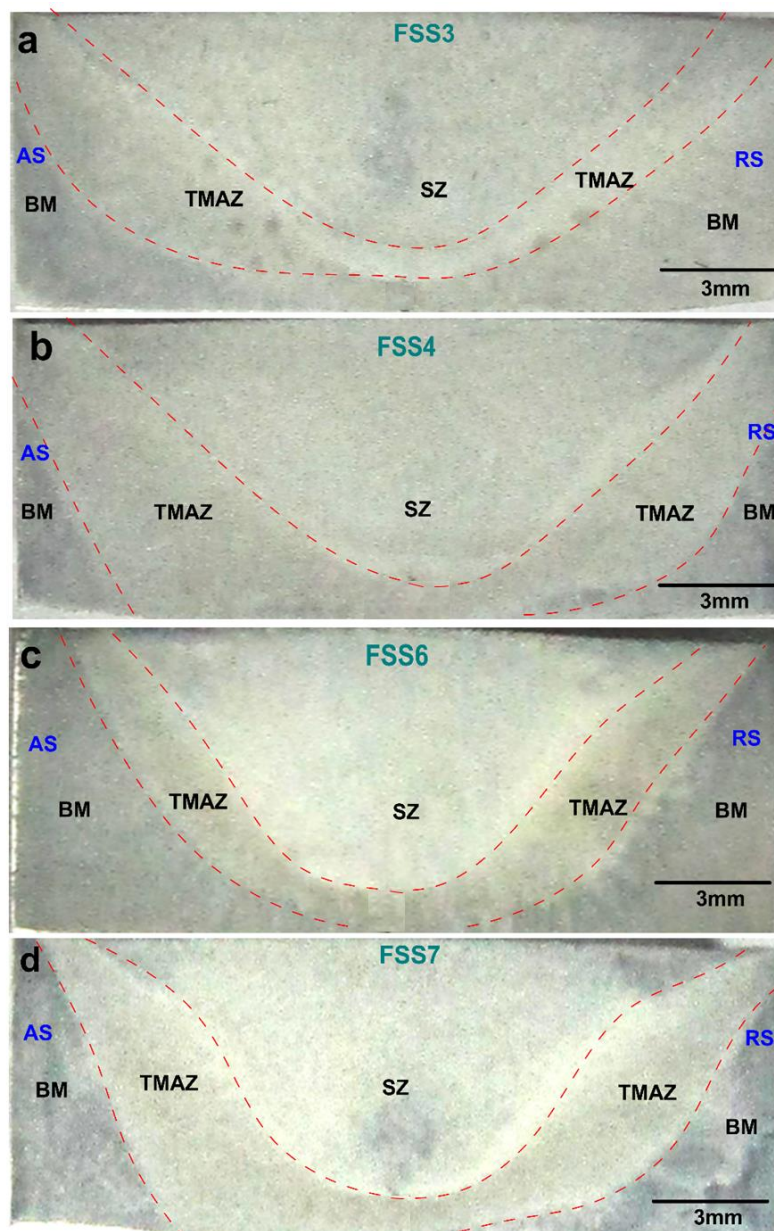


Figure 6.3 Cross section of FSW P91 steel pipes, sample number (a) FSS3 (b) FSS4 (c) FSS6
(d) FSS7

6.3 Study of mechanical properties

6.3.1 Hardness behaviour

To understand the variation of microhardness values across the weld cross section, hardness values have been taken on both sides of the centre line of SZ of welded sample at every 2 mm interval. The hardness values of base metal and welded samples at different parameter combinations are shown in Figure 6.4. The average hardness of base metal is measured as 228.69HV. It is noticed that hardness value in SZ is much higher than TMAZ and BM. The samples welded at 100mm/min feed rate display relatively better hardness than that welded at 50mm/min feed rate. The sample number FSS7, welded at 550rpm and 100mm/min exhibit the highest hardness value (496.79HV). Higher hardness values in SZ of welded samples indicate the existence of a martensitic structure as well as higher dislocation density (Li et al. 2019). Grain refinement in SZ is also responsible for its higher hardness. Presence of sub grain boundary and dislocation density as a result of plastic deformation also enhanced the hardness values (Nagaraj and Ravisankar 2018). In advancing side of TMAZ, the maximum hardness value is exhibited as 427.81HV for the sample welded at 550rpm-50mm/min (FSS4) but in RS of TMAZ, the maximum hardness value is measured as 393.89HV for the same sample. The strengthening mechanism is also responsible for enhancement of hardness in TMAZ. The TMAZ also shows significant increase in hardness compared to BM. Again, the presence of martensitic phase as well as sub grain boundary is responsible for the higher hardness of TMAZ. The hardness value is drastically reduced at the boundary of TMAZ and BM, which indicates the sharp transition from TMAZ to BM (Li et al. 2019). Heat generation during FSW, which aids plastic deformation has a strong relation with the FSW process parameters. Higher hardness achieved in TMAZ and SZ indicate the brittleness of the material after FSW. Figure 6.5 reports the maximum hardness displayed welded samples compared to P91 BM.

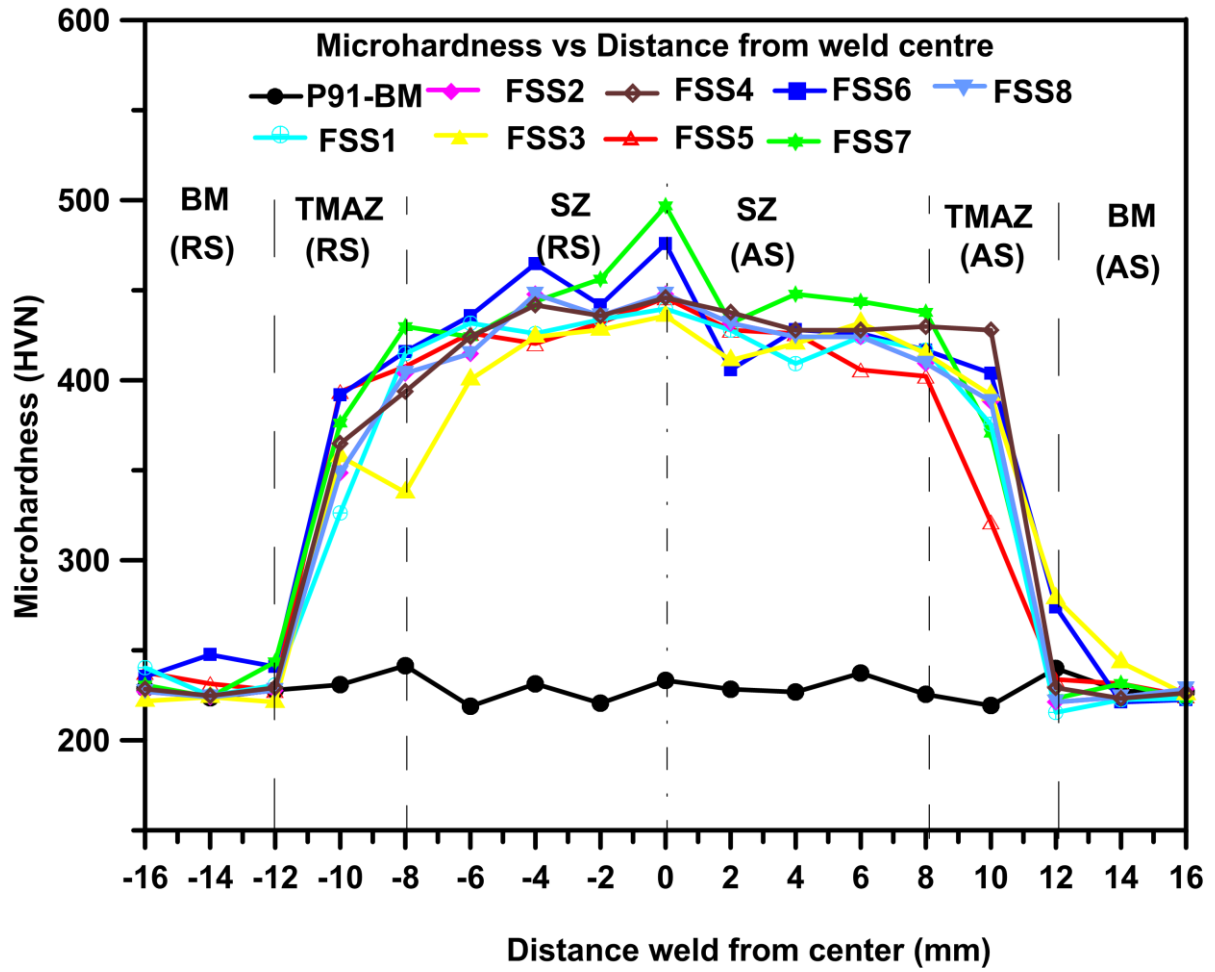


Figure 6.4 Hardness values across the cross section of welded samples

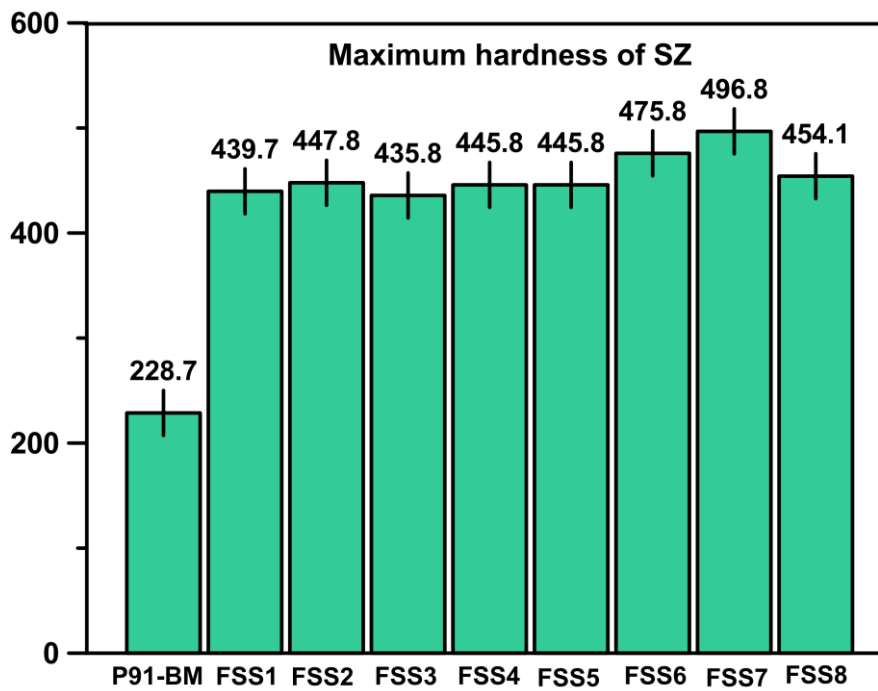


Figure 6.5 Maximum hardness of the welded samples compared to BM

6.3.2 Study of tensile properties

Figure 6.6 shows the stress-strain plot of BM and welded samples. The yield strength and ultimate tensile strength of as received BM have been measured (sample P91-BM) as 520.2MPa and 662.9MPa respectively. At 50mm/min welding speed, maximum joint efficiency has been determined as 101.3% for sample FSS4 (welded at 550 rpm spindle speed and 50mm /min welding speed). The top view and side view of a tensile tested sample are shown in Figure 6.7 where SZ is clearly visible. The failure is seen to occur outside the SZ but at the interface of TMAZ and BM. This confirms that the joint strength is higher than that of BM. Maximum joint strength of 703.5MPa has been achieved at 100mm/min welding speed and 500rpm spindle speed (FSS6) which roughly translates to around 106% efficiency. The percentage of elongation for base metal is ~13.5%. The post-FSW reduction in percentage elongation indicates the material to become brittle in nature. After the welding, the pipes have been let to natural cooling to the ambient temperature. In-situ normalizing process leads to development of un-tempered lath martensitic structure (Pandey et al. 2018). Un-tempered form of martensite structure is very hard and brittle which may have caused the brittleness of P91 steel after FSW. Deformation against an external load may be resisted by $M_{23}C_6$ (M stands for Fe, Cr, Mn and Mo) and MX (M stands for V, Nb and X for C, N) precipitates that pin down the dislocation movements along prior austenitic grain boundaries (PAGBs) (Pandey et al. 2018) and shift the dislocations within the matrix. Grain refinement of martensite laths and PAGBs enhanced the amount of high angle grain boundary (HAGB), which may cause the strengthening of the P91 steel, after FSW (Zhang et al. 2018a). Above 850°C temperature, $M_{23}C_6$ particles get completely dissolved in the matrix which may be the reason that beyond certain value of spindle speed, degeneration of mechanical properties occurs. Figure 6.8 shows the yield and ultimate tensile strength of P91 base metal as well as that of welded samples.

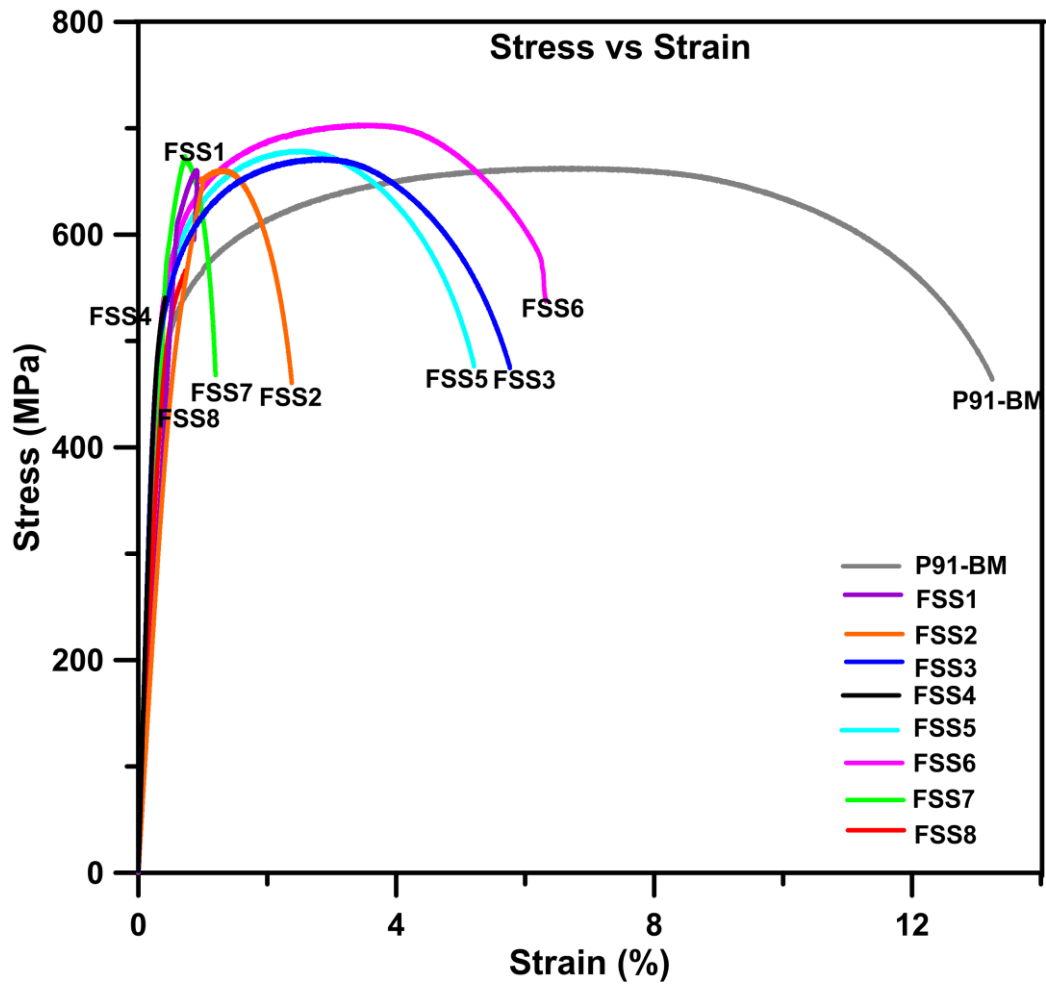


Figure 6.6 Stress vs strain plot of P91 welded specimens

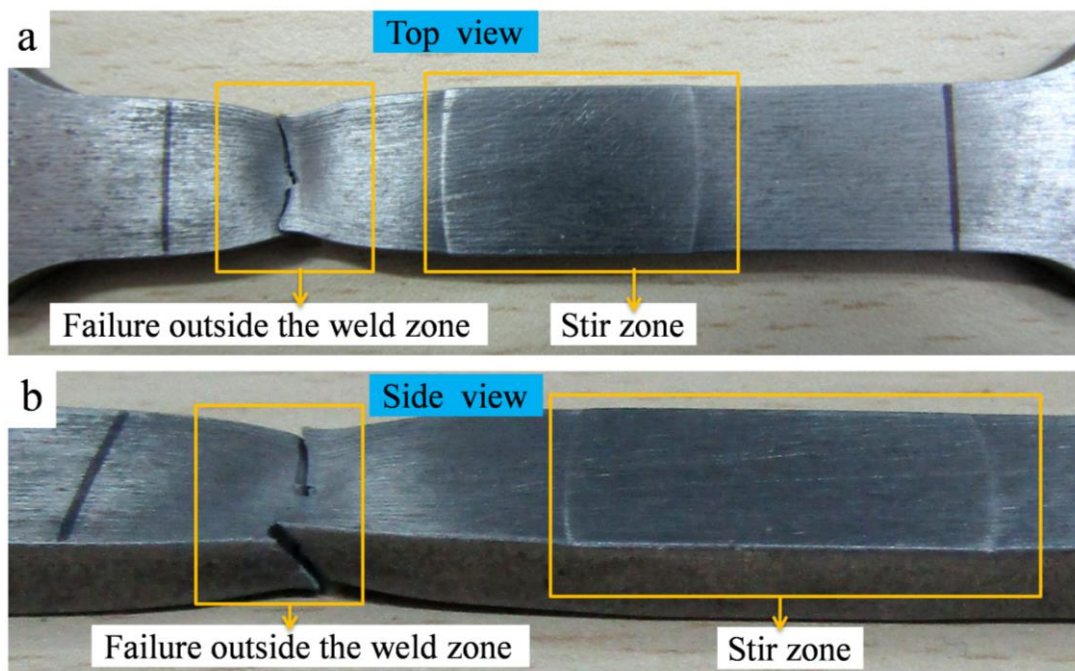


Figure 6.7 Tensile tested sample (a) top view (b) side view

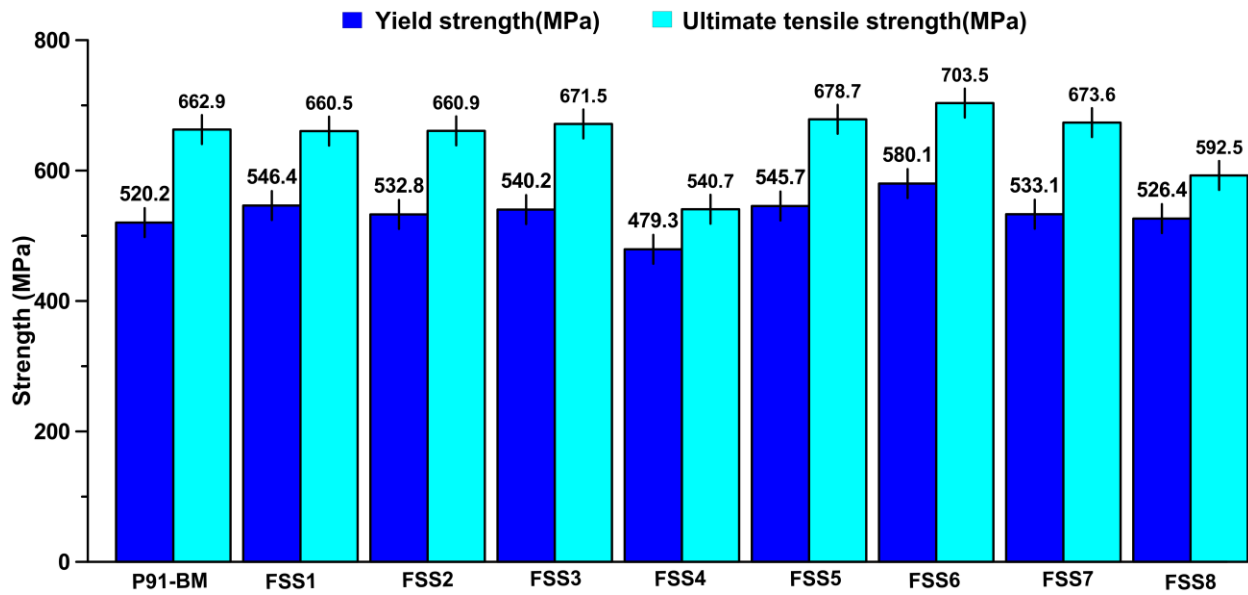


Figure 6.8 Yield and ultimate tensile strength of P91 base metal and welded samples

6.4 Metallurgical study

6.4.1 Optical microscopy of welded samples

Optical micrographs of friction stir welded samples are shown in Figure 6.9 and 6.10. Three different zones viz. SZ, TMAZ, and unaffected BM are clearly visible. Separation between SZ and TMAZ are more prominent towards AS than RS (refer to Figure 6.9(f, i, l)). Stir zone is identified by fine PAGBs, small amount ferrite grain and lath martensite. In TMAZ, broadening of martensite laths and coarsening of PAGBs are common as observed by Zhang et al. (2018a).

Peak temperature experienced during FSW influences the microstructure evolution in the SZ and TMAZ. In the current study, the peak temperature measured during welding varies from 760-890°C which is in the range of or marginally higher than A_{C3} point (A_{C3} temperature for P91 ranges around 800-840°C as per Zhang et al. (2018b)). At lower spindle speed, peak temperature does not exceed A_{C3} but at higher rotational speed it may do so (Zhang et al. 2018a) which is the reason for variation of grain structure in SZ at the same welding speed but for different spindle speeds. FSW of P91 steel within the range of these

temperature exhibit no phase transformations like transformation from α to γ in heating stage and γ to α in cooling stage (Zhang et al. 2018b). Sunilkumar et al. (2020) mentioned that $M_{23}C_6$ precipitation is stable upto 880°C. The microstructure of SZ is characterized by the presence of PAGBs, lath boundary and the precipitation of $M_{23}C_6$ particles (refer to Figure 6.9(b)). Grain size in SZ and TMAZ play a vital role in distribution of precipitations which in turn affects the hardness and strength of the joint.

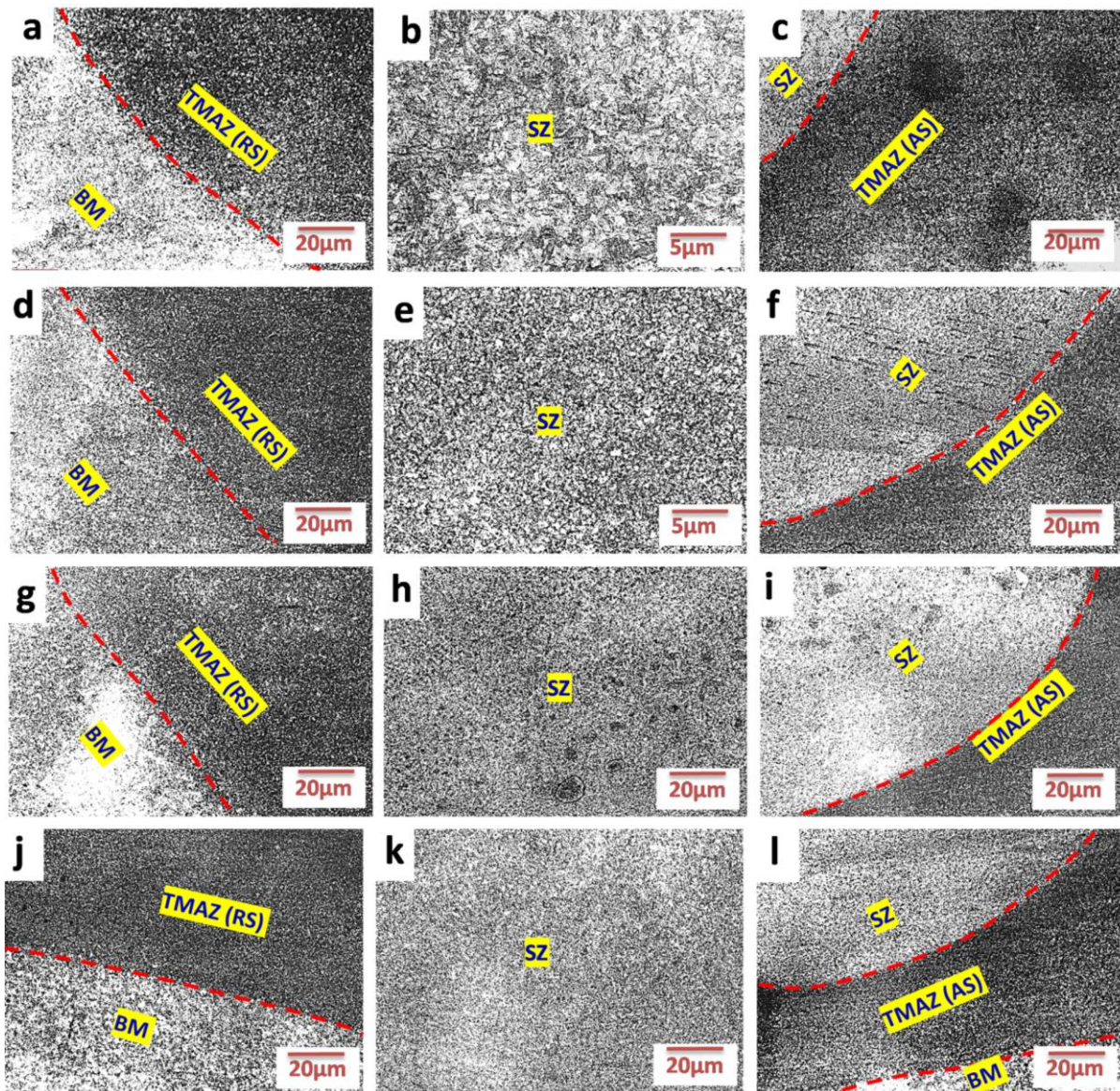


Figure 6.9 Optical micrograph of FSW P91 steel pipes:- sample FSS1 (a) TMAZ(RS) - BM (b) SZ, (c) SZ – TMAZ(AS); sample FSS2 (d) TMAZ(RS) - BM (e) SZ (f) SZ – TMAZ(AS); sample FSS3 (g) TMAZ(RS) - BM (h) SZ (i) SZ – TMAZ(AS); sample FSS4 (j) TMAZ(RS) – BM (k) SZ (l) SZ – TMAZ(AS) – BM

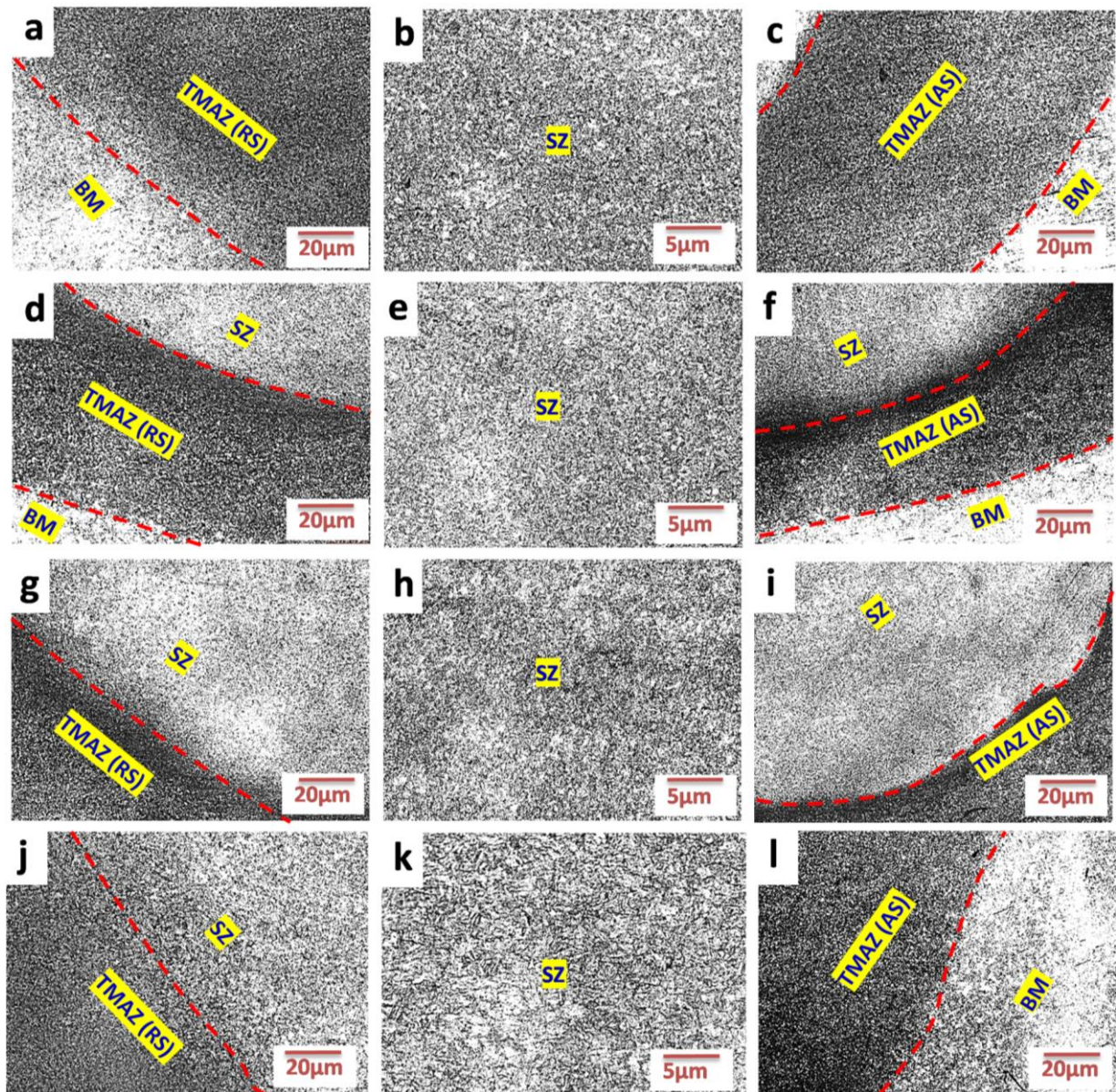


Figure 6.10 Optical micrograph of FSW P91 steel pipes: - sample FSS5 (a) TMAZ(RS) – BM (b) SZ (c) TMAZ(AS)-BM; sample FSS6 (d) SZ – TMAZ(RS) - BM (e) SZ (f) SZ-TMAZ(AS) - BM; sample FSS7 (g) SZ – TMAZ(RS) (h) SZ (i) SZ – TMAZ(AS); sample FSS8 (j) SZ – TMAZ(RS) (k) SZ (l) TMAZ(AS) – BM.

6.4.2 Scanning electron microscopy of welded samples

FESEM images of P91 base metal is presented in Figure 6.11. Main constituent of the as received P91 steel is martensitic lath which is typical to any low alloy steel. From SEM micrograph (Figure 6.11b), mainly $M_{23}C_6$ carbide and MX carbonitrides types of

precipitation are observed. The coarse precipitations $M_{23}C_6$ mainly occur on PAGBs, in the internal laths and in sub grain boundary (Pandey and Mahapatra 2016). The fine precipitates MX are observed inside the matrix and along the boundary. The size of the precipitates is measured by imageJ software and is found to vary between 40 to 530nm. The average size of precipitation is 192nm. The average size of coarse precipitations is 321nm. Some other precipitations like Cr-rich $M_{23}C_7$, M_2X (M stand for Cr, Fe and X stand for C, N) and M_7C_3 (M stand for Cr, Mn Fe) are also reported in P91 base metal (Pandey et al. 2018).

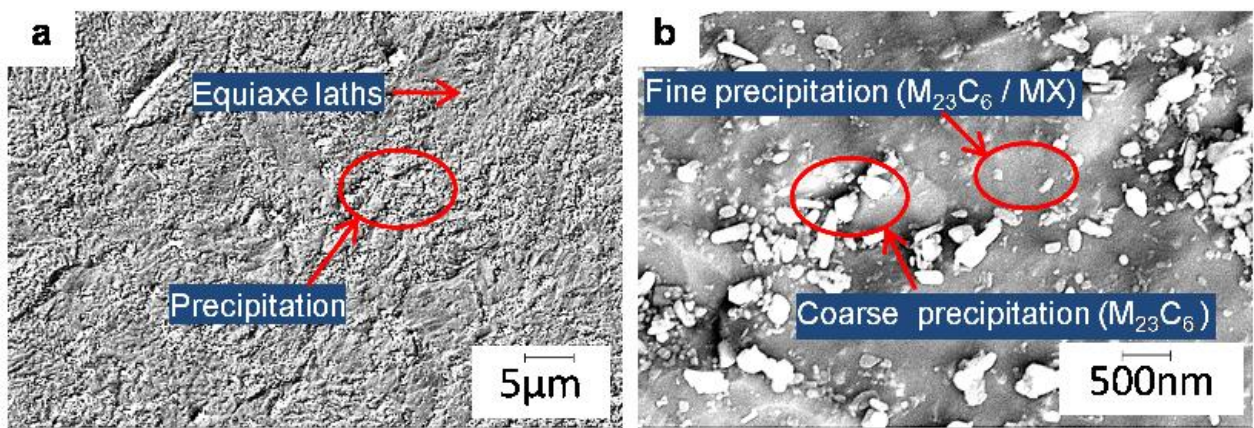


Figure 6.11 SEM images of as received P91 steel pipes

The scanning electron microscopy of samples welded at different parameter combinations are shown in Figure 6.12. Typical zones viz. SZ, TMAZ and unaffected BM can be clearly distinguished. Appearance of prior austenite grain is significantly refined in SZ (refer to Figure 6.13d). Zhang et al. (2018b) reported that after FSW, initial tempered martensite is transformed to lath martensite from BM to welded zone. At lower spindle speed, ferrite and laths appeared in SZ. At higher spindle speeds, only laths martensite appeared in the SZ. Subsequent to FSW of P91 steel, grain refinement in SZ occurs owing to dynamic recrystallization (DRX), grain growth produced by severe plastic deformation (SDP) and due to the cooling rate. DRX occurs in two ways, viz. continuous dynamic recrystallization (CDRX) and discontinuous dynamic recrystallization (DDRX). CDRX is generated by the

transformation of low angle grain boundary (LAGB) to high angle grain boundary (HAGB) (Han et al. 2014), whereas DDRX is occurs by the breakup of initial grain. For the current study, the cooling rate is relatively higher as the cooling reagent is used for fast cooling during welding. Higher cooling rate reduces the chance of austenite grain growth (Zhang et al. 2018b) and promotes the formation of prior austenite grain (PAG) and martensite laths which are the main reasons for grain refinement in the SZ.

No precipitation along grain boundary (GB) is observed in SZ. Hence, sliding of grain boundary may be easier in SZ (Sunilkumar et al. 2020). It has been perceived that coarse $M_{23}C_6$ dissolved partially and fine $M_{23}C_6$ dissolved fully in high temperature welded samples. It has further been noticed that fine MX precipitations remain same even after friction stir welding. This is because the dissolution temperature of MX is much higher than the peak temperature encountered in SZ. The hardening elements present in P91 are Cr and Mo. Average grain size in SZ is $\sim 6\mu\text{m}$ whereas the same for base metal is $\sim 11\mu\text{m}$. The average grain size of prior austenite grain is $\sim 7\mu\text{m}$. In SZ only fine precipitation is observed contrary to TMAZ where both coarse as well as fine precipitations are observed (refer to Figure 6.13(e)). The microstructure of AS and RS side are asymmetric due to variation in heat generation, which is approximately 100°C (Zhang et al. 2018a). The peak temperature for the FSW process lies between $750\text{-}900^\circ\text{C}$ which is in the range of A_{C1} to A_{C3} of P91 steel (Jafarzadegan et al. 2012, Ghosh et al. 2012). Austenite (γ), and ferritic + austenite ($\alpha+\gamma$) phases are observed in SZ and TMAZ after dynamic recrystallization. Martensite phase is also observed since higher cooling rate is achieved by circulating coolant inside the mandrel. It is reported that $M_{23}C_6$ precipitation is completely dissolved above 850°C which is greater than A_{C3} temperature of steel (Zhang et al. 2018a, Sawada et al. 2015, Pandey et al. 2016). In the present sample, except lath martensite and MX type of precipitation, no other precipitations are visible in SZ as seen in Figure 6.12(b, d, f, h,) and Figure 6.13(b, d, f, h,).

Whereas, precipitation and martensite particles are visible in TMAZ (refer to Figure 6.12(a, c, e, g) and Figure 6.13(a, c, e, g)). At fixed welding speed but with increasing spindle speed, both the heat generation and peak temperature increase. Due to this, $M_{23}C_6$ precipitation get dissolved into Fe matrix in the TMAZ (refer to Figure 6.13a).

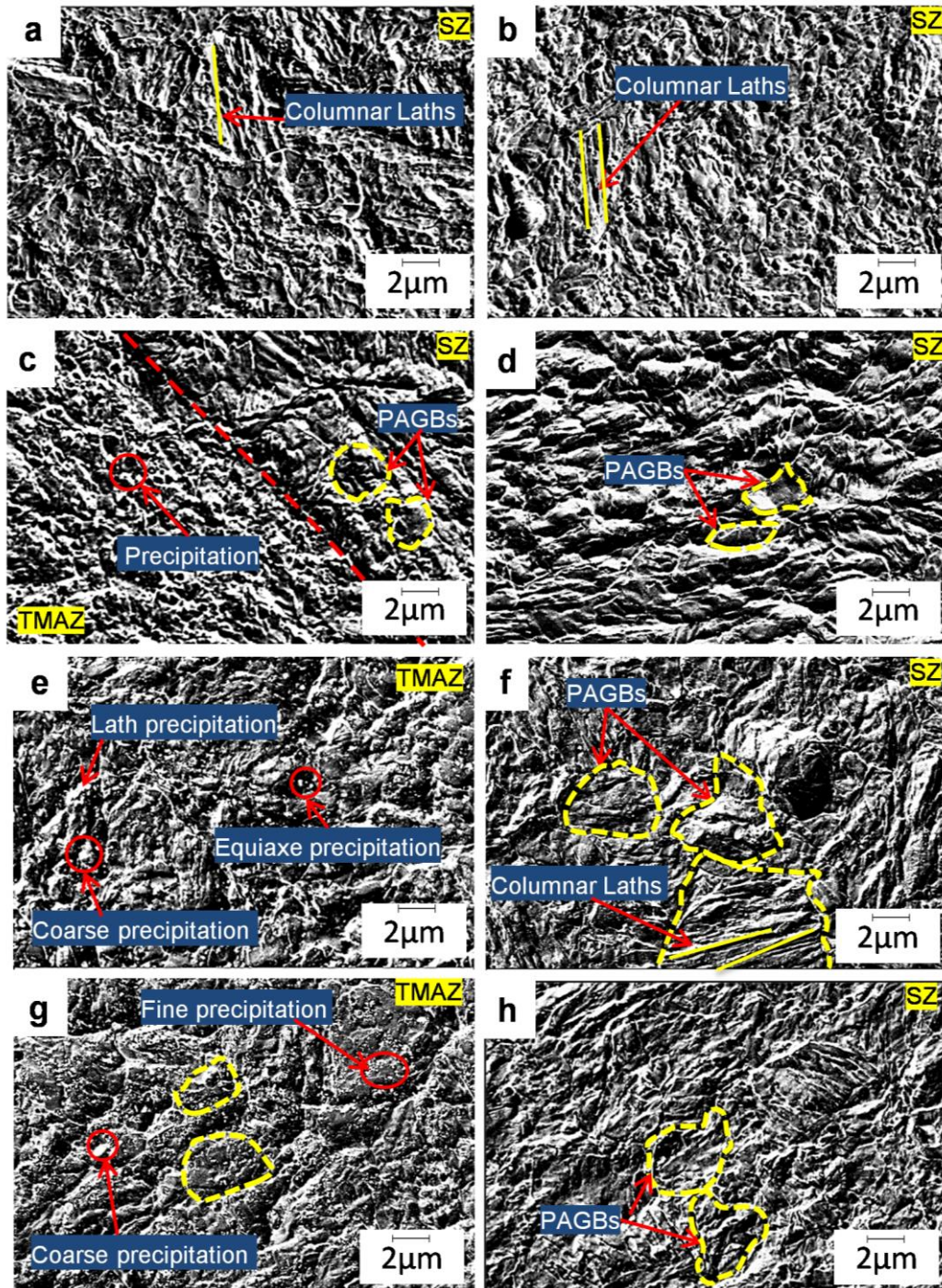


Figure 6.12 SEM micrograph of P91 weldments:- sample FSS1 (a) SZ-TMAZ (b) SZ; sample FSS2 (c) SZ-TMAZ (d) SZ; sample FSS3 (e) TMAZ (f) SZ; sample FSS4 (g) TMAZ (h) SZ

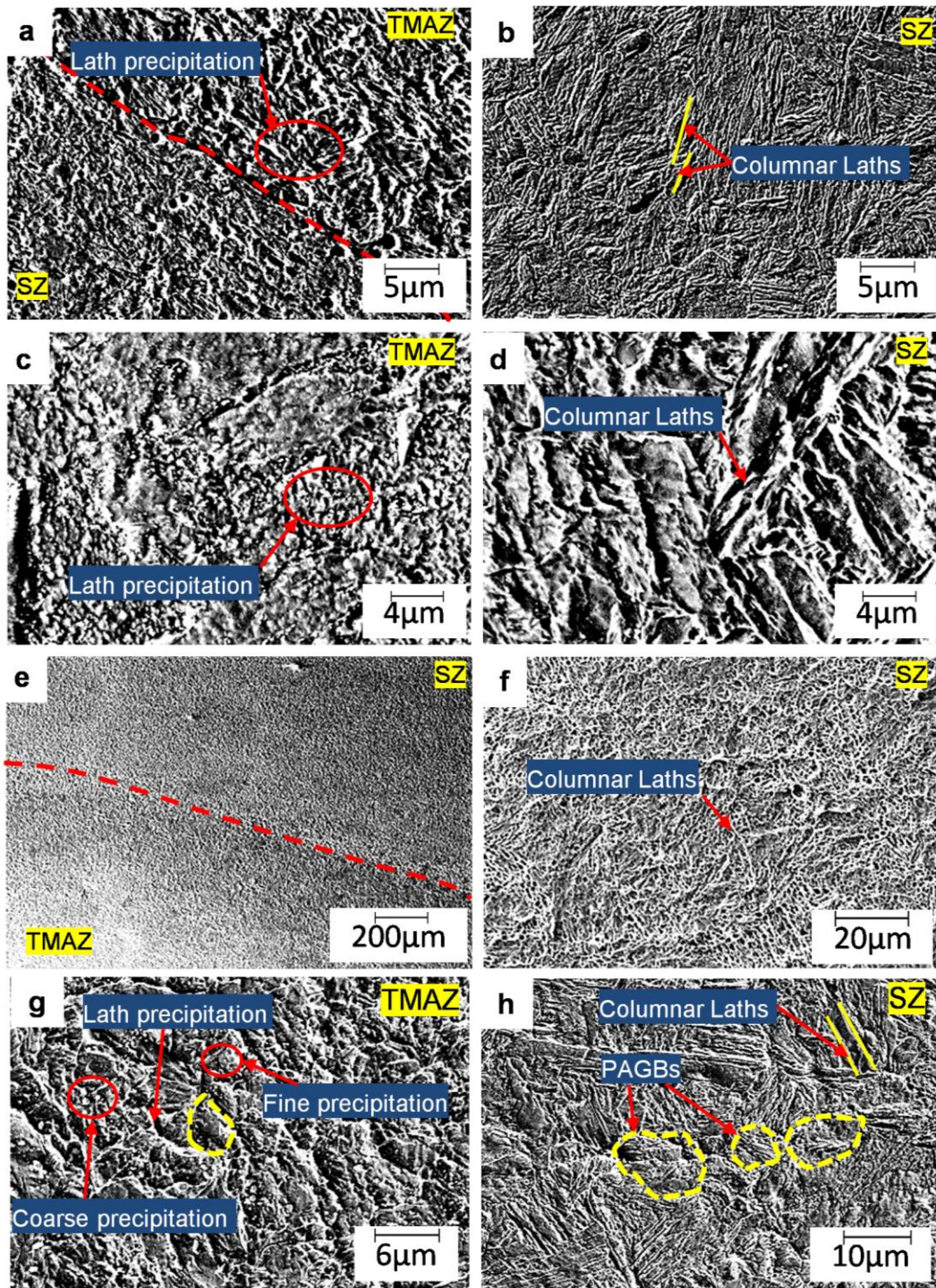


Figure 6.13 SEM micrograph of P91 weldments:- sample FSS5 (a) SZ-TMAZ (b) SZ; sample FSS6 (c) TMAZ (d) SZ; sample FSS7 (e) SZ-TMAZ (f) SZ; sample FSS8 (g) TMAZ (h) SZ

6.4.3 Energy dispersive X-ray analysis of welded samples

Line and Map EDX have been done on the welded samples. Line EDX has been carried out along the horizontal and the vertical direction of weld section to cover all the zones viz. SZ,

TMAZ, and BM of the samples. The secondary electron images of horizontal line AB and the vertical line CD of the samples FSS5 are shown in Figure 6.14 (a, b) and the corresponding elemental analysis plots are shown in Figure 6.14 (c, d). Figure 6.15 shows the color code for each element in EDX line analysis. Same color code is followed for all the EDX line analysis. Secondary images and elemental analysis plots of the sample FSS6 is shown in Figure 6.16 whereas the same for sample FSS7 is shown in Figure 6.17. The elements found in line EDX are Cr, Mn, Mo, V, Nb, Fe, C which is expected for P91 material. The EDX suggested that most of the fine particles are V and Nb rich which indicate that these fine particles are MX carbide particles (Paul et al. 2008).

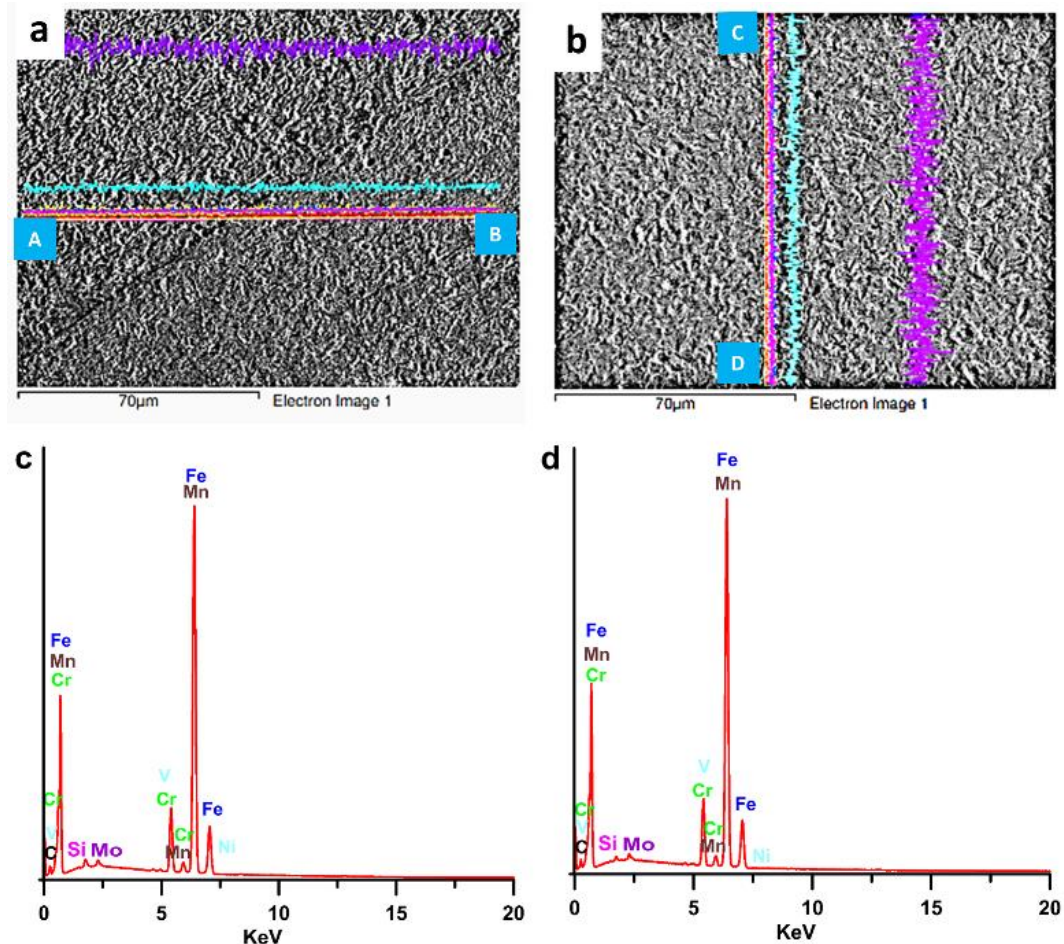


Figure 6.14 Line EDX analysis of sample FSS5 (a), (b) secondary electron images for line EDX analysis and (c), (d) corresponding line plots

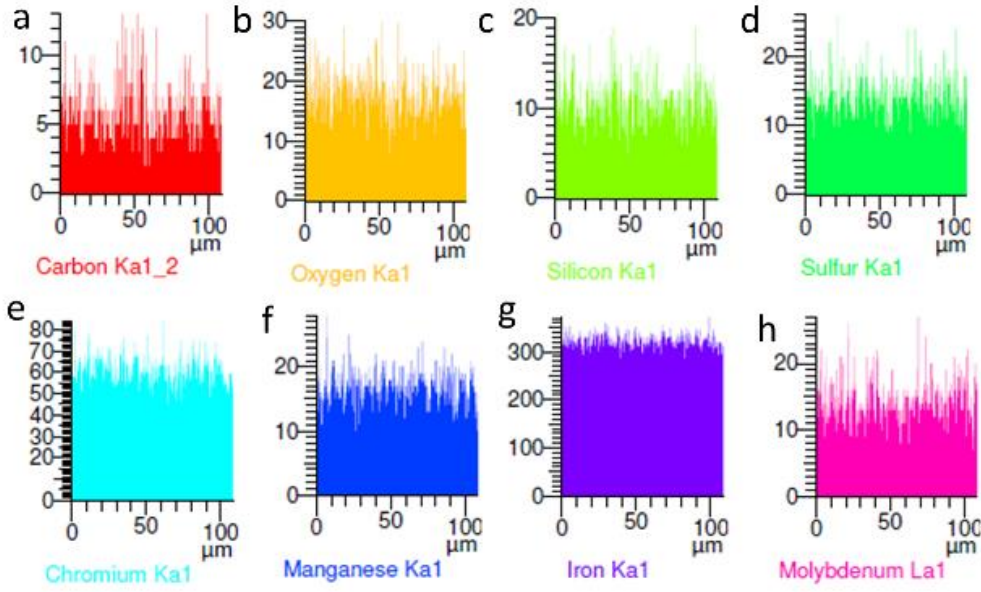


Figure 6.15 The color code used for different elements during line EDX (a) C (b) O (c) Si (d) S (e) Cr (f) Mn (g) Fe (h) Mo

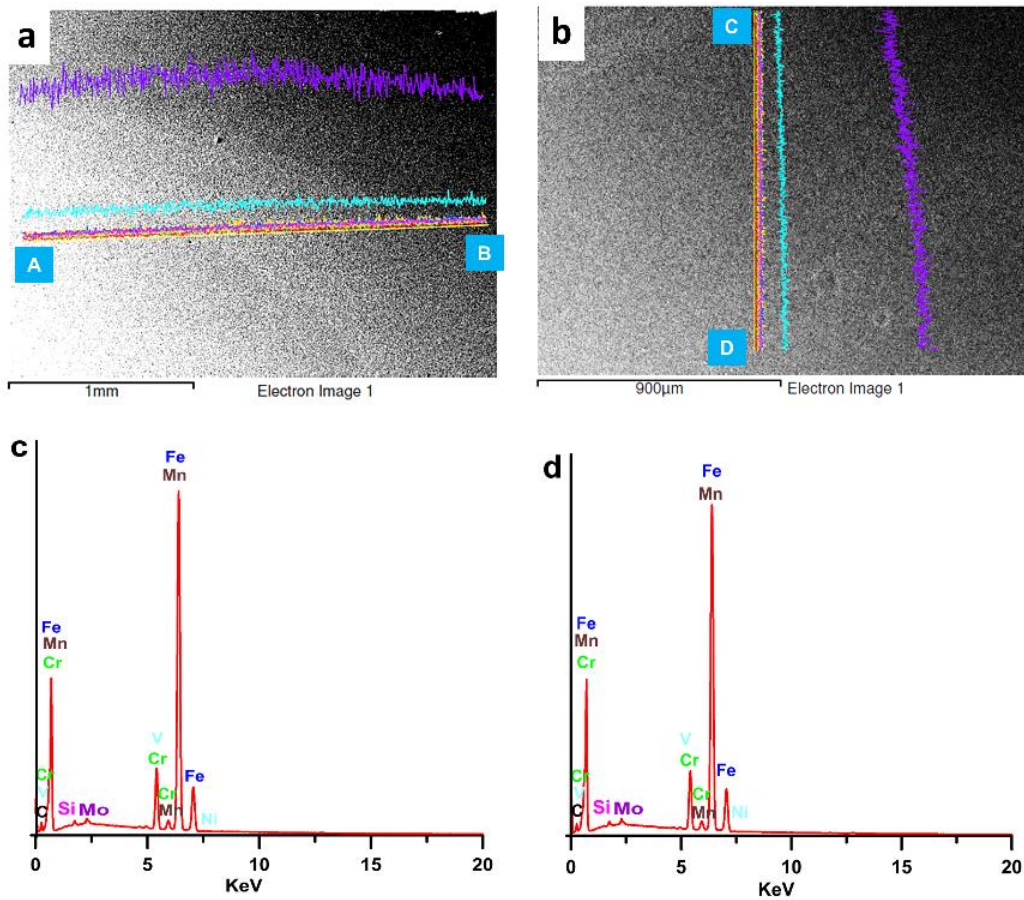


Figure 6.16 Line EDX analysis of sample FSS6 (a), (b) secondary electron images for line EDX analysis and (c), (d) corresponding line plots

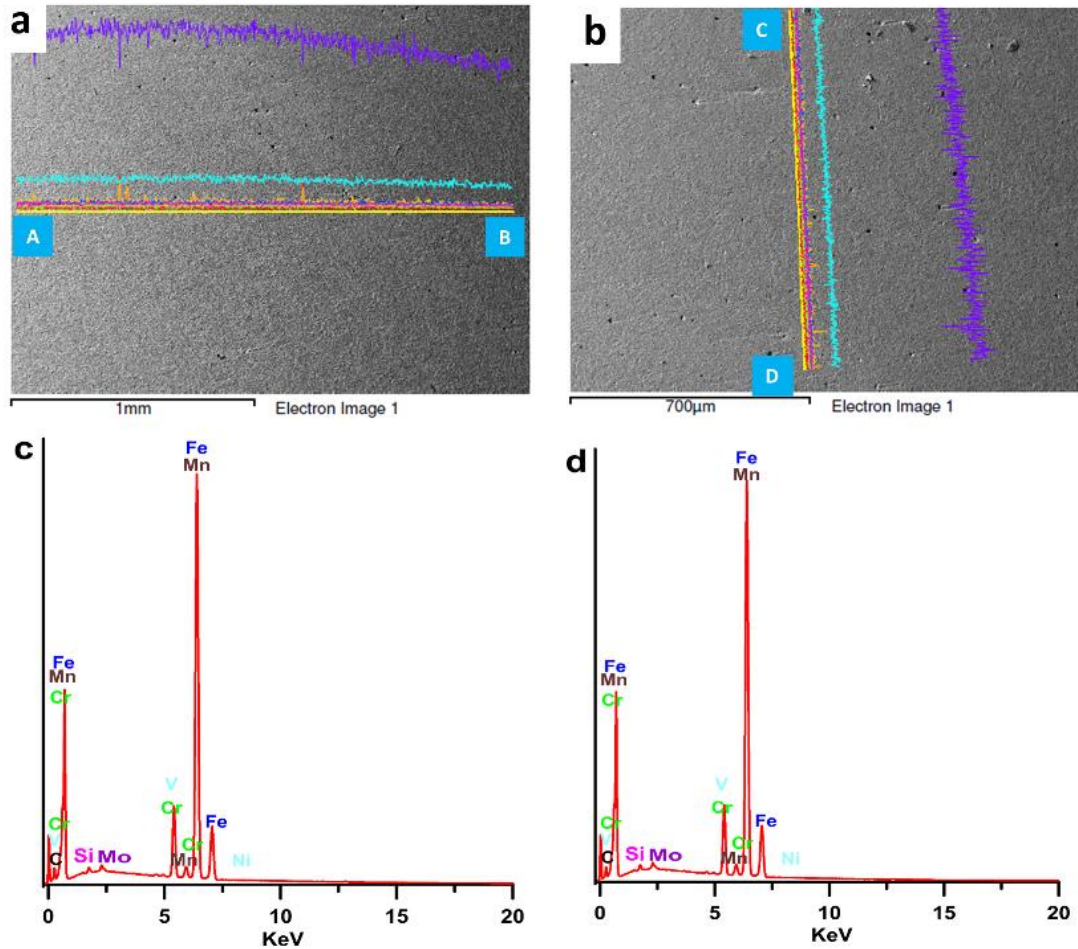


Figure 6.17 Line EDX analysis of sample FSS7 (a), (b) secondary electron images for line EDX analysis and (c), (d) corresponding line plots

Elemental mapping has been done for detailed elemental analysis of the welded samples. Same elements are found in map EDX analysis. The secondary electron image and the corresponding plots in elemental mapping for a welded sample are shown in Figure 6.18. The color codes used for different elements are shown in Figure 6.18. The weight percentage and atomic percentage of existing elements on P91 steel surface after FSW are given in Table 6.3. No elements of the PCBN coated tool has been observed in EDX results. This indicates that tool wear is negligible in case of the present FSW process carried out with different combination of parameters.

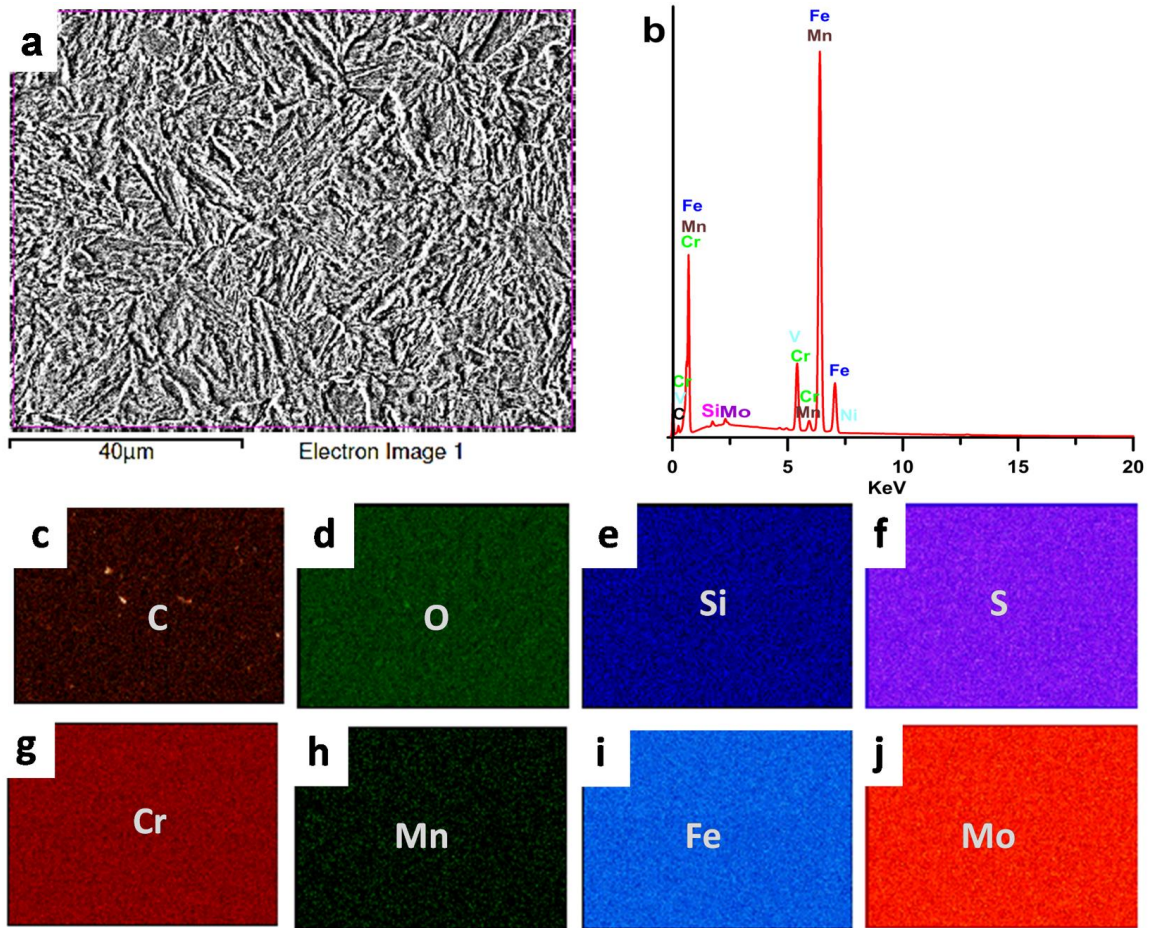


Figure 6.18 Map EDX analysis of welded sample (a) Map for EDX analysis (b) corresponding map plots (c) C (d) O (e) Si (f) S (g) Cr (h) Mn (i) Fe (j) Mo

Table 6.3 Weight and atomic percentage of existing elements found after map EDX analysis of welded sample

Element	Wt percent	Atomic percentage
C	3.99	15.89
O	0.64	1.92
Si	0.33	0.57
S	0.04	0.06
Cr	8.83	8.12
Mn	0.46	0.40
Fe	84.81	72.60
Mo	0.89	0.44

6.4.4 X-ray diffraction analysis of welded samples

X-ray diffraction analysis has been done to identify the several phases present in welded P91 steel samples as shown in Figure 6.19. Similar peaks are observed for all the welded samples as compared to the P91 base metal (refer to Figure 6.19). The diffraction peak involves α -Fe from the crystal faces of (110), (200), (211), (220) and (310) and of γ -Fe from the crystal faces of (111) and (200) within the scanning range of 40-120°. The γ - austenite phase appears between 40-50°, 2 θ angle. In case of welded samples, the γ -Fe peak is found to be more significant than in BM (Zhang et al. 2018b).

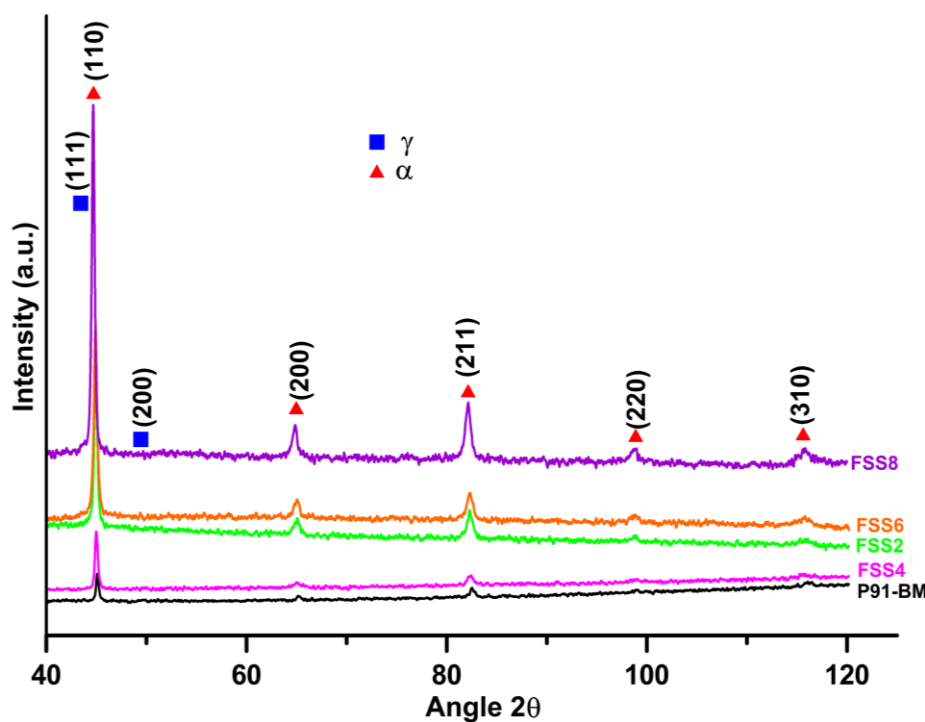


Figure 6.19 X-ray diffraction of welded samples

6.5 Closure

P91 steel pipes have been successfully joined by FSW by varying the process parameters viz. welding speed and spindle speed as presented in this chapter. The optimal combination of parameters led to defect free FSW joint. Hardness of the weld zone shows significant improvement compared to the P91 base metal. In fact, hardness of the SZ is found to be

almost double that of base metal. This is due to higher grain refinement and the precipitation of untempered martensite which resist dislocation motion. Tensile strength of welded samples displayed higher yield and ultimate strengths than the base metal particularly within the optimal range of process parameters. The weld strength is found to be higher for higher weld speed (100mm/min) for P91 pipe welding. Microstructure of SZ and TMAZ is found to depend upon the peak temperature during the welding process. The microstructure of SZ is mainly characterized by the presence of PAGBs. Coarse $M_{23}C_6$ mostly precipitate on PAGB, in internal laths and in sub grain boundary. The MX fine precipitates are observed inside the matrix and along the boundary. The microstructure evolution of the weld zone is found to strongly affect the performance of the weldments. EDX analysis revealed that no element deposited from the FSW tool in the weldments. Optimal combination of process parameters reported in the present study is effective in welding pipes made of P91 steel.

This page is left blank intentionally

Comparative study between AISI-316L and P91 pipe

welding

Outline of the Chapter: 7.1 Introduction, 7.2 Comparison of the weldments based on physical examination, 7.2.1 Surface of welded samples, 7.2.2 Cross section of welded samples, 7.3 Comparison of mechanical properties of weldments, 7.3.1 Hardness behaviour, 7.3.2 Study of tensile properties, 7.4 Comparison of metallurgical characteristics of the weldments, 7.4.1 Optical microscopy of welded samples, 7.4.2 Scanning electron microscopy of welded samples, 7.4.3 Energy dispersive X-ray analysis of welded samples, 7.4.4 X-ray Diffraction analysis of welded samples, 7.5 Closure

7.1 Introduction

In the current chapter, the performances of friction stir weldments for both AISI-316L and P91 pipes are compared and presented. As already mentioned both these pipes are employed in various power plant based applications and efficient joining of them is a vital concern to the industry. FSW has the potential to provide strong, efficient and cost effective joint. FSW has been carried out in force control (FC) mode with 35kN applied load for both the pipes.

7.2 Comparison of the weldments based on physical examination

Physical examination is done based on observation on top surface and cross sections of the welded samples for comparison in case of both the pipes. For welding of AISI-316L pipes, spindle speed was varied from 300 to 450rpm. Whereas, for P91 pipes, spindle speed was varied between 400 to 600rpm. For both the materials, the welding was carried out at welding

speeds of 50 mm/min and 100mm/min. The welding was carried out with 35kN downward force for both the pipes. Parameter combinations used for welding of the pipes in the current study are summarized in Table 7.1.

Table 7.1 FSW welding parameters for AISI-316L and P91 pipes

Sl. no.	Pipes metal	Sample no.	Spindle speed (rpm)	Welding speed (mm/min)	Downward force (kN)
1	AISI-316L	ASS1	300	50	35
2		ASS2	350	50	35
3		ASS3	400	50	35
4		ASS4	450	50	35
5		ASS5	300	100	35
6		ASS6	350	100	35
7		ASS7	400	100	35
8		ASS8	450	100	35
9	P91	FSS1	400	50	35
10		FSS2	450	50	35
11		FSS3	500	50	35
12		FSS4	550	50	35
13		FSS5	450	100	35
14		FSS6	500	100	35
15		FSS7	550	100	35
16		FSS8	600	100	35

7.2.1 Surface of welded samples

Figure 7.1 shows the appearance of the top surface of FSW pipes joint. Top surface of both the welds reveal that no such defects are apparent in the samples prepared under the force-control modes within optimized range of parameters.

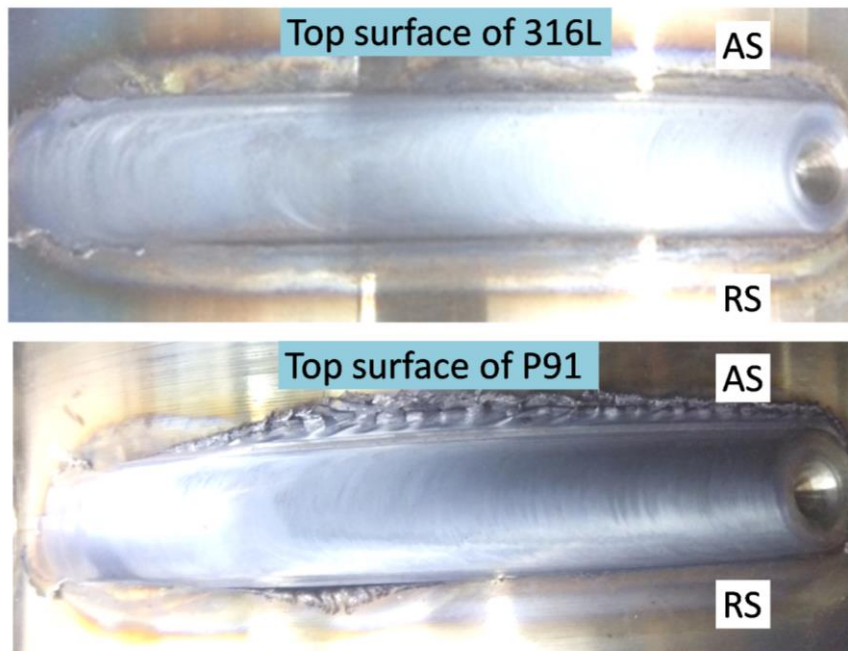


Figure 7.1 Photograph of the top surface of welded joints of AISI-316L and P91 pipes

7.2.2 Cross section of welded samples

Cross sections of both the welds reveal different the typical zones viz. SZ, TMAZ and BM. A defect free basin shape SZ is produced which can be clearly seen in Figure 7.2. This indicates that heat generation was sufficient for the joining process in case of both the pipes. TMAZ of AISI-316L steel sample is very small compared to P91 steel sample which may be due to higher thermal conductivity of P91 steel (Li et al. 2019). The spread of SZ is almost equal to the diameter of tool shoulder near the top surface of the weldments. No distinct heat affected zone (HAZ) is noticeable which is quite expected in steel like materials considering its lower thermal conductivity compared to aluminum (Kumar et al. 2020). Wider TMAZ is observed for P91 welded samples compared to AISI-316L welded samples (refer to Figure 7.2).

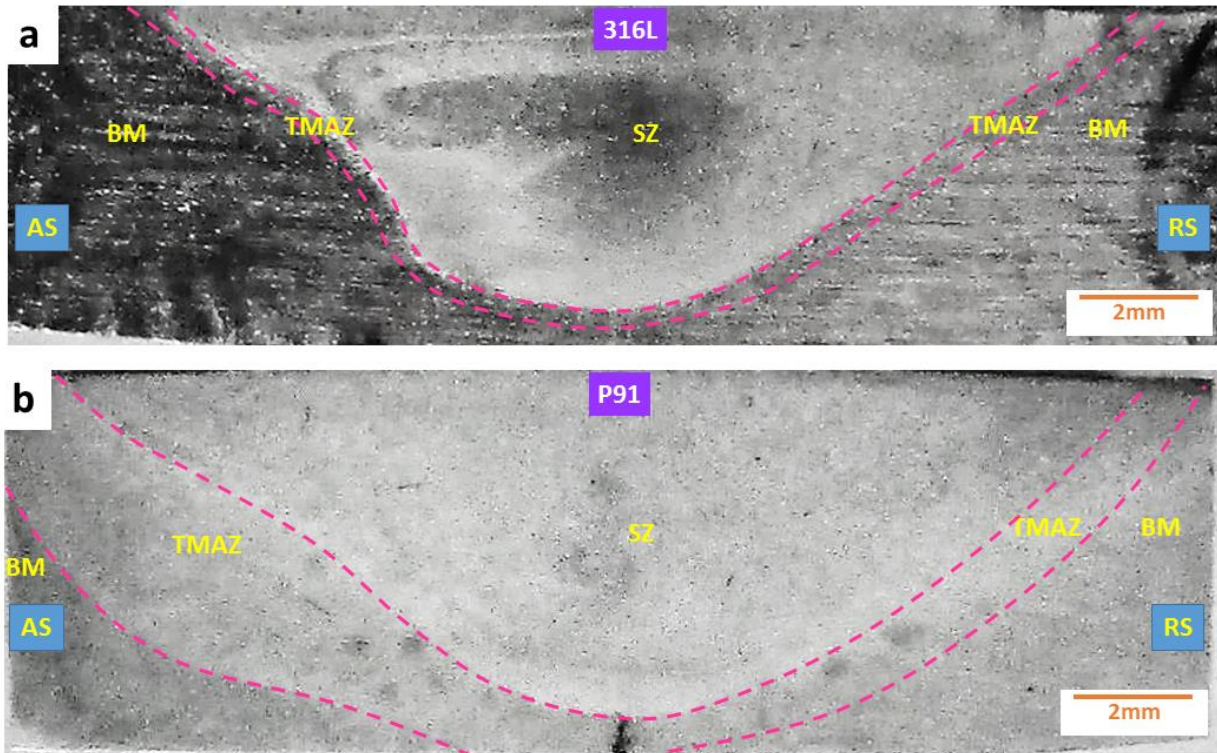


Figure 7.2 Surface appearances along the cross section of the weldments (a) AISI-316L pipe weldment (b) P91 pipe weldment

7.3 Comparison of mechanical properties of weldments

7.3.1 Hardness behaviour

Figure 7.3(a, b) depicts the variation of hardness of the AISI-316L and P91 weldment with distance from the center of SZ. In case of AISI-316L weldment, the maximum hardness value of SZ is obtained as 253.3HV, whereas for P91 pipe weldments the maximum hardness value of SZ is measured as 496.8HV (refer to Figure 7.4). Hardness values of P91 welded samples are significantly higher compared to the AISI-316L welded samples. This is due to higher grain refinement and the precipitation of un-tempered martensite, which resist dislocation motion in case of P91 steel.

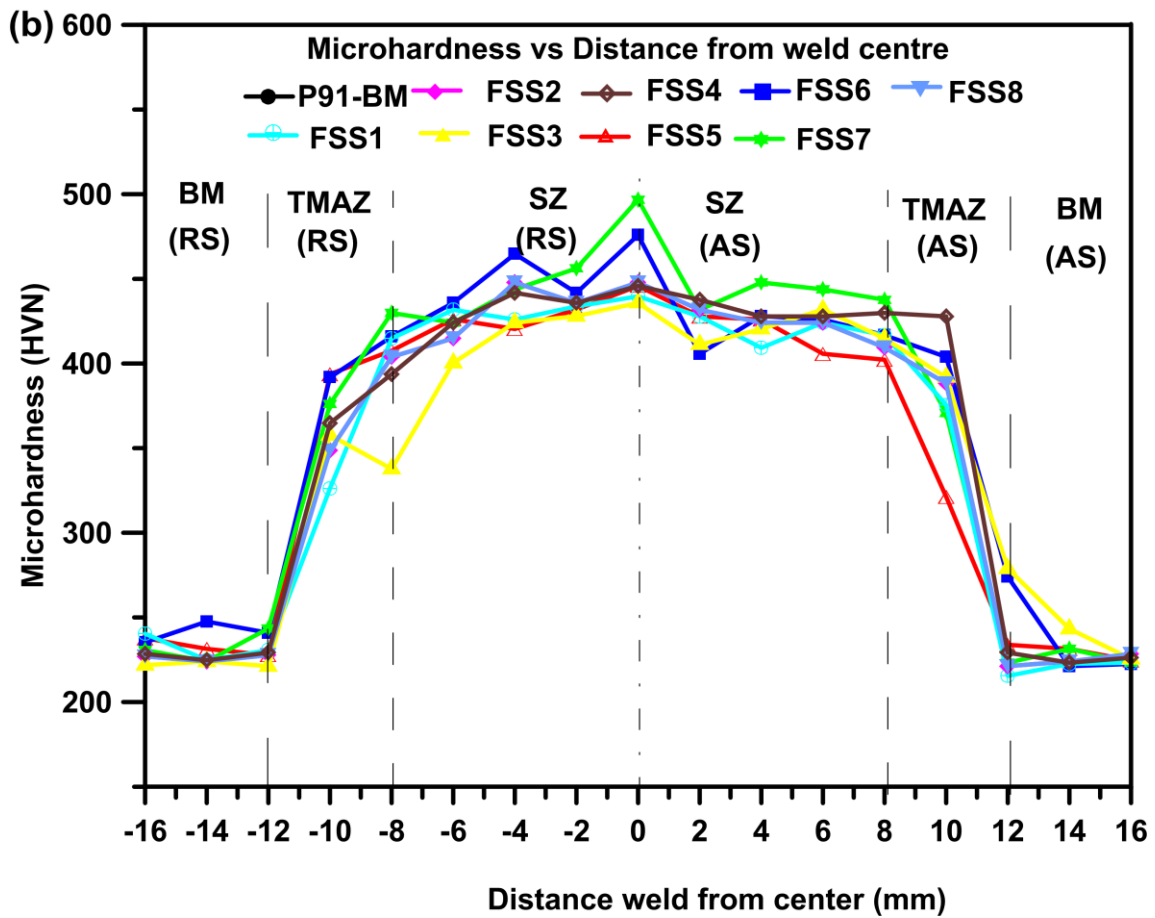
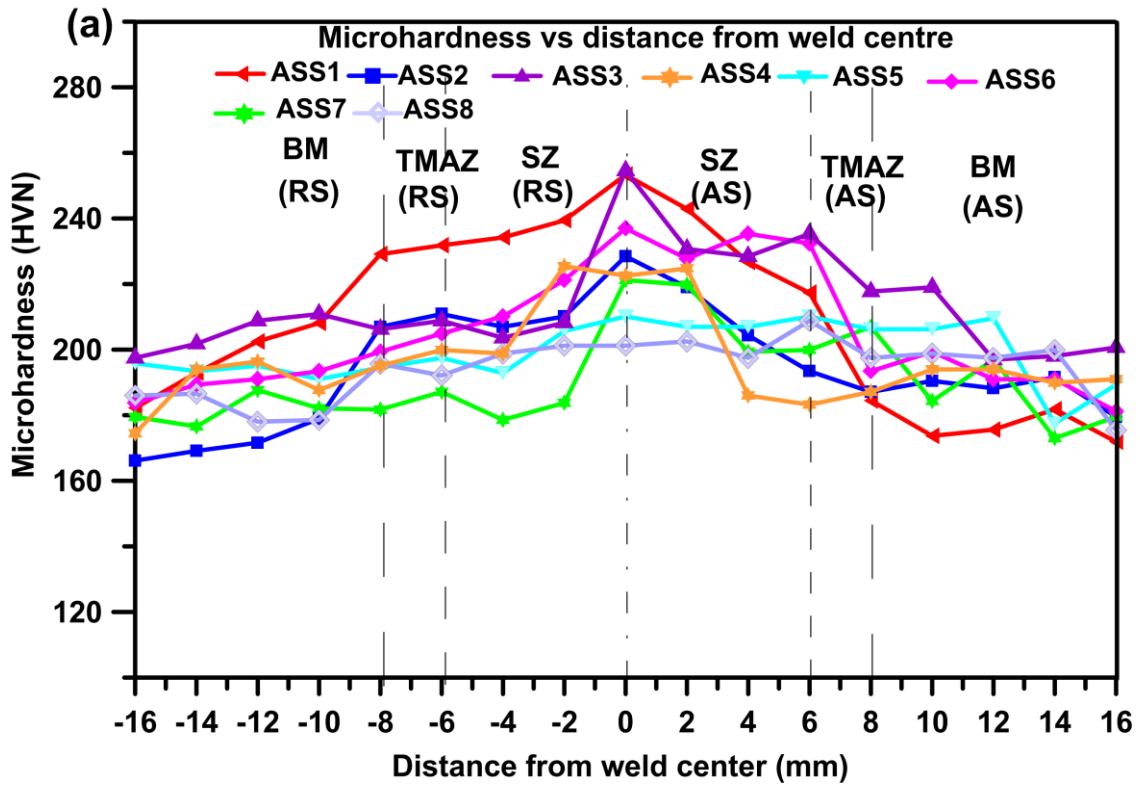


Figure 7.3 Variation of hardness values across the weld cross section (a) AISI-316L welded samples (b) P91 welded samples

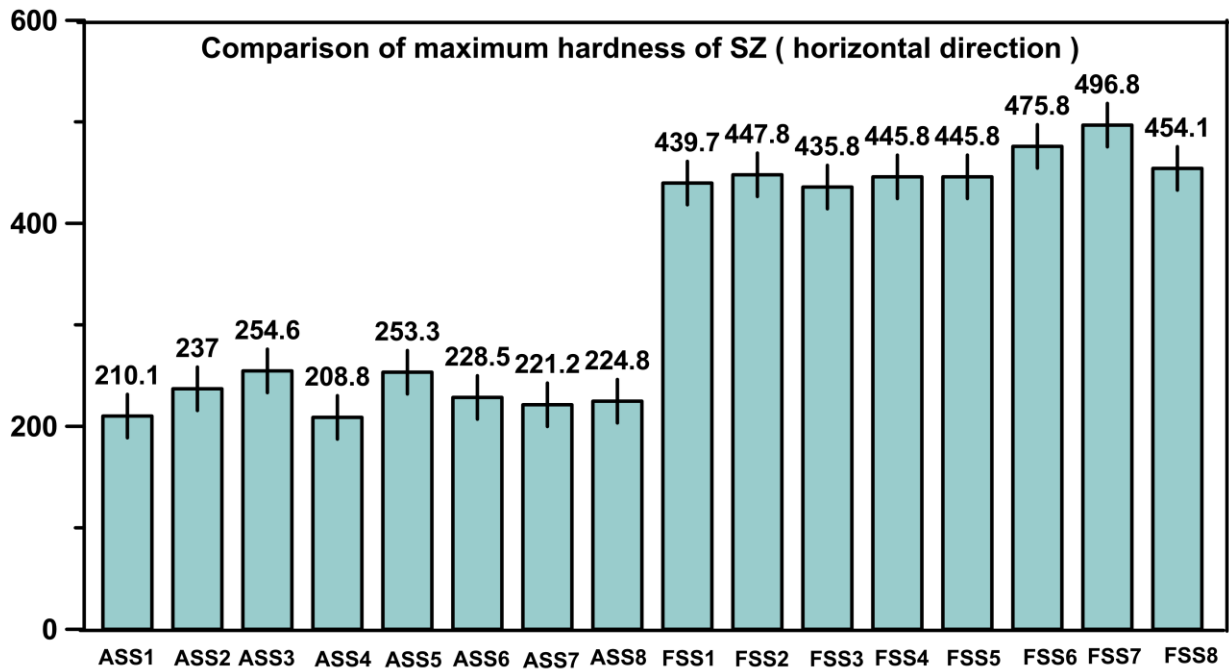


Figure 7.4 Comparison of maximum hardness values for AISI-316L and P91 welded samples in horizontal direction

Figure 7.5 (a,b) depicts the variation of hardness of the weldments with distance from top surface in the SZ. Hardness values have been recorded every 1mm interval from top to bottom surface of the weldments. Peak hardness is obtained at the top surface of SZ in most of the samples. The peak hardness value has been obtained for the sample ASS3 (in case of AISI-316L) (253.2 HV) (refer to Figure7.6). The hardness value is minimum near bottom region of the welds.

The microhardness results of P91 samples i.e. (FSS1-FSS8) are shown in Figure 7.5(b). For the sample FSS7, the maximum hardness value of SZ is obtained as 487.7 HV (top surface) (refer to Figure 7.6) and minimum value is measured as 434 HV (bottom region). The microhardness value decreases almost linearly with the distance from top surface of the weld. All the samples follow the same trend of hardness variation with depth.

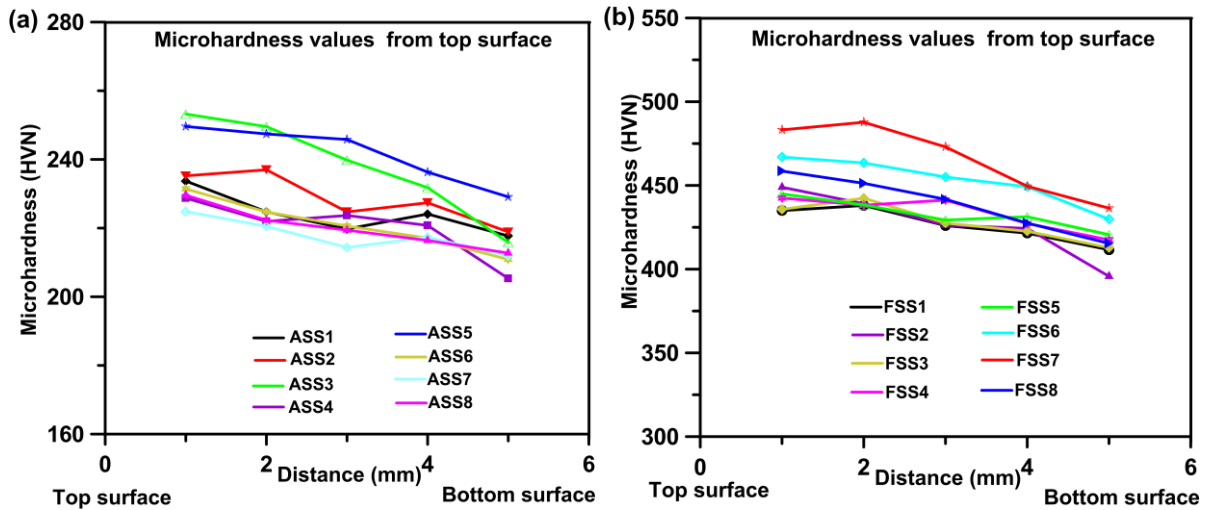


Figure 7.5 Variation of hardness values as a function of distance from top surface (a) AISI-316L welded samples (b) P91 welded samples

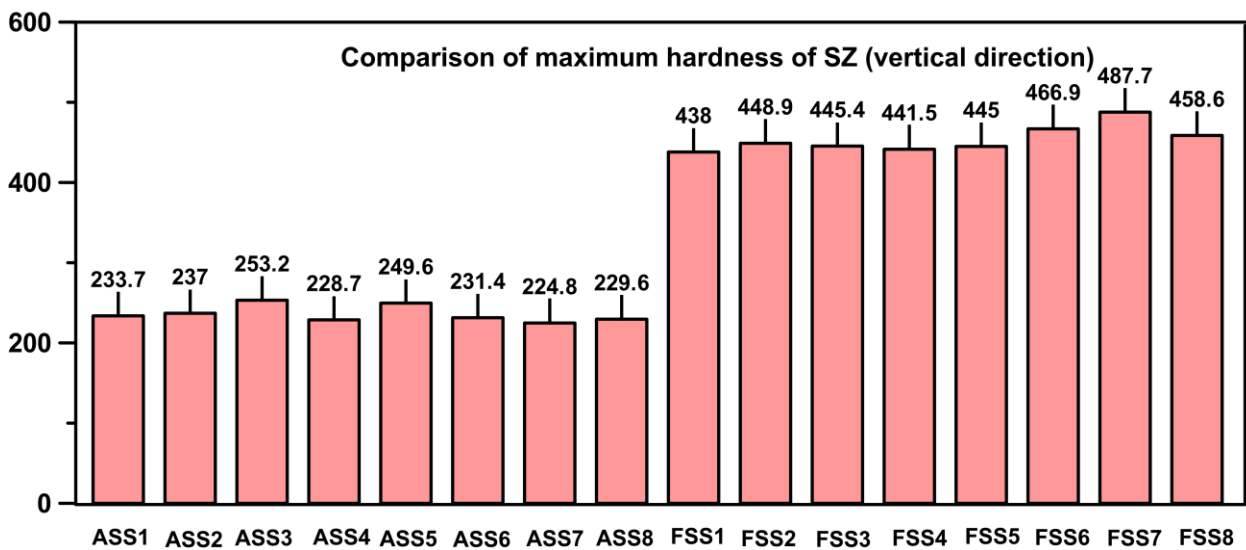


Figure 7.6 Comparison of maximum hardness values for AISI-316L and P91 welded samples in vertical direction

The variation in hardness results with depth in the welded region is because of thermal related phenomena like recovery and grain growth. The generated heat during welding does not readily reach the bottom surface and raise the temperature of that region. Moreover, it is reported that hardness value is lower at regions with slower heat release rate (Heidarian et al. 2022). Now, heat release rate is lesser for the lower regions compared to the top surface of the weldments. Because of these combined effects, less grain refinement

occurs at the bottom surface of the weldments leading to lower hardness in that region. Another reason for higher hardness at top surface of the weldment is due to maximum contact area for stir action between the tool shoulder and workpiece. This results higher grain refinement at top surface of the samples. Presence of sub grain boundary and dislocation density as a result of plastic deformation enhanced the overall hardness values of SZ in both the pipe weldments (Nagaraj et al. 2018).

7.3.2 Study of tensile properties

The results of the tensile test for the AISI-316L and P91 pipe samples are shown in Figure 7.7 and Figure 7.8 respectively. Figure 7.7 indicates that the yield strength of the samples display a good consistency particularly for lower welding speed (50mm/min). At lower welding speed the maximum value of yield stress (YS) is 296.3MPa (sample ASS1) and the maximum value of ultimate tensile stress (UTS) is 576.8MPa (sample ASS3). At this welding speed, maximum joint efficiency shows up for the sample ASS3, this exceeds 100%. The reduction of the grain size means the increase of grain boundary. This resists dislocation motion and imparts enhanced strength in the weldments. The resistance to deformation offered by SZ and TMAZ on the BM has a substantial effect on the joint strength. Due to accumulation of strain in BM, the stress state changes from uni-axial to multi-axial state, which leads to increase of the resistance to further deformation of the joint (Li et al. 2017). Hence, the joint efficiency of weldment has been improved. At higher welding speed (100mm/min), the maximum value of YS is 298.3MPa (sample ASS5) and the maximum value of UTS is 489.9MPa (sample ASS6). The maximum efficiency achieved around is 90% at this welding speed. Hence, it indicates that welding speed 50mm/min is more favourable for joining of AISI-316L steel pipes by FSW. Figure 7.9(a,b) shows the fracture location of AISI-316L welded samples joined at 400rpm-50mm/min (ASS3) and 400rpm-100mm/min (ASS7). For sample welded at 50mm/min, location of failure is observed outside of the

weldment, whereas failure occurs from the welded portion for 100mm/min sample. Hence, it can be stated that at same spindle speed, lower welding speed (50mm/min) yields better joint strength.

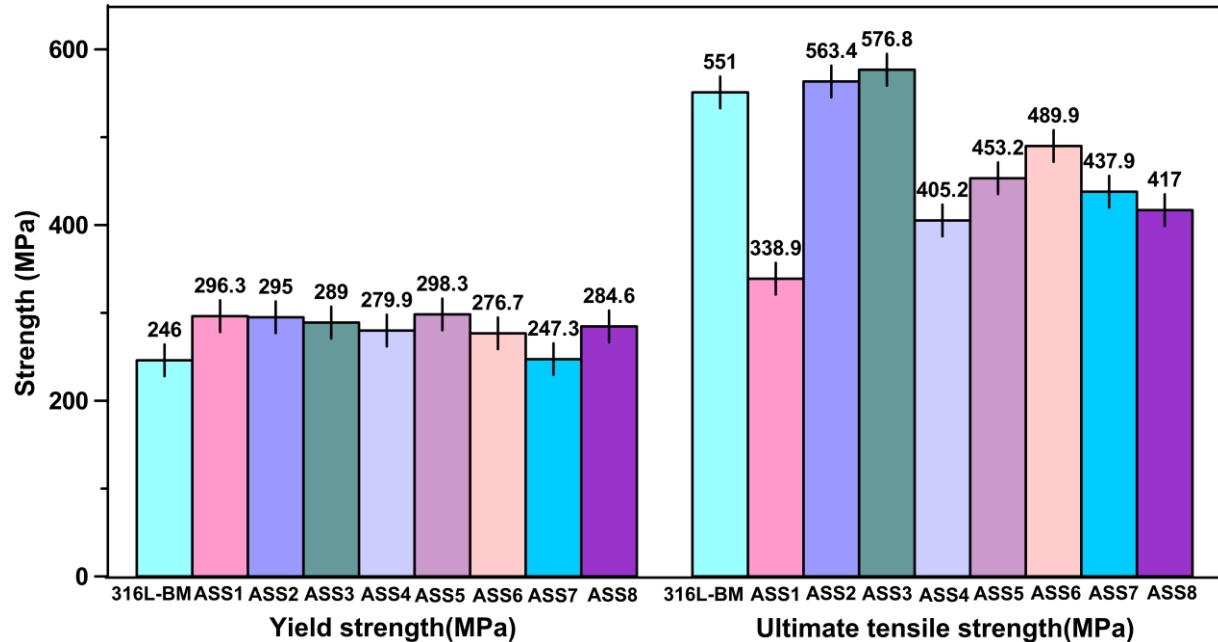


Figure 7.7 Yield and ultimate tensile strength of AISI-316L pipe weldments

For P91 pipe, YS of welded samples is mostly greater than that of BM. The increase of YS is basically due to work hardening and grain refinement. At lower welding speed (50mm/min) the maximum UTS is observed for sample FSS3 (671.5MPa). At higher welding speed (100mm/min), the maximum yield strength achieved is for sample FSS7 (580.1MPa) and the ultimate tensile strength is for sample FSS6 (703.5MPa) (refer to Figure 7.8). Joint efficiency above 100% is achieved for some of the P91 welded samples. Fracture location is observed outside of the weld zone for these samples, which confirms the enhancement of UTS of weldments. Grain refinement of martensite laths and prior austenitic grain boundary (PAGB) enhanced the amount of high angle grain boundary (HAGB), which may cause the strengthening of the P91 steel after FSW (Ronevich et al. 2017). The failure location of tensile tested samples is shown in Figure 7.9 (c, d), which also confirmed that the joint strength is higher as failure occurred outside of SZ.

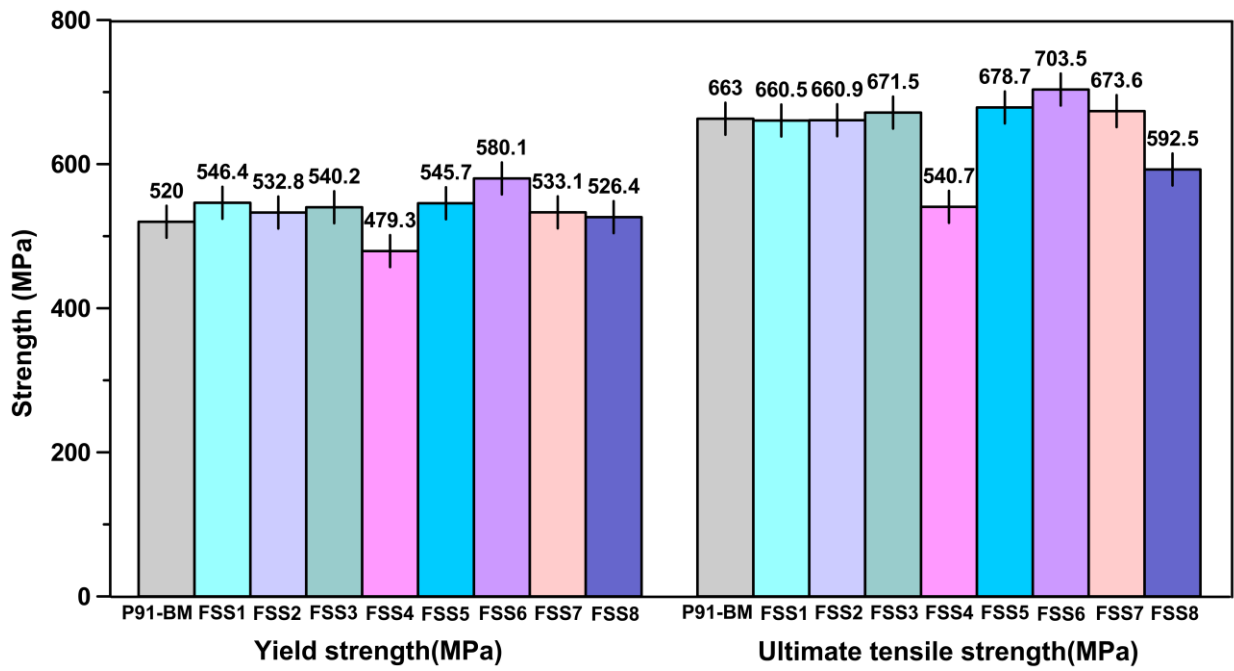


Figure 7.8 Yield and ultimate tensile strength of P91 pipe weldments

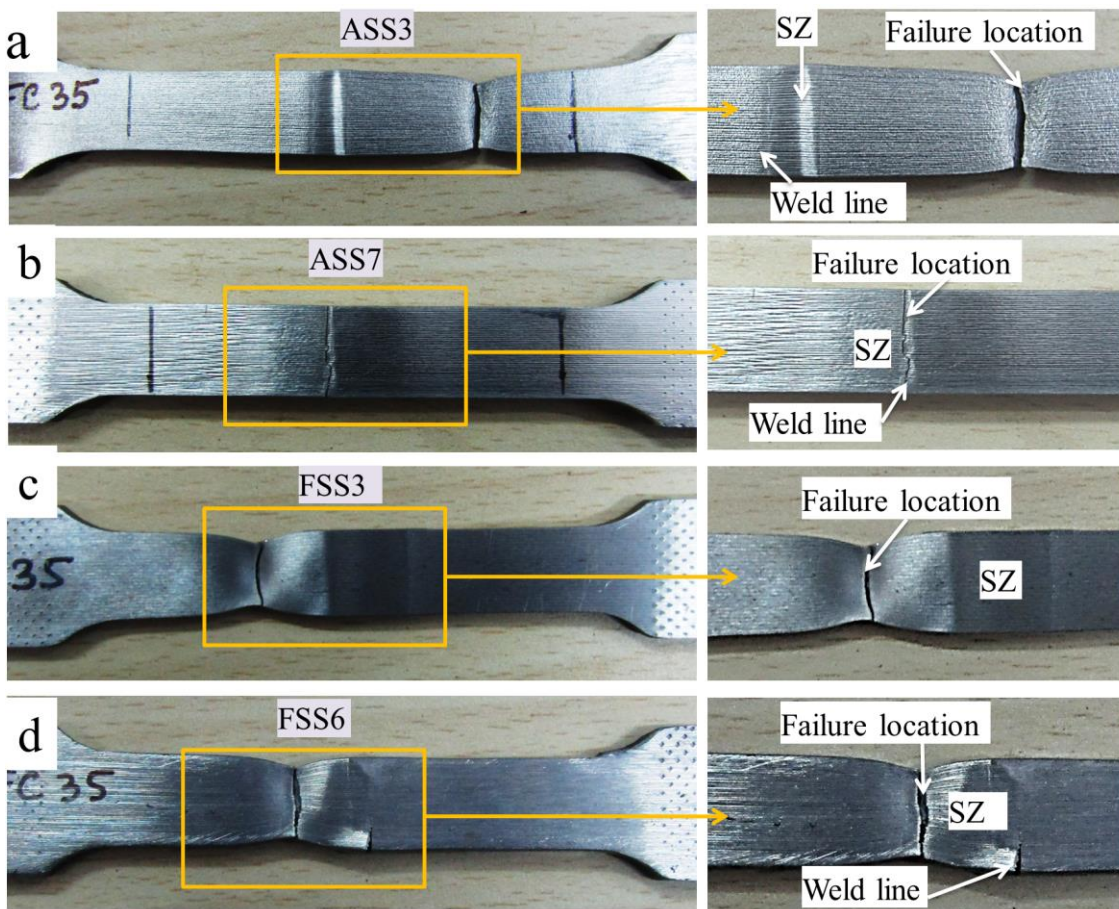


Figure 7.9 Failure location of tensile tested samples (a, b) AISI-316L welded samples and (c, d) P91 welded sample

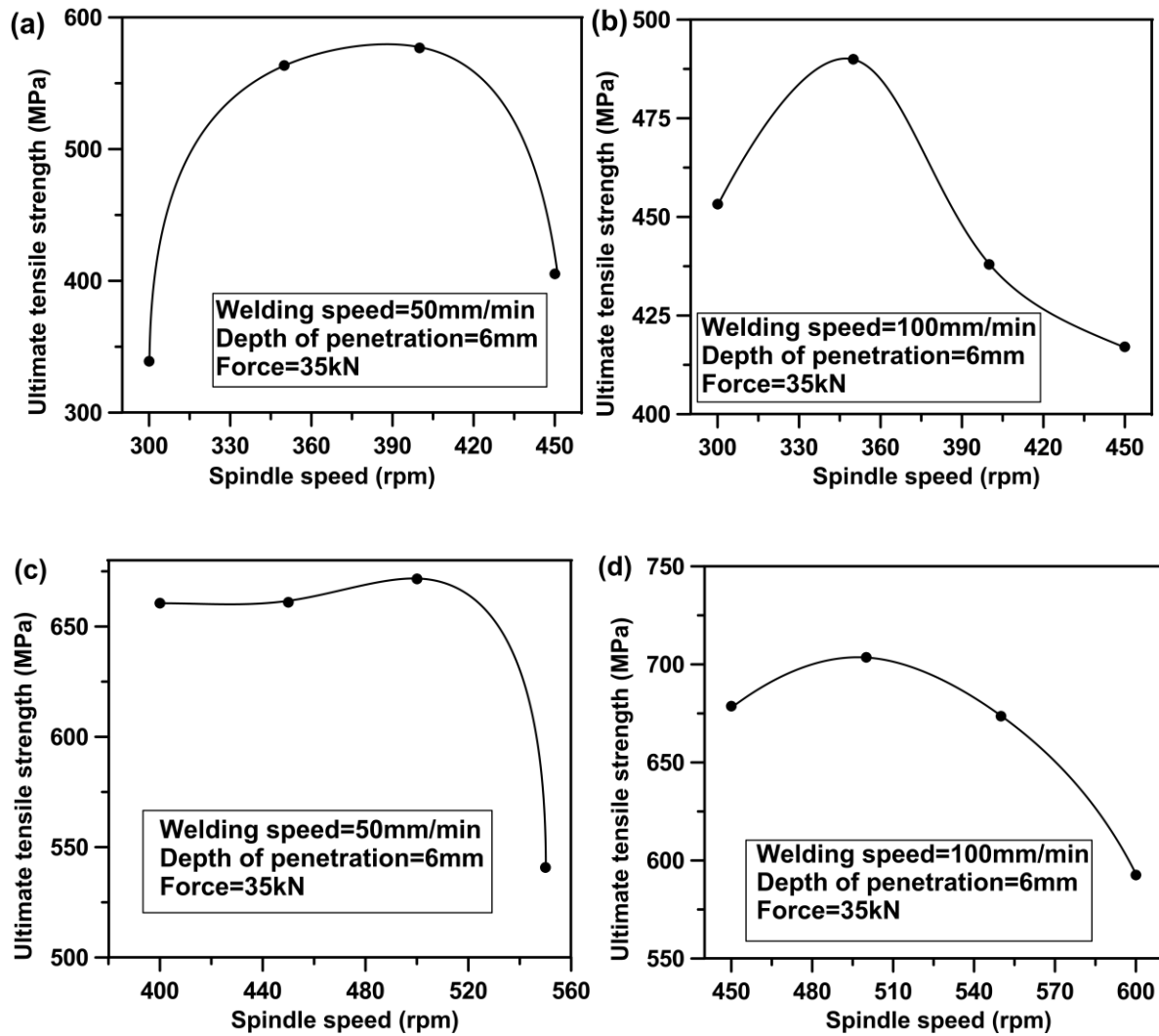


Figure 7.10 Influence of spindle speed on UTS of (a, b) AISI-316L welded samples (c, d) P91 welded samples

Figure 7.10(a, b) show that spindle speed has a significant effect on UTS of AISI-316L welded samples at fixed welding speed. For both the welding speeds, the tensile strength seems to be high at spindle speed of 350rpm. This is because for both the welding speeds, optimal amount of heat generation and strain hardening occurs at this spindle speed. However, the tensile strength suffers a major fall at 400 rpm and 100mm/min combination, which is due to excessive heat generation leading to extra softening of the material. Due to this, under the shoulder pressure material flushing occurs. This results in reduction of the joint strength.

In case of P91 pipes, higher tensile strength is displayed by samples welded at 400-500rpm and 50mm/min welding speed (refer to Figure 7.10(c)). For 100mm/min weld speed the weldments display even higher strength reaching above 700MPa for sample welded at 500rpm (refer to Figure 7.10(d)). However, beyond 500rpm, the tensile strength reduces drastically. Now, with increase of spindle speed, heat generation increases. Beyond certain range of rpm, heat generation is higher than the optimal requirement of the process. This may cause extra softening of the materials and is also not favourable for achieving good tensile strength for weldment as seen in Figure 7.10. The tensile strength is particularly lower for sample welded at 50 mm/min. This shows that at lower welding speed and higher spindle speed, excessive heat generation occurs deteriorating the weld strength.

7.4 Comparison of metallurgical characteristics of the weldments

7.4.1 Optical microscopy of welded samples

The micrograph of TMAZ-SZ and SZ of the AISI-316L samples welded at different spindle speeds but at fixed welding speeds of 50mm/min and 100mm/min are shown in Figure 7.11 and 7.12 respectively. The distinct SZ and TMAZ are easily perceptible for AISI-316L steel samples. Enlarged reoriented grains have been observed in TMAZ, whereas ultrafine equiaxed grains are observed in SZ. Allotropic changes like formation of sub-grain boundary and grain dislocation occur more in SZ (Sabooni et al. 2015). TMAZ is highly influenced by severity of material strain and heat generation. In this region, recovery process is responsible for minor grain refinement. In TMAZ, low peak temperature and low strain rate influence the dynamic recovery of the minor grain refinement. No indication of HAZ is observed as already stated. The nearly equiaxed grains have been observed in SZ for all welded samples (refer to Figure 7.11(b, d, f, h)).

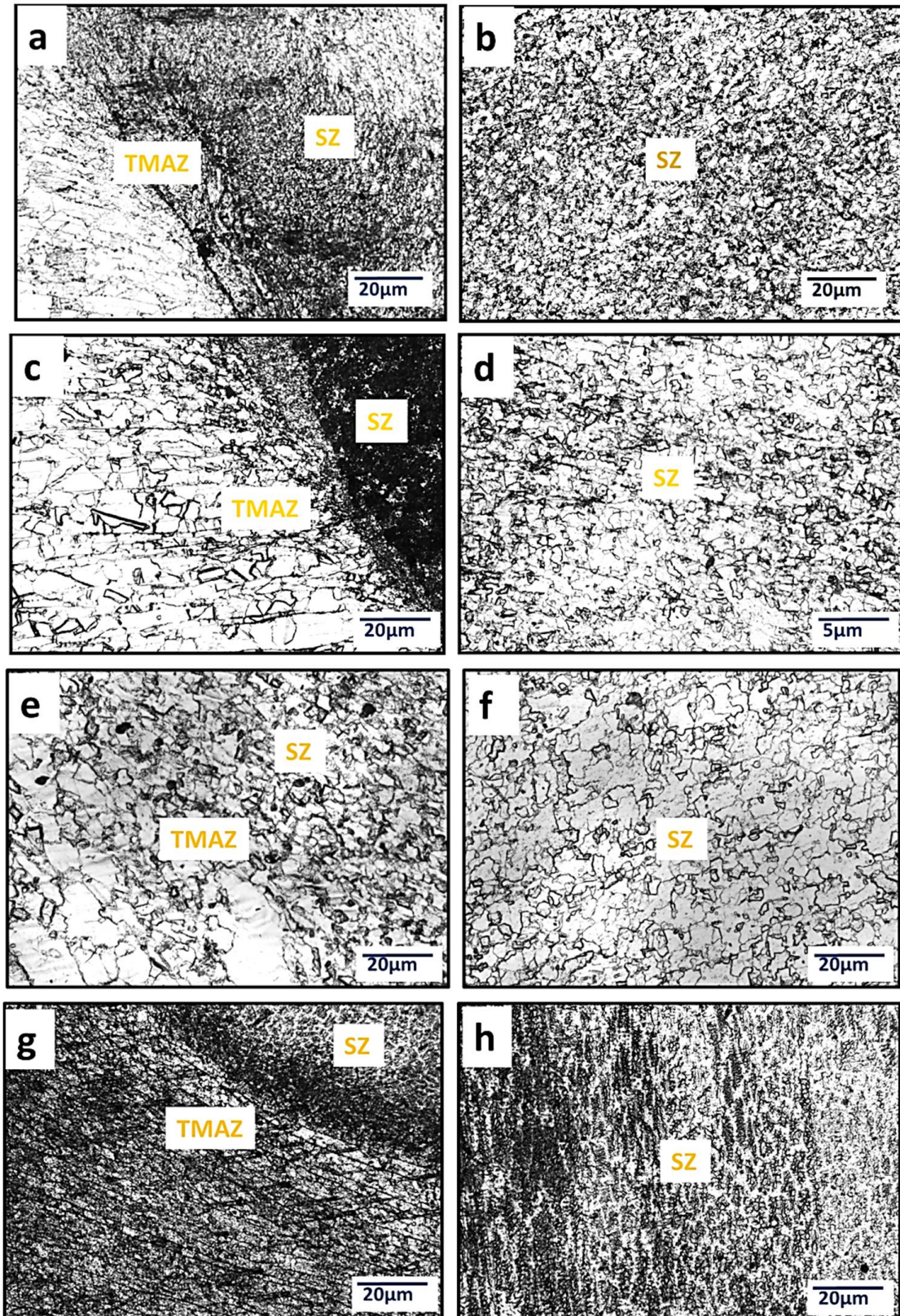


Figure 7.11 Optical micrograph of welded AISI-316L steel pipe samples (at 50mm/min) (a) SZ-TMAZ (ASS1), (b) SZ (ASS1), (c) SZ-TMAZ (ASS2), (d) SZ (ASS2) (e) SZ-TMAZ (ASS3), (f) SZ (ASS3), (g) SZ-TMAZ (ASS4), (h) SZ (ASS4)

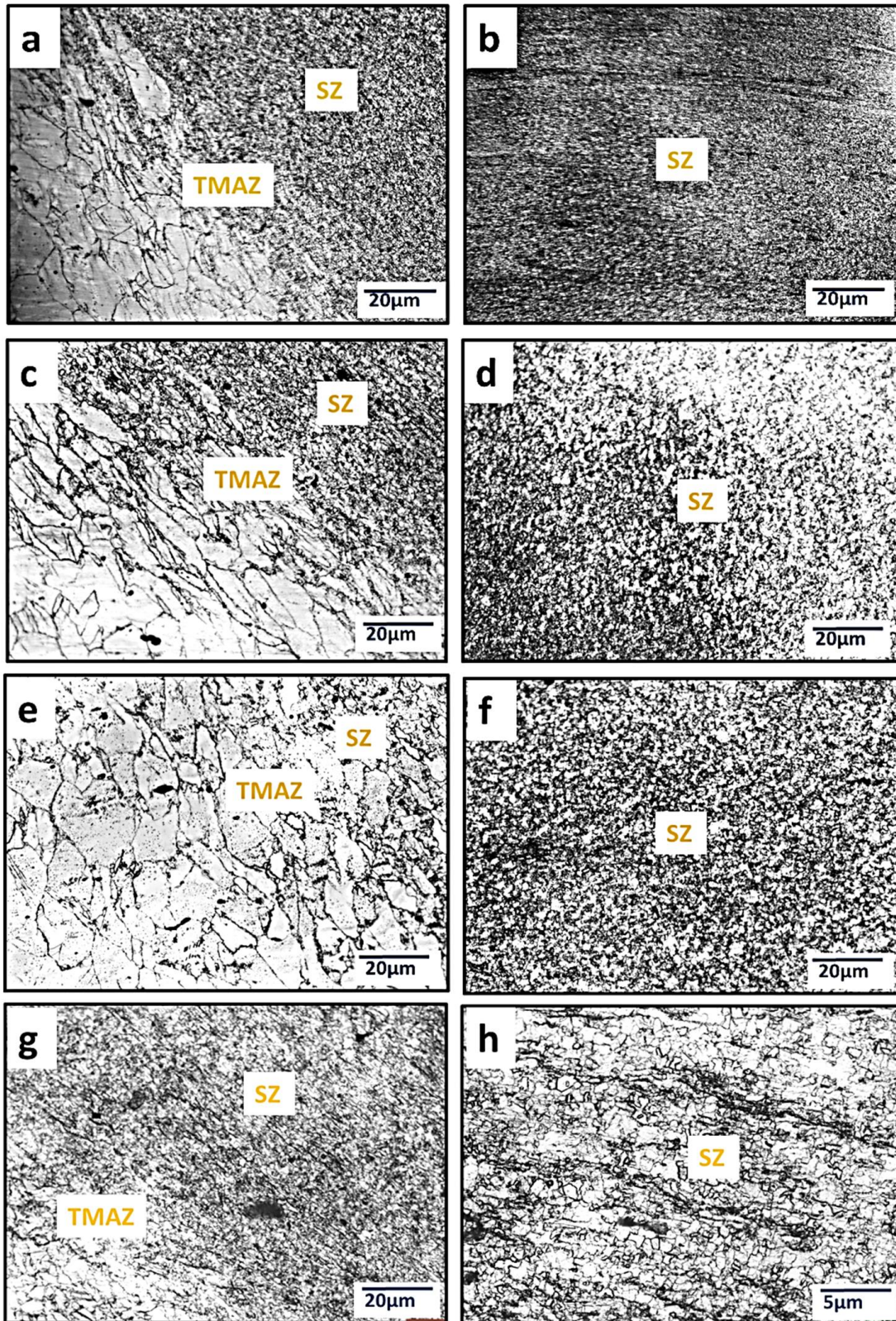


Figure 7.12 Optical micrograph of welded AISI-316L steel pipe samples (at 100mm/min) (a) SZ-TMAZ (ASS5), (b) SZ (ASS5), (c) SZ-TMAZ (ASS6), (d) SZ (ASS6), (e) SZ-TMAZ (ASS7), (f) SZ (ASS7), (g) SZ-TMAZ (ASS8), (h) SZ (ASS8)

In SZ, ultrafine grains are initially formed due to dynamic recrystallization induced by friction heating and severe plastic deformation (Bhattacharyya et al. 2021) followed by static recrystallization. Overall, uniform microstructure is observed in SZ as also reported by others (Mishra and Ma 2005). Apart from heat generation for deformation, recrystallization also plays an effective role on the grain refinement. The microstructure is altered at 450rpm and 50mm/min due to excessive heat generation (refer to Figure 7.11(g, h)), which also reduces the joint strength. Higher welding speed (100mm/min) also exhibits similar ultrafine equiaxed grains in SZ (refer to Figure 7.12(b, d, f, h)), whereas enlarged reoriented grains have been observed in TMAZ Figure 7.12(c).

Optical micrograph of FSW of P91 steel pipes welded at 50mm/min and 100mm/min are displayed in Figure 7.13 and 7.14 respectively. Optical micrograph revealed the SZ-TMAZ interface in Figure 7.13(a, c, e, g) and detailed SZ in Figure 7.13(b, d, f, h). Particularly in Figure 7.14(c), all the three zones i.e. SZ, TMAZ and BM can be clearly distinguished. Microstructure evolution of SZ and TMAZ depends on peak temperature during welding. Low heat generation and improper material flow is unfavourable to produce defect free weld. Heat generation, stir action and the cooling rate affect the evolution of microstructure in SZ, which differs from that of other zones. In the present work, the peak temperature measured at the tip of the tool varies from 750-850°C which is higher than A_{c3} point and lower than A_{c1} point of BM. Zhang et al.(2018a) state that at lower spindle speed peak temperature does not exceed A_{c3} point but at higher spindle speed it may exceed A_{c3} point which is the reason for variation of grain structure in SZ at same welding speed but at different spindle speed. The microstructure of SZ is characterized by the presence of PAGBs, lath boundary and the precipitation of $M_{23}C_6$ particles (where M stand for Fe, Cr, Mn and Mo). Martensite laths and coarsening of PAGBs are observed in TMAZ.

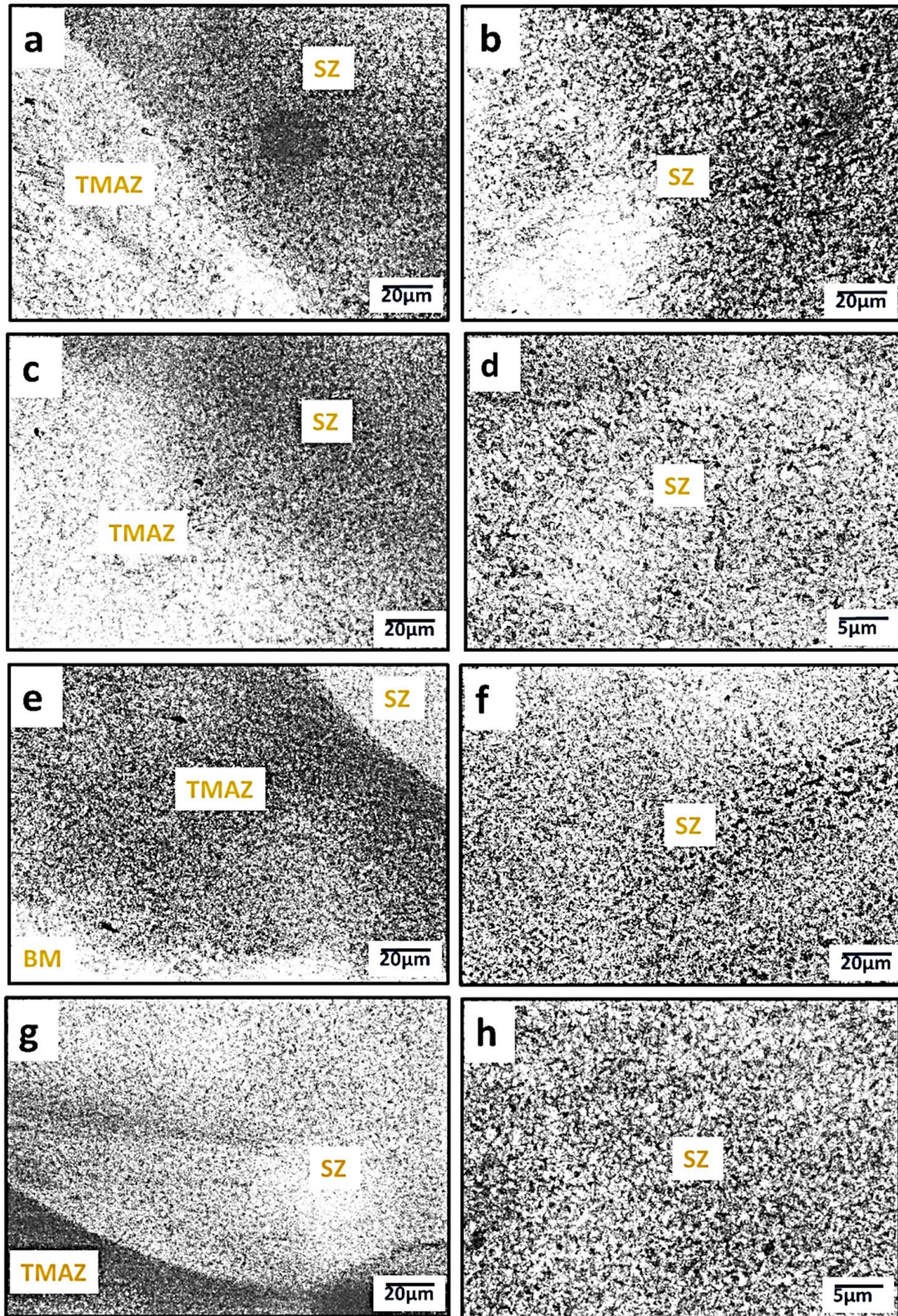


Figure 7.13 Optical micrograph of welded P91 steel pipe samples (at 50mm/min) (a) SZ-TMAZ (FSS1), (b) SZ (FSS1), (c) SZ-TMAZ (FSS2), (d) SZ (FSS2), (e) SZ-TMAZ (FSS3), (f) SZ (FSS3), (g) SZ-TMAZ (FSS4), (h) SZ(FSS4)

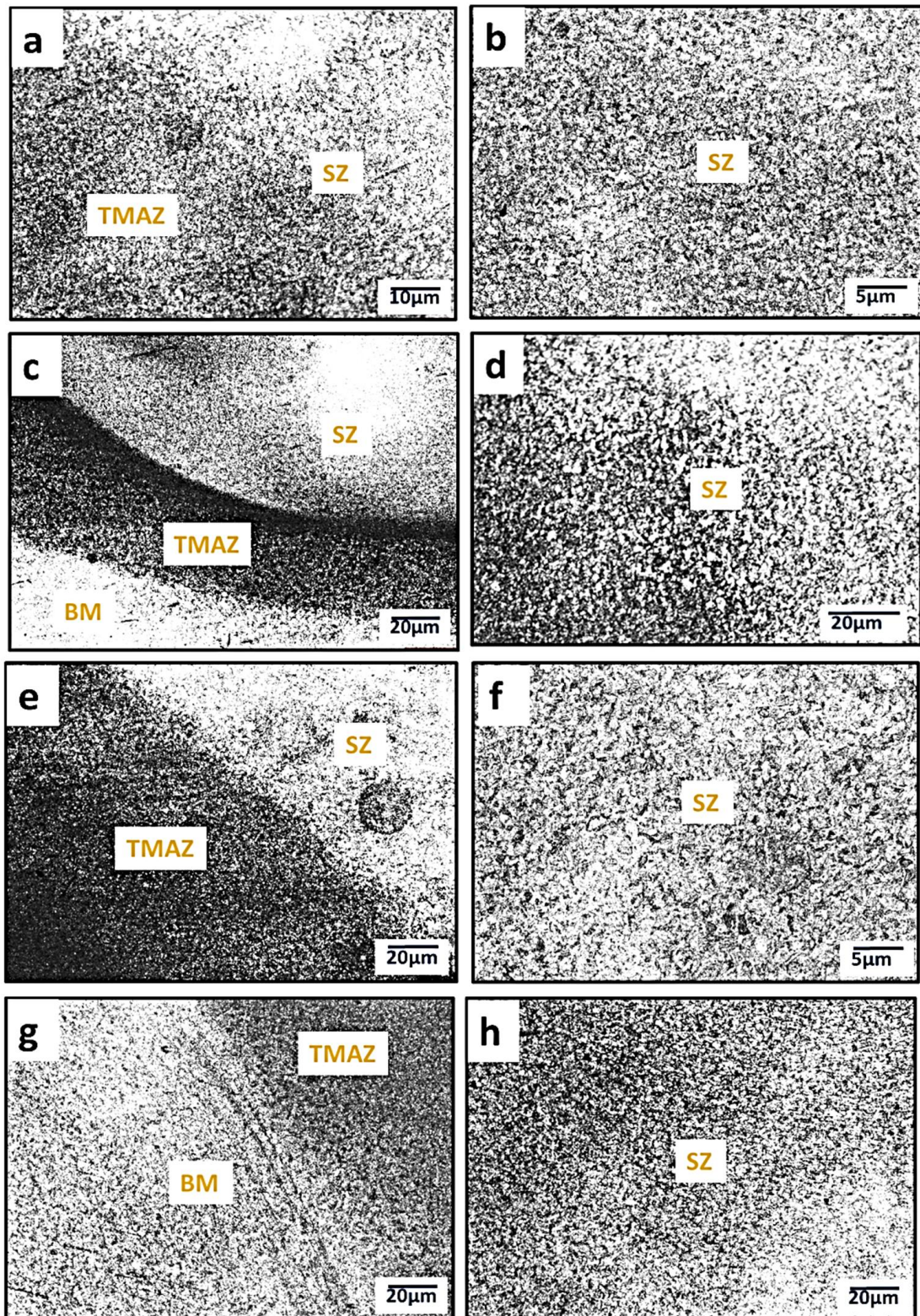


Figure 7.14 Optical micrograph of welded P91 steel pipe sample (at 100mm/min) (a) SZ-TMAZ (FSS5), (b) SZ (FSS5), (c) SZ-TMAZ-BM (FSS6), (d) SZ (FSS6), (e) SZ-TMAZ (FSS7), (f) SZ (FSS7), (g) TMAZ-BM (FSS8), (h) SZ (FSS8)

7.4.2 Scanning electron microscopy of welded samples

FESEM micrographs of AISI-316L and P91 welded samples are presented in Figure 7.15 and Fig.7.16 respectively. In Figure 7.15(a) and Figure 7.15(b), the SZ and TMAZ could be clearly distinguished. Ultrafine equiaxed grains have been observed in SZ whereas elongated grains are observed in TMAZ (refer to Figure 7.15(b)). Figure 7.15(a) and 7.15(b) depict the advancing side and retreating side of the adjacent fragment of TMAZ-SZ of the weldments respectively. In advancing side, grains are more refined compared to retreating side. The average grain size of SZ and TMAZ as measured by ImageJ software are $5.72\mu\text{m}$ and $13.86\mu\text{m}$ respectively. Strain rate and heat generation have opposite effect on grain size of the weldment but they both increase with increase of spindle speed. Strain rate however is the dominant factor compared to heat generation regarding grain refinement of ASS (Li et al. 2017). Higher the strain rate, lower is the grain size. At higher strain rate, less time is available for dislocation movement and grain boundary relocation. This results in dynamic recrystallized (DRX) fine grain microstructures. Owing to the stir action of the tool, the original twin boundaries is broken. The grain of the stir zone undergoes intense refinement due to DRX induced by friction heating and severe plastic deformation (Bhattacharyya et al. 2021). From SEM micrograph of the samples, no void, tunnel, porosity defect was found in the welded samples.

Friction stir welded P91 samples have been examined by SEM and shown in Figure 7.16. Plastic deformation and strain hardening caused by tool rotation, results in finer lath structure. Though, slower cooling rate results in coarse lath structure. Apart from lath martensite and fine MX precipitation, no other precipitations are visible in SZ (refer to Figure 7.16c). Ultrafine grains are observed at SZ, due to stir action provided by tool shoulder as well as the pin. In SZ, original grain undergoes a crystallographic spinning and gets destroyed (Hajian et al. 2015). Average grain size in SZ and TMAZ are $\sim 3.71\mu\text{m}$, $\sim 7.57\mu\text{m}$

respectively, which are relatively smaller compared to AISI-316L (refer to Table 7.2). Grain can slide easily due to precipitation free grain boundary in SZ (Zhang et al. 2018a). In SZ, the coarse carbide precipitation ($M_{23}C_6$) get dissolved partially, whereas fine carbide precipitation ($M_{23}C_6$) dissolve fully. But at the present operating temperature, carbonitride types of precipitation (MX) remain unchanged. In SZ, ferrite and lath martensite appear at lower spindle speed, whereas only lath martensite appeared at higher spindle speed. Prior austenite grain (PAG) is significantly refined in SZ due to dynamic recrystallization (DRX). In TMAZ, martensite laths and both types of precipitation (coarse and fine) are noticed (refer to Figure 7.16(b)). In TMAZ, the temperature cannot reach upto the temperature at which precipitations dissolve.

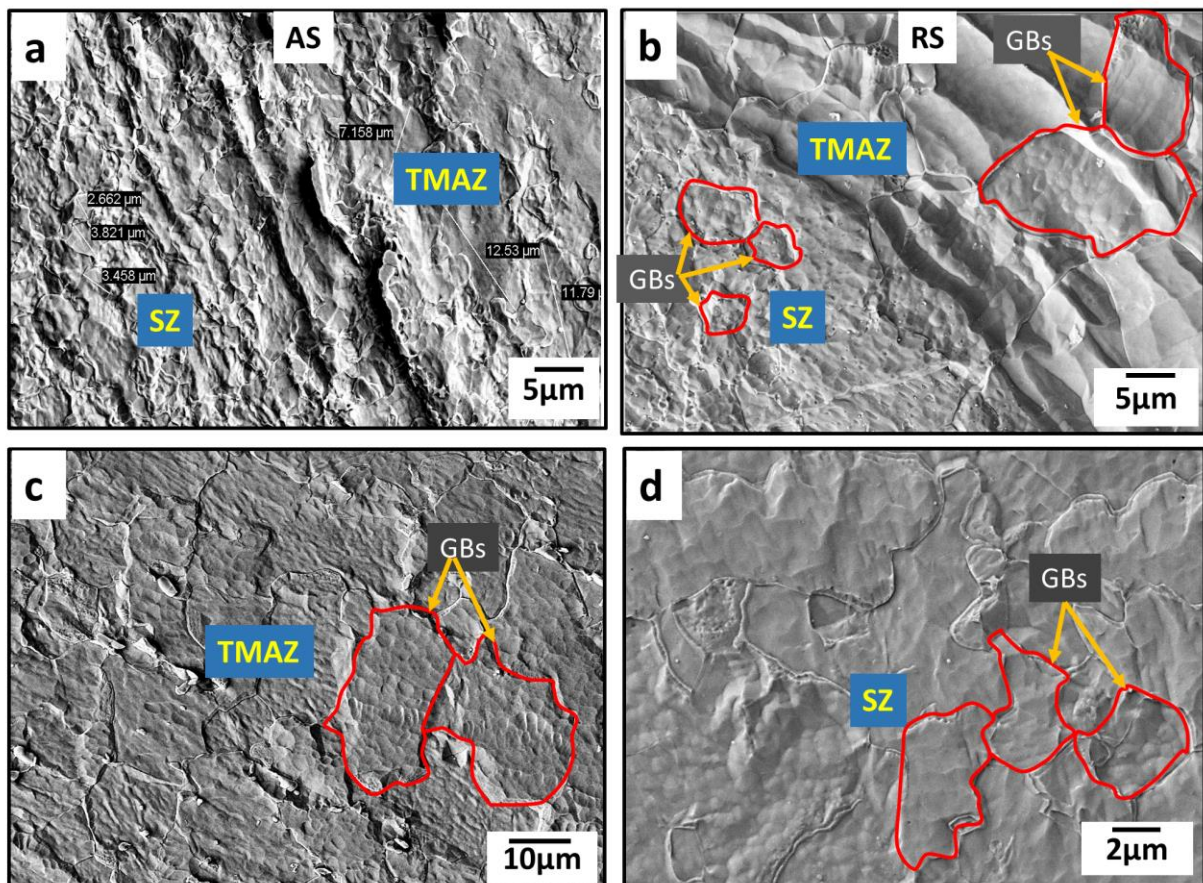


Figure 7.15 SEM micrograph of welded AISI-316L steel pipe sample (a) TMAZ-SZ(AS), (b) TMAZ-SZ(RS), (c) TMAZ, (d) SZ

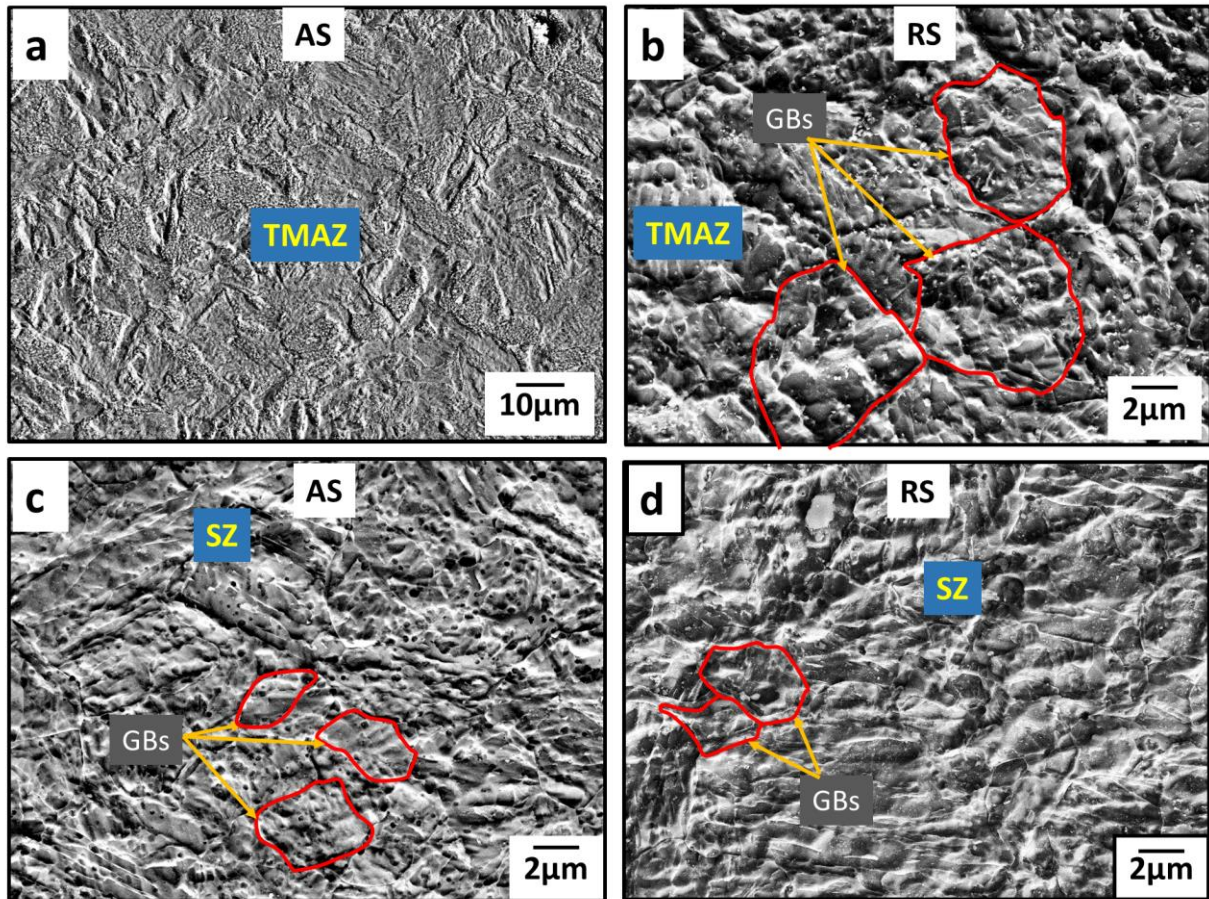


Figure 7.16 SEM micrograph of welded P91 steel pipes sample (a) TMAZ(AS), (b) TMAZ(RS), (c) SZ(AS), (d) SZ(RS)

In case of AISI-316L welded sample, the microstructure is mostly dependent on the strain rate. At higher strain rate, time taken for dislocation movement is less which results in fine grain microstructures in SZ due to DRX mechanism. On the other hand, in P91 FSS steel, the microstructure depends on the peak temperature along with the stain rate. Above 850°C temperature, carbide precipitation is completely dissolved. It has also been noted that in SZ, dynamic recrystallization of austenite (γ), and combined ferritic and austenite ($\alpha+\gamma$) phases occur for P91 sample but in case of AISI-316L, only austenite (γ) phase is present. For both types of steel, grain refinement in SZ is followed by dynamic recrystallization (DRX) and grain growth produced by severe plastic deformation (SDP).

Table 7.2 Average grain size at different zones of welded samples

Sample	Average grain size			
	SZ	TMAZ-AS	TMAZ-RS	BM
AISI-316L welded sample	5.72 μm	13.86 μm	14.76 μm	20.86 μm
P91 welded sample	3.71 μm	7.57 μm	8.51 μm	9.47 μm

7.4.3 Energy dispersive X-ray analysis of welded samples

Line EDX has been performed on the AISI-316L samples (refer to Figure 7.17). The secondary electron images along with the horizontal line A-B and vertical line C-D is presented in Figure 7.17 (a) and 7.17(c) respectively. The corresponding elemental line plots are presented in Figure 7.17(b) and 7.17(d) respectively. Line EDX was performed covering all the three zones i.e. SZ, TMAZ, and BM. Different elements present in the welded samples as found by line EDX are shown in Figure 7.18. EDX spectrum reveals the presence of elements (in weight percentage) as: Fe-63.76, C-3.93, Cr-16.52, Ni-8.56, Mn-1.54, Mo-1.92, Si-0.46, O-3.26, S-0.05. No other elements like CBN, W, Re was found in EDX analysis, which confirmed that negligible tool wear during welding.

EDX results for P91 welded samples are presented in Figure 7.19 and Figure 7.20. The scheme of the test is similar to AISI-316L samples. The elements identified are Fe-84.81, C-3.99, Cr-8.83, Mn-0.46, Mo-0.89, Si-0.33, O-0.64, S-0.04. From the EDX analysis of both the pipe weldments, no traces of the tool element are found. This implies that tool wear is almost negligible and the tool life is quite good. In fact, the same PCBN tool has been employed to carry out multiple pipes welding without visible changes in its geometry. Therefore, PCBN coated W-Re tool can be employed to successfully weld AISI-316L and P91 steel pipes.

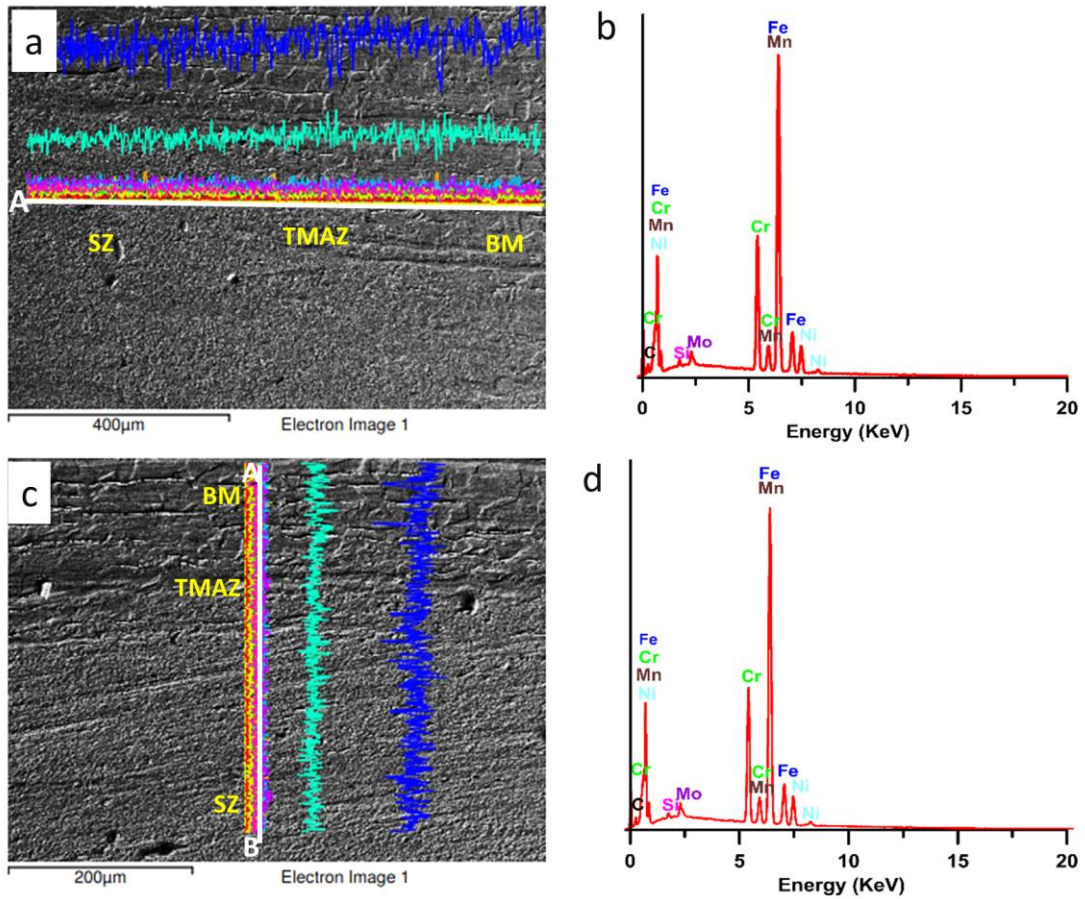


Figure 7.17 Line EDX analysis of welded AISI-316L steel pipes samples (a, b) secondary electron images and the corresponding plot of horizontal line (c, d) secondary electron images and the corresponding plot of vertical line

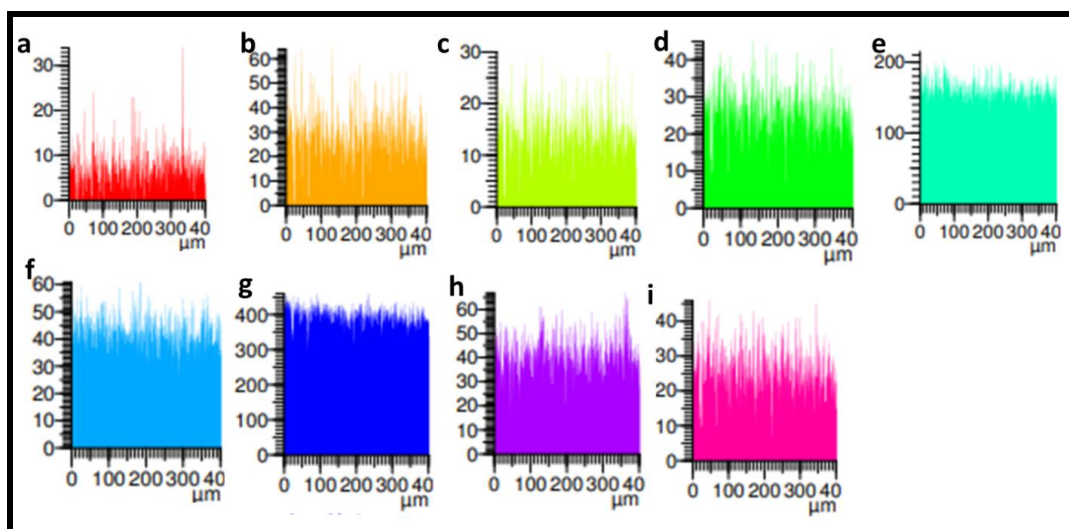


Figure 7.18 The colour code used to indicate different element during line EDX for AISI-316L welded sample (a) C (b) O (c) Si (d) Cr (e) Mn (f) Fe (g) Ni (h) Mo (i) S

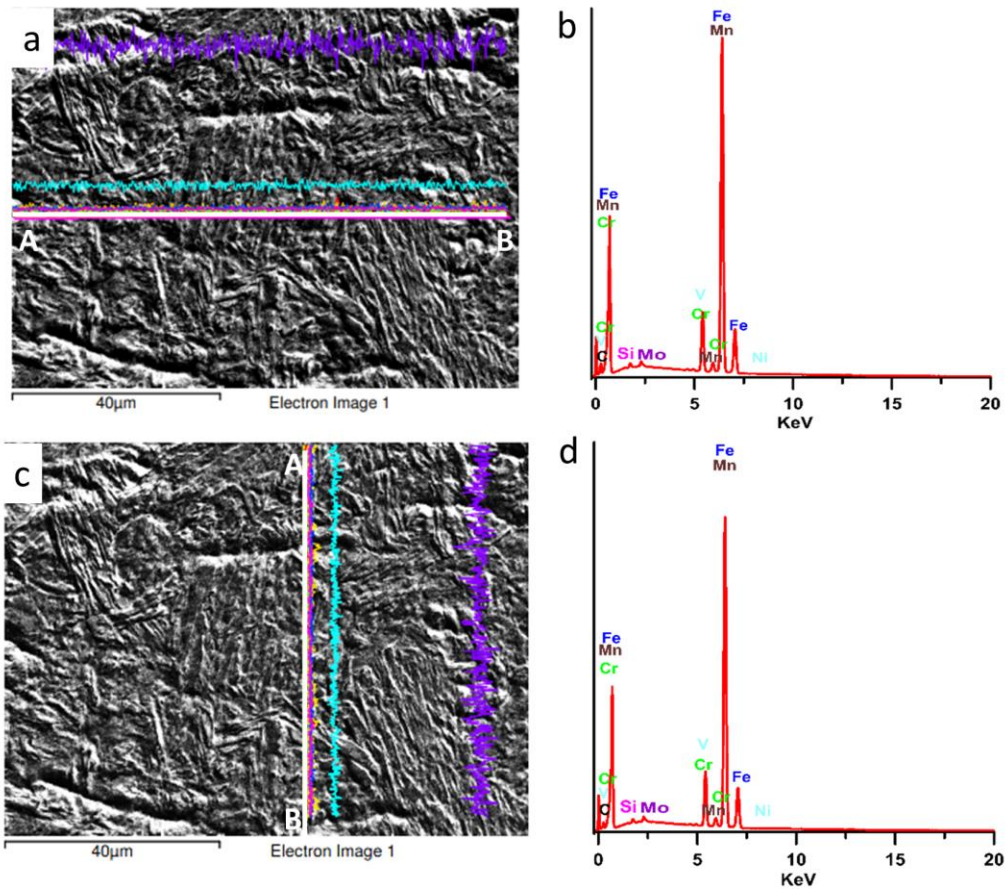


Figure 7.19 EDX analysis of welded P91 steel pipes samples (a, b) secondary electron images and the corresponding plot of horizontal line (c, d) secondary electron images and the corresponding plot of vertical line

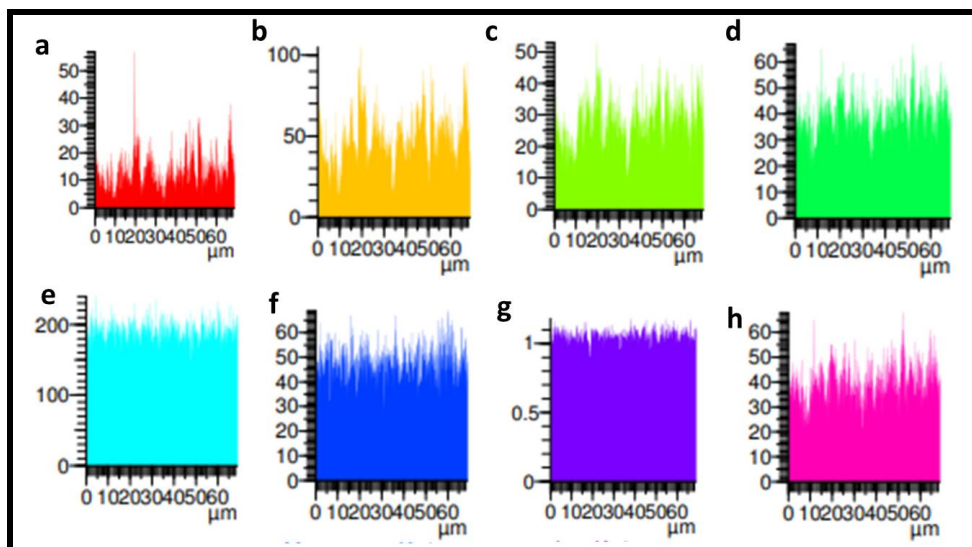


Figure 7.20 The colour code used to indicate different element during line EDX for P91 welded the sample (a) C (b) O (c) Si (d) S (e) Cr (f) Mn (g) Fe (h) Mo

7.4.4 X-ray Diffraction analysis of welded samples

The X-ray diffraction patterns of AISI-316L welded samples have been taken with angle varying from 0 to 95° as shown in Figure 7.21(a). Austenitic phase is observed in all the welded samples. No peak of sigma phase and delta ferrite are observed. According to Scherrer equation, grain size is inversely proportional to the peak intensity (Cullity 1978). Higher intensity peak is observed in welded samples which confirm the occurrence of grain refinement in the welded zone. Peaks are observed at same angle for all the welded samples. The diffraction peak involves γ -Fe from the crystal faces of (111), (200), (220), (311) within the scanning range of 0-95°.

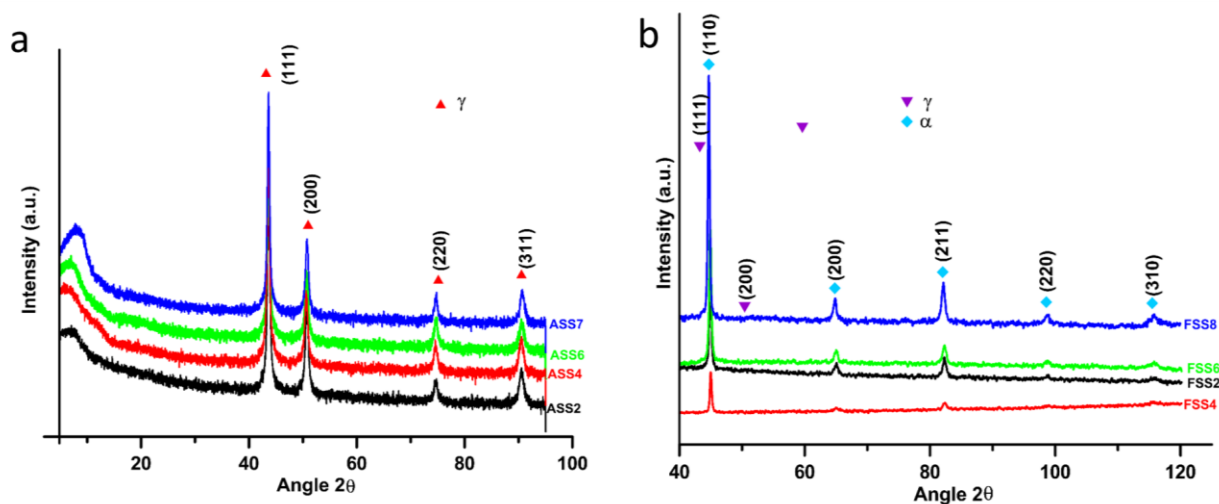


Figure 7.21 X-ray diffraction of AISI-316L and P91 welded sample

X-ray diffraction analysis has also been done in P91 steel welded samples. The diffraction peak involves α -Fe and γ -Fe within the scanning range of 40-120°. The highest peak intensity and the corresponding phase obtained from XRD analysis is shown in Figure 7.21(b). Peaks are observed at same angle for all the welded samples. The diffraction peaks contain γ -Fe from the crystal faces of (111) and (200) and α -Fe from the crystal faces of (110), (200), (211), (220) and (310). The peak of γ -Fe phase is more significant in SZ of welded sample. In the range of 40-50°, austenite diffraction peak appears (Zhang et al.

2018b) which indicates that there might be some of the retained austenite present in the samples.

Overall, from the above study, the common and individual aspects of both AISI-316L and P91 pipe welding can be compiled. Both the pipes experience grain refinement after welding, which results in significant increase in strength and hardness of the respective weldments. Hardness values are found to decrease from top to bottom for both the weldments due to lesser heating and lower heat release rate from the bottom regions (of the weldments). Both the weldments display increasing tensile strength up to a certain value of spindle speed which indicates the requirement of an optimal amount of heat generation for higher joint efficiency. AISI-316L pipe weldments exhibit specific microstructural features viz. distinct elongated grains in TMAZ and precipitation free grain boundary. Whereas, P91 weldments shows features viz. lath structure (due to slow cooling rate), PAG (due to DRX), and carbide precipitation along the grain boundary. Due to the additional precipitation hardening phenomenon, P91 pipe weldments display a higher hardness compared to AISI-316L weldments.

7.5 Closure

In this chapter, comparative study between AISI-316L and P91 pipe welding done at optimal range of parameters combinations is presented. Though, few welds showed defects which are as a result of either higher heat generation (in case of higher spindle speed or lower welding speed) or due to inadequate heat generation (in case of lower spindle speed or higher welding speed) during the process. Hence, the optimal range of weld parameters can be easily identified in case of both the steel pipes.

This page is left blank intentionally

Conclusions and future scope

Outline of the chapter: *8.1 Introduction, 8.2 Conclusions from the physical examination of weldments, 8.3 Conclusions from hardness behaviour of weldments, 8.4 Conclusions from the study of tensile properties, 8.5 Conclusions from the microstructure study, 8.6 Conclusions from energy dispersive X-ray analysis of welded samples, 8.7 Conclusions from X-ray diffraction analysis of the welded samples, 8.8 Future scope of work*

8.1 Introduction

The advancements in materials and friction stir welding research, present significant opportunities in meeting the upcoming needs of many industries viz. power generation plants, aerospace industries and automotive industries. FSW, as a solid-state joining process, does not suffer from the limitations of high temperature fusion welding. Pipe welding is frequently required in various applications involving transfer of fluids. In fact, the weldment becomes a point of higher concern when the temperature of the flowing fluid is high, especially in power plant based applications. FSW is a potential answer to this issue considering its high efficiency. Now due to the inherent challenges associated with circular pipe welding viz. weld configuration, curved geometry at the weld zone, ovality issues, etc. The suitability of FSW for pipe welding has not been thoroughly assessed. The present study attempts to fill this gap by conducting a systematic study on FSW of AISI-316L and P91 steel pipes, evaluating the mechanical performance of the weldments and correlating those results with their microstructural evolution.

8.2 Conclusions from the physical examination of weldments

Physical examination is done based on observation of the top surface and cross section of welded samples and the conclusions from the same are listed in the following text.

In case of the position-control mode experiments of AISI-316L steel pipes, a groove defect is observed along the advancing side of the welding zone. On the advancing side, a tunnel defect is also observed between the stir zone and the thermo-mechanically affected zone interface. These are expected to be more prominent at lower spindle speeds due to insufficient heat generation leading to a lack of material flow. Lower heat generation could be attributed to inadequate frictional heating in absence of maintaining the requisite vertical force under the position control mode. When welding in force control mode, no such groove defect or tunnel defect is noticed. However, when welding at lower and higher spindle speeds (at 300rpm-100mm/min and 450rpm-100mm/min for AISI-316L weldments) some defective welds were observed, which may be due to insufficient or excessive heat generation. The images of the top surface of welded P91 pipes exhibited defect free weld at almost all the parameter combinations. A few of them show a root defect at the bottom of the weld zone which is an indication of incomplete weld penetration. Each welded sample exhibits three typical regions i.e. SZ, TMAZ and BM. From cross section of the sample, it is clearly noticeable that the width of the SZ is higher at the top surface and gradually decreases at the bottom of the sample, which is comparable with a basin shape.

8.3 Conclusions from hardness behaviour of weldments

The hardness values of the welded samples at different zones viz. SZ, TMAZ and BM, are measured across the transverse direction. In SZ, the hardness values are relatively greater than in TMAZ because of grain refinement. As already discussed, smaller grain produces additional grain boundaries that constrain the dislocation movement, resulting in greater

hardness values in SZ. Hardness values at the SZ and TMAZ exhibit similar trends in all the samples (samples welded at position control mode and force control mode), getting lowered thereafter as one moves towards the BM region. The average hardness of AISI-316L base metal is measured as 179HV. For the sample joined at 100 mm/min welding speed with 325 rpm spindle speed, the peak hardness values in SZ and the advancing side of TMAZ were measured as 258.2 HV and 229.7 HV, respectively. The grain refinement in the SZ, presence of sub-grain boundaries and grain dislocation in the TMAZ are responsible for the improved display of strength and hardness of the weldments.

The hardness of the weld zone also shows significant improvement compared to the P91 base metal. In fact, the hardness of the SZ is nearly double that of the base metal. This is due to higher grain refinement and the precipitation of untempered martensite, which resists dislocation motion.

The weld zone displayed higher hardness compared to the base metal for both steels. In the case of AISI-316L, this increase in hardness was mainly due to grain refinement in the SZ. However, in the case of P91, this increase was significantly higher and was contributed by grain refinement, martensite formation, as well as the presence of higher dislocation density in the SZ.

8.4 Conclusions from the study of tensile properties

For FSW of AISI-316L steel, higher welding speeds (100mm/min) revealed comparatively lesser tensile strength than lower welding speed (50mm/min). At higher welding speeds, heat generation is not sufficient to attain proper joining up to the inner surface of the pipes. This may be the reason for early tensile failure of the samples. Over a range of parameter combinations, heat generation is more than the process requirement, which is also not favourable for achieving good weld strength and also the weld becomes brittle in nature. The

optimal combinations of parameters yield the highest tensile strength and joint efficiency over 100%. The maximum joint efficiency has been achieved as 104.68% for the samples welded at 400rpm and 50mm/min combination at force control mode for AISI-316L pipes.

The optimal combination of parameters also led to a defect free FSW joint in the case of P91 steel pipes. The tensile strength of welded samples displayed higher yield and ultimate strengths than the base metal, particularly within the optimal range of process parameters. The weld strength is found to be higher for higher weld speeds (100mm/min) for this grade of steel. The weld strength, however, is found to be maximum at a spindle speed of 500 rpm, after which it degenerates. This is due to higher heat generation (above 500rpm spindle speed) than the optimal quantity of heat required for the process.

Both the steels displayed more than 100% joint efficiency at the optimal combination of parameters. AISI-316L steel exhibited better joint strength at low welding speeds, whereas P91 steel showed the same at higher welding speeds. This indicated the requirement for higher heat generation in the case of P91 steel.

8.5 Conclusions from the microstructure study

The distinct SZ and TMAZ are easily perceptible in AISI-316L welded samples. The welded zone shows grain refinement, with the finest grains distributed over the SZ. This higher grain refinement in the SZ is a result of DRX, which is induced by severe heating and plastic deformation. The grain refinement in the SZ, presence of sub-grain boundaries and grain dislocation in the TMAZ are responsible for the improved display of strength and hardness of the weldments. Enlarged, reoriented grains are observed in TMAZ.

In case of P91 samples, microstructure of SZ and TMAZ is found to depend upon the peak temperature during the welding process. The microstructure of SZ is mainly characterized by the presence of PAGBs, lath boundary and the precipitation of $M_{23}C_6$

particles. Coarse $M_{23}C_6$ mostly precipitates on PAGB, in internal laths and at sub grain boundary. The MX fine precipitates are observed inside the matrix and along the grain boundary. The microstructure evolution of the welded zone is found to have a significant impact on performance of the weldments.

In the case of AISI-316L welded sample, the microstructure is mostly dependent on the strain rate. At a higher strain rate, the time taken for dislocation movement is less, which results in fine grain microstructures in SZ due to the DRX mechanism. On the other hand, in P91 steel, the microstructure depends on the peak temperature along with the strain rate.

8.6 Conclusions from energy dispersive X-ray analysis of welded samples

To analyse the elemental compositions of the welded zone, line EDX and EDX mapping have been performed on both the steel samples. To capture the elements present in each zone of the weldments, line EDX was drawn through all three zones (SZ, TMAZ, and BM). EDX spectrum reveals the presence of mainly C, Cr, Ni, Mn, Mo, Si, O, S inside the AISI-316L welded samples. No other elements like CBN, W, Re were found in the EDX analysis, which confirmed that negligible tool wear occurred during welding of AISI-316L steel by PCBN tool. Similar EDX analysis have also been done on the P91 welded samples. The elements identified are Cr, Mn, Mo, V, Nb, Fe, C which are expected for P91 material. No extra elements are observed in the line EDX. This indicates negligible tool wear and also the suitability of PCBN coated tools for welding the present pipe materials.

8.7 Conclusions from X-ray diffraction analysis of the welded samples

Diffraction studies revealed the presence of higher intensity peaks of austenitic phase in case of AISI-316L welded samples. No peaks of sigma phase and delta ferrite are observed. Higher intensity peak is observed in welded samples, which confirms the occurrence of grain refinement in the welded zone. In the case of P91 samples, an austenite diffraction peak

appears, which indicates that there might be some of the retained austenite present in the samples. Peaks are observed at the same angle for all the welded samples. The diffraction peaks comprise of γ -Fe and α -Fe.

8.8 Future scope of work

In the present work, the effect of FSW parameters i.e. spindle speed (rpm) and welding speed (mm/min), on the weld characteristics of industrial grade steel pipes viz. AISI-316L and P91 has been studied. The mechanical properties viz. hardness and tensile strength, of the pipe weldments are studied in detail. Microstructural evaluation of the pipe welds is carried out through an optical microscope, a field emission scanning electron microscope, energy dispersive X-ray analysis and X-ray diffraction analysis. The optimal parameter combination produced high quality joints in both AISI-316L and P91 steel pipes. At the optimal combination of parameters, defect free pipe welds with above 100% joint efficiency are obtained.

In the present study, FSW has been carried out mostly under FC mode with different combinations of welding speed and spindle speed at 35kN applied load as obtained from position control mode. Further investigation can be done by varying the downward force value.

The present work is mainly experimental in nature. Optimization tool can be employed for better optimization of the welding process by considering other weld parameters.

Future studies could make use of other characterization techniques viz. transmission electron microscopy (TEM), electron backscatter diffraction (EBSD), etc., for a better understanding of the microstructure of the welded joints.

Mechanical properties like fatigue and creep tests are not carried out in the present work. Future investigations might be carried out to evaluate the fatigue and creep properties of the pipe weldments as part of an all-round assessment of the pipe weldments

This page is left blank intentionally

References

- AHL SARMADI, M., SHAMANIAN, M., EDRIS, H., BEHJAT, A., MOHTADI-BONAB, M. & SZPUNAR, J. (2021), Effect of Friction Stir Welding on the Microstructure and Mechanical Properties of Super Duplex Stainless Steel. *Metallography, Microstructure, and Analysis*, 10, 383-391.
- AVILA, J. A., RUCHERT, C. O. F. T., MEI, P. R., MARINHO, R. R., PAES, M. T. P., RAMIREZ, A. J., (2015) Fracture toughness assessment at different temperatures and regions within a friction stirred API 5L X80 steel welded plates. *Engineering Fracture Mechanics*, 147, 176-186.
- AYDIN H. (2014), Relationship between a bainitic structure and the hardness in the weld zone of the friction-stir welded X80 API-grade pipe-line steel. *Material Technology* 48(1), 15-22.
- BESHARATI-GIVI, M. K. & ASADI, P. (2014), *Advances in friction-stir welding and processing*, Woodhead Publishing, 1-19.
- BHATTACHARYYA, M., KUNDU, A., RAJA, K. S., DARSELL, J., JANA, S. & CHARIT, I. (2021), Processing-microstructure-property correlations for temperature-controlled friction stir welding of 304L SS plates. *Materials Science and Engineering: A*, 804, 140635.
- BISADI, H., RASAEI, S. & FARAHMAND, M. (2014), Effects of pin shape on the tool plunge stage in friction stir welding. *Transactions of the Indian Institute of Metals*, 67, 989-995.
- BREWER, L. N., BENNETT, M. S., BAKER, B., PAYZANT, E. A. & SOCHALSKI-KOLBUS, L. (2015), Characterization of residual stress as a function of friction stir

- welding parameters in oxide dispersion strengthened (ODS) steel MA956. *Materials Science and Engineering: A*, 647, 313-321.
- CALLISTER, W. D. & RETHWISCH, D. G. (2018). *Materials science and engineering: an introduction*, Wiley New York.
- CAO, F., HUANG, G., GUAN, W., HOU, W., NI, R., SHEN, Y. & LIU, Q. (2022), Inhomogeneous microstructure and properties along the thickness of stir zone in friction stir welded SAF 2507 super duplex stainless steel joint. *Journal of Manufacturing Processes*, 73, 611-623.
- ÇEVIK, B., ÖZÇATALBAŞ, Y. & GÜLENC, B. (2016) Effect of tool material on microstructure and mechanical properties in friction stir welding. *Materials Testing*, 58, 36-42.
- CHABOK, A. & DEHGHANI, K. (2013), Effect of processing parameters on the mechanical properties of interstitial free steel subjected to friction stir processing. *Journal of materials engineering and performance*, 22, 1324-1330.
- CHO, H. H., HONG, S.T., ROH, J. H., CHOI, H. S., KANG, S. H., STEEL, R. J., & HAN, H. N. (2013) Three-dimensional numerical and experimental investigation on friction stir welding processes of ferritic stainless steel, *Acta Materialia*, 61, 2649-2661.
- CHEN, J., FUJII, H., SUN, Y., MORISADA, Y., KONDOH, K. & HASHIMOTO, K. (2012), Effect of grain size on the microstructure and mechanical properties of friction stir welded non-combustive magnesium alloys. *Materials Science and Engineering: A*, 549, 176-184.
- CHEN, Y. C., FUJII, H., TSUMURA, T., KITAGAWA, Y., NAKATA, K., IKEUCHI, K., MATSUBAYASHI, K., MICHISHITA, Y., FUJIYA, Y. & KATOH, J. (2012). Banded structure and its distribution in friction stir processing of 316L austenitic stainless steel. *Journal of Nuclear Materials*, 420, 497-500.

- CHEN, T. & LIN, W.-B. (2010), Optimal FSW process parameters for interface and welded zone toughness of dissimilar aluminium–steel joint. *Science and Technology of Welding and Joining*, 15, 279-285.
- CUI, H., XIE, G., LUO, Z., MA, J., WANG, G. & MISRA, R. (2016), The microstructural evolution and impact toughness of nugget zone in friction stir welded X100 pipeline steel. *Journal of Alloys and Compounds*, 681, 426-433.
- CUI, L., FUJII, H., TSUJI, N. & NOGI, K. (2007), Friction stir welding of a high carbon steel. *Scripta materialia*, 56, 637-640.
- CULLITY, B. (1978), Elements of X-Ray Diffraction, Addition-Wesley Co. *Readings, MA*, 102.
- CZERWINSKI, F. 2011. Welding and joining of magnesium alloys. *Magnesium Alloys- Design, Processing and Properties*, 469-490.
- DARRAS, B. M. (2012), A model to predict the resulting grain size of friction-stir-processed AZ31 magnesium alloy. *Journal of materials engineering and performance*, 21, 1243-1248.
- DUAN, R., XIE, G., XUE, P., MA, Z., LUO, Z., WANG, C., MISRA, R. & WANG, G. (2021), Microstructural refinement mechanism and its effect on toughness in the nugget zone of high-strength pipeline steel by friction stir welding. *Journal of Materials Science & Technology*, 93, 221-231.
- EDWARDS, P. & RAMULU, M. (2010), Identification of process parameters for friction stir welding Ti–6Al–4V. *Journal of engineering materials and technology*, 132(3).
- EMAMI, S., SAEID, T. & KHOSROSHAHI, R. A. (2018), Microstructural evolution of friction stir welded SAF 2205 duplex stainless steel. *Journal of Alloys and Compounds*, 739, 678-689.

- ESPARZA, J., DAVIS, W. & MURR, L. (2003), Microstructure-property studies in friction-stir welded, Thixomolded magnesium alloy AM60, *Journal of Materials*, 38, 941-952.
- FAHIMPOUR, V., SADRNEZHAAD, S. & KARIMZADEH, F. (2012), Corrosion behavior of aluminum 6061 alloy joined by friction stir welding and gas tungsten arc welding methods. *Materials & Design*, 39, 329-333.
- GAN, W., OKAMOTO, K., HIRANO, S., CHUNG, K., KIM, C. & WAGONER, R. (2008), Properties of friction-stir welded aluminum alloys 6111 and 5083. *Journal of engineering materials and technology*, 130(3).
- GHOSH, M., KUMAR, K. & MISHRA, R. (2012), Process optimization for friction-stir welded martensitic steel. *Metallurgical and Materials Transactions A*, 43, 1966-1975.
- GENEVOIS, C. & DESCHAMPS, A. (2005), A. denquin, B. Doisneau-cottignies. *Acta Mater*, 53, 2447.
- GIORJÃO, R. A. R., PEREIRA, V. F., TERADA, M., DA FONSECA, E. B., MARINHO, R. R., GARCIA, D. M. & TSCHIPTSCHIN, A. P. 2019. Microstructure and mechanical properties of friction stir welded 8 mm pipe SAF 2507 super duplex stainless steel. *Journal of Materials Research and Technology*, 8, 243-249.
- HABIBI, M., HASHEMI, R., TAFTI, M. F. & ASSEMPOUR, A. 2018. Experimental investigation of mechanical properties, formability and forming limit diagrams for tailor-welded blanks produced by friction stir welding. *Journal of Manufacturing Processes*, 31, 310-323.
- HAJIAN, M., ABDOLLAH-ZADEH, A., REZAEI-NEJAD, S. S., ASSADI, H., HADAVI, S. M. M., CHUNG, K. & SHOKOUHIMEHR, M. (2015), Microstructure and mechanical properties of friction stir processed AISI 316L stainless steel. *Materials & Design*, 67, 82-94.

- HAN, W., KIMURA, A., TSUDA, N., SERIZAWA, H., CHEN, D., JE, H., FUJII, H., HA, Y., MORISADA, Y. & NOTO, H. (2014), Effects of mechanical force on grain structures of friction stir welded oxide dispersion strengthened ferritic steel. *Journal of Nuclear Materials*, 455, 46-50.
- HEIDARIAN, M. & MOSTAFAPOOR, S. (2022), Microstructure and Mechanical Properties of Friction Stir Processed AISI 316 Stainless Steel: Evaluation of the Effect of Cooling Media and Multi-Step Processing on Microstructure and Mechanical Properties of Friction Stir Processed AISI 316 Stainless Steel. *Metallography, Microstructure, and Analysis*, 11,72-87.
- HIRASAWA, S., BADARINARAYAN, H., OKAMOTO, K., TOMIMURA, T. & KAWANAMI, T. (2010), Analysis of effect of tool geometry on plastic flow during friction stir spot welding using particle method. *Journal of materials processing technology*, 210, 1455-1463.
- HUMPHREYS, F. J. & HATHERLY, M. (2012), Recrystallization and related annealing phenomena, *Elsevier*.
- HUSAIN, M. M., SARKAR, R., PAL, T. K., PRABHU, N. & GHOSH, M. (2015), Friction Stir Welding of Steel: Heat Input, Microstructure, and Mechanical Property Correlation. *Journal of Materials Engineering and Performance*, 24, 3673-3683.
- IMAM, M., UEJI, R. & FUJII, H. (2015), Microstructural control and mechanical properties in friction stir welding of medium carbon low alloy S45C steel. *Materials Science and Engineering: A*, 636, 24-34.
- IMAM, M., UEJI, R. & FUJII, H. (2016), Effect of online rapid cooling on microstructure and mechanical properties of friction stir welded medium carbon steel. *Journal of Materials Processing Technology*, 230, 62-71.

- JAFARZADEGAN, M., FENG, A., ABDOLLAH-ZADEH, A., SAEID, T., SHEN, J. & ASSADI, H. (2012), Microstructural characterization in dissimilar friction stir welding between 304 stainless steel and st37 steel. *Materials Characterization*, 74, 28-41.
- KALLEE, S., LOHWASSER, D. & CHEN, Z.(2010), Friction Stir Welding-from basics to application. Woodhead Publishing, Cambridge, 118-163.
- KALVALA, P. R., AKRAM, J., MISRA, M., RAMACHANDRAN, D. & GABBITA, J. R. (2016), Low temperature friction stir welding of P91 steel. *Defence Technology*, 12, 285-289.
- KANG, S. H., VASUDEVAN, M., NOH, S., JIN, H. J., JANG, J. & KIM, T. K. (2016). Friction stir welding of F/M ODS steel plug and F/M steel tube. *Fusion Engineering and Design*, 109, 182-185.
- KARAMI, S., JAFARIAN, H., EIVANI, A. R. & KHEIRANDISH, S. (2016), Engineering tensile properties by controlling welding parameters and microstructure in a mild steel processed by friction stir welding. *Materials Science and Engineering: A*, 670, 68-74.
- KHODIR, S., MORISADA, Y., UEJI, R. & FUJII, H. (2012), Microstructures and mechanical properties evolution during friction stir welding of SK4 high carbon steel alloy. *Materials Science and Engineering: A*, 558, 572-578.
- KRUMML, T., POLA, J., OBRTL, K. & DEGALLAIX, S. (1997). Dislocation structures in the bands of localised cyclic plastic strain in austenitic 316L and austenitic-ferritic duplex stainless steels. *Acta materialia*, 45, 5145-5151.
- KUMAR, S. S., MURUGAN, N. & RAMACHANDRAN, K. K. (2016). Influence of tool material on mechanical and microstructural properties of friction stir welded 316L austenitic stainless steel butt joints. *International Journal of Refractory Metals and Hard Materials*, 58, 196-205.

- KUMAR, S. S., MURUGAN, N. & RAMACHANDRAN, K. K. (2018). Microstructure and mechanical properties of friction stir welded AISI 316L austenitic stainless steel joints. *Journal of Materials Processing Technology*, 254, 79-90.
- KUMAR, S. S., MURUGAN, N. & RAMACHANDRAN, K. (2019). Identifying the optimal FSW process parameters for maximizing the tensile strength of friction stir welded AISI 316L butt joints. *Measurement*, 137, 257-271.
- KUMAR, S. S., MURUGAN, N. & RAMACHANDRAN, K. (2020). Effect of tool tilt angle on weld joint properties of friction stir welded AISI 316L stainless steel sheets. *Measurement*, 150, 107083.
- LAKSHMINARAYANAN, A. & BALASUBRAMANIAN, V. (2012a), Assessment of fatigue life and crack growth resistance of friction stir welded AISI 409M ferritic stainless steel joints. *Materials Science and Engineering: A*, 539, 143-153.
- LAKSHMINARAYANAN, A. & BALASUBRAMANIAN, V. (2012b), Assessment of sensitization resistance of AISI 409M grade ferritic stainless steel joints using Modified Strauss test. *Materials & Design*, 39, 175-185.
- LARSSON, H., KARLSSON, L., STOLTZ, S. & BERGQVIST, E. (2000), Joining of dissimilar Al-alloys by friction stir welding. 2nd International Symposium on Friction Stir Welding, 26-28.
- LEE, C.-Y., CHOI, D.-H., YEON, Y.-M. & JUNG, S.-B. (2009), Dissimilar friction stir spot welding of low carbon steel and Al-Mg alloy by formation of IMCs. *Science and Technology of Welding and Joining*, 14, 216-220.
- LEE, W.-B. & JUNG, S.-B. (2004), The joint properties of copper by friction stir welding. *Materials Letters*, 58, 1041-1046.

- LEE, W.-B., LEE, C.-Y., CHANG, W.-S., YEON, Y.-M. & JUNG, S.-B. (2005), Microstructural investigation of friction stir welded pure titanium. *Materials Letters*, 59, 3315-3318.
- LI, H., JIANG, Z., FENG, H., ZHANG, S., LI, L., HAN, P., MISRA, R. & LI, J. (2015), Microstructure, mechanical and corrosion properties of friction stir welded high nitrogen nickel-free austenitic stainless steel. *Materials & Design*, 84, 291-299.
- LI, H., MACKENZIE, D. & HAMILTON, R. (2010), Parametric finite-element studies on the effect of tool shape in friction stir welding. *Proceedings of the Institution of Mechanical Engineers, Part B: Journal of Engineering Manufacture*, 224, 1161-1173.
- LI, H., YANG, S., ZHANG, S., ZHANG, B., JIANG, Z., FENG, H., HAN, P. & LI, J. (2017), Microstructure evolution and mechanical properties of friction stir welding super-austenitic stainless steel S32654. *Materials & Design*, 118, 207-217.
- LI, J., SHEN, Y., HOU, W. & QI, Y. 2020. Friction stir welding of Ti-6Al-4V alloy: Friction tool, microstructure, and mechanical properties. *Journal of Manufacturing Processes*, 58, 344-354.
- LI, S., YANG, X., WANG, F., TANG, W. & LI, H. (2019), Microstructural characteristics and mechanical properties of friction-stir-welded modified 9Cr-1Mo steel. *Journal of Materials Science*, 54, 6632-6650.
- LIAO, J., YAMAMOTO, N. & NAKATA, K. (2009), Effect of dispersed intermetallic particles on microstructural evolution in the friction stir weld of a fine-grained magnesium alloy. *Metallurgical and Materials Transactions A*, 40, 2212-2219.
- LIN, Y., WU, X.-Y., CHEN, X.-M., CHEN, J., WEN, D.-X., ZHANG, J.-L. & LI, L.-T. (2015), EBSD study of a hot deformed nickel-based superalloy. *Journal of alloys and compounds*, 640, 101-113.

- LIU, F. C. & NELSON, T. W. (2016), In-situ material flow pattern around probe during friction stir welding of austenitic stainless steel. *Materials & Design*, 110, 354-364.
- MERAN, C. & KOVAN, V. (2008), Microstructures and mechanical properties of friction stir welded dissimilar copper/brass joints. *Materialwissenschaft und Werkstofftechnik: Entwicklung, Fertigung, Prüfung, Eigenschaften und Anwendungen technischer Werkstoffe*, 39, 521-530.
- MERAN, C., KOVAN, V. & ALPTEKIN, A. (2007), Friction stir welding of AISI 304 austenitic stainless steel. *Materialwissenschaft und Werkstofftechnik: Entwicklung, Fertigung, Prüfung, Eigenschaften und Anwendungen technischer Werkstoffe*, 38, 829-835.
- MESHARAM, M. P., KODLI, B. K. & DEY, S. R. (2014), Friction Stir Welding of Austenitic Stainless Steel by PCBN Tool and its Joint Analyses. *Procedia Materials Science*, 6, 135-139.
- MESHARAM, S. D., PARADKAR, A. G., REDDY, G. M. & PANDEY, S. (2017), Friction stir welding: An alternative to fusion welding for better stress corrosion cracking resistance of maraging steel. *Journal of manufacturing processes*, 25, 94-103.
- MIRONOV, S., SATO, Y. S., KOKAWA, H., INOUE H. & TSUGE, S., (2011) Structural response of superaustenitic stainless steel to friction stir welding, *Acta Materialia*, 59, 5472-5481.
- MISHRA, R. S. & MA, Z. (2005), Friction stir welding and processing. *Materials science and engineering: R: reports*, 50, 1-78.
- MISHRA, R. & JEGANATHAN, V. (2017), Experimental investigation on friction stir welding of copper alloys. *International Journal of Research in Engineering and Innovation*, 1, 66-78.

- MISHRA, R. S., DE, P. S. & KUMAR, N. (2014a), Fundamentals of the friction stir process. Friction Stir Welding and Processing. *Science and Engineering. Springer International Publishing*, Cham, 13-58.
- MISHRA, R. S., DE, P. S. & KUMAR, N. (2014b), Friction stir welding configurations and tool selection. *Friction Stir Welding and Processing. Science and Engineering. Springer International Publishing*, Cham 95-108.
- MISHRA, R. S., DE, P. S. & KUMAR, N. (2014c), FSW of aluminum alloys. *Friction Stir Welding and Processing. Science and Engineering. Springer International Publishing*, Cham 109-148.
- MISHRA, R. S., DE, P. S. & KUMAR, N. (2014d), Introduction. In: Friction Stir Welding and Processing: Science and Engineering. *Springer International Publishing*, Cham, 1-11.
- MIURA, T., UEJI, R. & FUJII, H. (2015), Enhanced tensile properties of Fe–Ni–C steel resulting from stabilization of austenite by friction stir welding. *Journal of Materials Processing Technology*, 216, 216-222.
- MURTHY, K. K. & SUNDARESAN, S. 1998. Phase transformations in a welded near- α titanium alloy as a function of weld cooling rate and post-weld heat treatment conditions. *Journal of Materials Science*, 33, 817-826.
- MIYANO, Y., FUJII, H., SUN, Y., KATADA, Y., KURODA, S. & KAMIYA, O. (2011), Mechanical properties of friction stir butt welds of high nitrogen-containing austenitic stainless steel. *Materials Science and Engineering: A*, 528, 2917-2921.
- NAGARAJ, M. & RAVISANKAR, B. (2018), Enhancing the strength of structural steel through severe plastic deformation based thermomechanical treatment. *Materials Science and Engineering: A*, 738, 420-429.

- NAKATA, K. (2005), Friction stir welding of copper and copper alloys. *Welding international*, 19, 929-933.
- NAKATA K, INOKI S, NAGANO Y, HASHIMOTO T, JOHGAN S, Ushio M (2001), Proceedings of 3rd International Friction Stir Welding Symposium: Kobe, Japan. In: International Friction Stir Welding Symposium, [Cambridge], TWI Ltd..
- NANDAN, R., DEBROY, T. & BHADESHIA, H. (2008), Recent advances in friction-stir welding—process, weldment structure and properties. *Progress in materials science*, 53, 980-1023.
- NATHAN, S. R., BALASUBRAMANIAN, V., MALARVIZHI, S. & RAO, A. (2016), An investigation on metallurgical characteristics of tungsten based tool materials used in friction stir welding of naval grade high strength low alloy steels. *International Journal of Refractory Metals and Hard Materials*, 56, 18-26.
- PANDEY, C., GIRI, A. & MAHAPATRA, M. (2016), Evolution of phases in P91 steel in various heat treatment conditions and their effect on microstructure stability and mechanical properties. *Materials Science and Engineering: A*, 664, 58-74.
- PANDEY, C. & MAHAPATRA, M. (2016), Effect of long-term ageing on the microstructure and mechanical properties of creep strength enhanced ferritic P91 steel. *Transactions of the Indian Institute of Metals*, 69, 1657-1673.
- PANDEY, C., MAHAPATRA, M., KUMAR, P., SAINI, N. & SRIVASTAVA, A. (2017), Microstructure and mechanical property relationship for different heat treatment and hydrogen level in multi-pass welded P91 steel joint. *Journal of Manufacturing Processes*, 28, 220-234.
- PANDEY, C., MAHAPATRA, M. M., KUMAR, P. & SAINI, N. (2018), Some studies on P91 steel and their weldments. *Journal of Alloys and Compounds*, 743, 332-364.

- PAREEK, M., POLAR, A., RUMICHE, F. & INDACOCHEA, J. (2007), Metallurgical evaluation of AZ31B-H24 magnesium alloy friction stir welds. *Journal of materials engineering and performance*, 16, 655-662.
- PARK, H. S., KIMURA, T., MURAKAMI, T., NAGANO, Y., NAKATA, K. & USHIO, M. (2004), Microstructures and mechanical properties of friction stir welds of 60% Cu–40% Zn copper alloy. *Materials Science and Engineering: A*, 371, 160-169.
- PARK, S. H. C., SATO, Y. S., KOKAWA, H., OKAMOTO, K., HIRANO, S. & INAGAKI, M. (2003), Rapid formation of the sigma phase in 304 stainless steel during friction stir welding. *Scripta Materialia*, 49, 1175-1180.
- PASTA, S. & REYNOLDS, A. P. (2008), Residual stress effects on fatigue crack growth in a Ti-6Al-4V friction stir weld. *Fatigue & Fracture of Engineering Materials & Structures*, 31, 569-580.
- PAUL, V. T., SAROJA, S. & VIJAYALAKSHMI, M. (2008), Microstructural stability of modified 9Cr–1Mo steel during long term exposures at elevated temperatures. *Journal of Nuclear Materials*, 378, 273-281.
- PEEL, M., STEUWER, A., PREUSS, M. & WITHERS, P. 2003. Microstructure, mechanical properties and residual stresses as a function of welding speed in aluminium AA5083 friction stir welds. *Acta materialia*, 51, 4791-4801.
- PRADO, R., MURR, L., SHINDO, D. & SOTO, K. (2001), Tool wear in the friction-stir welding of aluminum alloy 6061+20% Al₂O₃: a preliminary study. *Scripta materialia*, 45, 75-80.
- PULI, R. & RAM, G. J. (2012), Dynamic recrystallization in friction surfaced austenitic stainless steel coatings. *Materials characterization*, 74, 49-54.
- RAI, R., DE, A. & BHADESHIA, H. H., and DebRoy, T. (2011), Review: friction stir welding tools. *Science and Technology of Welding and Joining*, 16, 325.

- RAJASEKARAN, R., LAKSHMINARAYANAN, A., DAMODARAM, R. & BALASUBRAMANIAN, V. (2021), Stress corrosion cracking failure of friction stir welded nuclear grade austenitic stainless steel. *Engineering Failure Analysis*, 120, 105012.
- RAMESH, R., DINAHARAN, I., KUMAR, R. & AKINLABI, E. (2017), Microstructure and mechanical characterization of friction stir welded high strength low alloy steels. *Materials Science and Engineering: A*, 687, 39-46.
- RAMESH, R., DINAHARAN, I., KUMAR, R. & AKINLABI, E. (2019), Microstructure and mechanical characterization of friction-stir-welded 316L austenitic stainless steels. *Journal of Materials Engineering and Performance*, 28, 498-511.
- RAZAL ROSE, A., MANISEKAR, K. & BALASUBRAMANIAN, V. (2012), Influences of welding speed on tensile properties of friction stir welded AZ61A magnesium alloy. *Journal of materials engineering and performance*, 21, 257-265.
- REYNOLDS, A. P., HOOD, E. & TANG, W. (2005), Texture in friction stir welds of Timetal 21S. *Scripta materialia*, 52, 491-494.
- REYNOLDS, A. P., TANG, W., GNAUPEL-HEROLD, T. & PRASK, H. (2003), Structure, properties, and residual stress of 304L stainless steel friction stir welds. *Scripta materialia*, 48, 1289-1294.
- RODRIGUES, D., LOUREIRO, A., LEITAO, C., LEAL, R., CHAPARRO, B. & VILAÇA, P. (2009), Influence of friction stir welding parameters on the microstructural and mechanical properties of AA 6016-T4 thin welds. *Materials & Design*, 30, 1913-1921.
- RONEVICH, J. A., SOMERDAY, B. P. & FENG, Z. (2017), Hydrogen accelerated fatigue crack growth of friction stir welded X52 steel pipe. *International Journal of Hydrogen Energy*, 42, 4259-4268.

- SABOONI, S., KARIMZADEH, F., ENAYATI, M. H. & NGAN, A. H. W. (2015), Friction-stir welding of ultrafine grained austenitic 304L stainless steel produced by martensitic thermomechanical processing. *Materials & Design*, 76, 130-140.
- SANTOS, T., HERMENEGILDO, T., AFONSO, C., MARINHO, R., PAES, M. & RAMIREZ, A. (2010), Fracture toughness of ISO 3183 X80M (API 5L X80) steel friction stir welds. *Engineering Fracture Mechanics*, 77, 2937-2945.
- SARMA, J., KUMAR, R., SAHOO, A. K. & PANDA, A. 2020. Enhancement of material properties of titanium alloys through heat treatment process: A brief review. *Materials Today: Proceedings*, 23, 561-564.
- SATO, Y., NELSON, T., STERLING, C., STEEL, R. & PETTERSSON, C.-O. (2005), Microstructure and mechanical properties of friction stir welded SAF 2507 super duplex stainless steel. *Materials Science and Engineering: A*, 397, 376-384.
- SAWADA, K., HARA, T., TABUCHI, M., KIMURA, K. & KUBUSHIRO, K. (2015), Microstructure characterization of heat affected zone after welding in Mod. 9Cr-1Mo steel. *Materials Characterization*, 101, 106-113.
- SHASHI KUMAR, S., MURUGAN, N. & RAMACHANDRAN, K. K. (2016), Influence of tool material on mechanical and microstructural properties of friction stir welded 316L austenitic stainless steel butt joints. *International Journal of Refractory Metals and Hard Materials*, 58, 196-205.
- SONG, K. H., FUJII, H. & NAKATA, K. (2009), Effect of welding speed on microstructural and mechanical properties of friction stir welded Inconel 600. *Materials & Design*, 30, 3972-3978.
- SORENSEN, C. & NIELSEN, B. (2009), Exploring geometry effects for convex scrolled shoulder, step spiral probe FSW tools. *Proc. TMS 2009 Annual Meet., San Francisco, CA, USA*, 85-92.

- STEVENSON, R., TOUMPIS, A. & GALLOWAY, A. (2015), Defect tolerance of friction stir welds in DH36 steel. *Materials & Design*, 87, 701-711.
- SUNILKUMAR, D., MUTHUKUMARAN, S., VASUDEVAN, M. & REDDY, G. M. (2021), Microstructure and mechanical properties relationship of friction stir-and A-GTA-welded 9Cr-1Mo to 2.25 Cr-1Mo steel. *Journal of Materials Engineering and Performance*, 30, 1221-1233.
- SUTTON, M. A., YANG, B., REYNOLDS, A. P. & YAN, J. (2004), Banded microstructure in 2024-T351 and 2524-T351 aluminum friction stir welds: Part II. Mechanical characterization. *Materials Science and Engineering: A*, 364, 66-74.
- TANG, W., YANG, X., LI, S. & LI, H. (2019), Microstructure and properties of CLAM/316L steel friction stir welded joints. *Journal of Materials Processing Technology*, 271, 189-201.
- TAKAHARA, H., TSUJIKAWA, M., CHUNG, S. W., OKAWA, Y., HIGASHI, K. & OKI, S. (2008), Optimization of welding condition for nonlinear friction stir welding. *Materials transactions*, 49, 1359-1364.
- THOMAS, W. M. & DOLBY, R. (2003), Friction stir welding developments. *Proceedings of the sixth international trends in welding research*, 203-211.
- THREADGILL, P., LEONARD, A., SHERCLIFF, H. & WITHERS, P. (2009), Friction stir welding of aluminium alloys. *International Materials Reviews*, 54, 49-93.
- TINGEY, C., GALLOWAY, A., TOUMPIS, A. & CATER, S. (2015), Effect of tool centreline deviation on the mechanical properties of friction stir welded DH36 steel. *Materials & Design (1980-2015)*, 65, 896-906.
- TOLEPHIH, M. H., MASHLOOSH, K. M. & WAHEED, Z. (2011), Comparative study of the mechanical properties of (FS) and MIG welded joint in (AA7020-T6) aluminum alloy. *Al-khwarizmi engineering journal*, 7, 22-35.

- VAN ROOYEN, N., BHATTACHARYYA, M., CHARIT, I. & MAUGHAN, M. R. (2022), Indentation investigation of 304L stainless steel friction stir weld simulated crack repair. *Materials Science and Engineering: A*, 142691.
- WEI, L. & NELSON, T. W. (2012), Influence of heat input on post weld microstructure and mechanical properties of friction stir welded HSLA-65 steel. *Materials Science and Engineering: A*, 556, 51-59.
- XUNHONG, W. & KUAISHE, W. (2006), Microstructure and properties of friction stir butt-welded AZ31 magnesium alloy. *Materials Science and Engineering: A*, 431, 114-117.
- YANG, J., WANG, D., XIAO, B., NI, D. & MA, Z. (2013), Effects of rotation rates on microstructure, mechanical properties, and fracture behavior of friction stir-welded (FSW) AZ31 magnesium alloy. *Metallurgical and Materials Transactions A*, 44, 517-530.
- ZHANG, C., CUI, L., LIU, Y., LIU, C. & LI, H. (2018a), Microstructures and mechanical properties of friction stir welds on 9% Cr reduced activation ferritic/martensitic steel. *Journal of Materials Science & Technology*, 34, 756-766.
- ZHANG, C., CUI, L., WANG, D., LIU, Y. & LI, H. (2018b), Effect of microstructures to tensile and impact properties of stir zone on 9% Cr reduced activation ferritic/martensitic steel friction stir welds. *Materials Science and Engineering: A*, 729, 257-267.
- ZHANG, Y., CAO, X., LAROSE, S. & WANJARA, P. (2012), Review of tools for friction stir welding and processing. *Canadian Metallurgical Quarterly*, 51, 250-261.
- ZHANG, Y., SATO, Y. S., KOKAWA, H., PARK, S. H. C. & HIRANO, S. (2008a), Microstructural characteristics and mechanical properties of Ti-6Al-4V friction stir welds. *Materials Science and Engineering: A*, 485, 448-455.

ZHANG, Y., SATO, Y. S., KOKAWA, H., PARK, S. H. C. & HIRANO, S. (2008b), Stir zone microstructure of commercial purity titanium friction stir welded using pcBN tool. *Materials Science and Engineering: A*, 488, 25-30.

ZHAO, Y., DONG, C., JIA, Z., YOU, J., TAN, J., MIAO, S. & YI, Y. (2021), Microstructure characteristics and corrosion resistance of friction stir welded 2205 duplex stainless steel. *Advances in Materials Science and Engineering*, 2021.

Suresh Gain
28/02/2023